J/ψ in pA

Maarten Bruinsma

J/ψ in pA

Performance of the First Level Trigger of Hera-B and Nuclear Effects in J/ψ Production

J/ψ productie in proton-kern botsingen

(met een samenvatting in het Nederlands)

PROEFSCHRIFT

ter verkrijging van de graad van doctor
aan de Universiteit Utrecht op gezag van
de Rector Magnificus Prof.Dr. W.H. Gispen,
ingevolge het besluit van het College voor Promoties
in het openbaar te verdedigen op
woensdag 15 mei 2002 des ochtends te 10:30 uur

door

Maarten Bruinsma

geboren op 17 november 1971 te 's Gravenhage

promotor: Prof.Dr. P.M. Kooijman
Faculteit der Natuur- en Sterrenkunde, Universiteit Utrecht
co-promotor: Dr. Th.S. Bauer
Nationaal Instituut voor Kernfysica en Hoge-Energie Fysica (NIKHEF)

ISBN 90 - 393 - 3032 - 8

Dit proefschrift werd mede mogelijk gemaakt met financiële steun van de Stichting voor Fundamenteel Onderderzoek de Materie (FOM).

voor al mijn ouders

Table of Contents

Preface

"Quand le mystère est trop impressionnant,
on n'ose pas désobéir."
Antoine de Saint-Exupéry, *Le Petit Prince*

In 1964 a group of physicists from Princeton University discovered a violation of CP invariance in the decay of neutral kaons [1]. This phenomenon ultimately distinguishes matter and antimatter and is thought to be necessary for understanding the abundance of matter over antimatter in the universe [2]. The origin of the CP asymmetry is one of the fundamental questions of particle physics.

In 1973, Japanese physicists Kobayashi and Maskawa showed how to incorporate CP violation into the theoretical framework of electro-magnetic and weak forces [3]. They showed that a CP asymmetry arises naturally in the Standard Model if a third generation of quarks existed. The discovery of the predicted quarks [4, 5] provided compelling support of their hypothesis. However, a direct test of the Kobayashi-Maskawa model became possible only with the development of more advanced particle spectrometers.

The Hera-B experiment, where the research for this thesis has been done, was built to test the model of Kobayashi and Maskawa by measuring CP violation in B mesons. The model gave a clear prediction of how CP violation would show up as an asymmetry in the decay $B^0 \to J/\psi\, K^0_S$, but these predictions could never be confirmed before. Hera-B could be the first to prove them right (or wrong).

The principle of the Hera-B experiment is to exploit the existing proton beam of the HERA accelerator in Hamburg to produce the 10^{14} inelastic interactions needed for the measurement. A large particle spectrometer with particle identification sub-detectors registers these interactions. A unique trigger system, specifically designed to find J/ψ mesons in the abundant background, sifts on-line through these events to select 0.001% of possibly interesting events that should be recorded on tape.

The detector and the trigger system were foreseen to be completely installed in 1998. However, due to technological setbacks, they are yet to be commissioned. It has become clear meanwhile that the experiment will not be able to do a competitive measurement of CP violation in B decays.

Still, even with a trigger efficiency that is lower than designed, Hera-B records J/ψ mesons at unprecedented rates. J/ψ production in proton-nucleus and nucleus-nucleus collisions is currently under much interest of particle physicists. It is believed

that a study of J/ψ production can reveal the clearest evidence of a 'quark-gluon plasma', a state of matter of freely floating quarks and gluons. This state is believed to have been present at the earliest stages of the universe, and reproduced in frontal collisions of heavy ions. Since the collisions at HERA-B do not meet the conditions in which a quark-gluon plasma will occur, the experiment can measure in detail the baseline nuclear effects present in J/ψ production. These measurements are necessary to interpret the J/ψ data from heavy ion experiments such as NA50/NA60 at CERN and PHENIX at RHIC.

Outline

This thesis consists of two, essentially independent, parts: a study of the First Level Trigger performance and a measurement of nuclear effects in J/ψ production.

After giving an overview of the experiment in chapter 1 we present a more detailed description of the First Level Trigger in chapter 2.

The analysis of the performance of the First Level Trigger in the subsequent two chapters is confined to the reconstruction of $J/\psi \to e^+e^-$ decays. In chapter 3 we present an analysis of the performance of the ECAL pretrigger. The performance of the installed hardware and the resolution and efficiency of the pretrigger reconstruction algorithm are analysed in detail. We also give suggestions for improving the pretrigger performance in future running.

An analysis of the tracking performance of the First Level Trigger is given in chapter 4. The performance of the Outer Tracker, the data transmission and the FLT hardware in 2000 are analysed. The track parameter and momentum resolution are studied for electrons from a J/ψ and the track finding efficiency is measured from 2000 data and estimated for the next running.

The study on nuclear effects in J/ψ production from data taken in 2000 is presented in chapters 5 to 9. It can be considered as a pioneering study of effects which will be explored at Hera-B with high precision in the near future.

An overview of the theory of J/ψ production in proton-nucleus interactions is given in chapter 5. In chapter 6 we describe and analyse methods to measure the ratio of the luminosity, shared by two target wires. In chapter 7 we determine the J/ψ yield through the decays $J/\psi \to \mu^+\mu^-$ and $J/\psi \to e^+e^-$ and measure the A dependence of the J/ψ production cross section.

A study on the multiplicity and pseudo-rapidity of particles, produced in association with a J/ψ, is described in chapter 8. We also show how the associated particles can provide information on the collision and measure the dependence of the p_T of J/ψ on the multiplicity.

The thesis is concluded with a summary of the most important observations.

Chapter 1

The Hera-B experiment

In this chapter we describe the target and the detector of HERA-B. The emphasis is on sub-detectors and issues that are important for the analyses performed in this thesis. An overview of the trigger and the data acquisition is also given. The chapter is concluded with a summary of the updated physics program of HERA-B.

1.1 Purpose and design of Hera-B

The HERA-B experiment has been designed to measure CP violation in the 'golden' decay $\overline{\mathrm{B}}^0/\mathrm{B}^0 \to \mathrm{J}/\psi\,\mathrm{K}^0_\mathrm{S}$. An interference between $\mathrm{B}^0 - \overline{\mathrm{B}}^0$ mixing and the decay gives rise to a measurable difference in the decay width for $\mathrm{B}^0 \to \mathrm{J}/\psi\,\mathrm{K}^0_\mathrm{S}$ and $\overline{\mathrm{B}}^0 \to \mathrm{J}/\psi\,\mathrm{K}^0_\mathrm{S}$. In kaon decays, CP violation is already well established. The CP violation effects in B decays, however, can be more cleanly related to an irreducible complex phase in the CKM matrix of the standard model.

Although this measurement is no longer part of the physics program of HERA-B, it has been decisive in the requirements for the target, the detector and the trigger. The experiment has been built to reconstruct as many $\mathrm{B}^0 \to \mathrm{J}/\psi\,\mathrm{K}^0_\mathrm{S}$ decays as possible. The decay $\mathrm{B}^0 \to \mathrm{J}/\psi\,\mathrm{K}^0_\mathrm{S}$ has a branching fraction of only 4.5×10^{-4}. The experimental detection of this decay is, however, relatively easy. Both the J/ψ and the K^0_S have an unambiguous signature.

The J/ψ decays to a lepton pair with a branching ratio of 12%. These leptons can be separated from hadrons with particle identification detectors. In contrast to the more abundant directly produced J/ψ, a J/ψ from a B meson is significantly detached from the primary interaction point. Due to their long lifetime ($\tau_\mathrm{B} = 1.6$ ps) and the relatively high momentum ($\langle p_\mathrm{B} \rangle$ =121 GeV/c), B mesons travel on average 10.7 mm before decaying. Conversely, a detached J/ψ must have originated from a B.

The K^0_S is reconstructed through the decay $\mathrm{K}^0 \to \pi^+\pi^-$, which has a branching ratio of 69%. At HERA-B, the K^0_S travels on average approximately 50 cm before decaying, a signature that is not easily mimicked by background.

In order to do a significant measurement of CP violation, approximately 1000 fully reconstructed $\mathrm{B}^0 \to \mathrm{J}/\psi\,\mathrm{K}^0_\mathrm{S}$ decays are needed. Taking into account the branching ratios and the efficiencies for reconstruction and flavour determination, a sample of the

order of 10^9 B mesons must be produced.

HERA-B produces B mesons in fixed target pA collisions at a centre-of-mass energy of $\sqrt{s} = 41.6$ GeV. At this energy, the $b\bar{b}$ production cross section is approximately 20 nb. Since the total inelastic cross section ranges between 10 and 20 mb per nucleon, only about one in a million inelastic interactions will produce a B meson. A total of 5×10^{14} inelastic interactions must be produced in order to obtain the required sample of golden B decays. If this sample is to be recorded within one year of data taking (10^7s), the rate of inelastic interactions must be no less than 40 MHz.

This interaction rate, combined with the extreme signal to background ratio of $\mathcal{O}(10^{-11})$, imposes a challenge to the detector and trigger that is unique among high-energy physics experiments.

1.2 HERA

The HERA-B experiment is one of four experiments in HERA[1], the largest accelerator of DESY[2], a large particle physics laboratory in Hamburg, Germany. HERA is a storage ring facility that can accelerate protons to 920 GeV and electrons or positrons to 30 GeV. The protons and electrons/positrons run in opposite directions in two separate beam pipes, installed in a quasi-circular ring of 6336 m circumference. The main objective of HERA, whose construction was completed in 1992, is to produce electron-proton collisions at high centre-of-mass energies.

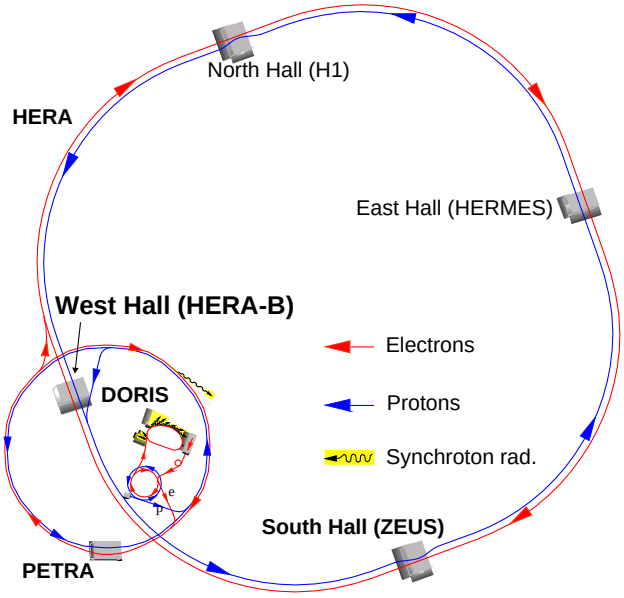

Figure 1.2.1: *The HERA accelerator and its pre-accelerators. HERA accelerates and stores a proton beam of 920 GeV and an electron beam of 30 GeV in two intertwining storage rings of 6.3 km length. The older accelerators at DESY, DESY III and PETRA now function as pre-accelerators. The Hera-B detector is one of four detectors installed in HERA.*

The HERA proton ring contains 220 bunches, of which only 180 are actually filled. Since the pre-accelerator PETRA has room for 60 bunches and DESY III for 10, the filling scheme shown in figure 1.2.2 naturally arises. The last 15 bunches remain empty to enable a safe dump of the beam. Each of the proton bunches contains approximately

[1] Hadron-Elektron-Ring-Anlage
[2] Deutsches Elektronen Synchrotron

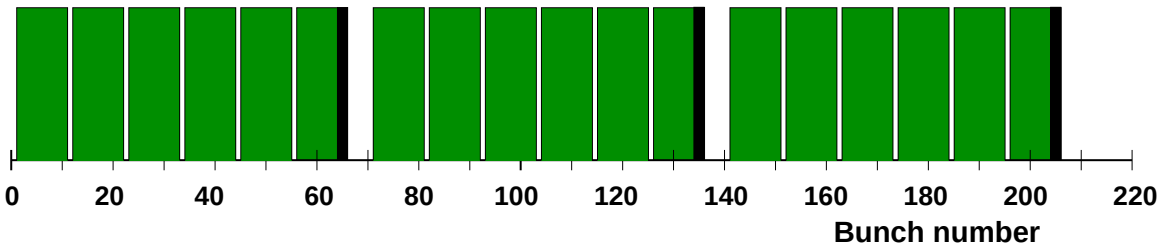

Figure 1.2.2: *Filling scheme of proton bunches in HERA. Three trains of 60 proton bunches are each headed by two pilot bunches. The 180 filled proton bunches consist of approximately* 10^{11} *protons each and are separated by 96ns.*

10^{11} protons. The bunches are 30 cm (1 ns) long and are separated from each other by a bunch crossing period of 96 ns.

The HERA ring contains four straight sections of 360 m, in which four large experiments are installed. The experiments ZEUS and H1, located in the south and north halls, respectively, use the colliding proton and electron beams for deep-inelastic scattering measurements. HERMES, situated in the east hall, uses the polarised electron beam and a polarised gas target for measurements of the spin structure of the nucleon. The HERA-B experiment, where the research for this thesis was done, is located in experimental hall West. It uses the proton beam of HERA for fixed target collisions.

beam circumference	6336 m
proton beam energy (after 1998)	920 GeV
typical proton current	100 mA
number of bunches(filled)	220(180)
bunch spacing	96 ns
proton bunch length	∼1 ns
$\sqrt{s}$ at HERA-B	41.6 GeV
HERA-B luminosity	$\sim 10^{33}$ cm^{-2}s^{-1} (tunable)

Table 1.2.1: *Parameters of the HERA proton beam during running in 2000.*

1.3 The target system

The HERA-B experiment is in principle not limited by luminosity. However, at most about five simultaneous inelastic proton-nucleon interactions can be resolved by the HERA-B detector. More than this would lead to too high an occupancy, jeopardising a good identification of tracks. The simultaneous interactions should be well separated in space, so that they can be resolved individually.

The target system consists of two stations of four wires each, positioned around the proton beam axis as depicted in figure 1.3.1. These wires can be inserted individually

or jointly in the halo of the proton beam, approximately 4-6σ (transverse beam width) from the beam centre, until the desired interaction rate is achieved.

Protons in the halo do not contribute to the luminosity for the two e-p collider experiments. Instead, they would likely drift further to the aperture boundaries and be absorbed by one of the collimators. These protons are efficiently used during HERA-B data taking: approximately 50% of the total proton loss was due to inelastic interactions at HERA-B.

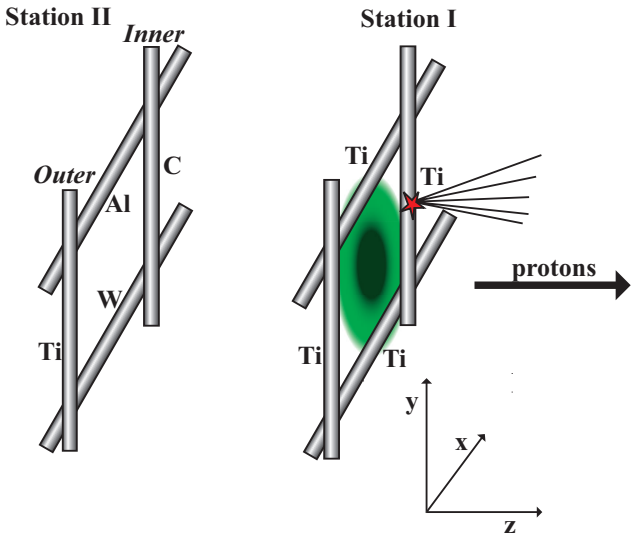

Figure 1.3.1: *The target system consist of eight wires of different materials, positioned in the halo of the proton beam. The wires can be moved inwards or outwards until the desired luminosity is reached. In 2000, data has been taken with a titanium (Below I) and carbon (Inner II) wire inserted at the same time. The total interaction rate was usually 5 MHz.*

1.3.1 Choice of target materials

The choice of target materials is subject to several considerations. While passing through a target wire, the proton is subject to multiple scattering, which is the main cause of inefficient proton loss and increased background. For this reason target materials with small atomic number are preferred. On the other hand, the production of $b\bar{b}$ events relative to inelastic interactions should be as large as possible. Since b production approximately scales with the mass number A and inelastic interaction with $A^{0.72}$, this favours heavy nuclei. The charged track multiplicity per inelastic interaction, however, increases with $A^{0.2}$. This makes interactions on target with large A more difficult to reject at the trigger level and more difficult to reconstruct.

Since it was not a priori clear what would be the optimal choice, several target materials were installed. During the commissioning of the detector, prior to the data taking in July and August 2000, the outer and upper wires caused significant background problems. This rendered them unusable for physics running. The tungsten wire (Below II), the heaviest of the targets installed, gave rise to large fluctuations in the interaction rate, presumably due to large scattering inside the heavy material and the smoothness of the surface. As a result, only a carbon (Inner II wire) and a titanium (Below I) target could be used. Characteristic parameters of these target materials are shown in table 1.3.1.

Target	A	X_0	σ_{tot} (λ_{tot})	σ_{inel} (λ_{inel})	$\langle n_{ch} \rangle$
C	12.01	18.8 cm	331 mb (60 g/cm^2)	231 mb (86 g/cm^2)	14.2 $\pm$ 0.1
Ti	47.88	3.56 cm	995 mb (80 g/cm^2)	637 mb (125 g/cm^2)	18.0 $\pm$ 0.1

Table 1.3.1: *Atomic number (A), radiation length (X_0), total cross section (σ_{tot}) (mean free path due to all collisions (λ_{tot})) , inelastic cross section (σ_{inel}) (mean free path due to inelastic collisions (λ_{inel})) and average charged track multiplicity per interaction for the target materials used in this analysis. Cross sections are for 60-240 GeV nucleon projectiles. From [6], $\langle n_{ch} \rangle$ from [7].*

1.3.2 Interaction rate monitoring

The interaction rate is continuously monitored by a scintillator hodoscope. This hodoscope registers the passage of one or more charged particles. The number of interactions for a particular bunch i is distributed according to Poisson statistics.

$$P(N;\mu_i) = \frac{\mu_i^N e^{-\mu_i}}{N!}, \tag{1.3.1}$$

where μ_i is the average number of interactions for bunch i. The total interaction rate can be measured by determining the number of non-empty events. The count rate $R_{\rm hod}$, as measured by a hodoscope with acceptance $\mathcal{A}$, is then proportional to the number of events with one or more interactions:

$$R_{\rm hod} = \frac{1}{220 \times 96 \ \ {\rm ns}} \sum_{i=1}^{180} (1 - e^{-\mu_i \mathcal{A}}), \tag{1.3.2}$$

since only 180 of the 220 bunches are filled. If the acceptance of the hodoscope is sufficiently small, so that $A\mu_i \ll 1$, the interaction rate is proportional to the hodoscope rate:

$$R_{\rm int} \equiv \frac{1}{220 \times 96 \ \ {\rm ns}} \sum_{i=1}^{180} \mu_i \approx \frac{R_{\rm hod}}{\mathcal{A}}. \tag{1.3.3}$$

The interaction rate is set to a fixed value before data taking. The target wires automatically move into the halo of the proton beam until the desired target rate is achieved. During data taking, the wires will slowly move inwards as the halo gets depleted of protons because of target operation. Continuous feedback between the hodoscope counters and the target steering mechanics provides a stable interaction rate at the desired value.

1.3.3 Rate sharing among target wires

The multiple interactions per event should be equally distributed among the inserted target wires. This minimises the probability that two or more interactions occur on a single target wire, which would be difficult to disentangle.

Each of the target wires is equipped with a charge integrator, which measures the current of δ-electrons induced by the protons passing through the target wire. This current is transformed to an output frequency that is proportional to the number of inelastic interactions produced on that wire. A battery provides a baseline frequency to the charge integrator output.

Unfortunately, this baseline was not stable during data taking in 2000. As a result, the relative contributions of the target wires fluctuated significantly, as shown in figure 1.3.2. An accurate determination of the relative target contributions is essential for the measurement presented in this thesis. We will not rely on the charge integrators, but re-evaluate the relative target contributions from data (chapter 6).

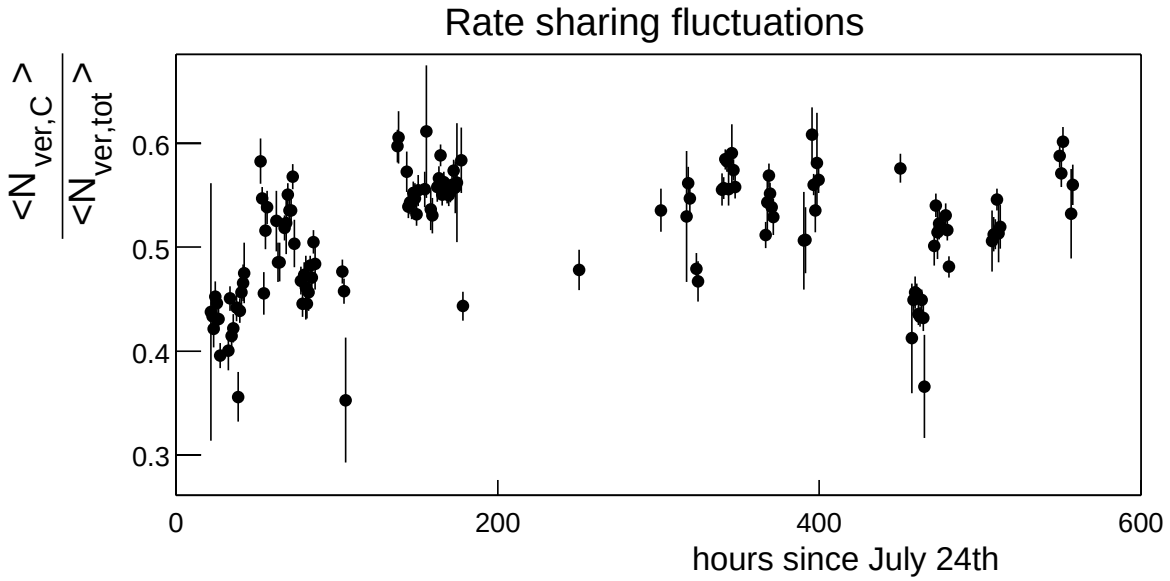

Figure 1.3.2: *Rate sharing fluctuations during running with a titanium and carbon wire. The plot shows the contribution of the carbon wire to the total interaction rate. Although the number of vertices on the carbon wire is on average approximately 50% of the total, significant fluctuations can be observed.*

1.4 The HERA-B detector

The HERA-B detector is a forward particle spectrometer with angular acceptance of 10 to 220 mrad in horizontal direction and 10 to 160 mrad in the vertical direction. It translates to 90 percent of the 4π solid angle in the centre-of-mass frame of the pN collision.

The density of charged tracks decreases with the distance r to the beam pipe approximately as $1/r^2$. The average track multiplicity of 100 charged tracks (including secondary particles) is concentrated near the beam pipe. For each of the sub-detectors, the average hit occupancy should not exceed 20 percent. Consequently, sub-detectors near the beam pipe have fine granularity, whereas the detector systems further from

the beam axis have larger detector cells.

The detector consists of sub-detector systems for different purposes: a set of tracking detectors for track reconstruction and momentum determination, a vertex detector for (secondary) vertex reconstruction, and several detectors for particle identification. Figure 1.4.1 shows an overview of the HERA-B detector.

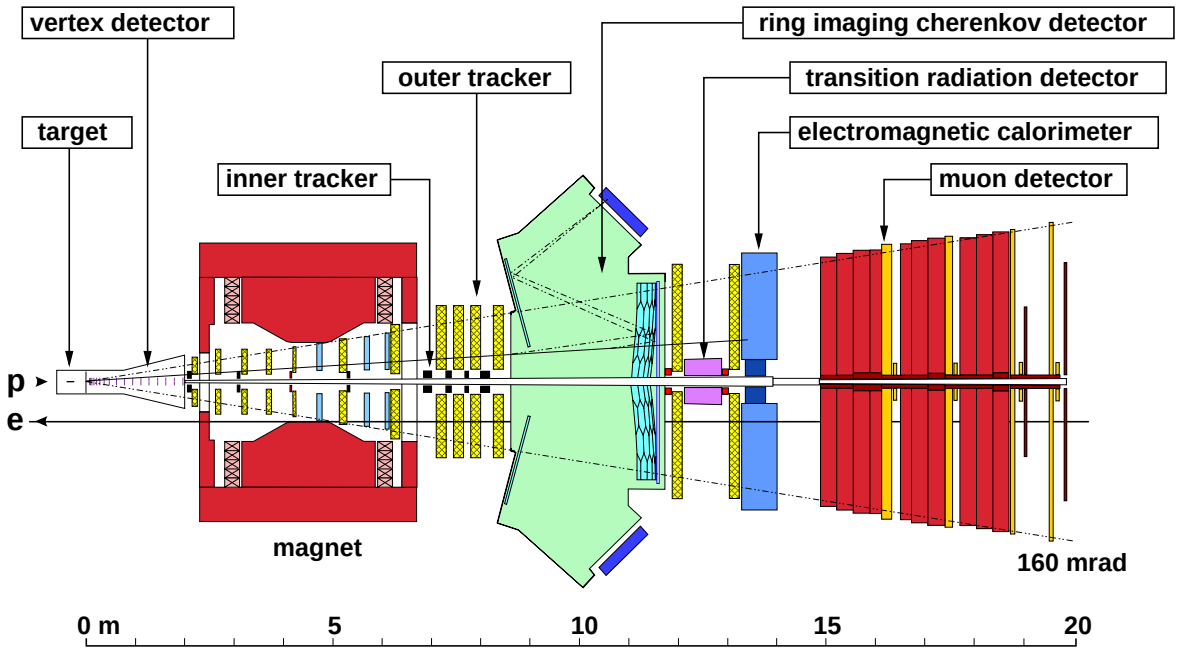

Figure 1.4.1: *Schematic overview of the* HERA-B *detector as seen from above. The detector is a forward spectrometer with sub-detectors for track finding (Inner Tracker and Outer Tracker), vertex reconstruction (Vertex Detector) and particle identification (RICH, calorimeter, MUON system). The detector is 20 m long and has an angular coverage of 10 to 220 mrad in the horizontal (bending) plane and 10 to 160 mrad in the vertical direction.*

The coordinate system of HERA-B is defined as follows: the z-axis is in the direction of the proton beam, and $z = 0$ is near the target station. The y-axis is pointing upward and the x-axis points towards the centre of the accelerator, with $x = 0$ and $y = 0$ given by the proton beam axis.

In the following we give an overview of the HERA-B detector. A detailed description of all sub-detectors can be found elsewhere [8, 9, 10].

1.4.1 The tracking system

The tracking system for momentum determination extends in z from the exit window of the vertex vessel ($z = 210$ cm) to the front of the calorimeter ($z = 1325$ cm). It consists of a dipole magnet and 13 tracking stations or 'superlayers', as depicted in figure 1.4.2.

The HERA-B magnet has an integrated field strength of 2.2 Tm. The magnetic field points upward and bends charged particles in the horizontal direction. The

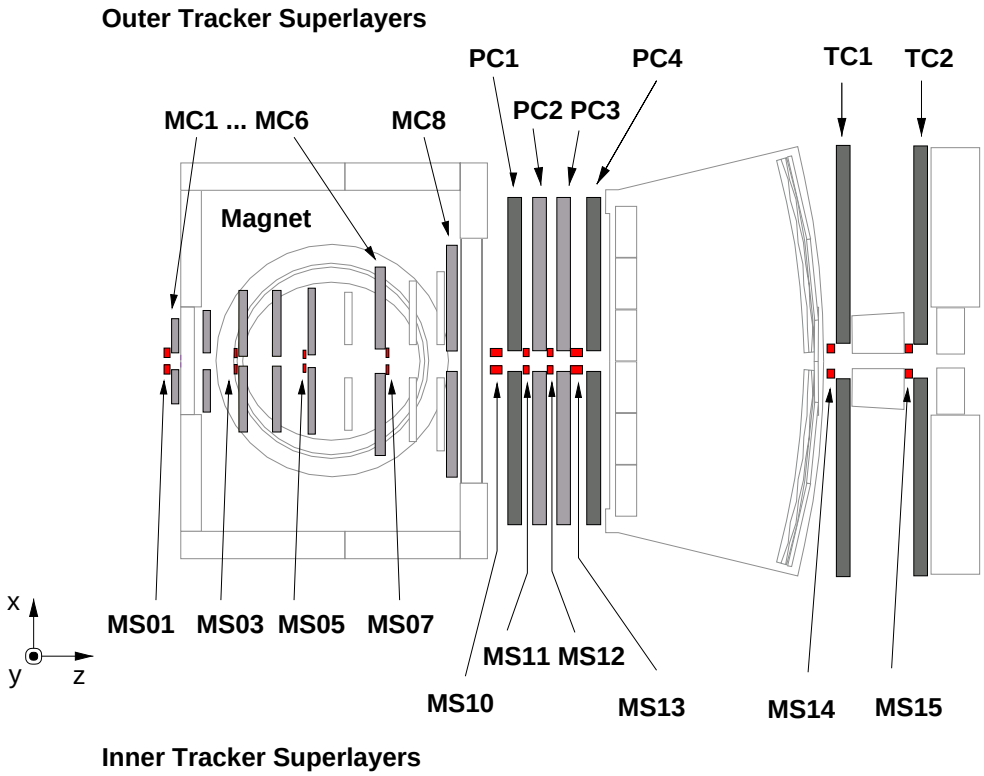

Figure 1.4.2: *Overview of the tracking system of Hera-B, showing the location of the different superlayers. The region around the beam-pipe (<25 cm) is equipped with Inner Tracker stations, and the outermost region is covered by the Outer Tracker. Three groups of superlayers can be distinguished: The magnet chambers MC1-MC8 and MS01-MS03 are installed inside the magnet. The pattern recognition chambers PC1-PC4 and MS10-MS13 are situated between the magnet and the RICH and the trigger chambers TC1, TC2 and MS14, MS15 are located between the RICH and the ECAL [11].*

HERA electron beam pipe crosses the magnet and is covered by an additional magnet to compensate the magnetic field, so that the electron beam can pass HERA-B undisturbed.

To adjust for the particle flux, which decreases with the distance to the beam axis, two different technologies are used. The Inner Tracker superlayers, that cover the area between 5 to 25 cm from the beam pipe, are composed of micro-strip gas chambers with gas electron multipliers (GEM-MSGC [12]). A strip pitch of 300 μm provides a hit resolution of 80 μm and keeps occupancies at an acceptable level.

The outer region, from 25 cm to up to 3 m from the beam axis, is covered by Outer Tracker superlayers. The Outer Tracker is built from honeycomb drift chambers [13] with cell sizes of 5 mm in the region close to the beam pipe, and 10 mm in the outermost region.

Every tracking superlayer consists of several layers of drift chambers or micro-strip planes arranged in three different orientations: 0 mrad, +80 mrad and -80 mrad w.r.t. the y-axis. This enables tracks to be reconstructed in all three spatial coordinates,

while keeping combinatorial ambiguities for space point reconstruction low.

Three parts in the tracking system can be distinguished, each with a different purpose:

Pattern Recognition Chambers (PC)
The main part of the tracking system is a set of four pattern recognition chambers, installed in the field-free region between the magnet and the RICH. These superlayers consist of many densely staggered layers. This, and the absence of a magnetic field facilitates the search for charged tracks. The first and the last of these PC chambers are also used by the First Level Trigger, described in the next chapter.

Trigger Chambers (TC)
The First Level Trigger of HERA-B performs a track search, initiated by pretriggers from the calorimeter or the MUON system. To sufficiently narrow down the search window for track finding, two tracking stations are installed close to the calorimeter.

Magnet Chambers (MC)
The main purpose of a set of seven tracking stations inside the magnetic field was to enable an efficient reconstruction of K^0_S decays. In addition, these chambers facilitate the extrapolation to the vertex detector of the track segments reconstructed in the PC chambers.

The momentum resolution, estimated in a Monte Carlo simulation [14], ranges between 1.5% and 2%, depending on the momentum of the particle. The width of the J/ψ signal, reconstructed in the $J/\psi \rightarrow \mu^+\mu^-$ channel, is 55 MeV/c^2.

1.4.2 The vertex detector

B mesons have an average decay length of 10.7 mm at HERA-B. To identify events with a B meson, both the primary vertex and the secondary vertex should be reconstructed with sufficient precision. This requires an accurate determination of the parameters of charged tracks close to the target.

For this purpose a vertex detector system (VDS) in the field-free region near the target is installed. The VDS consists of eight stations of silicon micro-strip detectors. Each station has four modules of two double sided silicon detector planes, arranged in four quadrants, as depicted in figure 1.4.3.

The strips on the four silicon planes of one module are positioned with angles of -2.5, 2.5, 87.5 or 92.5 degrees with respect to the vertical axis. This gives equal precision for the track reconstruction in both the vertical and horizontal track direction.

The readout pitch of 50 μm ensures that the hit occupancy never exceeds 5%. The track and vertex resolution are dominated by multiple scattering. Consequently, the amount of material in the path of tracks is minimised. The VDS uses so-called Roman pots, in which modules can be inserted to a position as close as 1 cm from the beam axis.

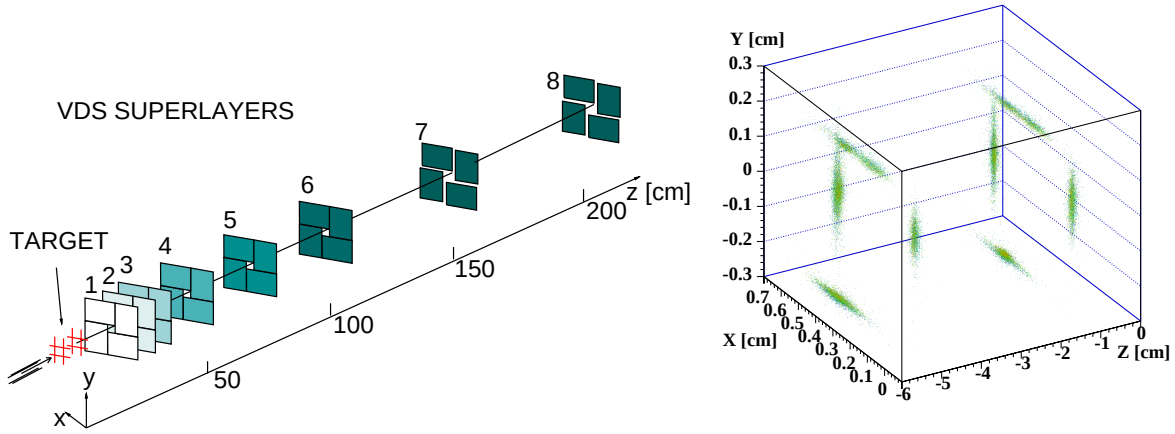

Figure 1.4.3: *Layout of the Vertex Detector System (left) and distribution of primary vertex coordinates as reconstructed from VDS track segments(right). The primary vertex resolution is approximately* 500 μm *in the* z *direction. The eight target wires are clearly visible.*

The impact parameter resolution is 35 μm for high-momentum particles ($p >$ 50 GeV/c). The resolution of primary vertices is approximately 500 μm in z and 40 μm in x or y.

1.4.3 Particle identification

The final state particles from a golden decay are a $\mu^+\mu^-$ or a e^+e^- pair from the J/ψ and a $\pi^+\pi^-$ pair from the K^0_S. To reduce the background in the reconstruction of these decays, several detectors for particle identification are used. Electrons are identified with an electro-magnetic calorimeter and a transition radiation detector, muons with a MUON detector, and a RICH detector is used to separate pions from kaons.

RICH

The Ring Imaging Cherenkov Counter (RICH) is located between the TC chambers and the PC chambers of the tracking system. Its purpose is an efficient and pure separation between kaons and pions. It uses a tank filled with freon (C_4F_{10}) in which relativistic particles emit Cherenkov radiation. This Cherenkov radiation is emitted at an angle θ_C w.r.t. the direction of the particle, which depends on the refractive index n of the radiator gas and on the velocity $\beta = v/c$ of the particles:

$$\cos\theta_C = \frac{1}{n\beta}. \tag{1.4.1}$$

A spherical mirror projects the photons, radiated in a cone, onto a circle. A planar mirror then reflects the photons onto an array of photo-multiplier tubes, where they are detected.

Since the momentum p of a particle is determined by the main tracker, the mass m

can be extracted from the angle of the Cherenkov ring using the approximate equality

$$\theta_C^2 = \theta_0^2 - \frac{m^2}{p^2}. \tag{1.4.2}$$

Here, $\theta_0 = 1/n$ is an offset defined by the type of gas. For freon we have $\theta_0 = 52\,\text{mrad}$. Figure 1.4.4 shows the correlation between $1/p^2$ and θ_C^2. Clear bands are visible that correspond to electrons, pions, kaons and protons. The momentum ranges over which a good particle identification (defined as a four sigma separation of the bands) can be achieved, are also indicated [10].

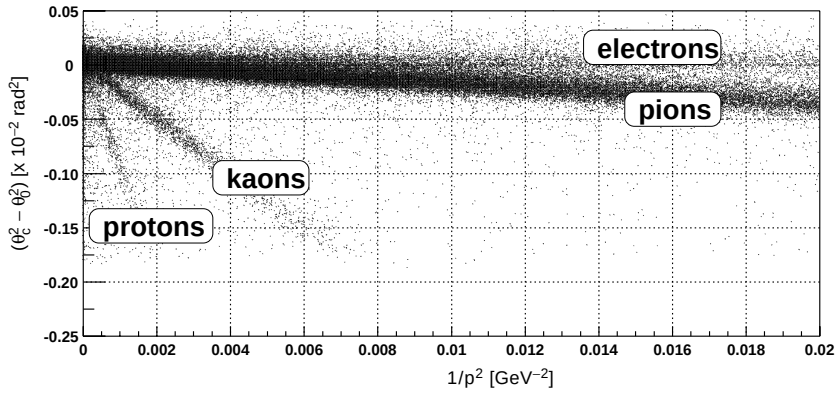

4 σ	separation:
e − π	3.4 − 15 GeV/c
π − K	12 − 54 GeV/c
K − p	23 − 85 GeV/c

Figure 1.4.4: *Correlation between the reconstructed momentum and the Cherenkov angle reconstructed by the RICH [10]. The RICH provides a separation of kaons and pions in a broad momentum range, as indicated.*

ECAL

The electro-magnetic calorimeter (ECAL), installed 13.5 m from the target, measures the energy deposited by the particles. About 6000 cells sample shower particles in scintillators, sandwiched between thin layers of absorber material (a W-Ni-Fe alloy in the inner part and lead in the outer and middle parts). Wavelength shifting fibres, running perpendicularly to the scintillators, guide the light to photo-multipliers (PMTs). The PMTs transform it to an analogue electrical pulse that is subsequently digitised and converted to a value for the energy.

The ECAL is sub-divided in three parts to adjust for the particle flux differences, as shown in figure 1.4.5). The innermost region is equipped with ECAL cells of $\Delta x \times \Delta y = 2.24 \times 2.24\ \text{cm}^2$ and has a depth of 33 radiation lengths (X_0). The middle and outer regions have square cell sizes of 5.6 cm and 11.18 cm, respectively, and a depth of $20X_0$.

The ECAL allows to separate electro-magnetically showering particles (e,γ) from hadrons. Whereas hadrons deposit only a fraction of their energy E in the ECAL, electrons deposit their full energy. Together with the momentum p, reconstructed by the main tracker, electrons can be identified as having $E/p \approx 1$. Furthermore, the ECAL is used to provide the starting point for electron track reconstruction by the FLT.

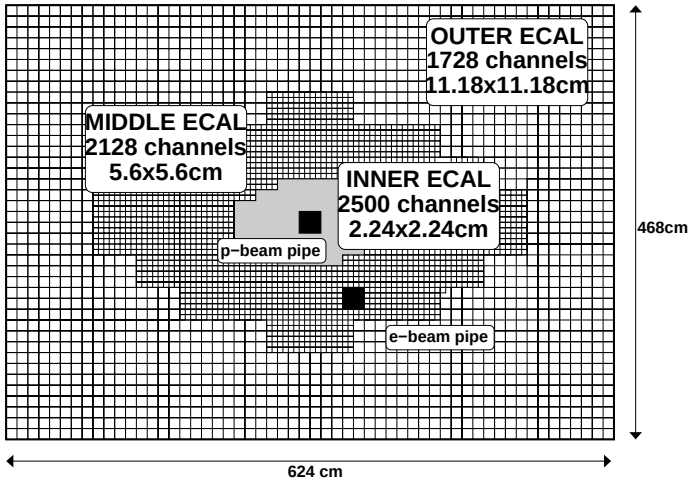

Figure 1.4.5: *Layout and segmentation of the ECAL. The ECAL consists of three regions of different cell sizes:* 2.24×2.24 cm^2 *for the Inner ECAL,* 5.6×5.6 cm^2 *for the Middle ECAL and* 11.2×11.2 cm^2 *for the Outer ECAL.*

The energy resolution has been measured [10] in part of the Inner ECAL to be $\sigma_E/E = 0.22/\sqrt{E} \oplus 0.017$ for electro-magnetically showering particles.

A transition radiation detector (TRD) is foreseen to be installed in the inner region of the detector, where track densities are high. The TRD will provide additional separation of electrons and hadrons in the momentum range between 5 and 150 GeV.

MUON

The MUON system consists of four superlayers interleaved with concrete and steel absorbers, as depicted in figure 1.4.6. These absorbers stop practically all pions and kaons, whereas muons of more than 5 GeV traverse the detector completely.

The inner region ($x, y < 33$ cm) is equipped with gas pixel detectors of 9×9 mm^2 cell size, and 30 mm wire length. In the outer region, proportional wire tube chambers with cell sizes of 1.2 cm provide sufficient granularity.

The last two MUON superlayers, MU3 and MU4, are also used for the First Level Trigger. They are read out on the cathode side, which is segmented in pads of 6.5×6.4 cm^2 (MU3) and 12.9×13.0 cm^2 (MU4). A coincidence between a hit in a pad of MU3 and one in MU4 provides the starting point of a muon reconstruction by the FLT.

1.5 Trigger and data acquisition

1.5.1 Trigger overview

The high event rate and interaction rate and the extreme signal to background ratio of 10^{-11} presents a unique challenge to the trigger. The initial bunch crossing rate of 10 MHz must be reduced to an output rate of 50 Hz at which events can be written to tape. Even at an interaction rate of 40 MHz, a $B^0 \to J/\psi\, K^0_S$ decay is not expected to be found much more than once per hour.

The trigger system is specifically designed to select events containing a J/ψ decaying to $\mu^+\mu^-$ or e^+e^-. The overwhelming majority of these J/ψ will not be from a B

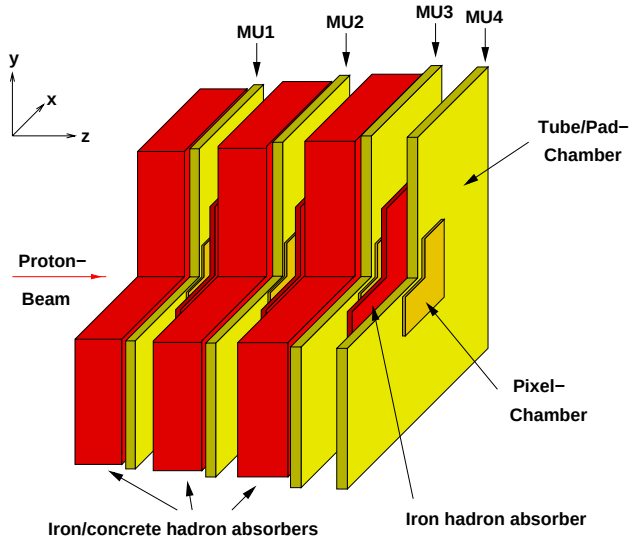

Figure 1.4.6: *The MUON system comprises three hadron absorbers and the four superlayers MU1, MU2, MU3 and MU4. MU1 and MU2 consist of tube chambers in three orientations (+20,0,-20 degrees), and gas pixel chambers in the inner part. The tubes of MU3 and MU4 have one orientation, but are also read out on the cathode to provide a trigger signal.*

decay. Nevertheless, even directly produced J/ψ are sufficiently rare to bring about the required event rate reduction of about one million. This rate reduction is achieved by a trigger chain that consists of four steps.

First Level Trigger

The most critical and challenging part of the trigger system is the First Level Trigger (FLT). It consists of custom-made hardware processor boards that perform a track reconstruction in the main tracker. This track reconstruction is initiated by an energetic cluster in the ECAL or a coincidence of hits in the MUON system, both of which give a first estimate of the track parameters. These track candidates are further reconstructed in the main tracker. After determining the momenta of these tracks, a mass reconstruction is done from pairs of found tracks. A mass cut of typically $m > 2$ GeV/c^2 gives the required rate reduction, while remaining efficient for a J/ψ. The First Level Trigger is described in detail in the next chapter.

Second and Third Level Trigger

When the event is accepted by the FLT, all data are transmitted from the detector to the Second Level Buffer (SLB). One of the 240 PCs that make up the Second Level Trigger (SLT) farm will process this event, improving the accuracy in the track parameters of the tracks already found by the FLT. The SLT includes the measured drift times of the Outer Tracker in the reconstruction. A fit using drift times improves the track parameter resolution by a factor of 10. The tracks are further traced through the magnet and the vertex detector. The two tracks of the J/ψ candidate must originate from a common vertex. If necessary, this vertex can also be required to be detached from the primary vertex, firmly indicating a B decay.

After one of the nodes of the SLT has accepted the event, this PC will assemble the full event from the SLB. Third Level Trigger (TLT) algorithms, executed on the

same SLT farm, can then perform full track and vertex fitting in the vertex detector. Alternative (i.e. non-J/ψ) triggers from the FLT, such as single high-p_T leptons, are processed here.

Fourth Level Trigger/FARM

After the SLT/TLT, the event rate is sufficiently reduced to allow a full event reconstruction by a second farm of PCs. A final event selection can further reduce the rate of events written to tape, if necessary. Online alignment, calibration and data quality monitoring processes also reside at the FARM.

Trigger Level	input rate	reduction	time	hardware
FLT	10 MHz	200	12 μs	custom-built processors
SLT	50 kHz	100	4 ms	PC farm
TLT	500 Hz	10	100 ms	PC farm
FARM	50 Hz	-	2-4 s	PC farm

Table 1.5.1: *Rate reduction of the different trigger levels. The output rate of 50 Hz is dictated by the maximum rate that can be written to tape, and this depends on the size of an event. The FARM performs a full event reconstruction, and additional trigger cuts can be implemented here if necessary.*

1.5.2 Data acquisition

The trigger chain is embedded in a data acquisition (DAQ) system that is capable of handling the large amount of data to be transferred between the trigger stages. A schematic overview of the data acquisition system is shown in figure 1.5.1.

All detector channels, amounting to a total of almost 600.000, are read out for every bunch crossing of 96 ns. The data are temporarily stored on the front-end of the detector in a cyclic readout buffer of 128 bunch crossings, while a FLT decision is awaited.

The detector data that are used by the FLT, are directly transmitted to the FLT network for every bunch crossing. Pretrigger linkboards provide an interface to the pretrigger electronics, and FLT linkboards send the hit information from some of the tracking superlayers to the FLT processors.

When the FLT accepts the event, the data stored in the readout buffer are transmitted to the Second Level Buffer (SLB), built up from 134 SHARC[1] boards. The SLB stores the data until the SLT has decided to keep or reject the event. One of the PCs of the SLT farm will request those data from the SLB, that are needed to re-evaluate the FLT tracks. If the event is accepted, the complete event is sent to that PC. After the execution of TLT algorithms (if any) and data compression, the event is transmitted to the FARM via a fast-Ethernet connection, where it is reconstructed and finally written to tape.

[1]Super Harvard ARchitecture Computer, a digital signal processing(DSP) IC with on-chip memory.

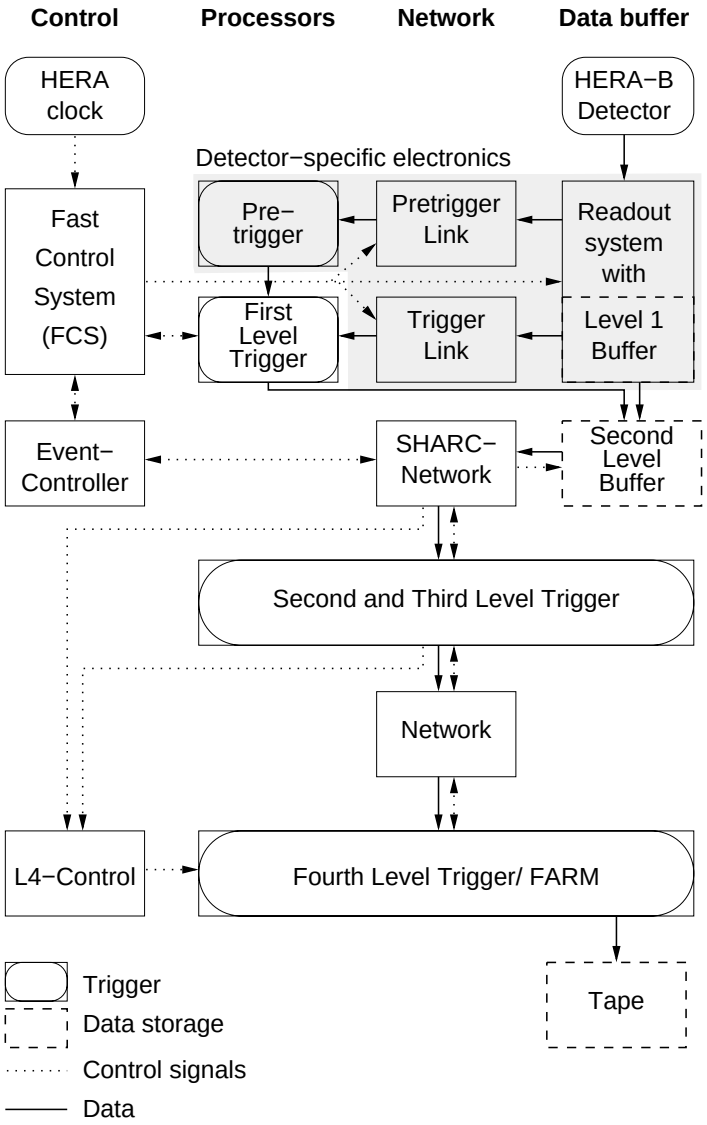

Figure 1.5.1:
Schematic overview of the data acquisition (DAQ) system, showing the interconnectivity between the different trigger stages and data buffers. The data flow from detector to tape is indicated by the solid arrows.

1.6 New physics goals

The HERA-B detector was planned to be completed in 1998. One year of running would then have sufficed to establish CP violation in B decays. However, during the construction and commissioning of the detector and trigger, unforeseen technical problems appeared (for details see [10]). This caused a serious delay: to date (2002) the detector is still not completely commissioned. In addition, the detector, even when completed, will most likely not reach design specifications.

Meanwhile, Belle and BaBar, two other experiments that set out to measure CP

violation in B decays, have had considerable success: CP violation in B decays has been established [15, 16].

Since HERA-B is no longer competitive for this measurement, the emphasis of the physics program has shifted towards other measurements. The main physics goals for future running are [17]:

- **$b\bar{b}$ production cross section**
  The two measurements of the $b\bar{b}$ production cross section at centre-of-mass energies comparable to that of HERA-B are imprecise and mutually inconsistent (see Fig. 5.1.5). From the data of 2000, the cross section has been measured with an uncertainty of 50% [18]. In future running, HERA-B will be able to measure this with an estimated uncertainty of 10%.

- **Production of J/ψ, ψ' and χ_c; polarisation and nuclear effects**
  The models for charmonium formation give different predictions for production cross section ratios of charmonium states and for the decay angle distributions. Measurements by HERA-B would help to distinguish between these models. In addition, HERA-B has a rich potential in measuring nuclear effects in the production of charmonium, which is described in more detail in section 5.4.2.

- **Drell-Yan production, polarisation and nuclear effects**
  Results on the decay angle distribution of Drell-Yan pairs produced in πA collisions indicate a violation of the Lam-Tung relation [19]. HERA-B can verify whether this effect is present pA collisions too. Measurements of the A dependence of the Drell-Yan production cross section can provide insight into the modification of the quark densities at high x in nuclear matter.

- **Υ production**
  With a sizeable sample of Υ, the same physics issues as described for charmonium can be addressed. For the Υ system, the theoretical uncertainties in the model predictions are smaller.

- **Direct production of photons at high-p_T**
  The production of high-p_T photons is sensitive to the nuclear gluon density at high values of x. The data at fixed target energies suffer from large systematic uncertainties and can be improved by HERA-B.

- **Charm physics**
  The standard model prediction for the $D^0 \to \mu^+\mu^-$ branching ratio is $\mathcal{O}(10^{-19})$. HERA-B could improve the measured upper limit of 4.1×10^{-6} by two orders of magnitude, closing in on the level predicted by some SUSY models. In addition, trigger schemes have been developed for the accumulation of D mesons through semi-leptonic decays. If a sizeable sample can be collected, a wide variety of physics topics can be addressed, ranging from the nuclear gluon density to FCNC decays.

Part I

Performance of the First Level Trigger

Chapter 2

Description of the First Level Trigger

One of the main components of the HERA-B detector is the First Level Trigger (FLT). As the first stage of a multi-level trigger system it has to cope with a large input rate and a short decision time. The requirements, purpose and implementation of the FLT are presented in this chapter. It gives background information necessary for the following chapters, where the performance of the FLT for the reconstruction of electrons is studied in more detail.

2.1 Purpose of the FLT

The purpose of a trigger is to reduce the total number of collected events, while events, that are interesting for further analysis, are retained as much as possible. Such events, therefore, need to have a characteristic signature that is distinctively different from the uninteresting background. Typical characteristics in many trigger systems are the occurrence of energetic particles. Such particles can signal the decay of particles containing heavy quarks, whose high mass is transformed into energy of the light decay products.

The FLT of HERA-B is specifically designed to select $J/\psi \rightarrow \mu^+\mu^-$ and $J/\psi \rightarrow e^+e^-$ decays. It is, however, not limited to this decay. In particular, the installation of a detector dedicated to the early identification of hadrons with very large transverse momenta (High-Pt chambers) has enabled the selection of a variety of interesting B decays, as listed in table 2.1.1.

As part of a multi-level trigger chain, the FLT is subject to several external constraints:

- **Rate reduction and efficiency**
  The Second Level Trigger (SLT), that processes the events that are accepted by the FLT, has been designed to handle an input rate of at most 50 kHz. Given the 10 MHz input rate to the FLT, it requires a FLT suppression factor of 200.

- **Event rate and interaction rate**
  The HERA-B detector records events in every bunch crossing (BX) cycle, which often contain multiple interactions. Each of these events needs to be scanned

Channel	Trigger signature	Measurement
$B^0 \to J/\psi\ K^0_S$	massive l^+l^-, 2nd vertex	CP violation ($\sin(2\beta)$) [8]
$B^0 \to J/\psi$ X	"	$\sigma_{b\bar{b}}$, B lifetime[8]
$B^0_s \to J/\psi\ \phi$	"	B^0_s lifetime, $\Delta\Gamma_s$ [10]
$B^0 \to K^*(892)\ \mu^+\mu^-$	"	FCNC, new physics [10]
$B^0/D^0 \to \mu^+\mu^-$	"	FCNC, new physics [8]
$J/\psi,\psi',\Upsilon \to l^+l^-$	massive lepton pair	QCD studies [20]
$D^0 \to K^+\ l^-\bar{\nu}_l$	high p_T lepton	D mixing, QCD studies [21]
$B^0_s \to D^-_s\ l^-\nu_l$	"	B^0_s lifetime, $\Delta\Gamma_s$
$pA \to \gamma X$	high p_T photon	gluon density [22]
$b \to s\ \gamma$	high p_T photon, hadron	FCNC, new physics [23]
$B^0_s \to D^-_s\ \pi^+$	high p_T hadrons, lepton	B^0_s mixing [24]
$B^0_s \to D^-_s\ 3\pi^\pm$	"	B^0_s mixing [24]
$B^0 \to \pi^+\pi^-$	high p_T hadrons	CP violation ($\sin(2\alpha)$) [9]
$B^0 \to K^+\ \pi^-$	"	CP violation ($\sin(2\gamma)$) [9]

Table 2.1.1: *Overview of decay channels and their trigger signature. For more information on the feasibility of measurements using these decays see references. The physics motivation can be found in several textbooks (see e.g. [25]).*

by the FLT in order to determine whether they could contain one of the decays of table 2.1.1. The FLT must sift through 500 million track candidates per second and process 1 Tb/s of data from the tracking chambers. The processing of one event may not preclude the processing of another. Such 'dead time' would decrease the total efficiency.

- **Maximum decision time**
  The front end electronics of the HERA-B detector can store raw detector data in a cyclic pipeline buffer of 128 bunch crossing cycles. After 128 bunch crossings the event is overwritten with new data. Any FLT decision to further process this event has to arrive at the front-end within 128×96 ns $= 12.3\ \mu$s. This time, the maximum FLT latency, includes sending data to the FLT, processing this data and transmitting the decision back to the detector through the Fast Control System.

- **High occupancy**
  The hadronic interactions recorded by the HERA-B detector can lead to occupancies of up to 30% in the tracking chambers. A fast decision based on such events requires simplified algorithms, that use a subset of the incoming data. The use of local methods should keep combinatorics at an acceptable level.

2.2 Algorithm

These requirements can only be met by a processor system with a highly parallel and pipelined architecture [26, 27, 28]. This ensures the fastest and most efficient use of the computing capabilities. The algorithms used in the FLT therefore need to fit in this parallel architecture. Moreover, the short processing time precludes the transmission of the vast amount of detector data from one processor to the other. The design of the FLT is built on the philosophy of 'move process, not data'.

As summarised in table 2.1.1, the events of interest are characterised by the occurrence of hadrons, electrons or muons with high transverse momenta. The FLT should be able to identify their tracks out of a multitude of other charged tracks. An especially suitable algorithm for such high density track finding and one that satisfies the constraint of possible parallelisation is the Kalman filter [29].

The Kalman filter technique was developed to determine the dynamical evolution of a system from a set of measurements at different times. The knowledge of the dynamical system, described by a state vector, improves with each consecutively added measurement. The algorithm essentially comprises two[1] steps. The first is a prediction step, in which the current knowledge of the state vector is used to make an estimate for the next measurement. Such a projection is the best possible estimate based on all previous measurements. The next step is the filter step. Here further measurements are included to refine the knowledge of the state. A measurement that differs too much from the prediction is disregarded as not belonging to the evolution of this state. One can thus efficiently discard noise and measurements from other states, making the Kalman filter, essentially designed as track fit procedure, suitable for high density pattern recognition. In HERA-B, with its high track densities, the Kalman filter is widely applied as a track finding method.

Figure 2.2.1 illustrates how tracks are found in the FLT. The FLT uses a subset of the tracking and muon superlayers, all positioned in the field free region behind the magnet, where particles form straight tracks. The direction of the track search is towards the target, i.e. reverse to the direction of the particle flow.

The starting points of track searches ('track seeds') are given by pretriggers. Three different subdetectors can issue such pretriggers, corresponding to the three different kinds of particles of interest: electrons, muons or energetic hadrons. These are the ECAL, the MUON system and the High-Pt chambers, respectively. A pretrigger defines an initial Region of Interest (RoI), a search window to which to the track finding in a nearby tracking chamber is confined.

The FLT subsequently determines the track that may have led to this pretrigger signal. It searches within the given RoI in the tracking chamber for hits that confirm the passage of a charged particle. When a hit is found, it will use the position of this hit in the RoI to refine the estimate of the track parameters. It will subsequently provide a similar, but narrower RoI to a more upstream tracking chamber. A track search is then performed in this narrower RoI. As this process continues, the estimate of the track parameters will gain in accuracy, and the size of the RoIs decreases until the last tracking chamber used in the FLT is included.

[1] a third step, called 'smoother' is disregarded since it is not used in the algorithm of the FLT.

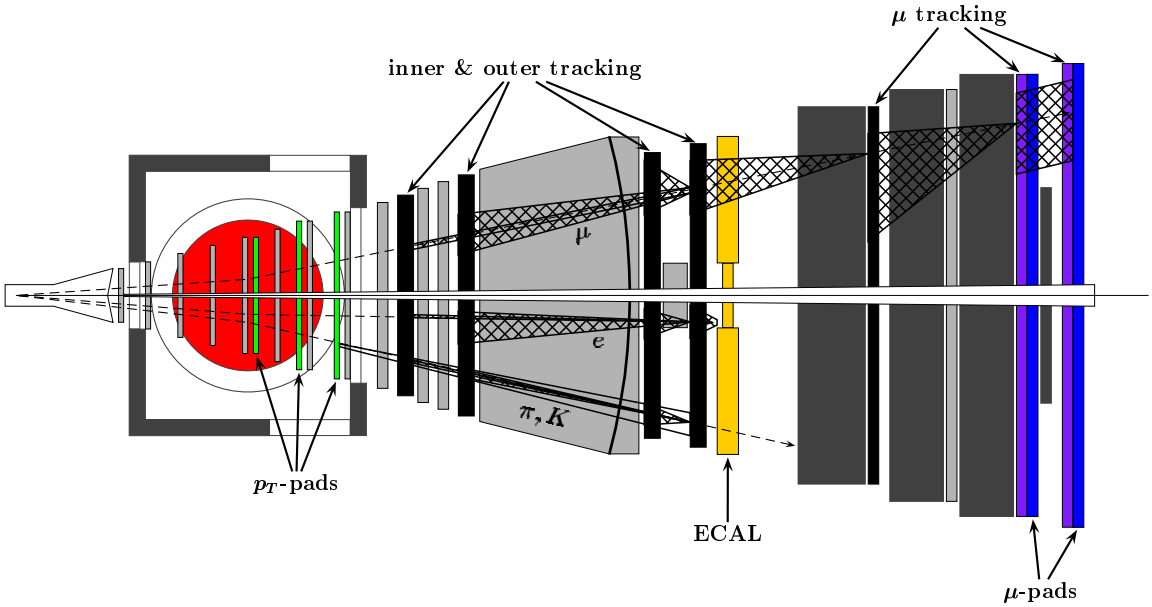

Figure 2.2.1: *Illustration of the track finding algorithm of the FLT. The hatched areas show search areas (not to scale) used in the track finding procedure. With each added measurement, the knowledge of the track improves and the size of the search windows decreases.*

By then, the RoIs should be sufficiently small so that ghost tracks due to combinatorics are at an acceptable level. Moreover, the track parameters are known to an accuracy that is sufficient to allow a first momentum determination, by assuming that these tracks have originated from the average target position at $(x, y, z) = (0, 0, 0)$. When the momenta are known, track pairs can be combined to determine the invariant mass. Massive resonances such as J/ψ or Υ can be selected for example by combining lepton pairs and demanding the invariant mass to be larger than 2.0 GeV/c^2.

2.3 Hardware implementation

The necessary computational speed can only be achieved by hardware, that is specifically designed for this purpose. Ordinary micro-processor based systems are too slow by at least an order of magnitude. The FLT is built as a network of custom-built processor boards.

The FLT has three tasks to perform. It first needs to find tracks, then the momenta of such tracks need to be determined, and finally the invariant mass of pairs of tracks must be calculated.

Dedicated processor boards have been developed for each of these tasks [30]. Track Finding Units (TFU) perform the track reconstruction. Track Parameter Units (TPU) do the momentum determination, and the mass calculation and decision taking is done by a Trigger Decision Unit (TDU). The positive trigger decision is distributed to the entire readout system by the Fast Control System. The event is then further

processed by the Second Level Trigger. Figure 2.3.1 gives a schematic overview of the functionality of the different components of the FLT.

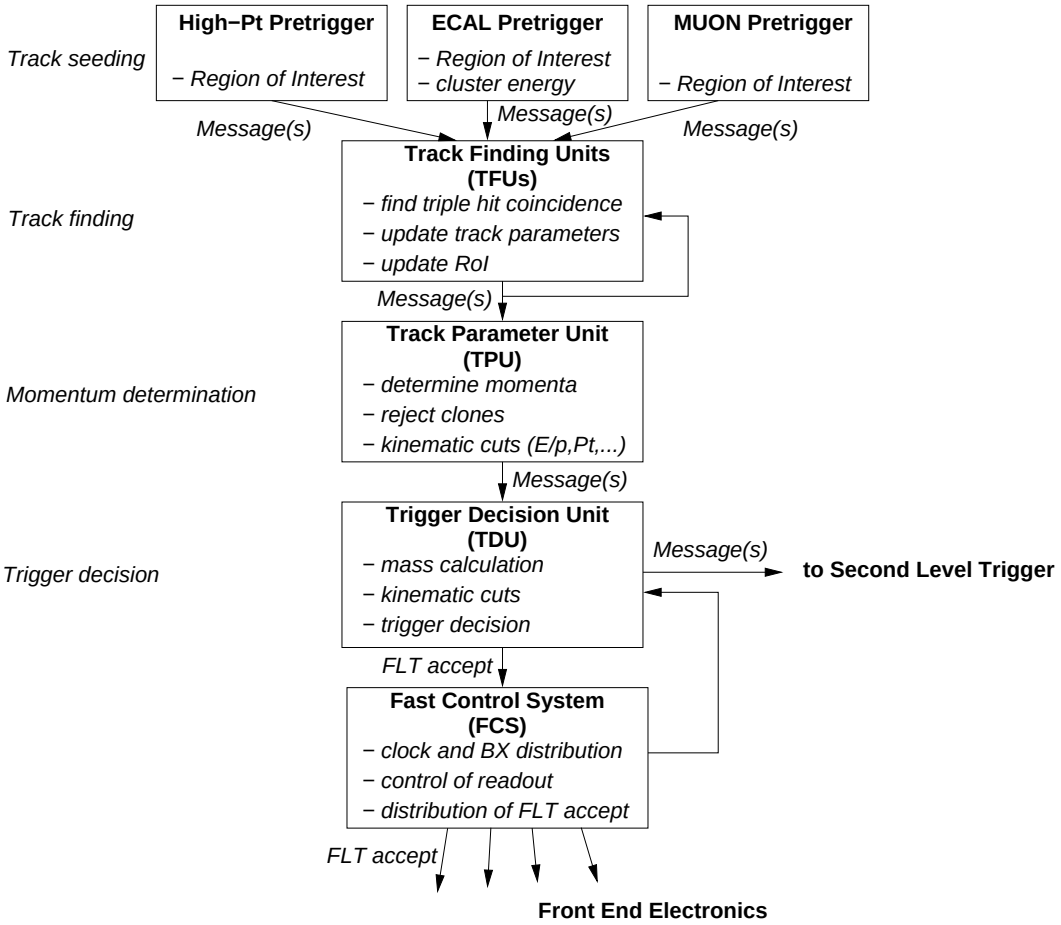

Figure 2.3.1: *Interconnectivity and functionality of FLT processors. The pretrigger processors and the Track Finding Units (TFUs) receive detector data in every bunch crossing. The different processor boards communicate with each other through 'messages'.*

In total about 100 TFUs are used in the FLT. Each of these handles a specific part of one of the superlayers of the main tracker or the muon system. Two types of data flow can be distinguished, indicated by arrows in figure 2.3.2: detector data to the processor boards (Pretrigger boards or TFUs) and track parameter information from one TFU to another TFU or to the TPU.

2.3.1 Messages

The philosophy of 'move process, not data' is put into practice by the communication through messages. They are 80 bits long and contain all the information necessary for track propagation. As such, they are the analogue of state vectors of the Kalman filter algorithm, and describe the best possible estimate of the track parameters at that point. Table 2.3.1 shows the content of an FLT message.

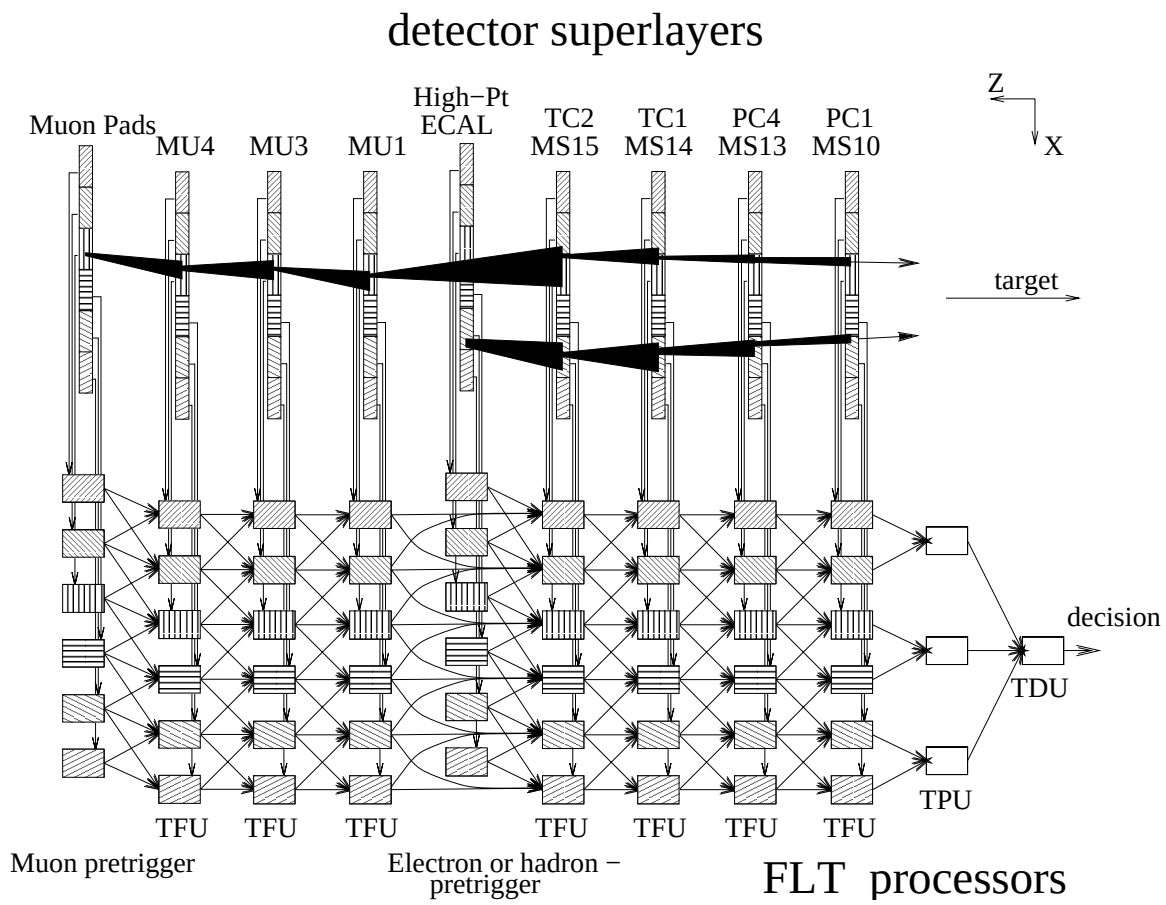

Figure 2.3.2: *FLT network arrangement, indicating the correspondence between processors and detector planes. The FLT comprises a network of 70 Track Finding Units, each of which can scan for space points in a designated part of tracking system.*

As a state vector of the track, the message contains track parameters such as the position and the slope and its estimated uncertainty. The FLT assumes that tracks are not bent in the vertical direction and the track search is essentially restricted to finding the position and slope of the track in the horizontal (bending) plane[1]. In this plane, the track is described by the variables ξ, dξ and ddξ, as illustrated in figure 2.3.3.

Beside the track parameters, the message contains flags or variables that are needed for steering of the algorithm. For example, the attached BX number serves as a time stamp of the message, that allows the FLT to operate independently from the bunch clock. A destination identifier, TDI, is a coded address for selecting processors that must accept and process the message further. The inclusion of flags such as *all* or $flag$ enable the selection of photons of very large transverse momentum for which no charged track should be searched. The variable $flag$ is set by the ECAL pretrigger if the cluster has an transverse energy of 3 GeV or more. The variable *all* is set when hits have been found in all tracking stations.

[1]for muons, the y position is actually updated once by the TFUs of MU1

Variable	Size (nr of bits)	Updated	Description
TDI	8	Y	destination identifier.
nξ	1	Y	nr of RoIs to search (1 or 2)
ξ	10	Y	x coordinate at TC2 2.3.3
dξ	8	Y	minimum slope in x (see Fig. 2.3.3)
ddξ	8	Y	size of window in slopes (see Fig. 2.3.3
η	9	N	slope in y (non-bending plane)
w	2	N	nr of adjacent cells in TC2 (see Fig. 2.3.3)
all	1	Y	flag when hit in every TFU (for photons)
BX	8	N	bunch crossing number
ID	2	N	pretrigger identifier
P	7	N	initial estimate of momentum
$flag$	1	N	pass to next TFU (for photons)
E^+	7	N	Bremsstr. energy (positive charge hyp.)
E^-	7	N	Bremsstr. energy (negative charge hyp.)
	total 79		

Table 2.3.1: *Variables in an FLT(TFU) Message. The column 'Updated' indicates whether or not the value of the variable changes within the TFU network. Messages that passed the TPU have a slightly different content: they contain the momentum vector, instead of the track parameters.*

Many variables in the messages are not updated during the track search but are forwarded unchanged to the next processor. Such variables are set once by one of the pretriggers and are necessary for further track propagation (η, w) or later identification (ID, BX, P, $flag$, all).

Kinematic quantities can be coded into the corresponding message variables in an arbitrary manner. Any one-to-one mapping can in principle be used for this coding. To obtain an optimal accuracy given the limited number of bits available, the coding is adjusted to the intrinsic resolution of the detector: in the region close to the beam pipe ($x < 25$ cm), where the Inner Tracker provides a finer granularity than in the outer regions, x is coded into ξ with an accuracy of 0.12 cm per unit of the most significant bit. In the outermost regions, covered by 10 mm Outer Tracker modules, the bin size is 1.73 cm.

2.3.2 Pretriggers

ECAL Pretrigger

The task of the ECAL pretrigger [31] is the early identification of electron candidates and the determination of their energies and positions. The ECAL pretrigger boards

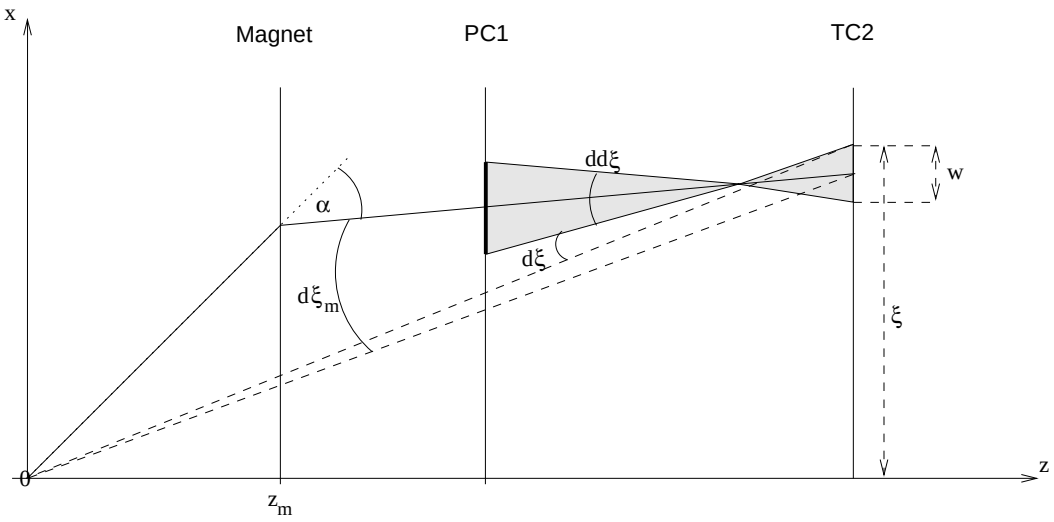

Figure 2.3.3: *Illustration of kinematical parameters of the FLT. Indicated are the variables that describe the slope and position in the horizontal bending plane, from which the total momentum is determined.*

perform a fast cluster search on groups of three by three ECAL cells around an energetic central tower, as depicted in figure 2.3.4.

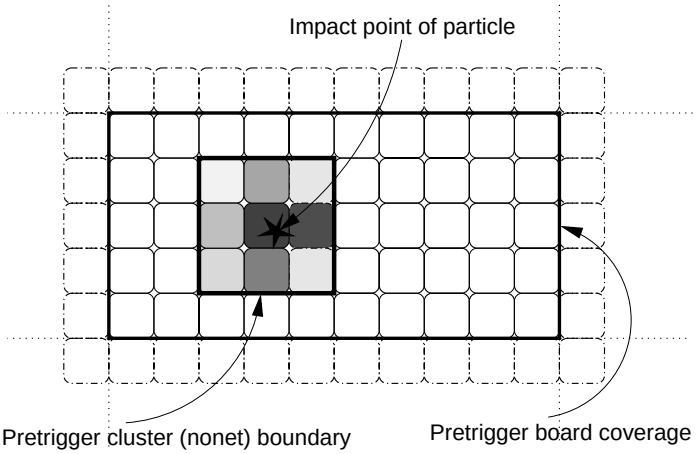

Figure 2.3.4: *Cluster reconstruction by the ECAL pretrigger. Within at most 50 calorimeter cells, an ECAL pretrigger board finds clusters of nine cells with sufficient transverse energy.*

Like the rest of the FLT network, the ECAL pretrigger is built up of dedicated processor boards. The analogue signals from the photo-multipliers are integrated and digitised by readout boards. Each of the channels is separately calibrated and the resulting energy is coded into 12 bits. These energies, compressed to 7 bits, are subsequently sent to one or more pretrigger boards.

One pretrigger board receives the energy values of up to 50 ECAL channels. It first identifies central towers of possible energetic clusters by scanning for local maxima in the energy deposition of cells. The energy of the neighbouring cells is then added to the total energy of this pretrigger candidate. A pretrigger message is created if the

cluster satisfies the following criteria:

$$E_{\text{central cell}} > E_{TH}/2, \tag{2.3.1}$$
$$E_{\text{total}} > E_{TH}, \tag{2.3.2}$$

where E_{TH} is a programmable threshold value. This value can be chosen to effectuate a transverse energy cut of E_T on the cluster:

$$E_{TH} = E_T \left(\frac{\sqrt{x^2+y^2+z^2}}{\sqrt{x^2+y^2}} \right). \tag{2.3.3}$$

Alternatively one can correct for the bending in the magnetic field, and set

$$E_{TH} = K_{TRIG} \left(\frac{1}{\sqrt{x^2+y^2}} + \frac{1}{\sqrt{x^2+|y|^3}} \right), \tag{2.3.4}$$

with x and y in cm. A sufficiently reduced pretrigger rate is achieved by requiring a minimum transverse energy of 1 GeV, which corresponds to a K_{TRIG} value of approximately 700 GeVcm.

The x and y coordinates of the cluster are determined from the centre of gravity (COG) of the cells. An additional 'S-shape' term corrects for a systematic shift due to the shape of the cluster [32]:

$$x = \frac{1}{E_{\text{tot}}} \sum_{i=l,c,r} E_i x_i + A \sinh^{-1} \left(\frac{B}{E_{\text{tot}}} \sum_{i=l,c,r} E_i x_i \right), \tag{2.3.5}$$

$$y = \frac{1}{E_{\text{tot}}} \sum_{i=u,c,d} E_i y_i + A \sinh^{-1} \left(\frac{B}{E_{\text{tot}}} \sum_{i=u,c,d} E_i y_i \right), \tag{2.3.6}$$

where A and B are parameters that depend on the cell width and the cluster shape, respectively.

If the transverse energy satisfies a higher transverse energy threshold (typically 3 GeV), $flag$ is set in the message. The FLT will not try to find a charged track for this message, but forward it through the network as is. This enables the selection of $b \to s\gamma$ decays or directly produced photons (see table 2.1.1).

In the future, the ECAL pretrigger will include Bremsstrahlung recovery. Knowing the energy and spatial coordinates of the electron candidate from the pretrigger, one can predict the possible positions in the calorimeter of photons radiated before the magnet. The energy deposited by such a photon can then be added to that of the cluster already found. An estimated 30% of the electrons emit Bremsstrahlung before the magnet. Recovering this energy increases the efficiency of the pretrigger, without a significant increase of the background.

When the energy and position of these clusters have been determined, the pretrigger composes a message to be sent to the first TFUs of the FLT network. It contains all the information necessary for track finding.

MUON Pretrigger

The MUON pretrigger [33] provides track seeds for muon candidates. It is more than 1000 times more probable for muons to penetrate the thick absorber walls of the MUON detector than it is for hadrons. The occurrence of a track in the MUON system is therefore a straightforward and clean way to separate muons from the hadron background.

Muon candidates are identified by a coincidence of hits in the last two superlayers of the MUON system (MU3 and MU4). These superlayers consist of tube chambers in the outer regions, and pixel chambers for the inner part ($|x| < 33$ cm, $|y| < 42$ cm). The cathode of the tube chambers of MU3 and MU4 is capacitively coupled to rectangular pads, with separate readout electronics for the pretrigger. For the inner part of these superlayers, a similar segmentation is achieved by combining blocks of 6×4 pixel cells into 'pseudo-pads'.

From hits in the pads or pseudo pads of these two superlayers coincidences are determined according to the scheme shown in figure 2.3.5. Tracks in the outer part generally have a lower momentum than tracks in the inner part, causing a larger spread in angles due to multiple scattering. For this reason the coincidence scheme of the pads allows more coincidences than that of the pixel pseudo-pads.

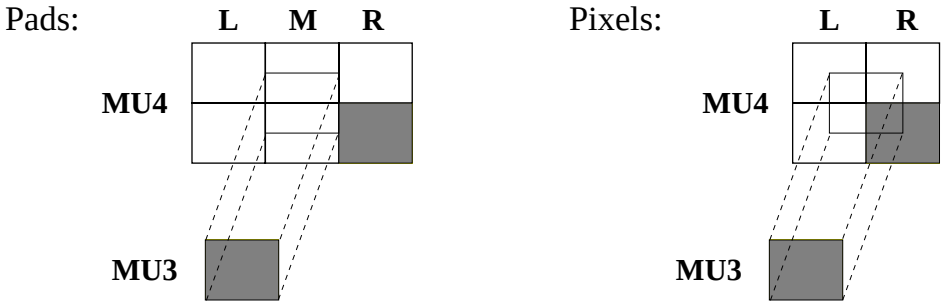

Figure 2.3.5: *MUON pretrigger coincidence scheme for pads and pseudo-pads (pixels), showing the six, respectively four possible coincidences. An example of a possible coincidence is indicated in grey. The pad scheme comprises more coincidences than the pixels, since the spread in track angles, due to multiple scattering, is larger there.*

When a coincidence is found, a message is constructed and transmitted to the FLT network. The FLT uses the tube and pixel chambers of MUON stations MU4, MU3 and MU1, and the main tracker superlayers TC2, TC1, PC4 and PC1 for the reconstruction of muon tracks. Of the muon superlayers used in the trigger, MU1 is the only one with chambers in all three orientations. Since the vertical position determined by the pretrigger is not precise enough, the vertical slope parameter η is updated in the message using a triple hit coincidence found in MU1.

High-Pt Pretrigger

The purpose of the High-Pt pretrigger [34] is an early identification of charged particles with large transverse momentum, p_T. The majority of these are hadrons ($\pi^{\pm}$, $K^{\pm}$, p). This enables the selection of hadronic B or B_s decays shown in table 2.1.1.

Similar to the muon pretrigger, the High-Pt pretrigger determines hit coincidences in different superlayers. The High-Pt pretrigger uses dedicated pad and pixel chambers installed in the magnet. Particles with a low momentum are deflected here due to the magnetic field. In contrast, particles with high momenta form approximately straight tracks even in the magnet. An appropriate coincidence scheme as illustrated in figure 2.3.6 selects straight tracks under large angles, which effectively implies a p_T cut.

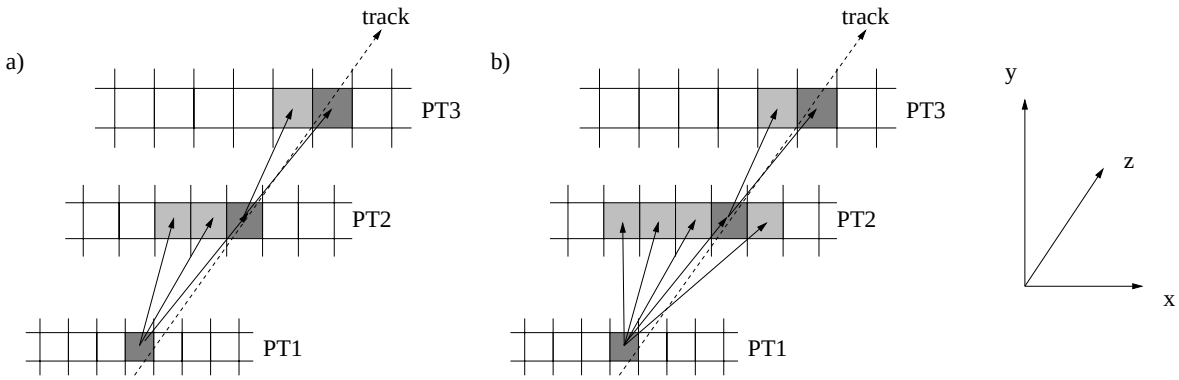

Figure 2.3.6: *Two possible coincidence schemes for the High Pt pretrigger system. a) is the 1-3-2 scheme, corresponding to a p_T cut of about 1.8 GeV/c. b) is the 1-5-2 scheme, which effectuates a cut at a lower value of p_T.*

The High-Pt superlayers PT1, PT2 and PT3 are positioned in the magnet region at distances from the target of 470 cm, 560 cm and 610 cm, respectively. The cell sizes in PT2 and PT3 are projective copies of the cell sizes in PT1 (varying from 4×4 mm^2 to 8×8 mm^2), with scale factors determined by the z position. Therefore there is always a one-to-one correspondence between cells in the vertical (non-bending) plane.

When a triple coincidence is found, the High-Pt pretrigger generates a message with track parameters extrapolated to TC2. They enter the FLT network like ECAL pretriggers, but their RoI is larger, due to the large extrapolation from PT3 to TC2.

Pretrigger summary

Table 2.3.2 shows characteristics of the hardware used for the three different pretrigger types. The detector data (4th column) of the MUON and High-Pt systems is transferred by optical fibres to the processor boards by pretrigger linkboards, located on the front end. They are similar to the FLT linkboards that will be discussed in more detail in the next section.

The average number of messages is estimated for a fully equipped and functional detector and for an interaction rate of 20 MHz. The number of output messages issued by the ECAL pretrigger can be tuned by choosing a certain threshold value (it roughly decreases exponentially with increasing E_{TH}). The limit is given by the maximum number of messages that can be handled by the FLT network. In this way, one can

Pretrigger	nr. of boards	latency	data flow in	av. messages/event
ECAL	128	3.8μs	55 Gb/s	≈ 1 ($E_T > 0.8$ GeV)
MUON	58 (+40 linkboards)	2.3μs	10.6 Gb/s	$\approx$ 1-2
High-Pt	44 (+70 linkboards)	1.1μs	23.6 Gb/s	≈ 1

Table 2.3.2: *Data flow and latency of the pretrigger systems. The message output rate is estimated for 20 MHz interaction rate.*

optimise the efficiency, while the pretrigger output rate is just acceptable for the FLT network. The number of messages per event from the High-Pt pretrigger increases by roughly a factor 2 if the 1-5-2 coincidence scheme (Fig. 2.3.6) is chosen instead of the 1-3-2 scheme.

It is not yet clear at which maximum pretrigger rate the FLT will be able to run finally. This depends on the target rate and on the final performance of the tracking detectors.

2.3.3 FLT processors

All pretrigger messages are transmitted to the FLT network of processor boards, which perform the track reconstruction. The three types of processors (TFU, TPU and TDU) of the FLT network have a lot in common, in spite of the fact that their purposes are very distinct. The main parts are:

- an input buffer (FIFO) for incoming messages.
- a processing part. Calculations are performed using Lookup Tables, which are arranged in a synchronous pipeline architecture and operate at a clock frequency of 50 MHz.
- detector data interface and buffer (only TFUs) for the part of the detector that is handled by this unit.
- an output FIFO for transmission of processed and updated messages.
- VME interface for initialisation, testing and monitoring.

A key component in the FLT processors is the Lookup Table (LUT). It is the building block for the set of calculations an FLT processor needs to perform. Complex calculations are broken up into smaller sub-calculations that can be done by a set of LUTs. The LUTs of the FLT are up to 18-bit-addressable RAM, with 8 bits data at each address. As such, they can perform any function of up to 18 bits and return an 8 bit result.

The LUTs are arranged in parallel on sequential pipeline stages that are clocked by a 50 MHz internal clock. At an event rate of about 10 MHz, each processor can consequently handle up to an average of about 5 messages per event. Since the 10

TFUs that cover an entire superlayer operate in parallel, the processing power of the FLT amounts to the evaluation of up to 500 million (sic!) tracks per second.

The latency of one pipeline stage is 20 ns. The number of pipeline stages should be kept small enough so that tracks are completely evaluated by the processor network within the maximum allowed latency of about 10 μs.

Track Finding Units

The main processors of the FLT are the TFUs. Upon the receipt of a message from one of the pretriggers or from another TFU, they scan for hits that confirm the passage of a charged track. The functionality is essentially comprised of three steps:

(i) Read a message from the input buffer (FIFO) and transform the global track parameters into local coordinates. These coordinates are used to address a part of the detector data where hits are expected to be found.

(ii) Read in detector channels of the three stereo layers and find triple hit coincidences between them in a given search window.

(iii) Combine the coordinates of the coincidence(s) found with the parameters of the incoming message to refine the track parameters. Code the refined track parameters in an updated message (or messages) and send it to the next processor.

Each TFU covers a designated part of the tracking system in which it looks for hits. Figure 2.3.7 shows the segmentation of a tracking superlayer in TFU sectors.

The detector data are stored by the TFU in the Wire Memory (WIM). It contains the last 128 events and for each event up to 384 detector channels per stereo layer. From the track parameters of the incoming message a local RoI is extracted. This is the first channel and the range for each of the three stereo angles in which the TFU looks for hit coincidences. Along with the BX number, this defines an address in the Wire Memory from which an array of up to 32 bits (channels) is extracted.

The first channels of the different stereo layers are aligned with respect to each other according to the vertical position of the expected space point. The hit pattern from the WIM is processed by a Coincidence Matrix, that returns the coordinates of valid triple coincidences. In figure 2.3.9 the valid coincidences are shown.

The set of allowed coincidences also takes into account the uncertainty on the vertical slope of the track. A small deviation in vertical direction would change the relative position of the positive and negative stereo angles with respect to the zero degree layer. A parameter h (height) indicates the magnitude of such a deviation. The set of coincidences most central around the extrapolated vertical position are the six with $h = 0$. A positive (negative) shift in the vertical direction would give rise to the possible extra coincidences of $h = 1$ ($h = 2$). To include all 12 possible coincidences indicated in Fig. 2.3.9 we must set $h = 3$.

For each of the coincidences found in the RoI, the coordinates are calculated and transmitted one after the other. During this time, the TFU is not able to handle a new message. The pipeline processing is stalled until all found coincidences are processed.

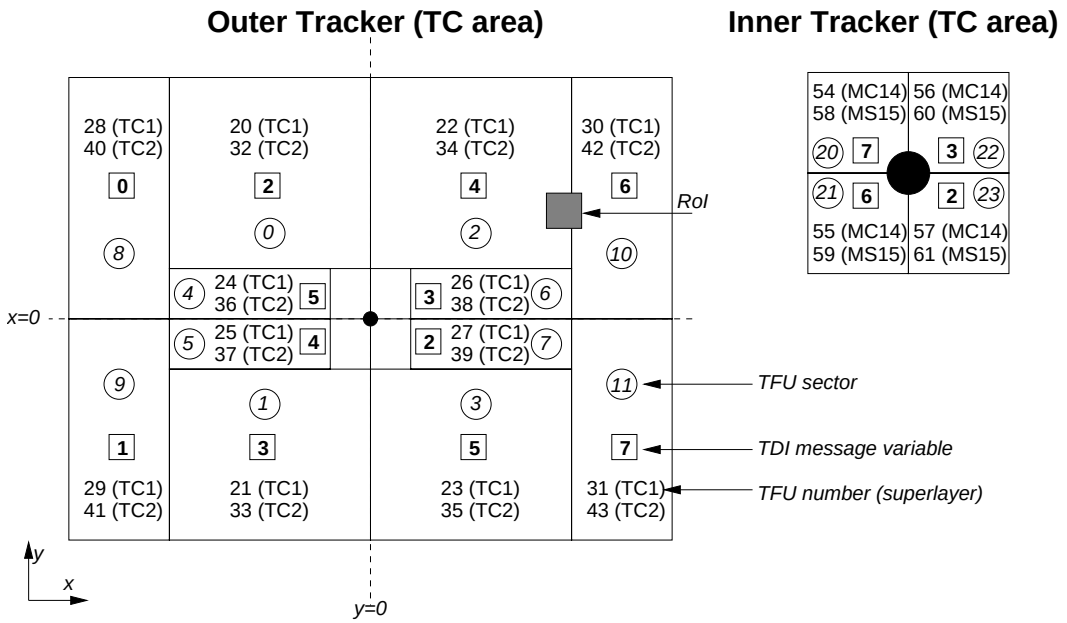

Figure 2.3.7: *Segmentation of the TC tracking stations in TFU sectors. A total of 16 TFUs, 12 for the Outer Tracker and 4 for the Inner Tracker, can confirm the passage of a charged particle in a section of the tracking station. The superlayers PC1 and PC4 are covered by 12 TFUs each: 10 for the Outer Tracker and 2 for the Inner Tracker. For the RoI indicated by a grey area, the TFUs of sectors 2 and 10 will look for coincidences, and* $TDI = 40$.

For each of these coincidences a new message is created, the parameters of which are calculated in the remaining pipeline steps of the TFU.

With the coordinates of the space point found, the track parameters are refined and an updated message is compiled. The TFU determines which of the TFUs in the next superlayer should further process this updated message, and codes this in the message variable TDI (see figure 2.3.7).

Number of boards	70
Total detector data flow in	$\approx$ 1 Tbit/s ($\leq$ 12 Gbit/s per TFU)
Number of Pipeline stages	22
Total number of LUTs	38
Clock frequency	50 MHz
Total latency per TFU	$\approx$ 800 ns

Table 2.3.3: *Data flow and latency of the TFU.*

Data transfer

The TFUs receive data from in total about 100.000 detector channels unsparsified in every bunch crossing of 96 ns. This transfer is accomplished by optical links from

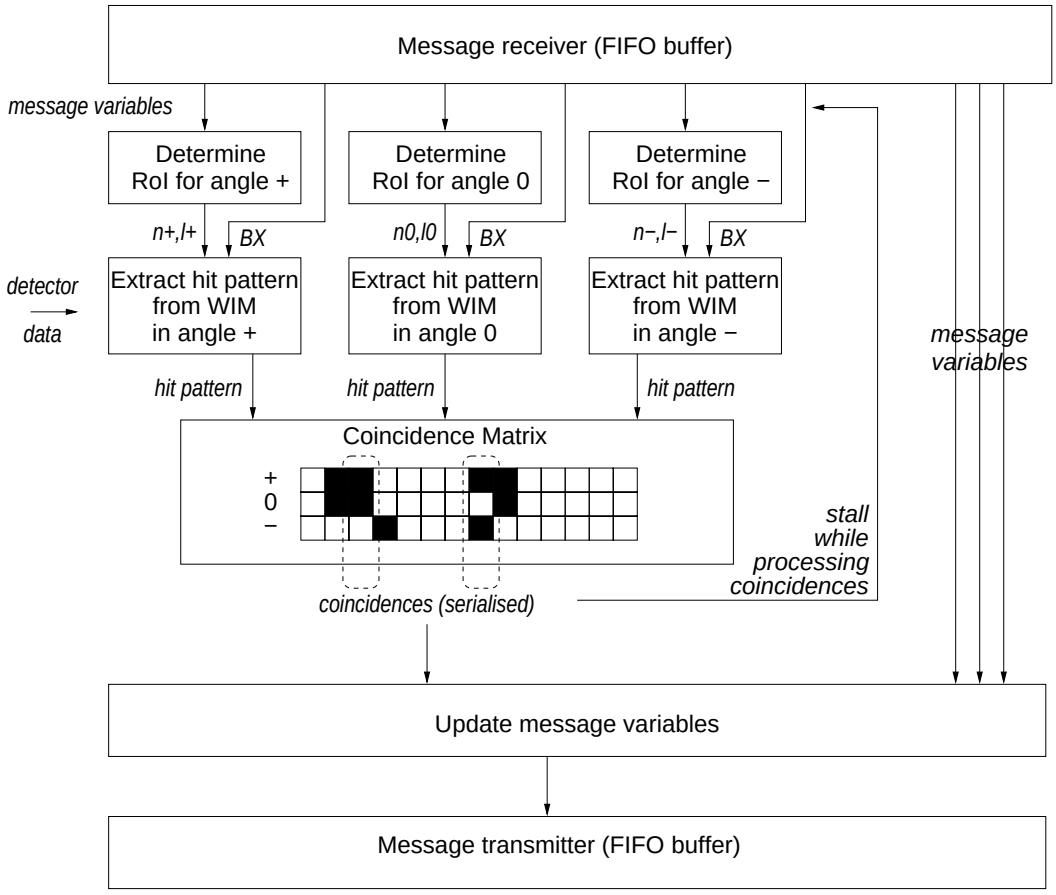

Figure 2.3.8: *Overview of the functionality of a TFU. The incoming messages are stored in a FIFO and processed one after the other by the TFU. For each of these messages, the TFU calculates a local search window in which it scans for a triple hit coincidence. If a coincidence is found, it uses the position of the zero degree hit to refine the track parameters in the message.*

the front end of the detector to the trailer, where the FLT network is installed. FLT linkboards (FLTLB) [35] provide the interface between the detector readout electronics and the TFUs.

The FLT network operates independently of the HERA-B bunch clock. Therefore the detector data need to be time stamped with the BX number. This BX number is provided by the Fast Control System (FCS) to the front end of the detector. The FLTLB uses this BX number and attaches it to each packet of 24 bits of detector data it sends to the TFUs.

The TFUs need to receive the hit patterns from the detector in a well ordered way. The detector cells must be arranged in contiguous, equidistant Wire Memory channels. This is in contrast to the real layout of the tracking chambers: the Outer Tracker has border regions, where cells with 10 mm cell pitch overlap with cells of 5 mm, as indicated in figure 2.3.10.

The FLTLB rearranges the detector data and creates well ordered and consecu-

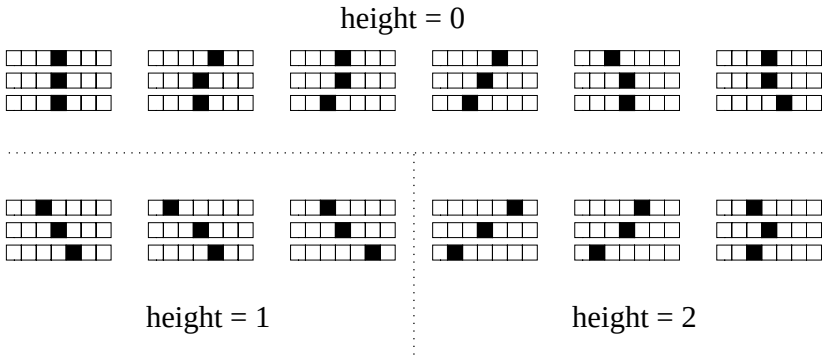

Figure 2.3.9: *Triple coincidences between hits (black squares) of the Outer and Inner Tracker, which are considered valid space points by the coincidence matrix of the TFU. First, second and third row refer to + degree 0 degree and - degree stereo layers respectively. Height refers to the size of the RoI in vertical direction and is explained in the text.*

tive hit patterns of uniform pitch for the TFU. The data from 10 mm cells can be transmitted twice ('doubled') to effectively become two channels of 5 mm pitch. Alternatively, the logical OR'ing of two consecutive 5 mm channels will create one channel of 10 mm pitch. Physically neighbouring channels that do not arrive consecutively from the readout electronics, will be re-ordered to do so in the output of the FLTLB.

For a track to be reconstructed by the FLT, hits need to be found in all superlayers used and for all[2] three angles. For ECAL pretrigger messages, that need to be confirmed by triple coincidences in four stations, this means that all 12 hits must be recorded. With an Outer Tracker cell efficiency of $\epsilon_{\mathrm{OTR}} = 98\%$, this would imply a track efficiency of $\epsilon_{\mathrm{OTR}}^{12} = 78\%$. To increase this efficiency, the FLT uses double layers, and requires only that at least one of the two cells records a hit. The maximum FLT electron track efficiency for an OTR cell efficiency of 98% then increases to

$$\epsilon_{\mathrm{FLT\ track}} = \left[1 - (1 - \epsilon_{\mathrm{OTR}})^2\right]^{12} = 99.5\%. \tag{2.3.7}$$

In figure 2.3.11 we illustrate the correspondence between detector channels and hit patterns for the TFU. Whereas the OR'ing of the double layer channels is performed on the TDC, any additional logical rearrangement of detector channels has to be performed by the FLTLB. In addition, the FLTLB serialises the data along with the BX number and transmits this data via optical fibres to the TFUs.

Each FLTLB is equipped with eight parallel links, schematically depicted in figure 2.3.12. Each link handles up to three 34 pin (32 signal + 2 GND) TTL inputs from the readout electronics. Each of these inputs is connected to a Programmable Logic Device (PLD). These PLDs can be programmed to perform any required logical operation between the individual channels. The output of the three PLDs of one link drive a common bus of 24 bits going to a Motorola Autobahn IC for serialisation. For every BX cycle, the FLTLB creates two 32 bit packets, containing 24 bits of detector data

[2]The possibility to reduce this stringent requirement to demanding only two of three hits in each stereo view is presently under study.

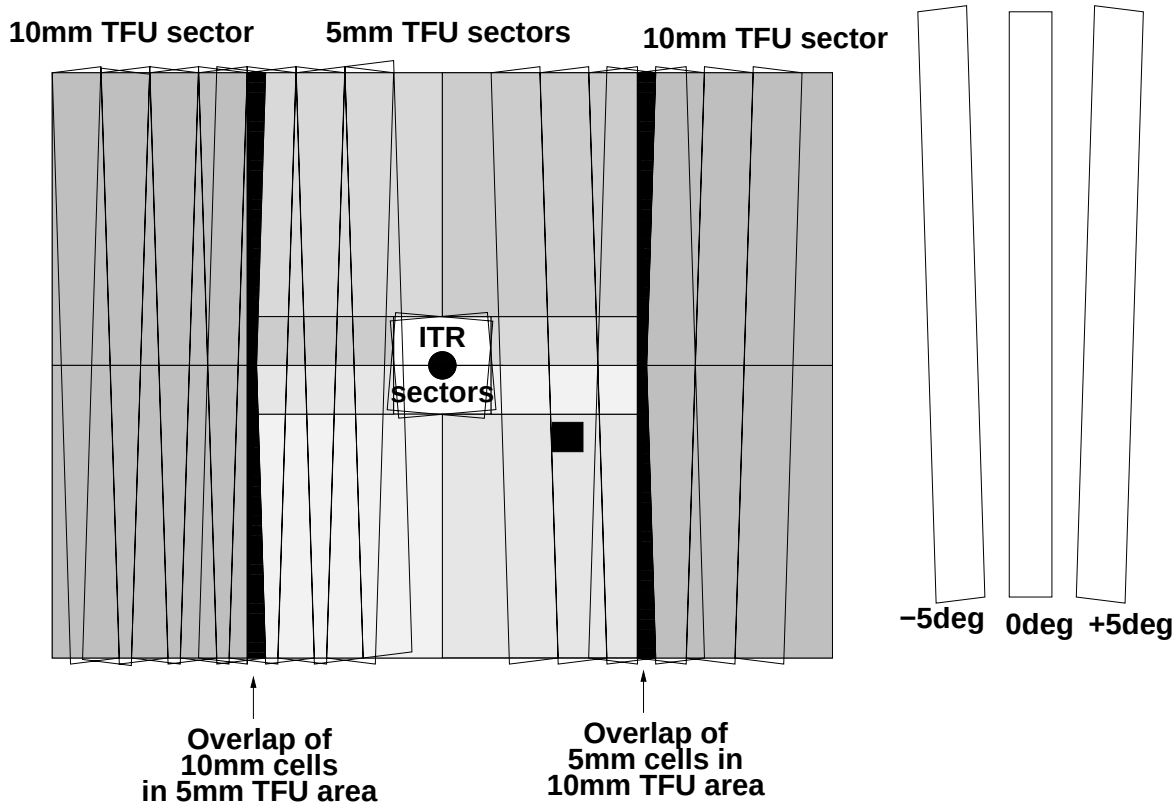

Figure 2.3.10: *Layout of Outer Tracker superlayer (PC), made up of modules of 5 mm and 10 mm cell pitch in three different stereo angles. Regions, where modules of different cell pitches overlap, are indicated in black. The TFU sectors are indicated by various shades.*

and an 8 bits BX number, that it receives from the FCS. The serialised 32 bit packages are sent to an optical transmitter that drives a fibre of 50 meters going to one of the TFUs.

The FLTLB can be switched to several operation modes via control signals from the FCS. Besides the default operation, in which detector data is transferred, the FLTLB can be set to send test patterns or board specific information (serial number, link number). This is useful for testing and debugging purposes.

A second backplane connection provides the supply voltage and an interface for in-system-programming (ISP) of the PLDs. All PLDs of a FLTLB are interconnected through a 'JTAG' chain. Via this JTAG backplane and an addressable scan port, all installed FLTLBs can be (re)programmed remotely, i.e. without access to the detector where the linkboards are installed. Linkboards may have to be reprogrammed to alter or improve the mapping of detector channels to WIM cells in the TFU. Furthermore this allows the masking of hot or dead channels to improve the performance of the FLT: dead detector channels can be switched on or hot channels can be masked off in the transmission to the TFUs.

A recent and very useful addition [36] to the linkboard functionality enables this

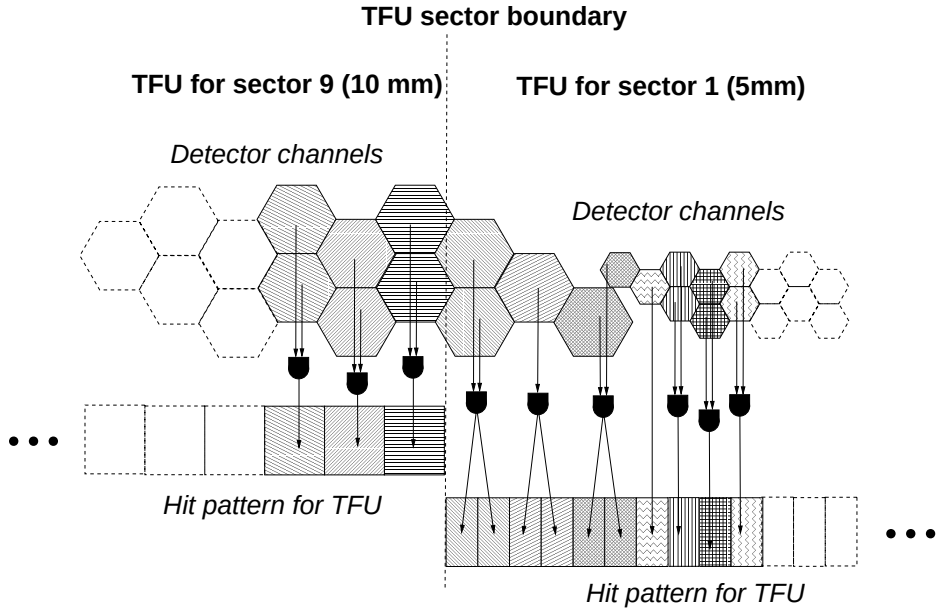

Figure 2.3.11: *Mapping of detector channels to TFU Wire Memory channels. The black symbols indicate a logical 'OR' operation. Shown is a border region between a 5 mm and a 10 mm Outer Tracker sector. The boundary of the TFU sectors is indicated by a dotted line. The hit patterns are transmitted to two different TFUs.*

masking via the FCS port, without reprogramming of the PLDs. This is a faster and more versatile way. Problems due to the fact that the PLDs should not be reprogrammed more than 100 times are thus avoided.

Number of boards installed	156 (105 for tracking system and 51 for MUON)
Total data flow (in≈out)	≈ 0.6 Tbit/s (4 Gbit/s per FLTLB)
Number of PLDs per FLTLB	25 (24 for mapping, 1 for board control)
Clock frequency	20.84 MHz (2×BX clock)
Serial (optical) output	900 MHz
Latency	≈ 80 ns (excl. fibre propagation)

Table 2.3.4: *Characteristic parameters of the FLT linkboards.*

Track Parameter Units

When messages have successfully passed through the network of TFUs, they are transmitted to a Track Parameter Unit (TPU). The TPU translates the track parameters in the message into a charge and a momentum vector. Messages that do not satisfy a cut on transverse or total momentum can be filtered out.

Electron candidates can undergo additional cuts here. The majority of the ECAL seeded tracks arriving at the TPU are not from electrons or positrons, but from the

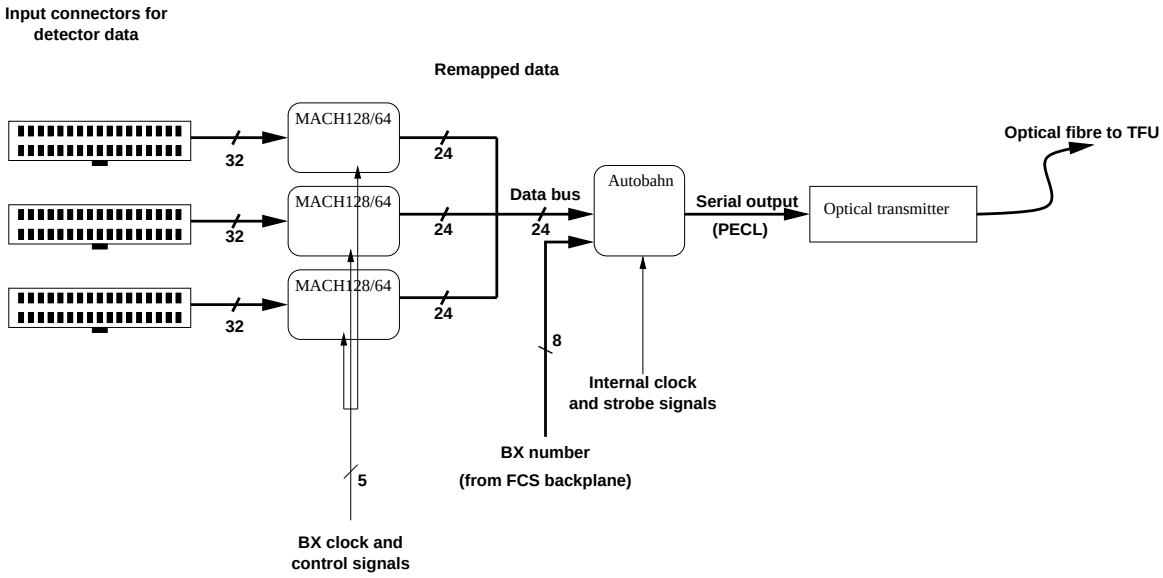

Figure 2.3.12: *Schematic of an FLTLB link. Each FLTLB comprises eight links. The clock signals and BX numbers are received from the FCS backplane, as well as control signals that select the mode of operation in the mapping PLDs (MACH128/64). An internal 25 MHz clock is used exclusively for the serialisation by the Autobahn ICs.*

more abundant energetic hadrons. The TPU can reduce the hadron background by requiring the pretrigger cluster energy to be within 50% equal to the momentum.

Moreover, since the charge of the track has been determined, the TPU can determine the location of a possible additional cluster due to Bremsstrahlung before the magnet. Depending on this charge it is to be found either to the left or to the right of the cluster found by the ECAL pretrigger. The energy of the Bremsstrahlung cluster is added to the original cluster.

ECAL pretrigger clusters with very large transverse momenta, that were forwarded unaffected through the network of TFUs, are treated as photons: the total momentum is taken as the cluster energy, and the particle direction is given by the cluster coordinates.

The TPU can furthermore compare the found tracks and reject clones, i.e. tracks with almost identical parameters. Each incoming message is compared to the last 20 messages that have already been found by the TPU. A message is rejected if the values p_x/p_z and p_y/p_z are the same as those of an already found message within a window of one, while the ID and the BX number are exactly the same. Such messages are expected to have originated from the same track, but could occur more than once, due to the overlap of detector regions of different TFUs or because of duplicated coincidences.

The TPU can also discard additional tracks when the number of tracks found in this event has already reached a certain value, typically four to eight. The number of track pair combinations to be evaluated by TDU can thus be kept at a tractable level.

The messages that have passed all these cuts are transmitted to the last processor

of the FLT, where the final trigger decision is made. These messages have a structure that is different from that of the TFU (table 2.3.1). Instead of the pretrigger cluster energies P, E^+ and E^-, the messages now contain the calculated momentum vector.

Number of boards used	4
Number of Pipeline stages	12
Total number of LUTs	54
Clock frequency	50 MHz
Total latency per TPU	260 - 660 ns

Table 2.3.5: *Characteristic parameters of the TPU.*

Trigger Decision Unit

The Trigger Decision Unit (TDU) makes the decision whether or not to accept an event. Such a decision can be based on the number of found messages of a certain type (ID) or on the reconstructed invariant mass of a message pair.

The first type of decision, called 'count trigger', can be made on any combination of messages. The requirement is a minimum number of tracks of a certain type (electron, muon, hadron). A variety for physics channels can be selected by requiring (a combination of) leptons or hadrons with large transverse momentum (see table 2.1.1). The count trigger module can have 14 trigger types programmed, which correspond to the occurrence of any number of (high-p_T) electrons, hadrons, muons and photons or a combination of them.

During most of the FLT running in 2000 the TFU network was not used for default 'physics' data taking. The pretrigger messages were directly forwarded to the TDU and here a trigger accept signal was issued when there were at least two ECAL messages or at least two MUON messages. In this way, J/ψ candidates could be selected, while the FLT was in a commissioning phase.

The second type of decision is based on a high invariant mass of a message pair, called 'pair trigger'. To increase the computional speed, the TDU is equipped with four pair trigger modules that process message pairs in parallel. The pair trigger module calculates the invariant mass of each pair and codes this in four bits. The mass is used along with other information of the message pair (see table 2.3.6) as input to the TDU trigger lookup table, where it is used for a trigger decision. In principle, any of the 2^{18} possible trigger patterns can be defined as triggerable. A positive decision is typically made when the mass is above 2 GeV/c^2.

Messages that have passed the pair trigger or the count trigger are forwarded to a pre-scaler. Here, any of the triggers can be down-scaled by a predefined factor that ranges from 1 to 65536.

The triggers that pass the pre-scaler are stored in a trigger memory. Upon the arrival of a trigger, the TDU notifies the Fast Control System (FCS). The FCS then distributes a 'Trigger Accept' to all readout electronics on the detector, unless the

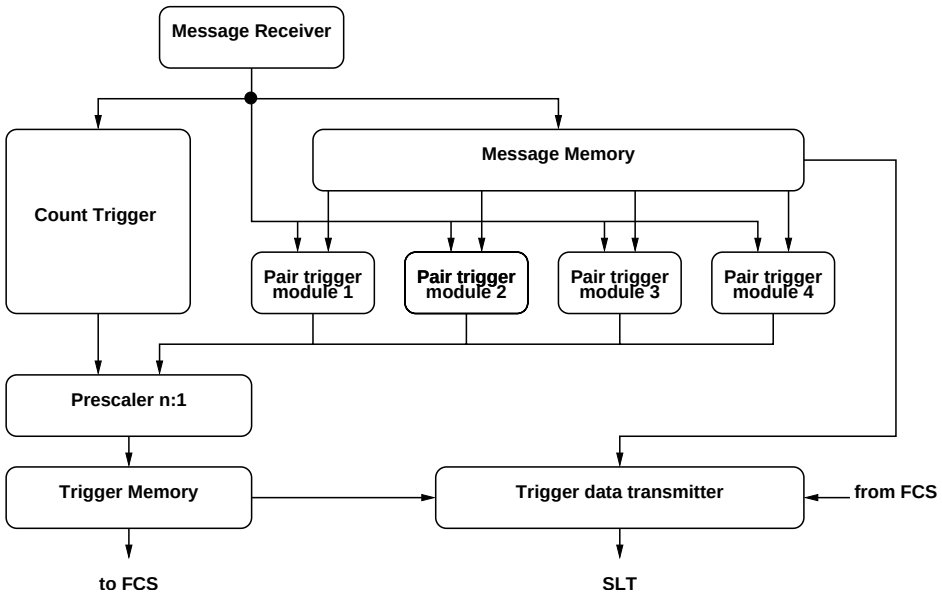

Figure 2.3.13: *Schematic diagram of TDU functionality. The mass reconstruction of message pairs is performed by one of four pair trigger modules, which work in parallel. The output of the trigger module is the eight bit pattern of table 2.3.6, on which a trigger decision is based.*

readout is still busy with a previous event. The readout electronics respond on a 'Trigger Accept' by transmitting the complete detector data to the Second Level Buffer (SLB). The TDU receives such a trigger accept too. Upon receipt, it transmits a record of 300 bytes containing up to 24 messages to the SLT. The SLT uses these messages as track seeds for a re-evaluation and refining of the found tracks.

bits	trigger information	description
0	QXOR	set when charge of tracks is different
1..2	ID1	particle type of 1st track
3..4	ID2	particle type of 2nd track
5..7	Pt1	p_T of 1st track
8..10	Pt2	p_T of 2nd track
11..13	Easym	normalised difference in energies
15..18	M	mass, $2 + 0.2 \times (\text{value} - 1) < m < 2 + 0.2 \times \text{value}$

Table 2.3.6: *Input to the TDU pair trigger lookup table. A trigger decision can be based on any combination coded here. Typically, a positive trigger decision is reached for any nonzero value of bits 15-18 (mass), while bit 0 is set and ID1=ID2.*

Number of boards used	1
Number of Pipeline stages	5
Total number of LUTs	20
Clock frequency	50 MHz
Total latency per TDU	540 - 2120 ns

Table 2.3.7: *Technical properties of the TDU.*

2.4 Design performance

We conclude with a description of the design performance of the FLT. Quantities that define the performance are:

- **rejection power.** The rejection factor of the FLT is an environmental constraint. The SLT, that processes the event after it has been accepted by the FLT, can cope with an event rate of not more than 50 kHz. Parameters, such as cut values for mass or p_T, are tuned so that the FLT output rate does not exceed the maximum allowed input rate of the SLT.

- **efficiency.** The probability to accept a signal event depends on the applied cuts. The efficiency is also affected by external conditions such as the pretrigger efficiency, the channel efficiency of the tracking chambers, chamber alignment, the intrinsic efficiency of the FLT algorithm, and errors in the electronic transmission.

- **resolution.** Given the limitations of the FLT algorithm, the track parameters are resolved with less accuracy than the off-line track reconstruction. Consequently, the invariant mass resolution of the FLT is also worse. This is a minor issue, as long as the resolution is sufficient for a mass cut that gives the required rejection power, without rejecting too large a fraction of the signal events.

The benchmark performance of the FLT is the resolution and efficiency for $J/\psi \to \mu^+\mu^-$ and $J/\psi \to e^+e^-$ decays. The resolution is measured from two samples of Monte Carlo events, generated by PYTHIA [37] and FRITIOF [38], that contain both leptonic decays. For these events we have run a detailed detector simulation using GEANT [39] and simulated the detector response with optimal hit efficiencies and resolutions. A complete event reconstruction is done on the simulated digitised hits. This event reconstruction is identical to the one used for data that were taken in the course of 2000. From the Monte Carlo hit information we compile raw data records that are processed by an FLT hardware emulation program, that is described in more detail in section 4.3.1.

2.4.1 Resolution

We define the resolution of the FLT as the accuracy to which the tracks, generated by the Monte Carlo simulation, are reconstructed by the FLT. It is determined from a fit

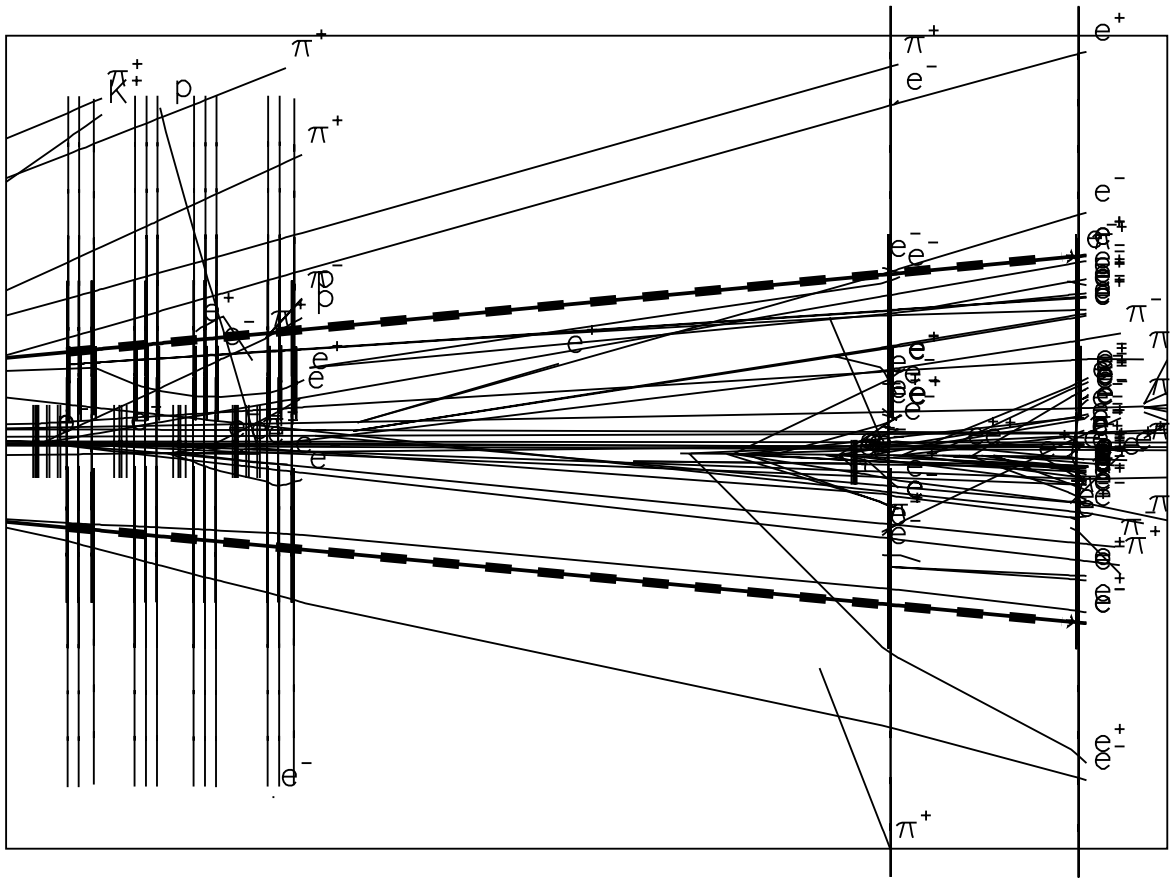

Figure 2.4.1: *Event display of a Monte Carlo generated* $J/\psi \rightarrow e^+e^-$ *decay, showing the electron tracks reconstructed by the FLT. The two Monte Carlo tracks are indicated as thick solid lines and the two FLT reconstructed tracks are shown as dashed lines.*

a of Gaussian distribution to the measured residuals. We consider here the momenta of the leptons into which the J/ψ decays and the invariant mass of the J/ψ.

The definition is inclusive in the sense that it also includes effects such as multiple scattering. A comparison of the resolution of the FLT to that of the off-line track reconstruction [40] is instructive. The latter can be considered to give the best attainable resolution, when restricted to tracking downstream from the magnet. It can thus be estimated to what extent FLT specific properties affect the resolution.

The main track parameters calculated by the TPU are the slopes in x and y and the longitudinal momentum of the lepton tracks before the magnet. The resolution for these parameters are summarised in table 2.4.1 in comparison to the resolution of the off-line track reconstruction. The resolution in the x direction is up to 50% worse than achievable off-line. The fact that the resolution in y of FLT tracks is better than of off-line tracks, is merely because the FLT uses the ECAL for the determination of y.

When these resolutions were evaluated, the lookup tables of the TPU were not yet fully optimised. Due to a binning effect, p_z as calculated by the FLT was systematically lower than the Monte Carlo values. For determining the resolution in p_z we have

Quantity	$J/\psi \to \mu^+\mu^-$		$J/\psi \to e^+e^-$	
	σ_{FLT}	σ_{RANGER}	σ_{FLT}	σ_{RANGER}
p_y/p_z	1.34(2) mrad	2.70(6) mrad	0.81(2) mrad	5.9(1) mrad
p_x/p_z	1.07(2) mrad	0.456(2) mrad	1.29(2) mrad	0.81(1) mrad
p_z	7.8(2)%	2.16(5)%	11.3(2)% (∼19%)	7.8(1)% (∼34%)
$m_{J/\psi}$	∼200 MeV/c^2	47(4) MeV/c^2	see Fig. 2.4.2.b	see Fig. 2.4.2.b

Table 2.4.1: *FLT lepton momentum and J/ψ mass resolution compared to values obtained from an off-line reconstruction (RANGER [40]). The resolution is obtained from a Gaussian fit to the residuals FLT minus Monte Carlo. For the electrons the p_z resolution quoted is obtained by excluding the radiative tail from the fit; the fraction of events in this radiative tail is quoted in brackets. The residuals in p_x/p_z are systematically shifted from 0 by 1.5 mrad. This is due to binning effects in the calculation of p_z by the TPU. For the mass calculation we have corrected for this.*

therefore not relied on the values of the TPU. Instead the momentum was estimated from the slopes obtained by the TFUs downstream from the magnet.

These values were also used to determine the invariant mass, since a emulation for the TDU hardware was not yet available. If the momenta obtained from the TPU are used, the mass resolution is about 30% worse than quoted in table 2.4.1. In figure 2.4.2 the reconstructed invariant mass spectra for both decay channels are shown.

The difference in mass resolution between the FLT and the off-line track reconstruction is best visible in the muon channel. The width of the J/ψ signal is about a factor three larger. An invariant mass cut of 2 GeV is expected to sufficiently reduce the non-J/ψ background. The FLT resolution is therefore adequate to impose such a

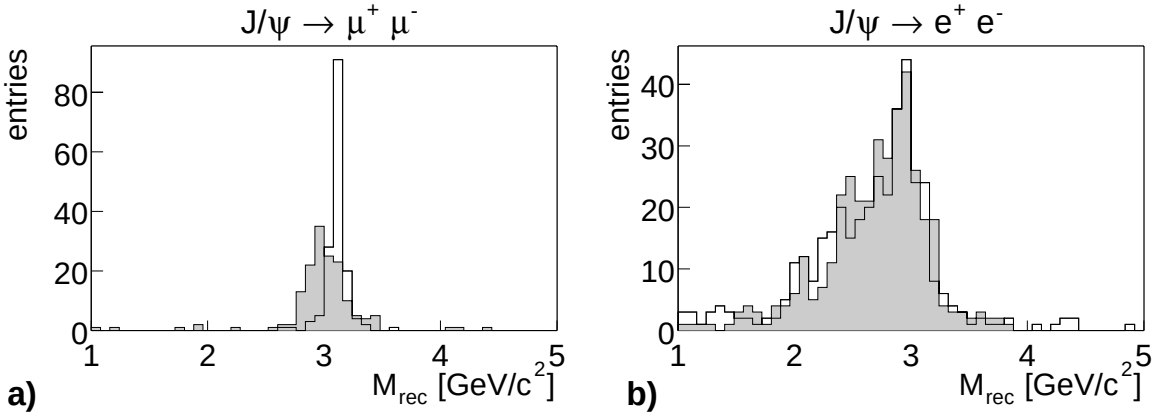

Figure 2.4.2: *Reconstructed mass spectra for $J/\psi \to \mu^+\mu^-$ (a) and $J/\psi \to e^+e^-$ (b). Shown are the results from an FLT hardware simulation (shaded histogram) and from off-line track reconstruction (open histogram).*

cut efficiently.

For $J/\psi \to e^+e^-$ events without a Bremsstrahlung correction this mass cut will cause an efficiency reduction. An estimated 10% of the signal will be below 2 GeV due to energy loss before or inside the magnet. With Bremsstrahlung recovery, the mass cut can be done with an estimated 99% efficiency.

2.4.2 Efficiency

The design efficiency for recording J/ψ decays is dominated by geometrical acceptance and kinematic cuts at the pretrigger level. The trigger efficiencies summarised in table 2.4.2 are based on design [8] specifications:

	single muon	$J/\psi \to \mu^+\mu^-$	single electron	$J/\psi \to e^+e^-$
Geometry	84%	70%	84%	70%
Pretrigger	96%	92%	71%	51%
FLT tracking	97%	94%	98%	96%
$M^{\mathrm{FLT}}_{\ell^+\ell^-} > 2$ GeV/c^2	-	99.8%	-	90%
total	78%	61%	58%	34%

Table 2.4.2: *Design trigger efficiencies for* $J/\psi \to \ell^+\ell^-$ *decays. For the electron pretrigger efficiency we assume a transverse momentum cut of* K_{trig} *=700 GeVcm. For the mass cut on the electrons we assume the Bremsstrahlung recovery to be absent in the FLT.*

Whether these efficiencies will be reached in future data taking remains to be seen. Trigger conditions such as kinematic cuts at pretrigger level are still subject to change.

A veto system, which rejects events with a large number of photons in the RICH [41] or a large energy deposition in the calorimeter [10], will be added to the FLT. This will prevent high multiplicity events from being processed by the FLT, that would otherwise put a disproportionate load on the processor network. It is expected to be over 98% percent efficient for J/ψ [42].

The FLT efficiency depends mainly on the detector performance. The FLT tracking is very sensitive to cell and pad efficiencies (Eq. 2.3.7). In the following chapters we will study the performance in more detail.

Chapter 3

Performance of the ECAL Pretrigger

Electron candidates in the FLT are charged tracks seeded by the ECAL pretrigger. Insight in the performance of the ECAL pretrigger is essential for understanding the performance of the FLT for finding electrons. Any inefficiency here directly reduces the total FLT efficiency.

Similarly, the resolution of the ECAL pretrigger affects the resolution and efficiency of the FLT in its totality. A good energy resolution enables an efficient and restrictive transverse energy cut by the pretrigger and a meaningful E/p cut by the FLT. Furthermore, the pretrigger provides a Region of Interest for subsequent track finding by the FLT. For this, both the spatial resolution and the energy resolution of the pretrigger must be adequate.

In this chapter we present a study on the resolution, efficiency and rejection power of the ECAL pretrigger. First, we discuss the properties of the ECAL pretrigger algorithm and how the limitations can affect the performance. We then prove that a pretrigger simulation exactly emulates the behaviour of the hardware. Some defects of the hardware are identified and discussed. Subsequently, this simulation is used to measure the resolution and the efficiency on Monte Carlo generated events. The pretrigger resolutions are compared to those of an off-line cluster reconstruction program. Several contributions of specific limitations of the ECAL pretrigger to the total resolution are separately evaluated. Electron energy losses and Bremsstrahlung recovery are studied. Sources of inefficiency are individually measured. The background rejection power of requirements on pretrigger candidates are studied.

3.1 Cluster reconstruction

3.1.1 Off-line cluster reconstruction

The off-line[1] reconstruction program CARE [31, 43] performs a stand-alone reconstruction of clusters in the ECAL. This reconstruction consists of two parts: cluster finding and shower searching.

[1] with off-line reconstruction we indicate the reconstruction carried out on the 4LT/FARM, which is actually done online

The cluster finding is based on a hierarchical method [44]. In order of decreasing energy, all ECAL cells above a certain energy threshold (150 MeV, 100 MeV, 50 MeV, for Inner, Middle and Outer ECAL, respectively) are selected to form a new cluster or are added to an already found cluster or group of clusters. In the subsequent shower search phase, groups of overlapping clusters are disentangled into individual clusters. Clusters are split if the energy of a cell in between two energetic ($E > 1$ GeV) cells is at least 200 MeV less than either of them.

The total energy of the cluster is the sum of the energies in the individual cells, $E = \sum_{i=1}^{n} E_i$. The cluster position (x, y) is the centre of gravity of the energy deposition, corrected for the shape of the cluster [43], which reads

$$x = \frac{1}{E}\sum_{i=1}^{n} E_i x_i + C_1 \sinh^{-1}(C_2(\frac{1}{E}\sum_{i=1}^{n} E_i x_i - x_{\text{central cell}})), \tag{3.1.1}$$

$$\tag{3.1.2}$$

and similar for y. A z coordinate is estimated as the penetration depth of the shower:

$$z = z_0 + A + B\ln(E). \tag{3.1.3}$$

The constants A and B have different values for the Inner, Middle and Outer parts of the calorimeter. The penetrations depths and the spread therein is therefore different for the different parts, as shown in Fig. 3.1.1.

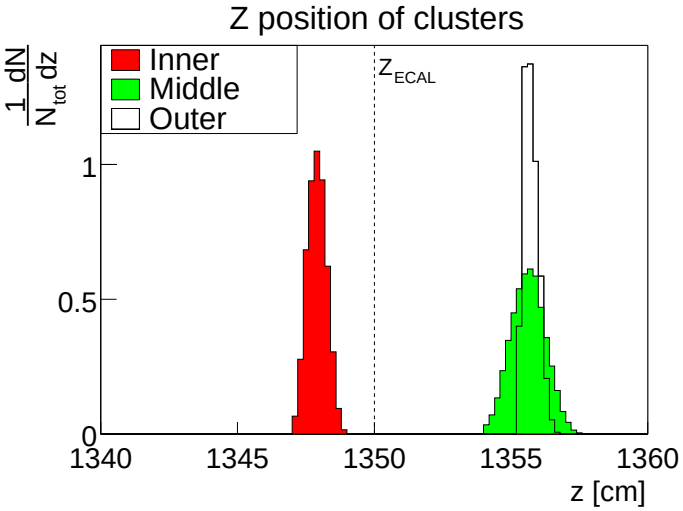

Figure 3.1.1: *Distribution of reconstructed z positions of ECAL clusters for Inner, Middle and Outer ECAL, as determined by the off-line cluster reconstruction program CARE from the energy in the cluster.*

The cluster reconstruction by CARE can be considered as an upper limit to what is achievable by the ECAL pretrigger. A comparison of the parameters of off-line clusters to those of pretrigger messages shows to what extent the intrinsic limitations of the ECAL pretrigger algorithm affect the resolution and efficiency.

3.1.2 Pretrigger cluster reconstruction

Whereas the off-line cluster reconstruction has no severe computation time limitation, this is not the case for the ECAL pretrigger. A decision by the FLT needs to be

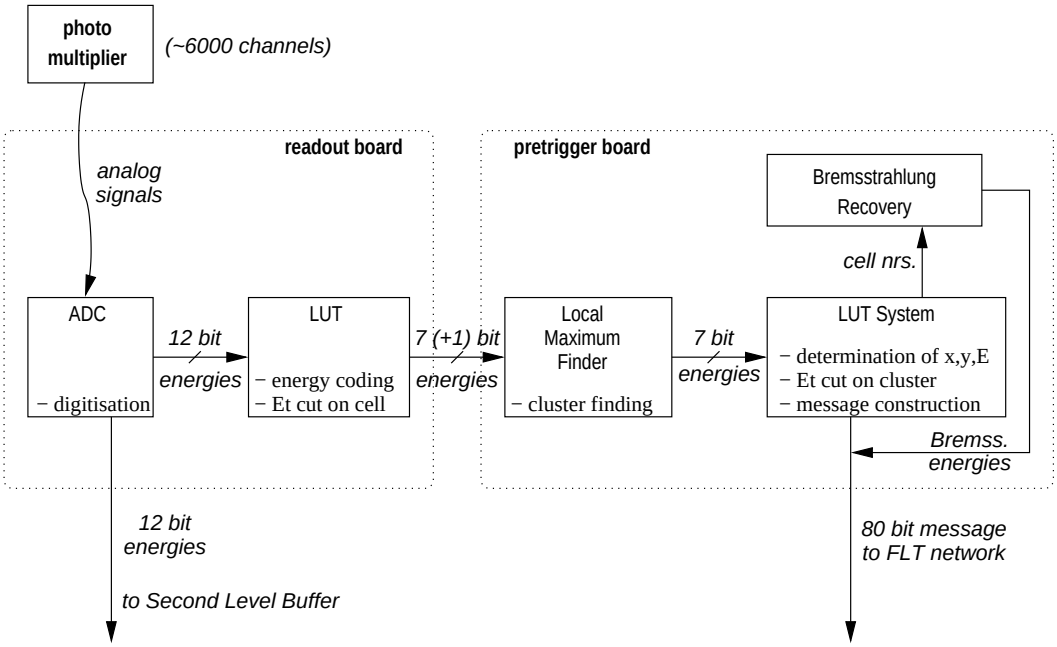

Figure 3.1.2: *Overview of the data path for the ECAL readout and pretrigger.*

made within 12.3 μs. To leave sufficient time for subsequent track finding and decision making by the FLT network, ECAL pretrigger messages must be issued within 3.8 μs. The cluster reconstruction by the pretrigger is similar to that of CARE, but some simplifications are applied.

Figure 3.1.2 shows an overview of the data path and the functionality of the pretrigger. The readout electronics digitise the analogue signals from the photo-multipliers into twelve bit energies. These twelve bits are sufficient not to have a considerable effect on the energy resolution. For the pretrigger, however, these energies are re-encoded into a compressed 7 bits per channel. The coding of the energies for the pretrigger is different for each of the three ECAL parts, specifically:

$$\begin{aligned} \text{Inner ECAL}: \quad & E_{\text{coded}} = 127 \times \min(\sqrt{E/280}, 1), \\ \text{Middle ECAL}: \quad & E_{\text{coded}} = 127 \times \min(\sqrt{E/100}, 1), \\ \text{Outer ECAL}: \quad & E_{\text{coded}} = 127 \times \min(\sqrt{E/65}, 1). \end{aligned} \tag{3.1.4}$$

This optimises the bit granularity for the radial dependence of the cluster energies.

Each channel, that satisfies a transverse energy cut of Eq. 2.3.1, is tagged as a central cell of a possible pretrigger cluster, by setting an additional bit. Before constructing a cluster, the pretrigger compares the energy of a central cell candidate to the energy of its closest neighbours. Only a central cell candidate that is more energetic than any of its closest neighbours, is used to form a pretrigger cluster.

Such pretrigger clusters can be chosen to consist of either five channels, arranged in a cross, or of a block of nine channels, called a nonet (see figure 3.1.3). Only channels that have the same cell size as the central cells are used: the pretrigger thus treats the different parts of the ECAL essentially as separate detectors. While cross summation

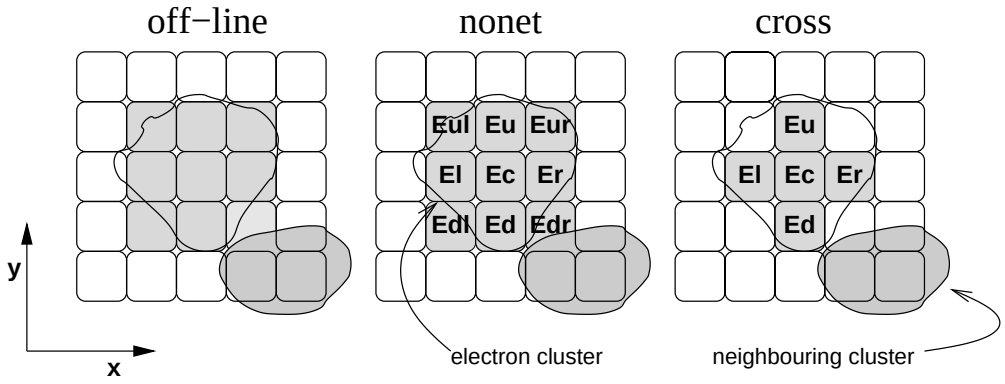

Figure 3.1.3: *Possible cluster shapes for pretrigger and off-line reconstruction. The total energy in the cluster is the sum of the energies deposited in the shaded cells. The lateral extent of the cluster is indicated by a line. Also shown is a neighbouring cluster that partially overlaps with the cluster of the electron.*

was chosen for data taking in 2000, the nonet summation will be used in future running. The energies in the cells of such a group are summed to obtain the total cluster energy. The pretrigger cluster coordinates (x,y) are determined from the centre-of-gravity of the energy deposition in the five cells of the pretrigger cross, and include the cluster shape corrections used off-line (Eq. 3.1.1):

$$x_{\mathrm{COG}} = x_c + \Delta x \frac{E_r - E_l}{E_l + E_c + E_r}, \tag{3.1.5}$$

$$x = C_1 \sinh^{-1}(C_2 x_{\mathrm{COG}} - x_c), \tag{3.1.6}$$

where x_c is the position of the middle of the central cell of the cluster, and Δx the distance between two cells (the calculation for y is identical). The calculation of the coordinates is the same for cross or nonet clusters.

The cluster coordinates and energy are coded in a message (see table 2.3.1), to be sent to the FLT network. This message also includes variables used for subsequent track finding, explained in section 3.9.3, and the energy in possible Bremsstrahlung clusters, discussed in section 3.8. If the pretrigger cluster satisfies the second transverse energy cut of Eq. 2.3.2, this message is transmitted to the FLT for further processing.

3.1.3 Pretrigger simulation

A simulation program called EcalSIM [45, 11] emulates the complete functionality of the ECAL pretrigger system. EcalSIM uses the raw ADC values from the readout boards and performs LUT operations that are bitwise identical to the operations performed by the hardware. The recorded 12-bit ADC values are first converted into the compressed 7 bit energies used by the pretrigger (Eq. 3.1.4). After identifying possible central cells of pretrigger clusters and scanning for local maxima, each pipeline step of the pretrigger is emulated until finally a set of FLT messages is constructed.

EcalSIM can be run on triggered data to reproduce the FLT messages found by the hardware. Since it performs calculations that are identical to those of the hardware,

the FLT messages generated by the simulation should be exactly the same. We will establish in section 3.4 that the simulation generally reproduces the behaviour of the hardware accurately. Dissimilarities are to be attributed to electronic defects of the pretrigger hardware. The simulation is a good tool to find such defects.

The simulation is very useful to study the functionality of the pretrigger in a controlled manner. Each single calculation step of the pretrigger can be carefully examined. The simulation can be run on minimum bias data to obtain an estimate of the background rejection. The effect of settings, such as the transverse energy threshold, cross or nonet summation, Bremsstrahlung recovery, pretrigger board coverage, etc., can be separately studied. Possible improvements in the algorithm can be studied first in the simulation, before applying them on the hardware.

EcalSIM can also be used on samples of Monte Carlo generated events. This allows a study of the pretrigger performance on specific physics channels, most notably $J/\psi \rightarrow e^+e^-$ decays. The efficiency to trigger on such decays, and its dependence on pretrigger settings, can thus be determined.

3.2 Influences on the ECAL pretrigger performance

Influences on the performance of the ECAL pretrigger can be divided into two categories: extrinsic effects and intrinsic effects. With intrinsic effects we indicate effects that are specifically due to the limitations of the pretrigger. The extrinsic effects refer to the environmental constraints in which the pretrigger has to operate: they equally affect the pretrigger and the off-line cluster reconstruction.

Extrinsic effects

- **Overlapping clusters**
  In the high multiplicity environment of HERA-B, the ECAL reaches occupancies of up to 10% [43]. Some clusters may partially overlap with a cluster of another particle. Even if the reconstruction can disentangle the separate clusters, the energies, and consequently the spatial coordinates, can be incorrect;

- **Electron energy loss**
  Upon reaching the ECAL, an electron has traversed approximately a full radiation length of detector material. Most of the Bremsstrahlung photons are radiated after the magnet and will be deposited in the cluster of the electron itself. A significant amount of energy is lost inside the magnetic field, however, and such energy loss is not readily recovered. As a consequence, electron cluster energies are systematically lower than the original momenta, affecting the efficiency of transverse energy cuts and electron identification;

- **Calibration**
  The ECAL is calibrated in an iterative procedure with as final stage the tuning of the $\pi^0 \rightarrow \gamma\gamma$ signal to its nominal mass. The calibration constants thus obtained are used in the lookup tables of the readout boards. However, these calibration

constants and pedestal values were regularly improved. Whereas off-line cluster reconstruction can benefit from a re-calibration of channels, the pretrigger necessarily operates with a calibration as-is. A suboptimal calibration dilutes the transverse energy threshold and reduces the background rejection power;

- **Beam conditions**
  The ECAL energy is collected during a gated time window of 60 ns after the bunch crossing. For out-of-time interactions, the analogue signals from the photo-multipliers, typically 50 ns long, may partially fall outside this integration window. As a consequence, the corresponding energy is underestimated. The result is that the transverse energy cut is not satisfied and no pretrigger message is issued. Off-time interactions can be recognised by the shifted value of the mean drift time of outer tracker drift channels. In the runs studied here, it proved to be negligible effect;

Intrinsic effects

- **Limited cluster size**
  Whereas off-line reconstructed clusters can take on various sizes or shapes, the shape of a pretrigger cluster is always a nonet or a cross. Moreover, channels neighbouring a central cell, but not of the same granularity as the central cell, cannot be incorporated in the pretrigger cluster. On the borders between the Inner and Middle or the Middle and Outer parts, the cluster energy will therefore be systematically underestimated, which reduces the efficiency of the transverse energy cut. Conversely, a nonet might include the energy of an overlapping cluster, leading to an overestimated cluster energy;

- **Fixed z position**
  The ECAL pretrigger assumes fixed cluster position in z of z_{ECAL} =1350 cm, which is approximately the average shower depth (figure 3.1.1). If the true z position is smaller than this, which is the case for the Inner ECAL, the Region of Interest transmitted to the FLT may be too small;

- **Binning**
  The cluster reconstruction and message composition of the pretrigger uses lookup table calculations [46]. The accuracy of (intermediate) results is limited to the number of bits that is allotted for the coded variables. For all calculations, energies are coded in 7 bits. The x and y coordinates are coded in 9 and 8 bits respectively.

  The bit granularity directly influences the resolution by a term of $\Delta_{\mathrm{bit}}/\sqrt{12}$, where Δ_{bit} is the bin size of one bit. The efficiency is also affected: an energy just above the threshold may be truncated to a value just below it, preventing a message being issued.

3.3 Operation in 2000

Part of the ECAL pretrigger was already available in 1998. The ECAL pretrigger was routinely used to provide a trigger for physics data taking, while the FLT network was being installed and commissioned. Generally, two ECAL pretrigger messages were required that satisfied a transverse energy cut of typically 1.0 GeV. This is higher than the nominal cut of 0.7 GeV, because there was no FLT to further reduce the rate.

At the end of the running period in 2000, the ECAL pretrigger electronics covered the complete inner and middle region and half of the outer region (see Fig.1.4.5). In these regions, however, the ECAL suffered from malfunctioning individual channels, predominantly due to radiation damage. A few readout or pretrigger boards had electronic problems and were excluded in data taking. In addition, the readout electronics suffered from pickup noise, which led to significant fluctuations of the baseline energy from channel to channel. Such irregularities are clearly visible in figure 3.3.1, that shows the average energy deposit in the calorimeter per cell and per event. In total about 500 channels, 10% of the coverage of the calorimeter, were not available due to electronic problems. The Bremsstrahlung recovery option was not yet available for the pretrigger.

3.4 Hardware performance

During the gradual installation in 2000, the performance of the ECAL pretrigger hardware was regularly studied. New energy calibration constants were determined on a weekly basis. Hot or noisy channels were masked out. However, not all malfunctioning channels had been identified when the runs studied here were taken. The ECAL pretrigger was not a very stable system. Some channels could become defective after the system was last studied. Moreover, the tools to study the performance were limited at the time, and some erratic behaviour may well have passed unnoticed.

It is instructive to separate hardware defects from the algorithmic properties, studied in the course of this chapter. Hardware defects are not an inherent property of the ECAL pretrigger. They can be solved by replacing the failing hardware, which is not possible for the intrinsic inefficiencies of the pretrigger algorithm.

Hardware defects can be traced by comparing the recorded pretrigger messages to the messages from the hardware simulation on the same data. Theoretically, the messages found in the simulation should be exactly the same as those actually recorded. Any systematic difference directly indicates malfunctioning hardware.

For the analysis of the hardware performance we study two runs that were taken under identical conditions. The FLT network was operated in *transparent* mode. This means that the incoming ECAL pretrigger messages propagated through the network unaffectedly. The messages were collected by the TDU, which notified the SLT upon the reception of one or more messages. Meanwhile, the SLT performed a calorimeter clusterisation similar to that used off-line [47]. The only trigger requirement was the occurrence of either a pretrigger message at the TDU, or a cluster reconstructed by the SLT. If the event was accepted by the SLT, the TDU record containing the ECAL

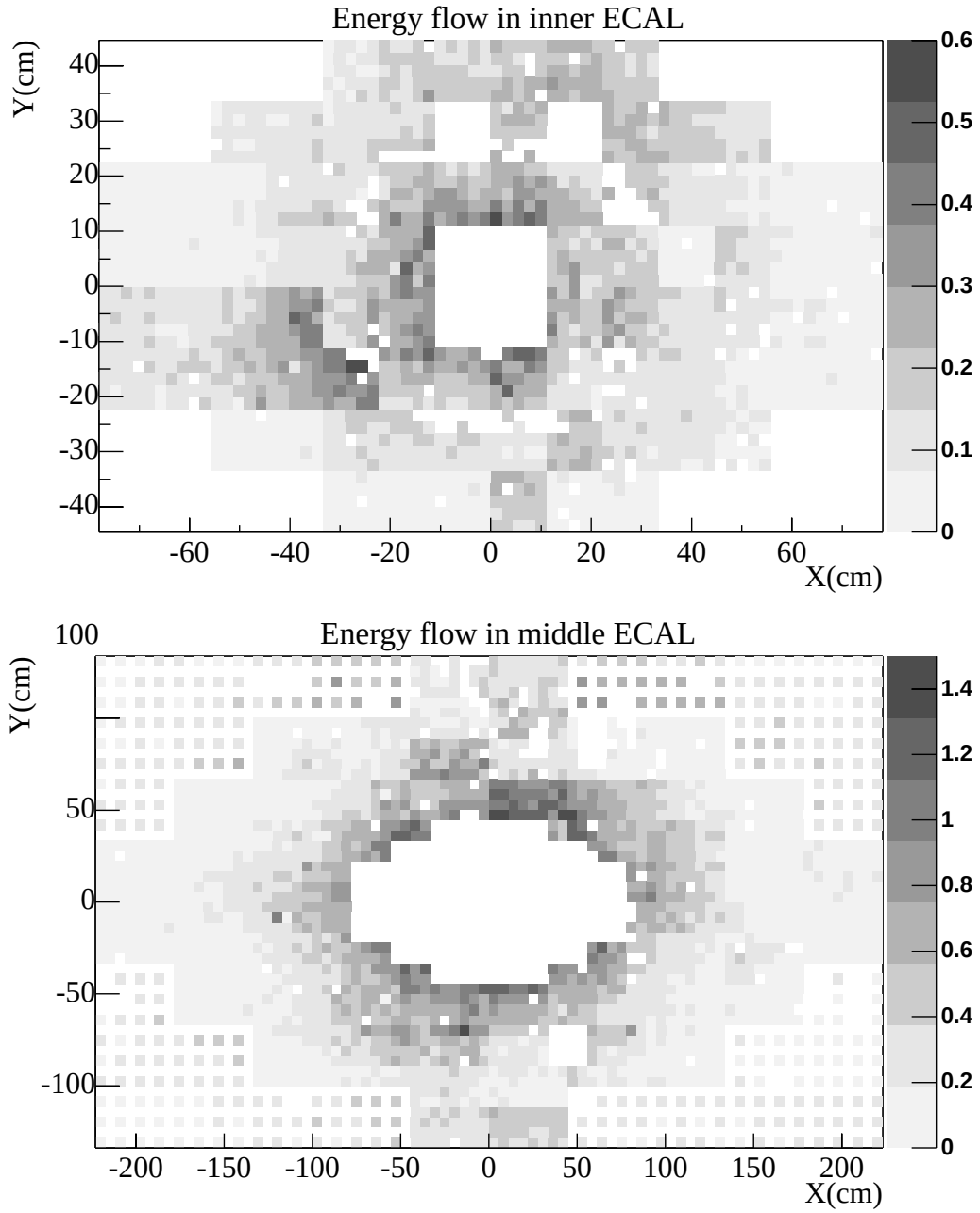

Figure 3.3.1: *Average energy deposition (in GeV) per event and per cell in Inner and Middle ECAL. Dead channels or failing readout/pretrigger boards are clearly visible. Irregular energy flow in the inner part is due to low energetic noise.*

pretrigger message(s) was stored in the data stream. Since a pretrigger message was not required, the hardware efficiency could be determined. To achieve a higher output event rate, only the ECAL was read out. The ECAL pretrigger LUT version (V-00-11) used in these runs included the cluster shape corrections of Eq. 2.3.6. Table 3.4.1 summarises the conditions of the two runs.

Run	17195	17197
Date	21-8-2001, 14:52-15:46	21-8-2001, 15:48-16:29
Events (triggered)	254224 (96%)	287473 (97%)
Target rate	5 MHz (± 0.2 MHz)	5 MHz (± 0.2 MHz)
Working channels	4745 of 5956	4745 of 5956
Noisy channels	600	600
Hot channels	24	24
ECAL LUT version	V-00-11	V-00-11

Table 3.4.1: *Data taking conditions for runs used for the measurement of the performance of the ECAL pretrigger hardware.*

Figure 3.4.1 shows the residual distributions of the raw message variables ξ, η and P between the recorded messages and the simulated messages. Here, only events are used that have exactly one simulated message and exactly one recorded message. The residuals are shown in multiples of the least significant bit.

The agreement between the simulated messages and the recorded messages is satisfactory. In 97% of the cases, the two are bitwise identical. Of the majority of the remaining 3%, the message variables are approximately the same, with residuals centred around zero. Nonetheless, there are also larger discrepancies visible.

In the spatial coordinates ξ and η, bit errors can be identified as residuals of an integer power of two. An example of such a bit error is shown in the residual distribution of η, where a peak is visible at $\eta_{\text{sim}} - \eta_{\text{rec}} = 64$. This particular peak is entirely due to one pretrigger board, that has set the sixth bit of η to zero in every message.

A considerable number of recorded messages have an energy (P) value that is much higher than that found in the simulation. Although the residual distribution shows no obvious peaks at certain powers of two, the scatter plot reveals clear correlations between such message pairs. Small (1 bit) differences in P can be accounted for by truncation differences between the simulation and the hardware. They cannot account for these large differences. Possible explanations are transmission errors between ECAL readout electronics and the pretrigger boards, and bit errors within the pretrigger board [11, 10].

Bit errors in the transmission to or within the FLT network were also be found. The spatial coordinates, x, y and the energy E of the cluster are used in five message variables (ξ, $d\xi$, $dd\xi$, η and P). The redundancy can be used to check the internal consistency of the message. The variable $d\xi$ is only a function of the total energy. Consequently, there is a one-to-one relation between $d\xi$ and P. In figure 3.4.2 we show that almost all messages are thus internally consistent.

In total 20 of the 186.113 recorded messages are internally not consistent. Based on the results of dedicated transmission tests [10], one expects at most one message to be corrupted by the FLT network. It is more plausible that the messages have been corrupted in the transmission to the first TFU. The inconsistent messages are not accompanied by any simulated message. Furthermore, the ξ and η values in these

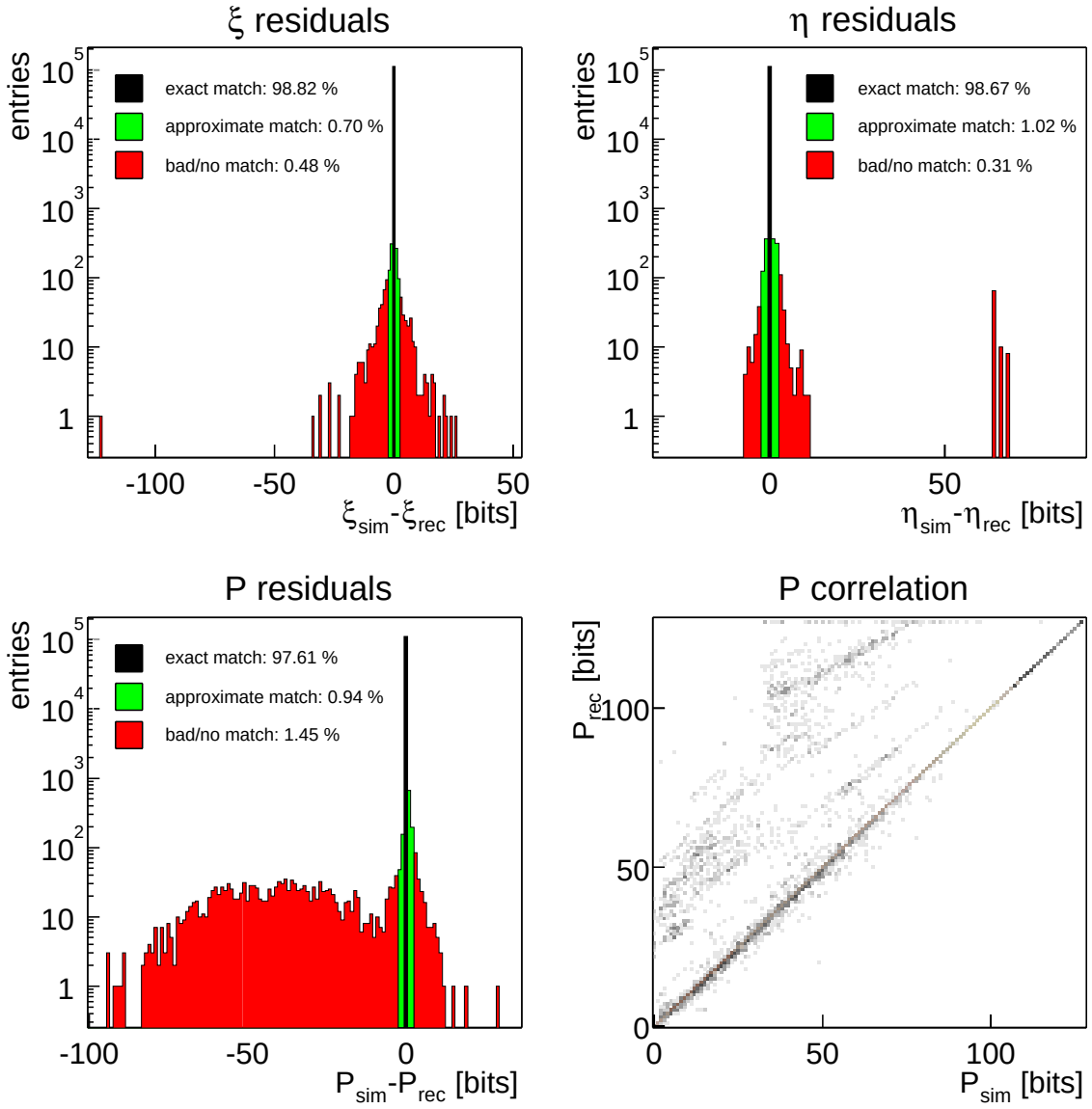

Figure 3.4.1: *Correspondence between simulated and recorded messages. Shown are residuals of the raw message variables ξ, η and P (see table 2.3.1), and a correlation plot for P.*

messages are improbable, and most likely are also corrupted. It is therefore not possible to localise these bit errors to any of the pretrigger boards.

Even if there are more such transmission errors than expected, they can not account for the bulk of the discrepancies in P. The energy values were already corrupted before the message was constructed. This hypothesis is further supported by the observation, that, when the P values are different, the ξ and η value are more often only approximately matched, i.e. showing a difference of one or two bits between the record and the simulation. Apparently, when determining the spatial coordinates from the centre-of-gravity of the pretrigger cluster (that depends on the energies of all five cells), the energies were already different from those seen in the simulation. The bad matches in

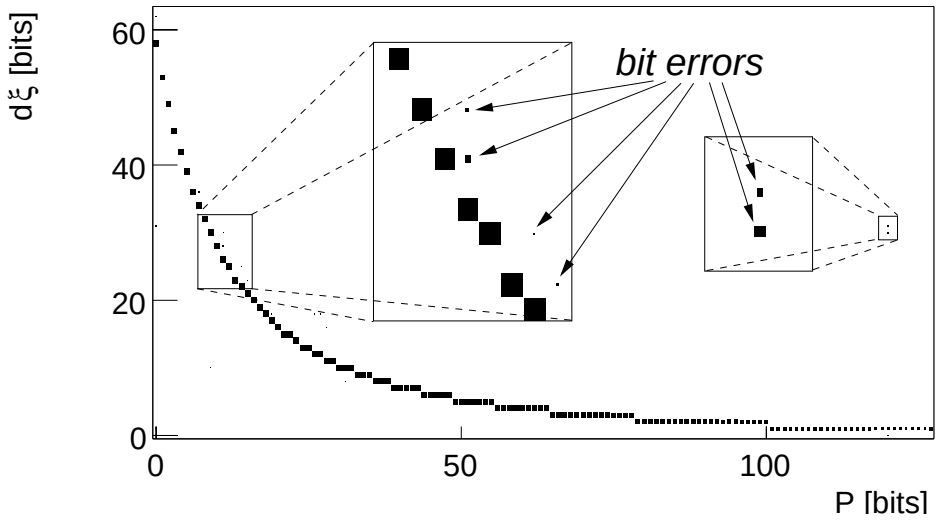

Figure 3.4.2: *Correlation between $d\xi$ and P of recorded pretrigger messages. The variable $d\xi$ is inversely proportional to P. A deviation from this behaviour indicates bit errors in the transmission of the message to or within the FLT network.*

P are not confined to any particular pretrigger boards, although there are some boards clearly worse than average.

To estimate the hardware efficiency, three classes of matches are defined: exact matches, approximate matches and bad matches. A simulated and a recorded message are considered approximately matched, if both ξ and η are identical within a window of two, regardless of any difference in P. A pretrigger message that is thus approximately correct, can probably still be successfully propagated through the FLT network. They do not reduce the probability to find the corresponding track[1]. This is not the case for the bad matches. Here, the variables in the recorded pretrigger message are off by more than two bits, and the corresponding RoI is probably too inaccurate for the subsequent track finding to be successful.

Table 3.4.2 shows the matching efficiencies according to these definitions for the different parts of the ECAL separately. In total more than 97% of the simulated

	exact match	approximate match	bad match	no match
Inner ECAL	95.80(7)	2.09(5)	0.61(3)	1.49(4)
Middle ECAL	95.21(8)	2.23(6)	0.99(4)	1.57(5)
Outer ECAL	91.41(18)	1.53(8)	2.35(10)	4.71(14)
Total	95.03(5)	2.07(3)	0.97(2)	1.93(3)

Table 3.4.2: *ECAL pretrigger hardware efficiencies (in %) for the Inner, Middle and Outer regions of the ECAL. The number give the probability that a simulated message is also found by the hardware. For definitions of exact, approximate and bad match, see text.*

[1] assuming that no E/p cut is performed by the TPU

messages are (approximately) found by the hardware. Similar numbers are obtained if recorded (instead of simulated) messages are taken as reference.

The Outer region of the ECAL performs significantly worse than the Inner and Middle parts. The pretrigger electronics in the Outer region were installed not long before the runs under study were taken. It is possible that many hot or noisy channels were not yet identified in this part.

In conclusion, we believe that the pretrigger simulation emulates the hardware exactly. The small amount of dissimilarities are caused by transmission errors between the readout electronics and the pretrigger. The simulation enables an identification of such hardware defects. If these defects are repaired, the agreement between simulation and hardware will probably be perfect.

3.5 Outline of the Analysis

In the course of this chapter we will use the pretrigger simulation to determine the resolution and efficiency of the ECAL pretrigger using Monte Carlo events. We restrict ourselves to the electron and positron from $J/\psi \rightarrow e^+e^-$ decays. For brevity, both the electron and the positron will hereafter be referred to as 'electron'. Two samples of Monte Carlo generated events are used, which contain, besides the $J/\psi \rightarrow e^+e^-$ decays, a typical underlying inelastic interaction. One sample is simulated with the full detector setup, and the other sample is simulated without tracking chambers in the magnet area.

The resolutions are measured from residuals between reconstructed cluster coordinates or energies and the Monte Carlo truth. The Monte Carlo reference position is the impact point of the electron track in the tracking chamber closest to the ECAL, extrapolated to the ECAL pretrigger reference plane at z=1350 cm. The reference energy is the electron energy remaining after the magnetic field has been traversed, and taken from the first hit in the tracking system after z =680 cm.

The resolutions of the ECAL pretrigger are compared to those of the off-line reconstruction described in section 3.1.1. The effect of specific limitations of the ECAL pretrigger, as outlined in section 3.2 can thus be quantitatively estimated.

Since there are considerable differences between the Inner, Middle and Outer parts (cell sizes, energy coding) and since they are treated as separate detectors by the pretrigger, the performance is measured for each of these parts separately.

3.6 Spatial Resolution

The spatial resolution, the precision with which the x and y position of the electron is reconstructed, must be sufficient to ensure that the RoI, sent to the FLT, is centred around the correct value. If the coordinates of the pretrigger cluster are off by more than the margin allowed by the FLT, the subsequent track reconstruction could fail.

The reconstruction of the coordinates for the pretrigger nonet is identical to that of the pretrigger cross: the energy deposits in the corners (E_{ul}, E_{ur}, E_{dl} and E_{dr}) is not used. By definition, therefore, the spatial resolutions are the same for both setups.

3.6.1 Measured resolutions

Figure 3.6.1 shows the distribution of the residuals of the Monte Carlo reference position and the pretrigger cluster coordinates for the Inner ECAL. For comparison, the results of the off-line cluster reconstruction are also shown. The distributions are fit by the sum of two Gaussians: one to describe the core distribution and one for the broader underlying spectrum. The shapes of the residual distributions are similar for the Middle and Outer parts of the ECAL. The resolutions for all three parts and for both off-line clusters and pretrigger clusters are summarised in table 3.6.1.

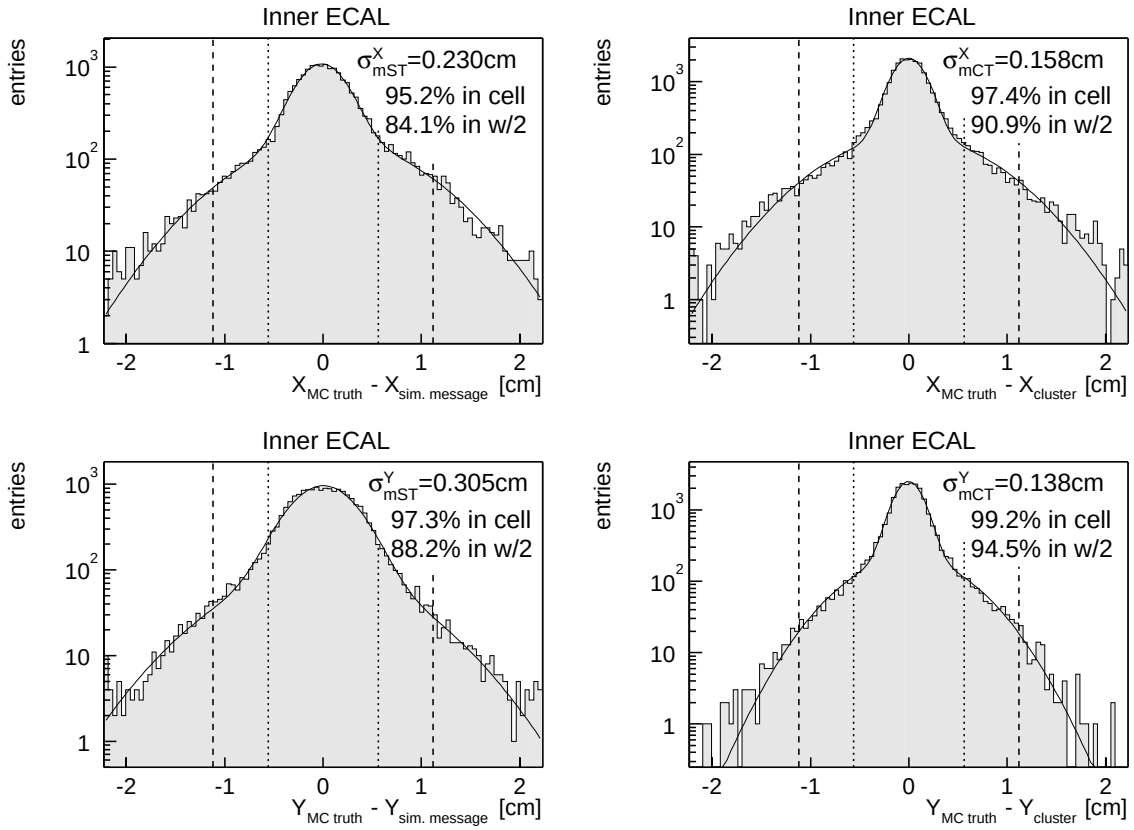

Figure 3.6.1: *Spatial resolution of pretrigger messages ($\sigma^{X,Y}_{mST}$) and off-line clusters ($\sigma^{X,Y}_{mCT}$)in Inner ECAL. Shown are residual distributions of x (top) and y (bottom) between Monte Carlo truth and simulated messages (left) or off-line reconstructed clusters (right). The quoted width refers to the Gaussian describing the core of the distribution. A dashed (dotted) line indicates the borders of (half) a cell.*

Since the coordinates are determined from the centre-of-gravity of the energy deposition, the spatial resolution improves with increasing cluster energies. Specifically, the resolution exhibits the energy dependence

$$\sigma_{x,y} = D_1 \oplus D_2/\sqrt{E}. \tag{3.6.1}$$

The constants D_1 and D_2 are different for the three ECAL regions. The resolutions of table 3.6.1 are the resolutions for energetic clusters, where the last term can be

	σ^x_{ST} (cm)	σ^y_{ST} (cm)	σ^x_{CT} (cm)	σ^y_{CT} (cm)
Inner ECAL	0.23(1) [0.46]	0.31(1) [0.39]	0.16(1) [0.38]	0.14(1) [0.27]
Middle ECAL	0.45(1) [1.07]	0.47(1) [0.92]	0.44(1) [0.94]	0.35(1) [0.68]
Outer ECAL	0.74(5) [2.58]	0.64(4) [2.25]	0.83(5) [2.28]	0.53(4) [1.79]

Table 3.6.1: *Spatial resolution of the ECAL pretrigger and off-line reconstructed clusters. The pretrigger and off-line resolutions are indicated by σ_{ST} and σ_{CT} respectively. The values are the widths of the Gaussians that describe the core of the residuals (see Fig. 3.6.1). The RMS values are given in square brackets.*

neglected. The tail in the residual distributions of figure 3.6.1 is predominantly caused by clusters of low energy. As will be discussed in more detail later, Bremsstrahlung emitted inside the magnet can distort the cluster shape, which also causes tails in the x residuals. This explains why the tails in the x residuals are larger.

The spatial resolution improves for a better energy resolution. The values of table 3.6.2 are made with an energy resolution that is similar to what is reached in reality. With an optimal energy calibration and only small pedestal fluctuations, spatial resolutions are up to 20% better than this.

For off-line reconstructed clusters, the resolution in y is systematically better than the resolution in x. This is because the spread of the angles at which the particles impede on the ECAL is larger in the horizontal plane: the clusters shape is generally more symmetric in the vertical direction.

3.6.2 Binning effects

The difference between the spatial resolution of the off-line reconstruction and the pretrigger is predominantly due to binning effects in the coding of η and ξ. The coding granularity is adjusted to the granularity of the detector. The resolution of the tracking chambers in vertical direction is worse than in horizontal direction. Where 9 bits are sufficient to resolve y in η, 10 bits are used to code x into ξ.

The coded values ξ and η are sent to one of the TFUs in TC2. Since the lookup tables of this TFU, that use these values to address a part of the Wire Memory cannot distinguish ECAL pretrigger messages from muon FLT messages, the messages must be coded identically. Whereas the coding of ξ follows the granularity of the calorimeter, the coding of η is adjusted to the vertical track resolution of the muon candidates.

The coding functions for η and ξ are shown in figure 3.6.2 together with the resulting resolutions in x and y. Except for a part of the inner region, the coding granularity of x is equal to 1/8 of the ECAL cell size.

Table 3.6.2 shows a comparison of the resolution in x and y between off-line cluster reconstruction and the pretrigger cluster reconstruction. It can be seen that binning effects in the coding can completely account for the difference between the two. The cluster size limitation of the pretrigger does not affect the spatial resolution, except on the border of different parts of the ECAL. The consequences of assuming a constant z coordinate for the clusters will be discussed in section 3.9.3.

Region	#bins	bin size	resolution
|x|<22.3 cm	40	0.56 cm/bit	0.16 cm
22.3<|x|<78.05 cm	200	0.28 cm/bit	0.08 cm
78.05<|x|<223 cm	208	0.70 cm/bit	0.20 cm
223<|x|<312.2 cm	64	1.39 cm/bit	0.40 cm

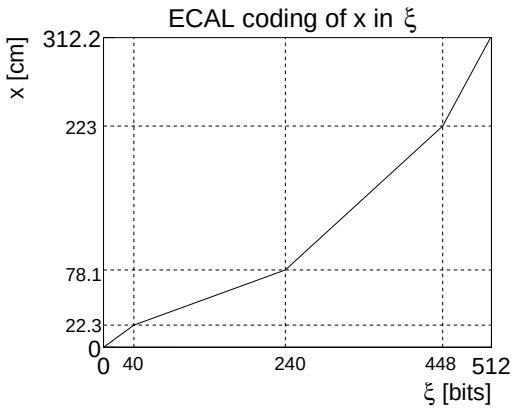

Region	#bins	bin size	resolution
|y|<28.8 cm	32	0.9 cm/bit	0.26 cm
28.8<|y|<297.6 cm	224	1.2 cm/bit	0.35 cm

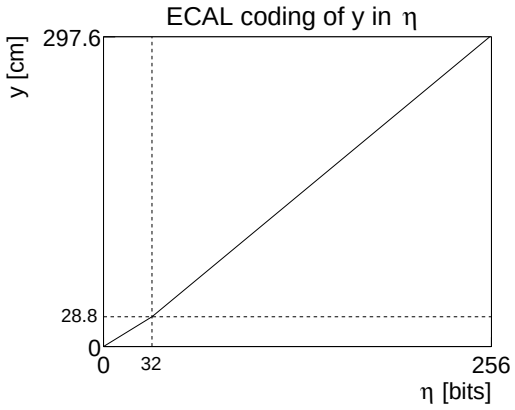

Figure 3.6.2: *Coding of x (top) and y (bottom) in ECAL pretrigger message. Only shown are positive values; the sign is given by the most significant bit in ξ or η. The resolution for the different ranges are shown in the table.*

3.7 Energy resolution

An accurate energy determination by the ECAL pretrigger serves several purposes. Firstly, the energy is used as a momentum estimate in the determination of the RoI. Secondly, it permits a meaningful E/p cut by the FLT, after the track reconstruction. And thirdly, and most importantly, it prevents the transverse energy cut of the pretrigger to become too diluted, and hence less powerful.

The energy resolution of the ECAL is energy dependent and consists of three terms:

$$\sigma_E = C_{\text{calibration}} E \oplus C_{\text{stochastic}} \sqrt{E} \oplus C_{\text{pedestal}}. \tag{3.7.1}$$

The constant $C_{\text{calibration}}$ reflects an uncertainty in the calibration constants, shower non-uniformities and energy leakage. The stochastic term arises from the statistical uncertainty in the number of photons ($\sigma \propto \sqrt{N_\gamma} \propto \sqrt{E}$) produced for a given energy. The last term is due to fluctuations of the pedestal value: for pretrigger clusters, that are typically very energetic, it can be neglected. The design [9] values of the ECAL

	σ_x [cm]			σ_y [cm]		
	Inner	Middle	Outer	Inner	Middle	Outer
off-line resolution	0.16(1)	0.44(1)	0.83(5)	0.14(1)	0.25(1)	0.53(4)
coding limitation	0.162	0.201	0.402	0.26	0.35	0.35
quadratic sum	0.23(1)	0.48(1)	0.92(6)	0.29(1)	0.44(1)	0.64(4)
pretrigger resolution	0.23(1)	0.45(1)	0.94(5)	0.31(1)	0.47(1)	0.64(4)

Table 3.6.2: *Contributions of coding granularity to the spatial resolution. The quadratic sum of the spatial resolution of the off-line reconstruction and the contributions of binning effects is in agreement with the measured resolution of the ECAL pretrigger.*

energy resolution are:

$$\begin{aligned} \text{Inner ECAL}: \quad & \sigma_E/E &=& \ 0.17/\sqrt{E} \oplus 0.016 \\ \text{Middle/Outer ECAL}: \quad & \sigma_E/E &=& \ 0.095/\sqrt{E} \oplus 0.010 \end{aligned} \tag{3.7.2}$$

This resolution is achieved only for a part of the ECAL. The energy resolution of the pretrigger is worse than this, due to limitations outlined in section 3.2. In this section we will study the two dominant limitations: binning effects in the energy coding and limited cluster sizes. Then the total energy resolution is determined, and the influence of these limitations is compared to the nominal resolution. Finally, the importance of electron energy loss is discussed.

3.7.1 Binning effects

The ECAL pretrigger receives the individual cell energies, each coded in 7 bits according to equations 3.1.4. This granularity dependent coding is also used for all the calculations inside the pretrigger board. In four (pipeline) steps the individual cell energies are summed to obtain the total cluster energy. Within each of the summations, precision is lost because of the encoding of the result. The resolutions resulting from the coding of Eq. 3.1.4 are:

$$\begin{aligned} \text{Inner ECAL}: \quad & \sigma_E^{\text{LUT}} &=& \ (2/127)\sqrt{280/12}\sqrt{E} \\ \text{Middle ECAL}: \quad & \sigma_E^{\text{LUT}} &=& \ (2/127)\sqrt{100/12}\sqrt{E} \\ \text{Outer ECAL}: \quad & \sigma_E^{\text{LUT}} &=& \ (2/127)\sqrt{65/12}\sqrt{E} \end{aligned} \tag{3.7.3}$$

Each time the energies are coded, such a resolution term is added in quadrature. Figure 3.7.1 shows how the total energy is determined by the pretrigger in steps of pairwise summations of the cell energies. Since the nonet (Fig. 3.1.3) uses more lookup table summations to determine the total energy, the binning effects are larger than for a pretrigger cross. Specifically, the total binning resolution from the lookup table

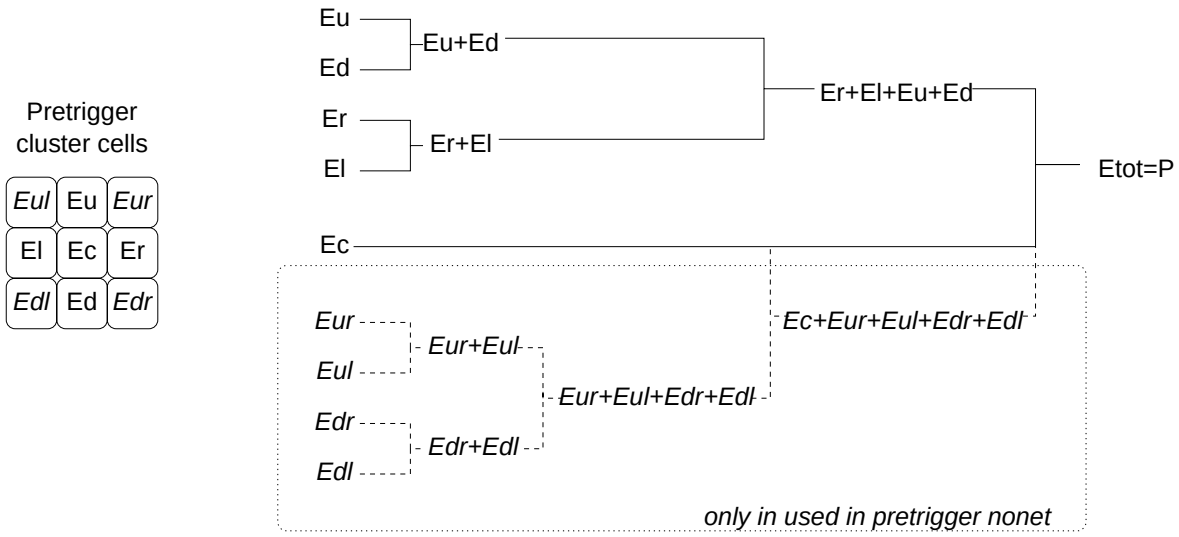

Figure 3.7.1: *Calculation of the total pretrigger cluster energy by sub-summations. The cell energies E_i are summed in groups of two by a lookup table. For the cross (nonet) summation 4(8) lookup tables are used in 3(4) pipeline steps.*

calculations of figure 3.7.1 are:

$$\text{Cross}: \sigma_E^{\text{LUT}} = C\sqrt{3(E_u + E_d + E_r + E_l) + E_c}, \tag{3.7.4}$$

$$\text{Nonet}: \sigma_E^{\text{LUT}} = C\sqrt{3(E_u + E_d + E_r + E_l) + 4(E_{ul} + E_{ur} + E_{dl} + E_{dr}) + 2E_c}. \tag{3.7.5}$$

The constant C is the factor before the $\sqrt{E}$ term on the right hand side of Eq. 3.7.4, 0.07607, 0.04546, 0.03665 for the Inner, Middle and Outer ECAL, respectively.

The total cluster energy is finally coded in the variable P of the pretrigger message using a coding function that is independent of the detector granularity:

$$P = \min(10(\sqrt{E} - \sqrt{5}), 127). \tag{3.7.6}$$

This gives rise to an additional resolution term of

$$\sigma_E^{\text{FLT}} = \frac{1}{5\sqrt{12}}\sqrt{E} \tag{3.7.7}$$

For all energies above 223.1 GeV, P is set to 127. The contribution of binning effects to the energy resolution are shown in figure 3.7.2 for the three different parts of the ECAL, and summarised in table 3.7.1.

These resolutions are in agreement with results obtained by directly comparing the coded energies to the unbinned values [11].

The minimum energy in the FLT energy coding

In the present coding of P (Eq. 3.7.6), there is a minimum total cluster energy assumed of 5 GeV. This assumption is incorrect. The pretrigger clusters are built around central

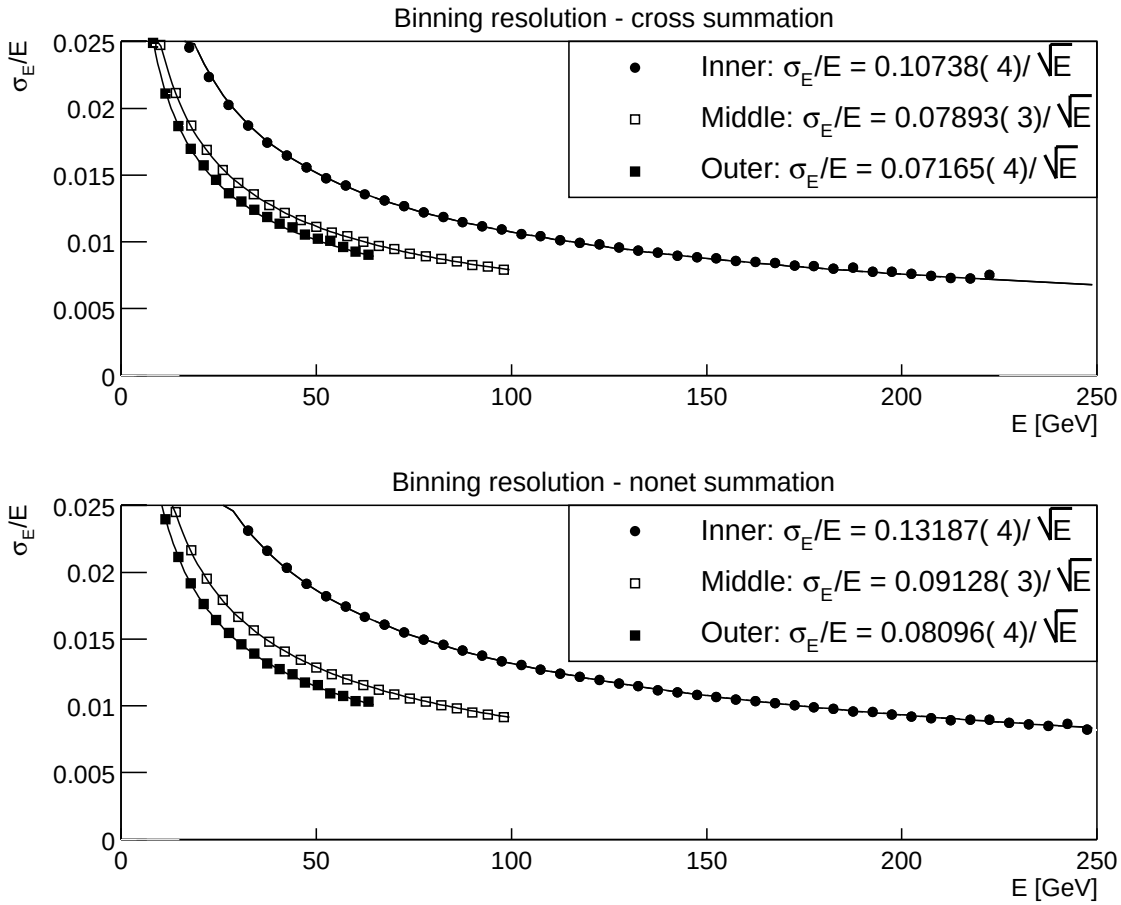

Figure 3.7.2: *Contribution of binning effects to the pretrigger energy resolution. Shown is the quadratic sum of the binning effects from the lookup table summations* σ_E^{LUT} *and the FLT energy coding* σ_E^{FLT} *(Eq. 3.7.7). Above the binning resolution from the summation of a pretrigger cross (Eq. 3.7.4) is shown, and below the resolution from the summation of the full nonet (Eq. 3.7.5).*

cells that have already passed a transverse energy cut of $E_T > E_{TH}/2$, executed by the readout board (Eq.2.3.2). The minimum total energy corresponds to the energy of a pretrigger cluster in the outermost corner ($|x| = 312, |y| = 232$), that just passes this cut. For an E_T cut of 1 GeV, this minimum energy is (Eq. 2.3.3) $E_{TH}/2 = 1.81 \times E_T = 1.81$ GeV, lower than the assumed value of 5 GeV. Any energies below 5 GeV are set to 5 GeV. Since the transverse energy cut for the total cluster is executed *after* the coding of P [11], pretrigger clusters in the outermost region can be lifted above the E_T threshold artificially. This should be prevented by choosing the right minimum energy of $1.81 \times E_{T,min}$ in the coding of the FLT message.

3.7.2 Fixed cluster shapes

The consequences of the fixed cluster size of the ECAL pretrigger are twofold:

	Pretrigger cross			Pretrigger nonet		
	Inner	Middle	Outer	Inner	Middle	Outer
LUT	0.0917(1)	0.0547(1)	0.0431(1)	0.1186(1)	0.0707(1)	0.05642(1)
FLT	0.057735	0.057735	0.057735	0.057735	0.057735	0.057735
LUT⊕FLT	0.1074(1)	0.0789(1)	0.07166(1)	0.1319(1)	0.0913(1)	0.0810(1)

Table 3.7.1: *Contribution of binning effects to the pretrigger energy resolution. The quoted values are $\sigma_E/\sqrt{E}$ as extracted from a fit as shown in figure 3.7.2. The contributions from the coding inside the pretrigger lookup tables and from the coding in the FLT message variable are separately given.*

- **Inability to disentangle overlapping clusters**
  If another particle also deposits energy in one of the cells of the pretrigger cluster of the electron, the pretrigger adds this energy to the pretrigger candidate. The resulting energy increase has three consequences: firstly, the number of pretrigger messages will rise exponentially with the interaction rate; secondly, the overestimated energy leads to a smaller RoI size, and therefore reduces the extrapolation efficiency. Thirdly, it jeopardises electron-pion separation through an E/p cut.

- **Energy loss in neighbouring channels**
  The lateral extent of the showers initiated by the pretrigger candidate can cause part of the energy to be deposited in neighbouring channels that are not included in the cluster. This leads to a systematic underestimate of the energy, especially on the borders of the different parts of the ECAL or if the cross setup is used.

  Figure 3.7.3 shows the average fraction of the total cluster energy in each of the nonet cells, determined from a Monte Carlo simulation. The corner channels, that are excluded in the cross, have 5-6% of the total energy. There could be a benefit from this effect too: since the lateral extent of hadronic showers is larger than that of electromagnetic showers, pions lose relatively more energy in excluded channels than electrons; In combination with an E_T cut, the exclusion of these channels therefore enhances electron-pion separation.

The average reduction of the energy due to losses in corner channels could be compensated by a correction factor, effectively lowering the E_T cut of the pretrigger. More important is the *spread* in this energy loss, since it reduces the energy resolution of the pretrigger.

The net result of these two effects on the pretrigger energy resolution is estimated by comparing the energy in the pretrigger cells to the energy in the corresponding off-line cluster. The off-line cluster reconstruction can split overlapping clusters and can reconstruct the full cluster also on the border of different ECAL parts. The results are shown in figure 3.7.4.

The spread in energy loss in the excluded (corner) cells of the pretrigger cross add about 2.5% to the energy resolution and less than 1% for the nonet summation. For

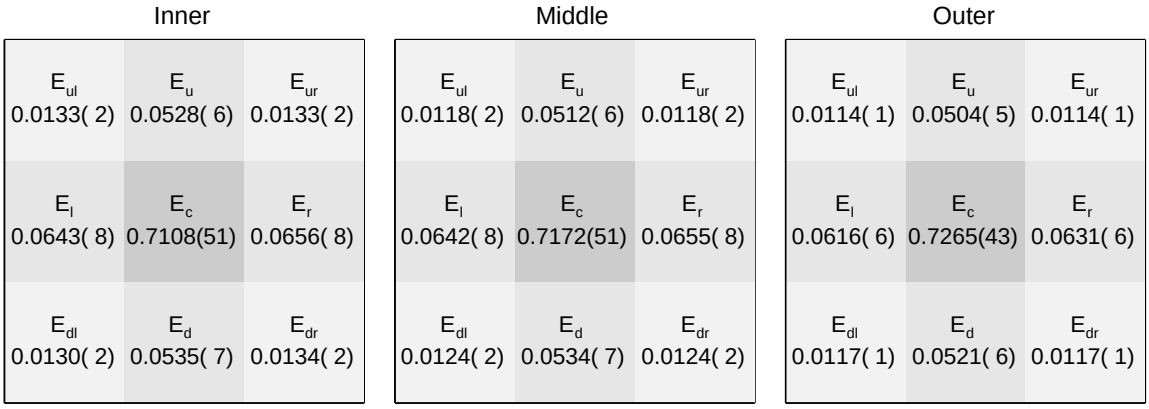

Figure 3.7.3: *Energy deposition in individual pretrigger cells by electrons from a J/ψ. Shown is the fraction of the total energy deposited in the different nonet cells. The corner channels, excluded in the cross summation, typically contain 5% of the total energy.*

the nonet summation it is caused by clusters on the borders of the different ECAL parts or overlapping clusters.

The energy resolution difference between the nonet and cross summation due to binning effects are never more than $0.03/\sqrt{E}$ (table 3.7.1). For average pretrigger cluster energies of 78 GeV, 33 GeV and 15 GeV in the Inner, Middle and Outer part of the ECAL, this difference is much smaller than the difference due to the spread in the missing energy. Therefore the nonet has a better energy resolution than the cross.

The nonet summation, however, suffers more from the overlapping clusters. The average energy excess grows in proportion to the track multiplicity, or, equivalently, with the number of clusters in the event. This is shown in figure 3.7.5. The off-line cluster nominally consists of the nine cells of the pretrigger nonet, except when clusters overlap. In this case, the energy deposit in one or more cells is (partly) incorporated into another cluster. The energy overestimate of the pretrigger is therefore largest when the number of cells in the corresponding off-line cluster is small. The probability that the energy in the pretrigger nonet is more than twice the off-line reconstructed energy is 0.31(5)% per interaction (for carbon). The subsequent track finding by the FLT may then be unsuccessful, as will be explained in section 3.9.3.

3.7.3 Total energy resolution

The pretrigger limitations reduce the energy resolution by two terms, the size of which depends on the region in the ECAL and on the type of energy summation. We obtained

$$\begin{aligned} \text{Inner}: \quad \sigma_E^{\text{pretr.}}/E &= \sigma_E^{\text{offline}}/E \oplus 0.132/\sqrt{E}; \\ \text{Middle}: \quad \sigma_E^{\text{pretr.}}/E &= \sigma_E^{\text{offline}}/E \oplus 0.091/\sqrt{E}; \\ \text{Outer}: \quad \sigma_E^{\text{pretr.}}/E &= \sigma_E^{\text{offline}}/E \oplus 0.081/\sqrt{E}, \end{aligned} \tag{3.7.8}$$

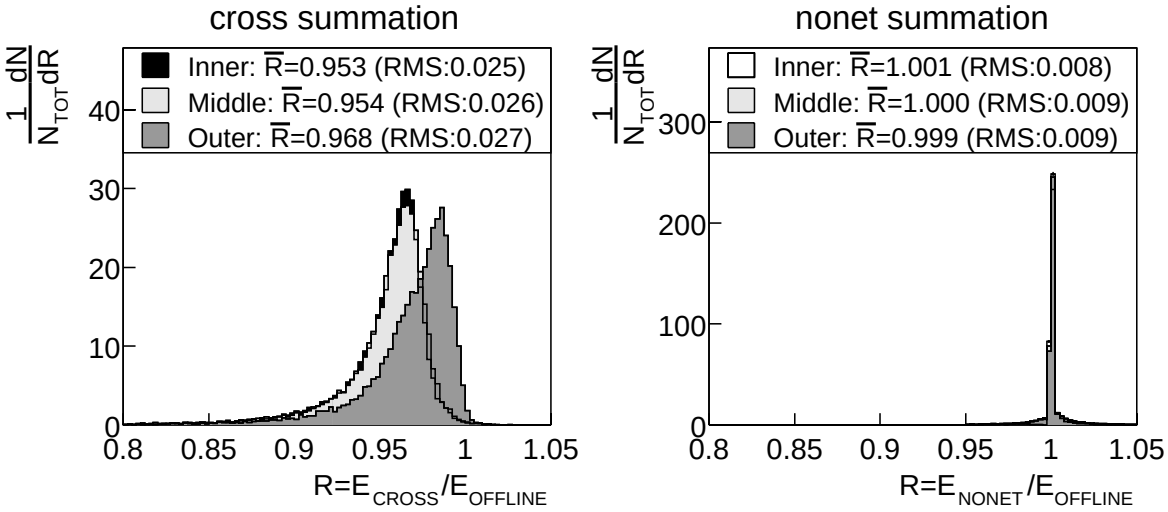

Figure 3.7.4: *Ratio of the pretrigger cluster energy to the energy of the off-line reconstructed cluster for the three different ECAL parts. The left figure shows the results for a cross summation, and the right figure gives the the values for the nonet.*

for the nonet summation, and

$$\begin{aligned} \text{Inner}: \quad \sigma_E^{\text{pretr.}}/E &= \sigma_E^{\text{offline}}/E \oplus 0.107/\sqrt{E} \oplus 0.025; \\ \text{Middle}: \quad \sigma_E^{\text{pretr.}}/E &= \sigma_E^{\text{offline}}/E \oplus 0.079/\sqrt{E} \oplus 0.026; \\ \text{Outer}: \quad \sigma_E^{\text{pretr.}}/E &= \sigma_E^{\text{offline}}/E \oplus 0.072/\sqrt{E} \oplus 0.027, \end{aligned} \tag{3.7.9}$$

for the pretrigger cross. The terms that are proportional to $1/\sqrt{E}$ are due to binning effects and the last term is caused by cluster size limitations. For the design resolutions of Eq. 3.7.3, the pretrigger limitations have a significant impact. Binning effects reduce this energy resolution (Eq. 3.7.3) by up to 30% when a cross summation is used, and by up to 40% for the nonet. The constant term, due to pedestal fluctuations is more than doubled because of the size limitation of the cross summation.

Figure 3.7.6 shows the energy dependence of the total energy resolution both for the off-line and for the pretrigger nonet cluster reconstruction. To avoid energy loss effects, which are discussed in the following section, the Monte Carlo reference energy was the electron energy directly after the magnet. The electron was furthermore required to have lost not more than 5% of its original energy.

The measurement confirms that the resolution difference between off-line reconstruction and the pretrigger nonet reconstruction is dominated by binning effects. If one adds the last term on the left hand side of Eq. 3.7.8 in quadrature to the off-line resolutions, the result is approximately equal to the pretrigger resolutions.

For figure 3.7.6 we have assumed an optimal calibration in the Monte Carlo simulation. The resulting resolutions are comparable to the design specifications (Eq. 3.7.3). Such a resolution has however not yet been reached for the complete ECAL, due to

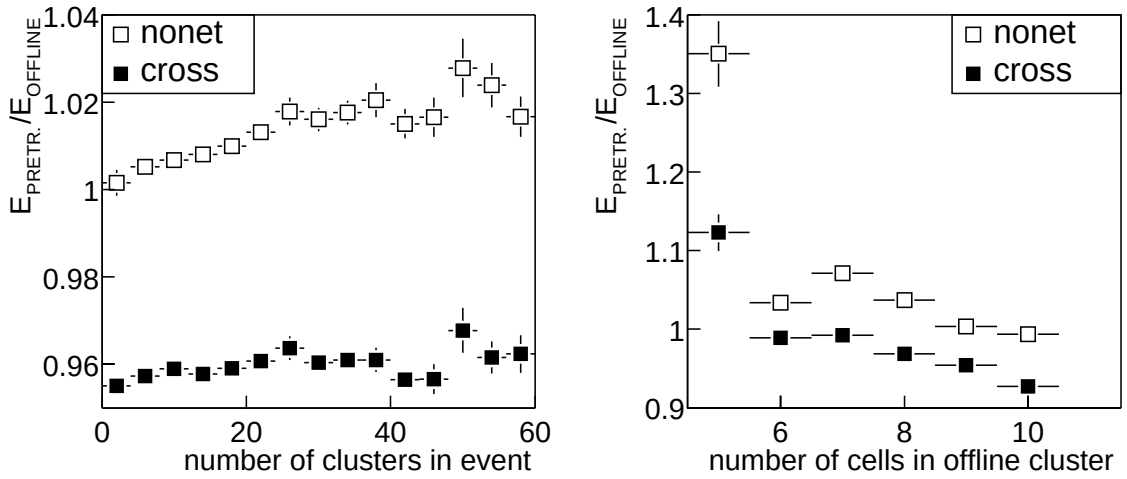

Figure 3.7.5: *Energy overestimation due to overlapping clusters. The left plot shows that the energy overestimation grows proportional to the total number of clusters in the event. The right plot shows that this is due to overlapping clusters.*

noise and calibration errors. The achieved energy resolution for the inner part, as measured from the width of the π^0 invariant mass, is [10]

$$\sigma_E^{\text{offline}}/E = 0.225(5)/\sqrt{E} \oplus 0.017(3), \tag{3.7.10}$$

which is more than 30% worse than the design values. The corresponding pretrigger energy resolutions, as given by equations 3.7.9 and 3.7.8, are about 10% worse.

3.8 Electron energy loss

An important external effect on the reconstruction of electrons is energy loss due to Bremsstrahlung. Charged particles interact electromagnetically with the Coulomb field of nuclei in the material. Bremsstrahlung loss is inversely proportional to the square of the mass of the incident particle. Electrons are therefore much more affected by this than other particles. For energetic ($E > 100$ MeV) electrons the spectrum of Bremsstrahlung energy loss in a medium of thickness X is given by [48]:

$$P(E) = \frac{1}{E_0}\frac{[\ln(E_0/E)]^{X/(X_0 \ln 2)-1}}{\Gamma(X/(X_0 \ln 2))}, \tag{3.8.1}$$

$$\langle E/E_0 \rangle = e^{-X/X_0} \tag{3.8.2}$$

$$\tag{3.8.3}$$

where E_0 is the incoming electron energy, E the energy remaining after the medium is traversed and X_0 the radiation length of the material.

Figure 3.8.1 shows the average fraction of the original electron energy remaining after passing the various tracking stations. The material between the target and the

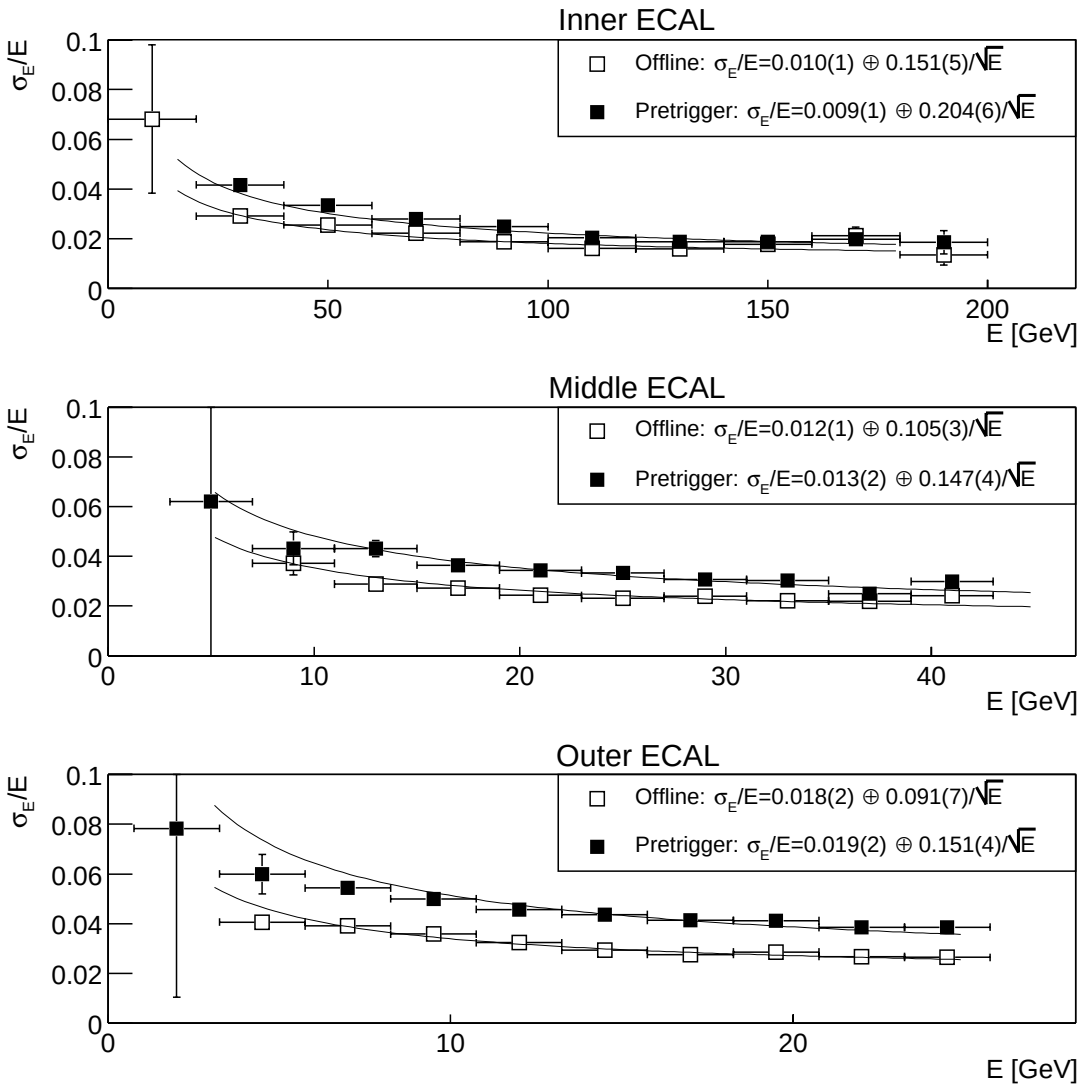

Figure 3.7.6: *Energy dependence of energy resolution for off-line and pretrigger cluster (nonet) reconstruction. The points are the widths of Gaussian fits to the residuals of the true (Monte Carlo) energies (at the end of the magnet) and the reconstructed energies. The energy dependence has been confronted with a fit of Eq. 3.7.1, without the term from pedestal fluctuations, the results of which are also given.*

ECAL amount to almost a full radiation length. The electron has typically lost more than half of its original energy upon reaching the ECAL.

When evaluating the significance of energy losses due to Bremsstrahlung, it is important to distinguish three regions of the detector: before the magnet, inside the magnet and behind the magnet. Bremsstrahlung is emitted in a narrow cone around the direction of the electron. Photons, radiated behind the magnet, end up in the cluster of the electron itself and form no major problem for the electron reconstruction. On average, only 70% of the original energy will be left after the electron has passed

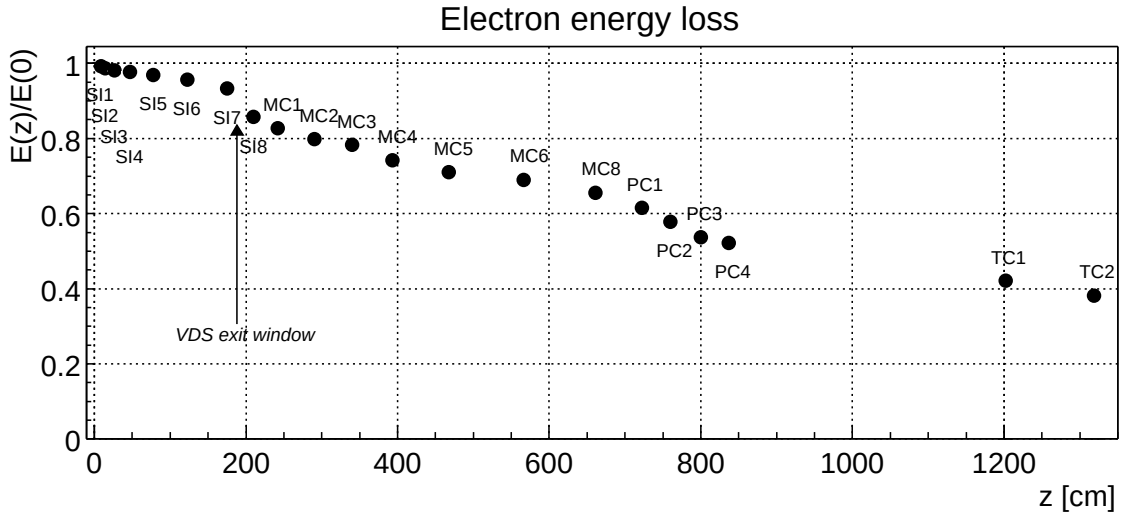

Figure 3.8.1: *Average electron energy loss in detector superlayers. Indicated is the average fraction of the original energy ($\langle E/E_0 \rangle$ of Eq. 3.8.1) at various superlayers in the vertex detector (SI) and the main tracker (MC, PC, TC). The superlayers MC2 to MC8 are inside the magnetic field. A considerable source of energy loss is the border of the vertex tank, between stations SI7 and SI8.*

the magnetic field.

More problematic are energy losses before and inside the magnet, since the electron is subsequently deflected in the horizontal plane. Consequently, the Bremsstrahlung will be deposited at a position in the ECAL different from that of the electron cluster.

Figure 3.8.2 shows the Bremsstrahlung energy loss spectrum for these two regions, determined in a Monte Carlo simulation. We have confronted the distributions to a fit of Eq. 3.8.1 to obtain the corresponding thickness X. Sources of energy loss in the region before the magnet are the vertex detector planes, the exit window of the vertex tank and the first tracking chamber (MC1/MS1). They correspond to a total thickness of $0.16X_0$. The tracking chambers inside the magnet correspond to a total thickness of $0.19X_0$, which translates into an average energy loss of approximately 20%.

Bremsstrahlung, radiated before the magnet ($z < 250$ cm), is deposited at a position where the linear extrapolation of the original electron track direction intercepts the ECAL. This position can be estimated from the position and energy of the electron at the ECAL:

$$\begin{aligned} x_{\mathrm{Brems}}^{z<250cm} &= x_{\mathrm{electron}} \pm (Z_{\mathrm{ECAL}} - Z_{\mathrm{MAGNET}}) \frac{1}{p_{\mathrm{electron}}} \int Bdl \\ &\approx x_{\mathrm{cluster}} \pm 585 \text{ GeV cm}/E_{\mathrm{cluster}}, \end{aligned} \tag{3.8.4}$$

where the sign is positive for electrons and negative for positrons. The value of 585 GeV cm is lower than the value of 604.8 GeV cm, that one would nominally obtain with the integrated magnetic field of 0.672 GeV/q, to correct for the mean energy loss inside the magnetic field.

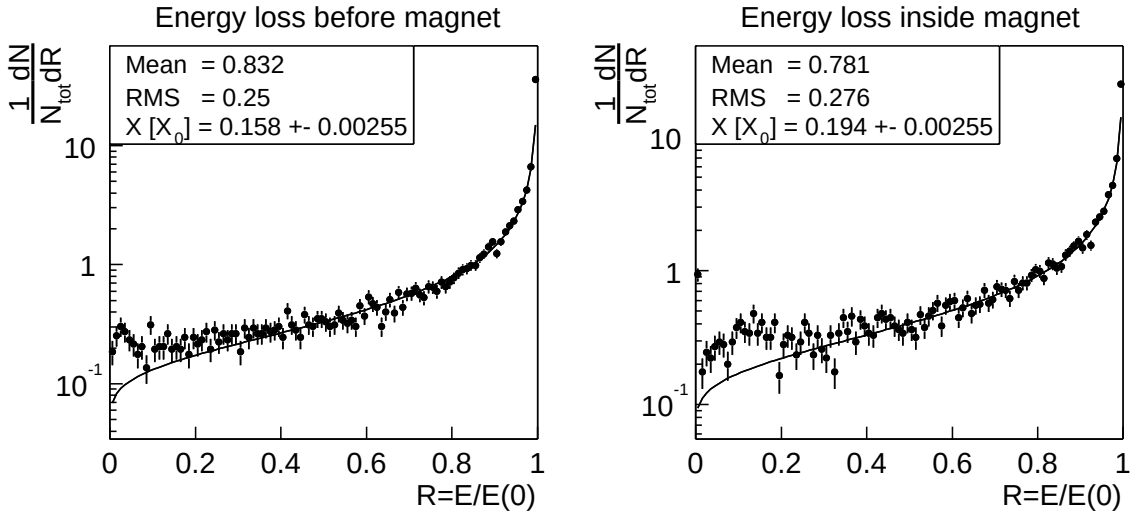

Figure 3.8.2: *Energy loss for electrons up to the magnetic field (left) and inside the magnetic field (right). The spectra are fit to a Bethe-Heitler p.d.f. of Eq. 3.8.1 and the extracted radiation lengths are also given.*

Bremsstrahlung radiated *inside* the magnet, is deposited between x_{cluster} and $x_{\text{Brems}}^{z<250\text{ cm}}$. Radiation at the end of the magnet may still be deposited inside one of the cells of the pretrigger. The pretrigger will then still include the Bremsstrahlung in the cluster. The cluster shape, however, will then be distorted and the centre-of-gravity will be shifted. Bremsstrahlung in the magnet is the main cause for the tails in the residual distributions of x (Fig. 3.6.1). Figure 3.8.3 shows how the original electron energy is typically deposited in the ECAL.

Bremsstrahlung recovery

Bremsstrahlung radiated before the magnet can be recovered[1] by the ECAL pretrigger [11]. Since the charge is not known, the pretrigger searches at both possible positions given by Eq. 3.8.4 for deposited energy. For each of these positions the closest calorimeter cell is determined, around which a nonet cluster is built. The Bremsstrahlung energies for the two possible charges are coded in the FLT message variables E^+ and E^- (table 2.3.1). After the corresponding track is reconstructed by the FLT and the charge is known, one of the two energies is added to the original cluster energy.

Figure 3.8.4 shows the energy found by the pretrigger in a Bremsstrahlung cluster as a function of the energy lost before the magnet. Currently, the coding of E^+ and E^- is identical to that of the electron cluster energy P (Eq. 3.7.6), which is not appropriate for the low energy range of Bremsstrahlung clusters. For this figure, we have ignored binning effects by taking the unbinned energies.

For energy losses above 1 GeV, the pretrigger finds a Bremsstrahlung cluster of more

[1] this option was not yet available in 2000, but will be used for data taking in 2002

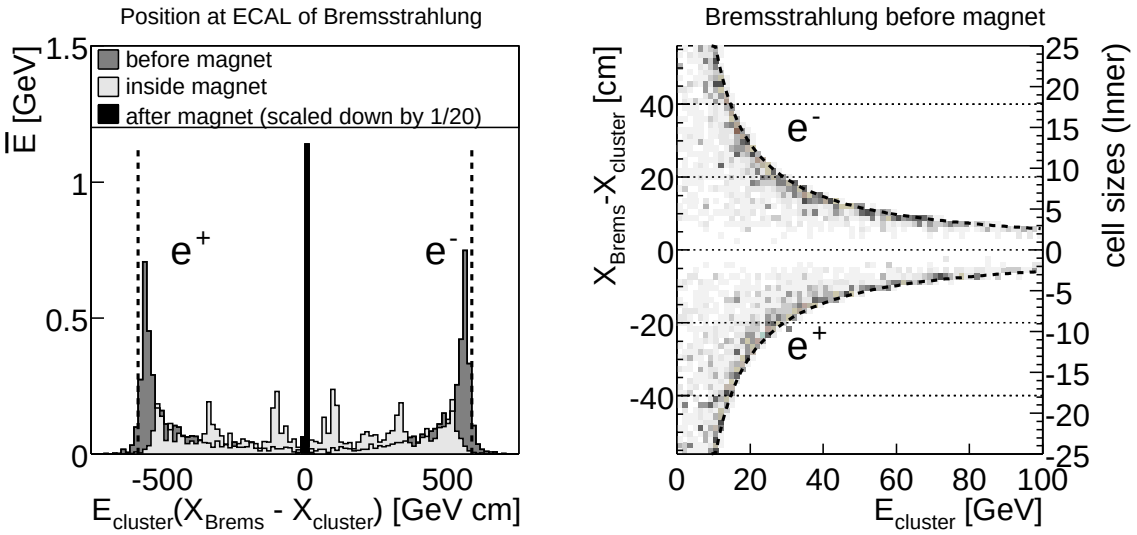

Figure 3.8.3: *Position in ECAL (z=1350 cm) and energy of Bremsstrahlung photons radiated before, inside and behind the magnet. Bremsstrahlung radiated before the magnet is mainly deposited around the expected position (Eq.3.8.4), indicated by the dashed line. The right plot shows that up to electron energies of 100 GeV, a cluster from Bremsstrahlung before the magnet is disjoint from the cluster of the electron.*

than 1 GeV with an efficiency of 85%. The average energy in such a Bremsstrahlung cluster is 23(5) GeV, 8.9(4) GeV and 4.8(3) GeV for the Inner, Middle and Outer ECAL, respectively. The average energy resolution of these Bremsstrahlung clusters for the different parts are 6.0(2)%, 6.9(3)% and 6.5(4)%, respectively. This is

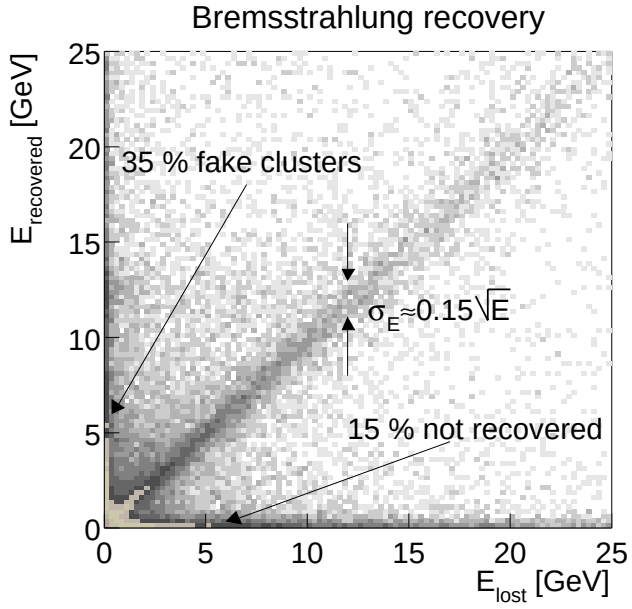

Figure 3.8.4: *Correlation between the energy lost before the magnet (x axis) and the energy recovered in the pretrigger Bremsstrahlung cluster (y axis). A nonet summation was used and the Bremsstrahlung distance was set to* $585/E$.

in reasonable agreement with design resolutions (Eq. 3.7.3).

Although the Bremsstrahlung recovery of the pretrigger is efficient, there is a high probability that energy will be found that is not from Bremsstrahlung. Due to high occupancies, the probability of finding accidentally a total energy in nine cells of more than 1 GeV, is as high as 35%. Such 'fake' Bremsstrahlung clusters lead to an overestimation of the electron energy. When the cross summation is applied in the pretrigger, this fake Bremsstrahlung rate drops to 20%, at the expense of a recovery efficiency of only 80%.

The overall effect of Bremsstrahlung recovery on the reconstruction of the original electron energy is shown in figure 3.8.5. A net improvement in energy resolution of 15% is observed. Significant tails in the residual distribution are visible, caused by unrecovered Bremsstrahlung (left side), and fake Bremsstrahlung clusters (right side).

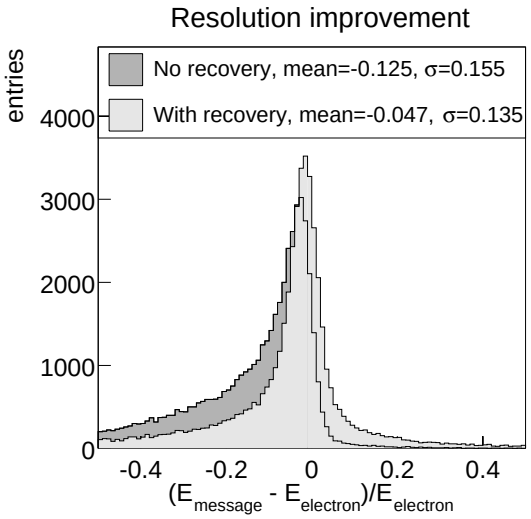

Figure 3.8.5: *Improvement of electron energy resolution through Bremsstrahlung recovery by the pretrigger. The energy residuals after Bremsstrahlung recovery (light shaded histogram) show a significant improvement w.r.t to the residuals without recovery (dark shaded histogram). The quoted energy resolutions are defined as a 68% confidence interval, obtained through integration of the histograms.*

It is foreseen that in future data taking the FLT will actually *require* Bremsstrahlung to be found as a means of electron identification. Such a requirement was commonly used in off-line analyses to obtain a clean J/ψ signal. If the Bremsstrahlung clusters will be required by the FLT, this will severely reduce the trigger efficiency for J/$\psi \rightarrow e^+e^-$ decays. The probability to find a Bremsstrahlung cluster of more than 1 GeV is about 30%. Demanding Bremsstrahlung clusters for both the electron and the positrons would therefore reduce the reconstruction efficiency for J/$\psi \rightarrow e^+e^-$ by more than a factor 10. The background would be rejected by a factor 40. As will be shown later, this background rejection power is less than that of an increased transverse energy threshold.

Figure 3.8.6 shows how the efficiency and the background rejection of the Bremsstrahlung requirement depend on the minimum energy in the Bremsstrahlung cluster. The background rejection has been estimated by looking at fake Bremsstrahlung clusters at the wrong side of the electron or positron. This may actually be too optimistic an estimate, since the occupancy in triggered events is higher than the occupancy of a single inelastic interaction, used for this figure. The probability to pick up a fake Bremsstrahlung cluster is proportional to the occupancy.

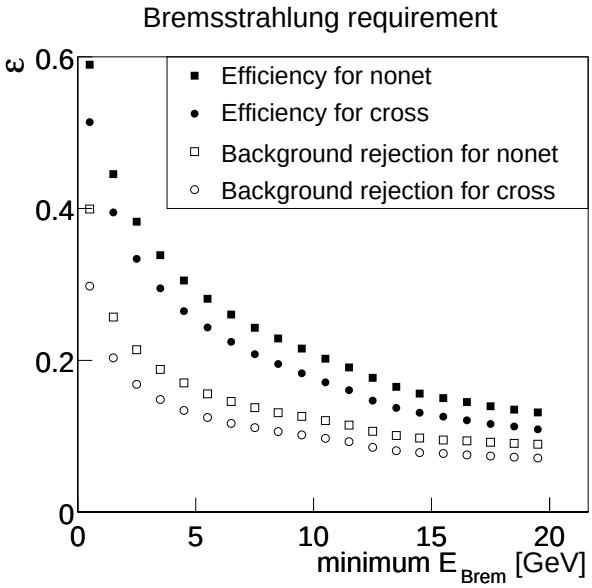

Figure 3.8.6: *Efficiency and rejection power of Bremsstrahlung requirement (for a single electron) as a function of the minimum energy required in a reconstructed Bremsstrahlung cluster. The background is measured from Bremsstrahlung found on the wrong side of the electron/positron cluster.*

Removal of magnet chambers

Whereas energy losses in front of the magnet can be (partly) recovered by the pretrigger, this is not the case for losses that occur inside the magnetic field. Although some of the Bremsstrahlung radiated in the magnet will be merged with either the electron cluster or the recovered Bremsstrahlung cluster, a significant fraction is lost. The pretrigger energies are therefore systematically lower than the original electron energies, as shown in figure 3.8.5. Moreover, the spread in the energy loss effectively reduces the energy resolution.

For future running, tracking chambers inside the magnet will be removed. They are not essential for the reconstruction of direct J/ψ decays. Their main purpose was the reconstruction of the K^0_S (from $B^0 \to J/\psi\, K^0_S$), which typically decays in the middle of the vertex detector. Since the measurement of CP violation in this decay channel is no longer part of the physics program of HERA-B , the magnet chambers have become obsolete. Another possible benefit of the magnet tracking chambers could be an increased efficiency for linking track segments in the pattern recognition area to track segments in the vertex detector. It has been shown that this can be done with an efficiency of more than 95% without magnet chambers too [14].

The removal of magnet chambers will significantly improve the reconstruction of electrons. Firstly, it reduces the tail in the residuals of x. Where previously only 84.1% of the pretrigger clusters was within half a cell size of the Monte Carlo truth, without magnet tracking chambers this increases to 90.4%. Consequently, the extrapolation efficiency increases significantly.

Secondly, and more importantly, it will improve the measurement of the electron energy. The energy resolution without magnet chambers, shown in figure 3.8.7, is 50% better than the energy resolutions for a full detector (Fig. 3.8.5).

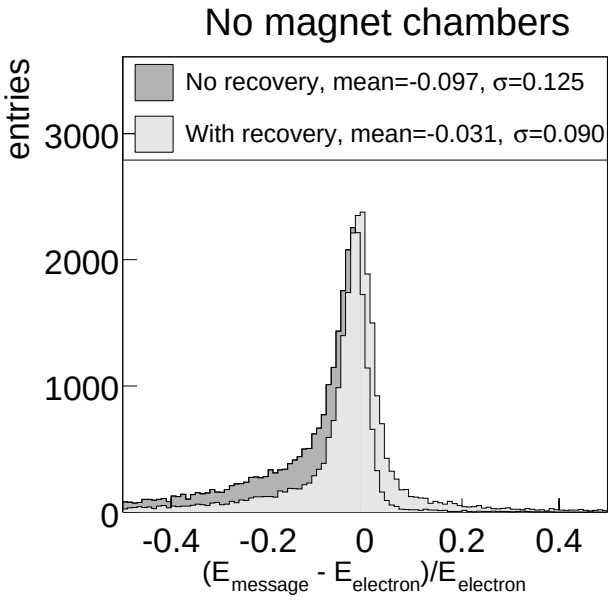

Figure 3.8.7: *Energy resolution of the pretrigger without magnet chambers. Shown are the energy residuals of figure 3.8.5, but here in a detector setup without the magnet tracking chambers.*

3.9 Efficiency and Background rejection

The purpose of the ECAL pretrigger is to limit the number of track candidates to be reconstructed by the FLT as much as possible to electrons with high momenta. The required reduction of pretrigger messages is achieved through the transverse energy cuts of Eq. 2.3.3.

In this section we will study the efficiency and the background rejection of the ECAL pretrigger. We restrict ourselves to electrons or positrons originating from a J/ψ. The electron reconstruction efficiency by the pretrigger can be factorised in several independent contributions:

$$\epsilon = \epsilon_{\text{geo}} \times \epsilon_{E_T,\text{central cell}} \times \epsilon_{E_T,\text{cluster}} \times \epsilon_{\text{RoI}} \times \epsilon_{E/p}. \tag{3.9.1}$$

The geometrical acceptance ϵ_{geo} is the probability that the electron reaches a sensitive part of the calorimeter. The efficiency of the transverse energy cuts $\epsilon_{E_T,\text{central cell}}$ and $\epsilon_{E_T,\text{cluster}}$ is the probability that the pretrigger cluster satisfies the requirements of equations 2.3.2. If the first three requirements are met, a pretrigger message will be sent to the FLT network. The last two contributions to the efficiency show possible losses in the FLT due to wrongly reconstructed pretrigger cluster parameters. The extrapolation efficiency ϵ_{RoI} describes possible losses due to an incorrect or too small search window encoded in the pretrigger message. Finally, the efficiency of a possible E/p-cut by the TPU, $\epsilon_{E/p}$, is considered to be part of the ECAL pretrigger performance since it is predominantly the energy resolution that determines this efficiency.

In this section these contributions are separately studied. For the transverse energy cuts and the E/p-cut the background rejection is also discussed.

3.9.1 Geometrical acceptance

The ECAL covers solid angles roughly between 10 and 230 mrad in horizontal direction, and 10 and 220 mrad in vertical direction. Table 3.9.1 shows the geometrical acceptance for $J/\psi \rightarrow e^+e^-$ decays, measured for each of the three ECAL parts separately. The

e- e+	Inner ECAL	Middle ECAL	Outer ECAL	Outside acc.
Inner	13.87(11)	10.03(8)	3.95(5)	7.59(9)
Middle	10.14(8)	9.02(7)	4.29(5)	6.96(8)
Outer	4.13(5)	4.07(5)	2.28(4)	2.80(5)
Outside acc.	7.73(9)	6.88(7)	2.70(5)	3.54(6)

Table 3.9.1: *Geometrical acceptance of the ECAL for* $J/\psi \rightarrow e^+e^-$ *decays. Shown is the probability (in %) of the electron to reach a part of the ECAL vs. the same probability of the positron.*

probability to find both leptons from the J/ψ inside the acceptance is 61.8%. When only one of the two is required, the acceptance is 96.5%. The Inner and Middle parts of the ECAL contribute more to the acceptance than the Outer part: when only the Inner and Middle ECAL are used, the probability to accept both J/ψ tracks is still 43.0%.

The positions of the two leptons are correlated. The leptons inherit a transverse momentum from the invariant mass of the J/ψ. The transverse momentum of one lepton is partly compensated by that of the other lepton and the two leptons tend to move in opposite directions.

3.9.2 Efficiency of transverse energy cuts

A cut on the transverse momentum is an effective way to reduce the number of track candidates to be reconstructed by the FLT. The leptons from J/ψ decays have transverse momenta that are on average larger than those of other particles produced in an inelastic interaction (see Fig. 3.9.1). Where the mean p_T of pions and kaons is 0.22 GeV, electrons from J/ψ decay have mean p_T of 1.45 GeV.

A cut on p_T requires knowledge of the momentum, which is not yet available. The transverse energy of the pretrigger cluster serves as a first estimate of this p_T, but is considerably different. First of all, the pretrigger does not know if the particles have bent inwards (i.e. towards $x = 0$) or outwards in the magnetic field. The transverse energies of Eq. 2.3.3 assume the average of these two hypotheses, namely that the particle is not deflected by the magnetic field.

Furthermore, the reconstructed cluster energy is not equal to the true energy of the particle. Besides resolution effects, energy losses cause the recorded energy to be systematically lower than the original electron energy. Although hadrons do not suffer from energy loss, they deposit only a fraction of their energy and produce less energetic clusters than electrons and photons. This effect is obviously advantageous for background rejection.

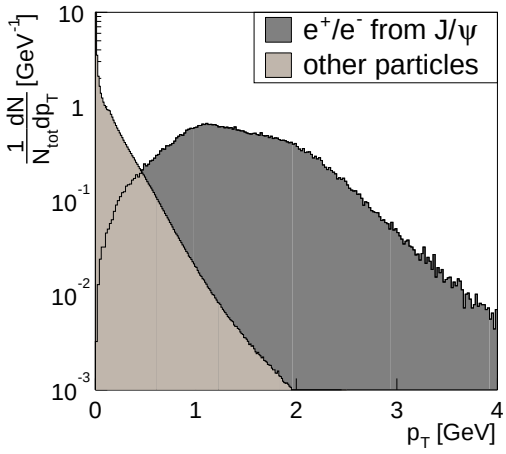

Figure 3.9.1: *Transverse momenta of electrons and positrons from J/ψ decays and of other particles in inelastic interactions.*

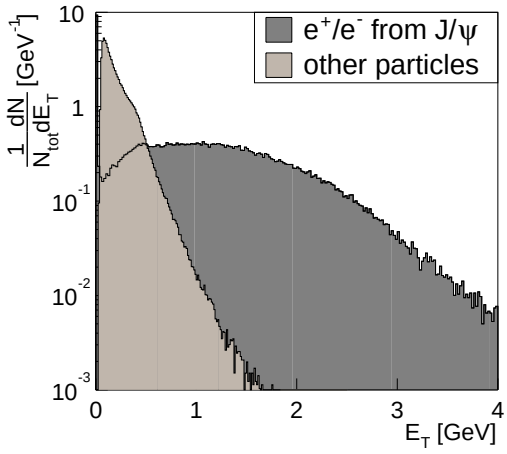

Figure 3.9.2: *Reconstructed transverse energies in ECAL clusters for electrons and positrons from J/ψ decays and of other particles in inelastic interactions.*

A cut on the transverse energy E_T is less efficient than a cut on p_T. Nevertheless, it gives a powerful background rejection, as shown in figure 3.9.2.

The E_T threshold of the ECAL pretrigger is tuned to keep the rate of track candidates to be processed by the FLT at an acceptable level. Which pretrigger message rate is still acceptable depends on several external conditions:

- **Trigger scenario**
  The FLT must reduce the event rate from 10 MHz to 50 kHz. This output bandwidth will typically be shared equally between electron triggers and muon triggers. If the FLT is operated in pair trigger mode, as designed, only 1 in 200 (background) events will pass the invariant mass cut. In this case, the rate of ECAL pretrigger messages can be as high as 10 MHz, an average of one message per bunch crossing. Alternatively, if only a single track requirement is applied, as was commonly done during data taking in 2000, the FLT reduces the input rate by only a factor 17 [10]. In this case, the ECAL pretrigger rate should not exceed 0.5 MHz.

- **Interaction rate**
  The pretrigger message is roughly proportional[1] to the interaction rate.

The dependence of the pretrigger message rate on the threshold and on the interaction rate is shown in figure 3.9.3. It is measured by integrating the E_T spectrum, reconstructed by the pretrigger, as shown in figure 3.9.2 (other particles).

[1] due to overlap of clusters, the number of pretrigger messages actually increases faster with the interaction rate

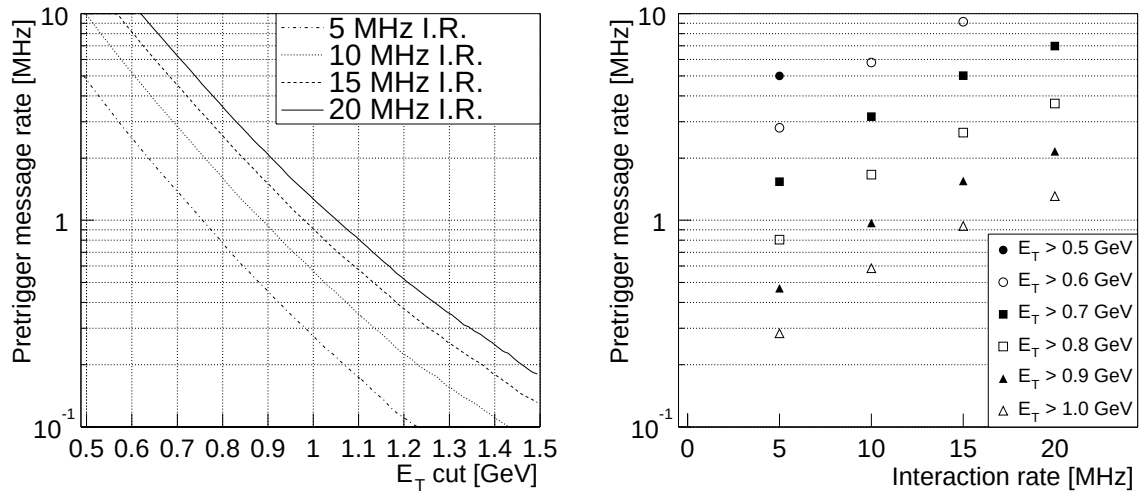

Figure 3.9.3: *Output rate of ECAL pretrigger messages as a function of E_T cut on pretrigger cluster (left) and interaction rate (right). The number of events per interaction is distributed according to Poisson statistics with expectation values of 0.5, 1, 1.5 and 2 to simulate interaction rates of 5, 10, 15 and 20 MHz respectively.*

The transverse energy cut is the dominant factor in the efficiency for $J/\psi \to e^+e^-$ decays. This cut is executed in two stages. First, the pretrigger only reconstructs clusters around central towers that are above half the transverse energy threshold. Finally, the sum of the energies in the nonet must be above the total threshold. Of these two cuts the latter is dominant. Figure 3.9.4 shows that for an E_T cut of 1 GeV, $\epsilon_{E_T,\text{central cell}}$ is 98%.

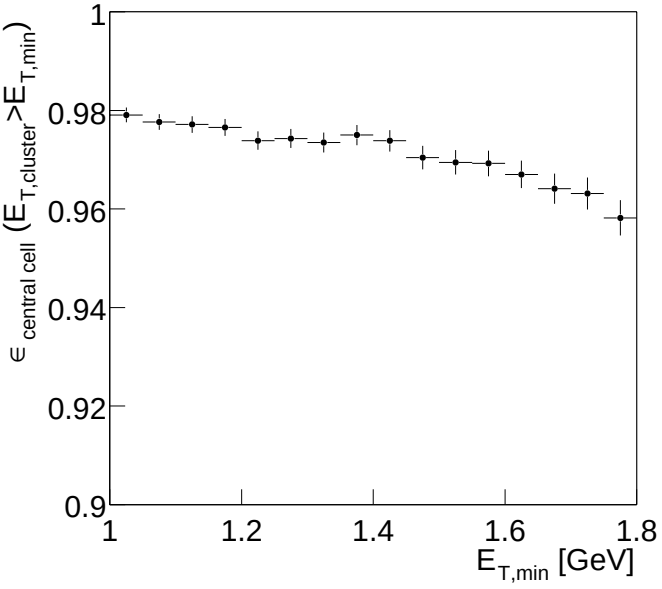

Figure 3.9.4: *Contribution of E_T cut on central cell to the total efficiency. The data points give the probability that a central cell passes the cut of $E_{T,\text{central cell}} > E_{T,\text{min}}/2$, if the full nonet satisfies $E_{T,\text{cluster}} > E_{T,\text{min}}$.*

The combined efficiency $\epsilon_{E_T} = \epsilon_{E_T,\text{central cell}} \times \epsilon_{E_T,\text{cluster}}$ is shown in figure 3.9.5 as a function of the transverse energy threshold. Also shown is the total efficiency for a pretrigger message to be issued, which includes the geometrical acceptance.

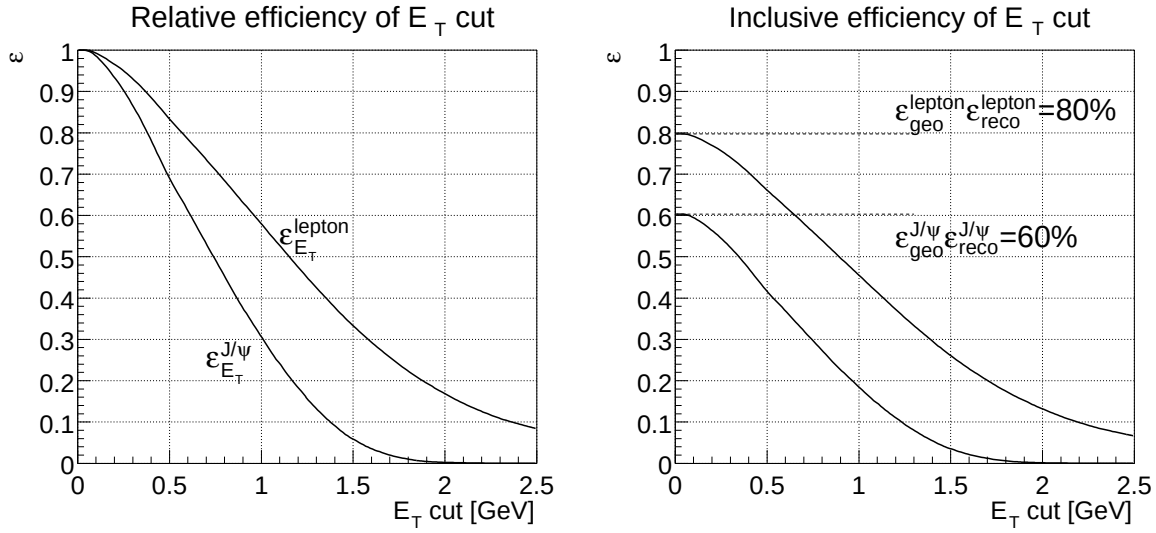

Figure 3.9.5: *Dependence of the pretrigger efficiency on the minimum required E_T. The left plot shows the combined efficiency of the transverse energy cuts $\epsilon_{E_T,\text{central cell}} \times \epsilon_{E_T,\text{cluster}}$. The right plot shows total efficiency, including geometrical acceptance. The efficiencies for one lepton and for both leptons from a J/ψ are separately shown. Here, an ideal calibration is used and all magnet chambers are included.*

For an E_T threshold of 1 GeV, the probability to issue a pretrigger message for each of the two leptons from the J/ψ is less than 20%, which is considerably lower than the design specifications of 35%. This is party due to the smaller geometrical acceptance, but mainly because this threshold is higher than was foreseen.

The efficiency and rejection power depend on the energy resolution of the pretrigger. The energy resolution effectively dilutes the threshold above which clusters are accepted. With a worse resolution, the number of candidates that satisfy the cut will increase or decrease, depending on the slope of the E_T spectrum near the E_T threshold. For any threshold value, the slope of E_T spectrum of the background falls off steeper than that of the electrons from J/ψ. Therefore with a worse energy resolution, the background rate will increase faster than the efficiency and the background rejection power diminishes. Figure 3.9.6 shows the efficiency and the background message rate as a function of the energy resolution.

The efficiency for selecting J/ψ leptons depends only weakly on the resolution, at least around an E_T threshold of 0.8 GeV; the slope of the E_T spectrum for these particles is reasonably flat around typical threshold values. The efficiencies given in figure 3.9.5 are practically independent on which energy resolution was assumed in the Monte Carlo.

In contrast, the background message rate increases with worsening energy resolution. To keep the rate of pretrigger candidates at a constant level, a worse energy

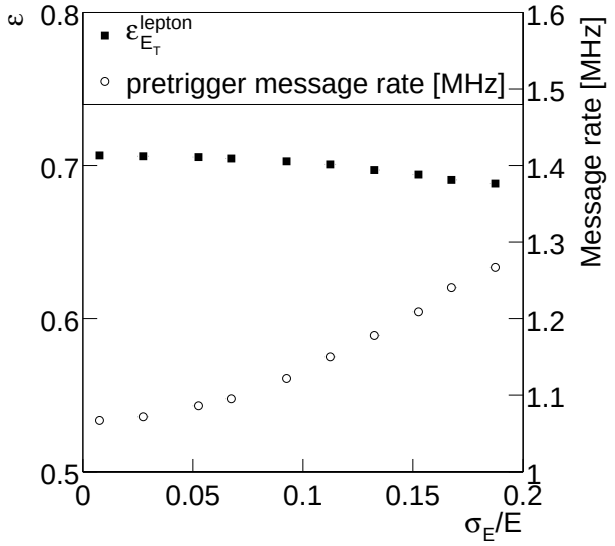

Figure 3.9.6: *Dependence of efficiency and message rate on energy resolution. The E_T cut was set to 0.8 GeV. The pretrigger efficiency for a lepton from a $J/\psi \to e^+e^-$ decay is shown in solid squares. The (background) message rate (in MHz) is shown as open squares for an interaction rate of 10 MHz.*

resolution will make a slightly higher transverse energy threshold necessary. It is a small effect, however: a message rate increase of 10% can be compensated by an increase of the E_T threshold by approximately 50 MeV, which reduces the J/ψ efficiency by only a few percent.

3.9.3 Extrapolation efficiency

If the transverse energy cuts are satisfied, a pretrigger message is sent to the FLT network. The pretrigger message encodes a Region of Interest (RoI) in the pretrigger message. Within this RoI, one or more of the TFU of TC2 will look for hits that confirm the passage of a charged track. If the RoI is incorrect or too small, the track finding may fail.

Definition of the RoI

The size of the RoI, Δ_{TC2}, depends on the reconstructed pretrigger cluster coordinates and energy. This size is the sum of an energy dependent term and a term due to the spatial resolution, which is different for the Inner, Middle and Outer ECAL.

The spatial resolution term w is defined in terms of the ECAL cell size w_{cell}:

$$w = \gamma w_{\text{cell}}, \tag{3.9.2}$$

where w_{cell} is 2.24, 5.6 and 11.2 cm for the Inner, Middle and Outer ECAL, respectively[2].

[2]Although w is a message variable, the TFU actually determines the cell sizes from the cluster coordinates (ξ and η) by means of a lookup table.

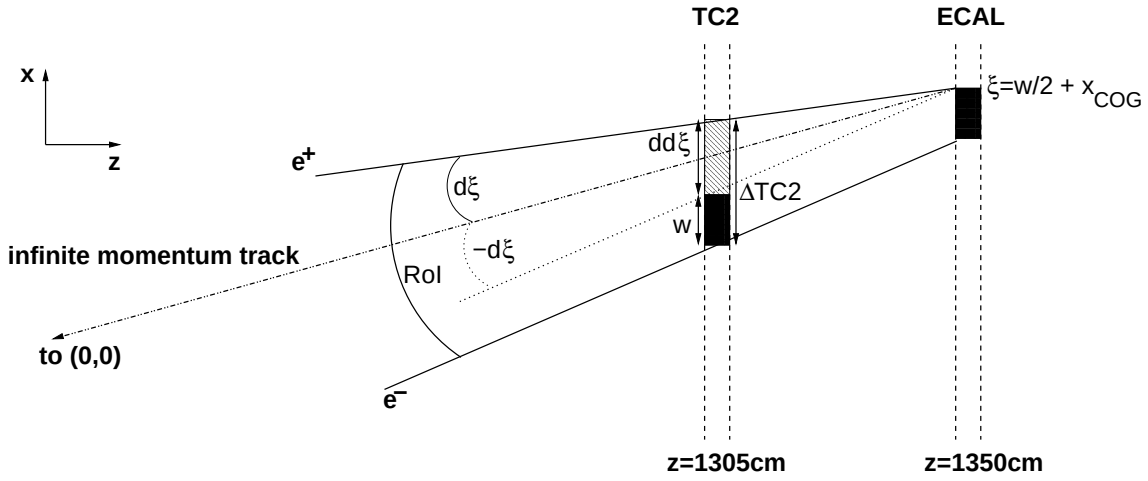

Figure 3.9.7: *Construction of the Region of Interest by the ECAL pretrigger. The search window covers the possible tracks of both negatively and positively charged particles ($dd\xi$) and the uncertainty due to the spatial resolution of the pretrigger cluster (w).*

The energy dependent RoI size is coded by the message variable $dd\xi$. It is defined to give the size of the RoI (in cm) at superlayer TC2, when increased by w:

$$dd\xi = \Delta_{\mathrm{TC2}} - w. \tag{3.9.3}$$

Depending on the charge, as yet unknown, the particle is deflected by an angle $d\xi$ or $-d\xi$ with respect to a track of infinite momentum. This deflection angle depends on the integrated field strength and position of the HERA-B magnet and is inversely proportional to the momentum of the particle, which is taken to be the pretrigger cluster energy. If the reconstructed cluster energy were larger than the momentum of the particle, the RoI size would be underestimated. A 'security' factor ρ is introduced to allow the energy to be larger than the momentum by a factor ρ.[3] The variable $d\xi$ then reads:

$$d\xi = \frac{0.224\rho}{E}. \tag{3.9.4}$$

The size of the RoI Δ_{TC2} incorporates the deflections in both (charge) directions and a down-scaled width,

$$\begin{aligned} \Delta_{\mathrm{TC2}} &= 2d\xi(z_{\mathrm{ECAL}} - z_{\mathrm{TC2}}) + w\frac{z_{\mathrm{TC2}}}{z_{\mathrm{ECAL}}}, \\ &= \frac{20.16\rho}{E} + 0.974\gamma w_{\mathrm{cell}}. \end{aligned} \tag{3.9.5}$$

The value of the parameters ρ and γ can be chosen at will. In the data taking period of 2000 they were set to $\rho = 2$ and $\gamma = 0.5$. The distribution of Δ_{TC2}, decoded from recorded messages, is shown in figure 3.9.8 for the three different ECAL parts.

[3] If the energy of the pretrigger cluster is *smaller* than the momentum the RoI will only be larger than necessary.

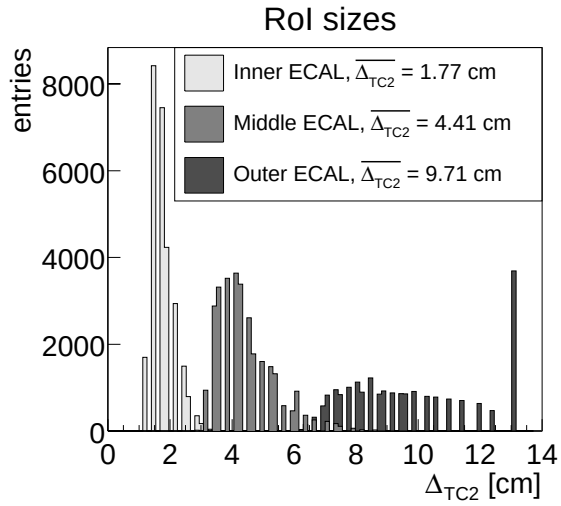

Figure 3.9.8: *Distribution of RoI sizes Δ_{TC2} for Inner, Middle and Outer ECAL. The values shown here are for $\rho = 2$ and $\gamma = 0.5$, the settings used for data taking in 2000.*

The value of $\rho = 2$ comfortably covers the uncertainty due to the energy resolution: the probability that the ECAL pretrigger overestimates the energy by more than a factor 2 is negligible, as can be seen in figure 3.8.5 (without recovery).

The value of 0.5 for γ is not well chosen, however. The value assumes that the spatial coordinates are accurate to within a quarter of a cell size. This corresponds to roughly two to three times the width of the core Gaussian in the residual distribution (table 3.6.1).

However, the residual distribution had considerable tails. Up to 20% of the residuals are outside this window, as summarised in table 3.9.2. We therefore may expect efficiency losses in the track finding by the FLT with these values of γ and ρ. The large window allotted for overestimated energies and for two charge hypotheses, partly compensates the overestimated spatial resolution. The extrapolation efficiency, evaluated later, is therefore higher than the values of table 3.9.2.

	$P(\Delta_x < w_{\text{cell}}/4)$	$P(\Delta_y < w_{\text{cell}}/4)$
Inner	84.1	88.2
Middle	86.4	89.3
Outer	79.6	81.2

Table 3.9.2: *Fraction of clusters (in %) inside window assumed for extrapolation. Shown is the probability P that the residual $\Delta_{x,y}$ between the pretrigger message and the Monte Carlo truth is within half or a quarter of an ECAL cell size.*

Fixed z limitation

The assumption of the ECAL pretrigger of a fixed z value of 1350 cm has a similar effect on the extrapolation efficiency as the spatial resolution. For the Middle and Outer ECAL, the true z position is systematically higher than 1350 cm (see figure 3.1.1). Consequently, the size of the RoI is underestimated and may lead to efficiency losses.

Since the z position of clusters in the Inner ECAL is always less than 1350 cm, the RoI size is overestimated and efficiency losses will be partly recovered.

Figure 3.9.9 shows the change in the spatial coordinates $\Delta_{|x|}$ from an extrapolation of z from the penetration depth to z =1350 cm. The effect of a fixed z position increases the RoI size in x for the Inner part by about one 1 mm, where the RoIs of messages from the Middle and Outer part are typically 5% of a cell size smaller.

The change of the RoI in vertical direction is not critical, since the y resolution of ECAL pretrigger messages far exceeds the y resolution assumed in the FLT.

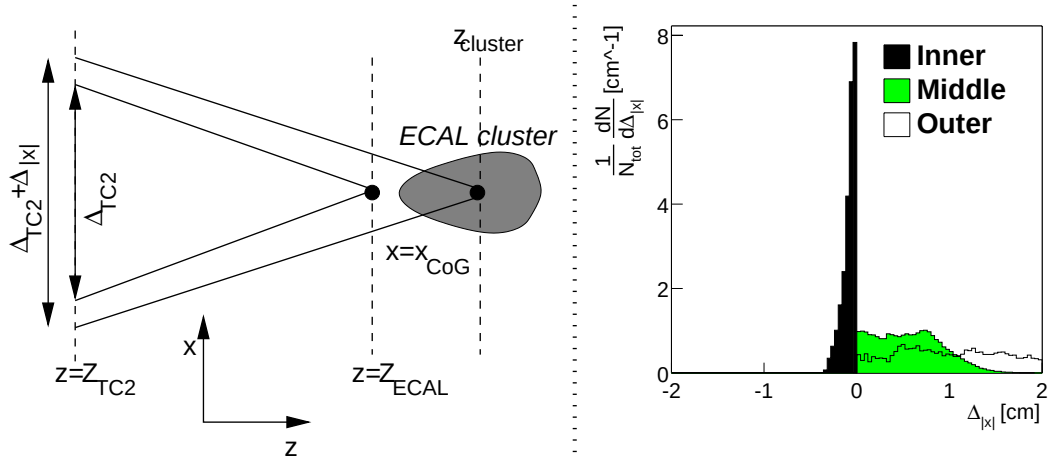

Figure 3.9.9: *Effect of a fixed-z limitation on the determination of the RoI. Shown is the change in the x coordinates due to an linear extrapolation from the penetration depth of the shower to the reference plane* $Z_{\mathrm{ECAL}} = 1350$ *cm, as illustrated in the figure on the left.*

Measurement of the extrapolation efficiency

The extrapolation efficiency ϵ_{RoI} is determined as the probability that the Monte Carlo impact point of the electron track at superlayer TC2 is inside the RoI of the message. The position and size of the RoI are extracted from the simulated message by decoding the message variables ξ, $d\xi$ and $dd\xi$. In this manner, binning effects are taken into account too. Figure 3.9.10 shows the residuals in the x position between impact points (inside or outside the RoI), and the centre of the RoI. The distributions for the three different ECAL parts are separately shown.

For given values of ρ and γ there are considerable differences in efficiency between the different ECAL parts. The average energy in pretrigger clusters is 79.1 GeV for the Inner ECAL, 33.2 GeV for the Middle ECAL, and 15.1 GeV for the Outer ECAL. Consequently, the compensation for inefficiencies from spatial resolution effects by the energy dependence in Eq.3.9.5 is highest in the Outer ECAL.

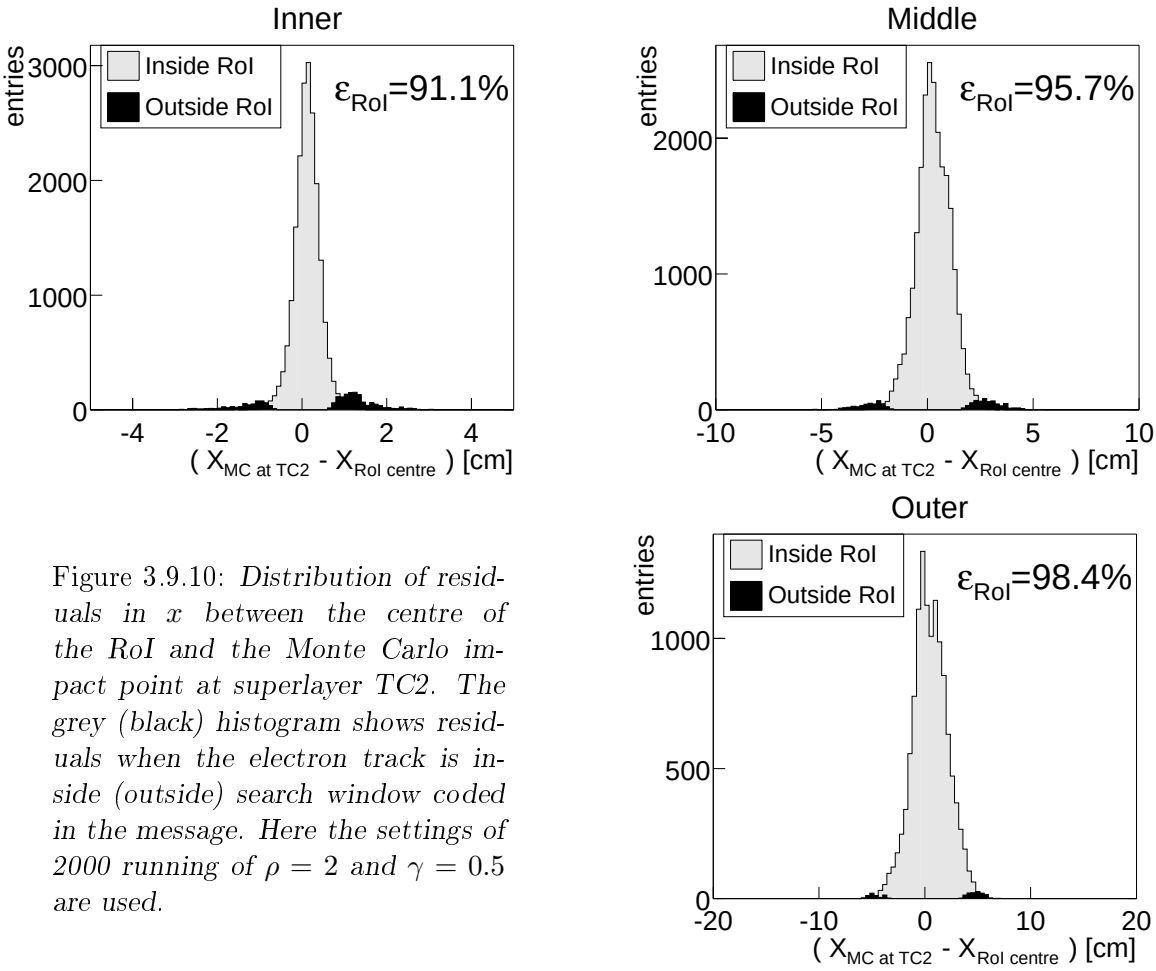

Figure 3.9.10: *Distribution of residuals in x between the centre of the RoI and the Monte Carlo impact point at superlayer TC2. The grey (black) histogram shows residuals when the electron track is inside (outside) search window coded in the message. Here the settings of 2000 running of $\rho = 2$ and $\gamma = 0.5$ are used.*

Optimisation of the RoI calculation

The values of ρ and γ chosen in 2000 lead to efficiency losses of up to 10%. Preferably, therefore, ρ and/or γ should be increased in future data taking. This will inevitably lead to an increase of the average size of the RoI, resulting in a significant increase of 'ghost' tracks. Choosing values of ρ and γ clearly is a trade-off between increasing the extrapolation efficiency ϵ_{RoI} and keeping the size of the RoI small.

Figure 3.9.11 shows the extrapolation efficiency ϵ_{RoI} as a function of ρ and γ for the different parts of the ECAL. The average RoI size, $\langle\Delta_{\mathrm{TC2}}\rangle$, scales linearly with ρ and γ (Eq. 3.9.5). Lines of constant $\langle\Delta_{\mathrm{TC2}}\rangle$ are parallel to the lines drawn in this figure.

The optimal values for ρ and γ are those values that minimise the average RoI size for a certain required efficiency. These optimal values can be obtained by equalising the slope of $\langle\Delta_{\mathrm{TC2}}\rangle(\rho,\gamma)$ to the slope of $\epsilon_{\mathrm{RoI}}(\rho,\gamma)$. If we would require $\epsilon_{\mathrm{RoI}} = 98\%$ for each of the ECAL parts, we thus obtain the values given in table 3.9.3.

For these values of ρ and γ, the average RoI sizes are about 1 cm larger than for the values used in 2000. Whether this increase is still acceptable for the FLT, depends mainly on the interaction rate and the resulting hit occupancies in the tracking chambers. This will be studied in the next chapter.

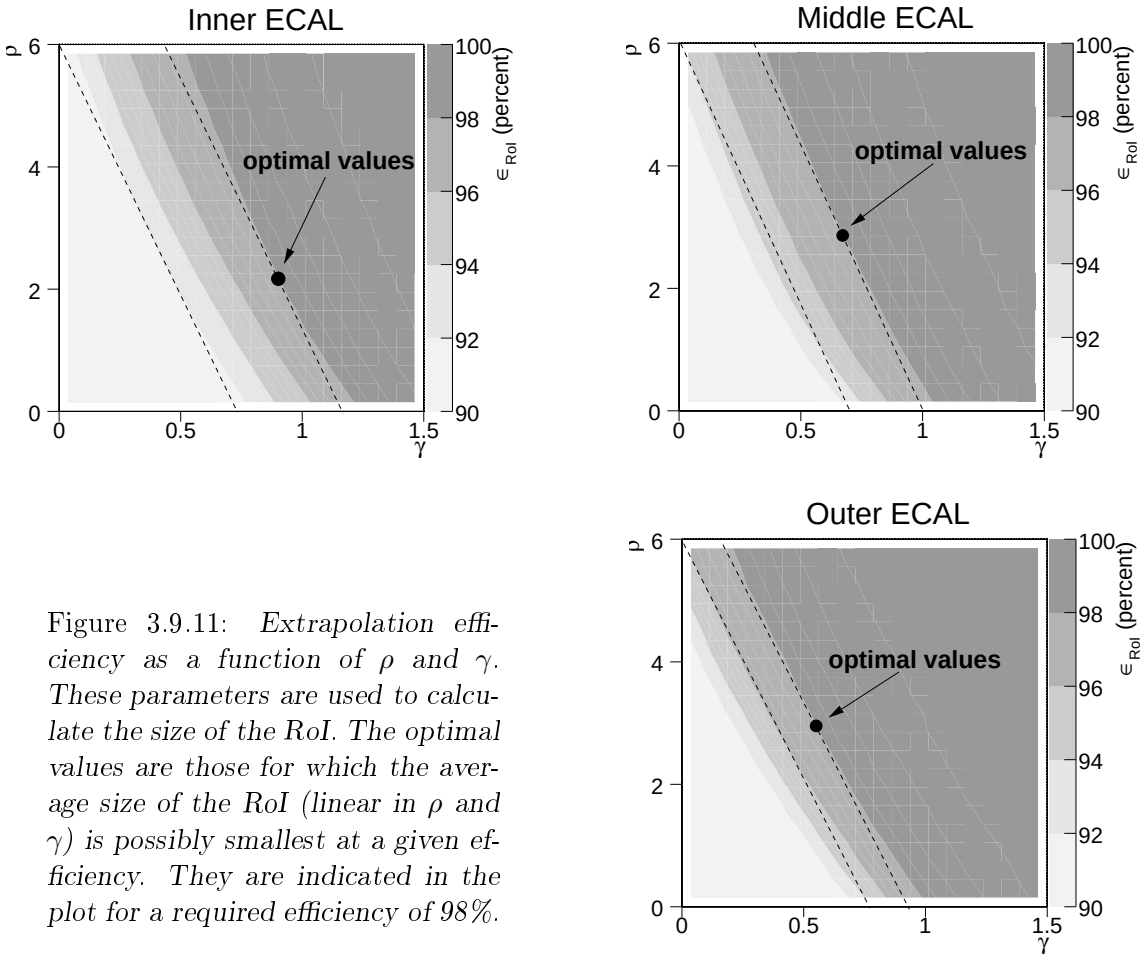

Figure 3.9.11: *Extrapolation efficiency as a function of ρ and γ. These parameters are used to calculate the size of the RoI. The optimal values are those for which the average size of the RoI (linear in ρ and γ) is possibly smallest at a given efficiency. They are indicated in the plot for a required efficiency of 98%.*

Extrapolation in vertical direction

The uncertainty in the vertical track direction is implicitly incorporated through the set of valid coincidences at the TFU (see Fig. 2.3.9). It allows the channel of one of the stereo angles to be displaced by two cells (for $h = 2$) w.r.t. the channel in the zero

	Inner ECAL	Middle ECAL	Outer ECAL
ρ	2.1	2.8	2.8
γ	0.9	0.7	0.55
ϵ_{RoI}	98%	98%	98%
$\langle\Delta_{\mathrm{TC2}}\rangle$	2.7 cm	5.9 cm	10.5 cm

Table 3.9.3: *Optimal values for ρ and γ for a required extrapolation efficiency ϵ_{RoI} of 98%. These values of ρ and γ give the smallest value of$\langle\Delta_{\mathrm{TC2}}\rangle$.*

degree superlayer. The corresponding vertical extent of such a displacement is:

$$\Delta y = \frac{2w_{\text{cell}}}{\tan(80\,\text{mrad})} = \begin{cases} 3\text{ cm} & \text{(Inner Tracker)} \\ 13\text{ cm} & \text{(Outer Tracker, 5mm)} \\ 26\text{ cm} & \text{(Outer Tracker, 10mm)} \end{cases} . \tag{3.9.6}$$

The uncertainty in the y position of the pretrigger cluster (table 3.6.2) is an order of magnitude less than Δy. The vertical size of the RoI does not cause a reduced efficiency.

3.9.4 The efficiency of an E/p-cut

A good energy resolution is necessary for an effective electron identification through an E/p-cut by the TPU. The energy recorded in the cluster is equal to the energy left after the electron has passed through the magnetic field.

Energy loss before or after the magnet will not affect the E/p ratio. Only energy loss *inside* the magnet reduces this ratio systematically. The momentum is determined by the FLT from the horizontal slope after the magnet, which is an estimate of the average momentum inside the magnet. Therefore the estimated momentum decreases by only half of the energy loss in the magnet, where the reconstructed cluster energy is reduced by the full energy loss.

Figure 3.9.12 shows the distribution of the E/p of electrons from J/ψ decays, and of the background. The average E/p of 0.90(1) for electrons is in agreement with the mean energy loss inside the magnet of 20% (see Fig. 3.8.1).

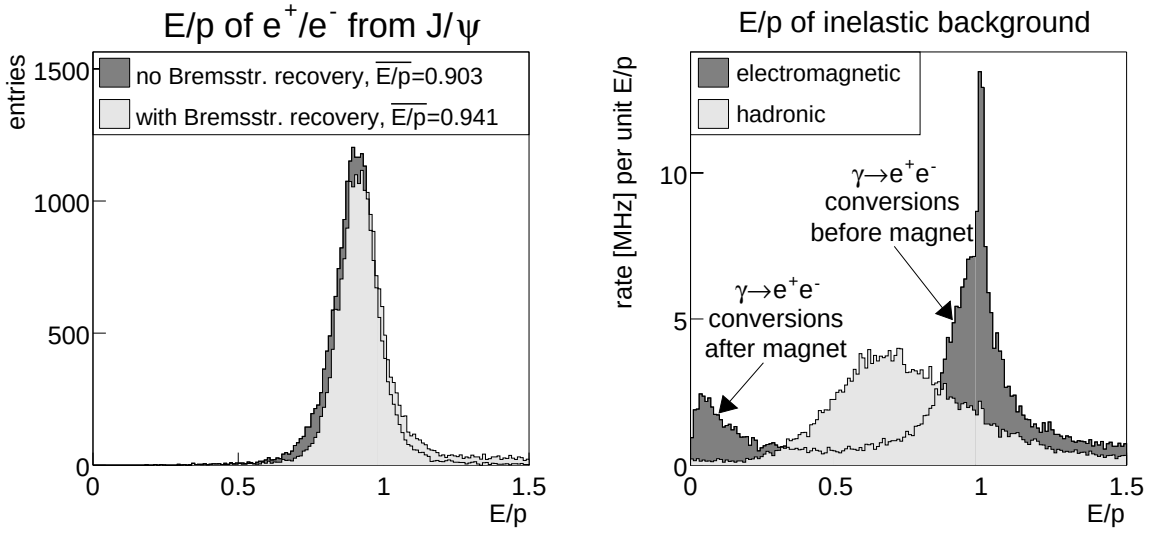

Figure 3.9.12: *Distributions of E/p ratio for signal and background messages. The momentum p is an estimate of the momentum measured by the FLT from the slope of the track after the magnet. The left plot shows the distribution for electrons from J/ψ decays, both with and without Bremsstrahlung recovery. The right plot shows the ratios for messages from inelastic background interactions. An interaction rate of 10 MHz and an E_T threshold of 0.5 GeV were used, and only clusters were considered that had a charged track inside the RoI.*

The background pretrigger messages are either due to charged hadrons or converted photons. If a photon conversion occurred behind the magnet, the electron track points straight to the target and the FLT will reconstruct an unrealistically high momentum. Such conversions are therefore easily rejected by the E/p cut. If the photons converted before the magnet, the electron and the positron will be split by the magnetic field, yielding two clusters, for each of which the energy matches the momentum.

In data taking of 2000, only a minimum E/p of 0.5 was required in order to reject late conversions and hadrons. It had not been realized that also a *maximum* on E/p can give a rejection of background. Such a cut discards fake matches: tracks that point to the pretrigger cluster, but which are not responsible for the bulk of the energy deposit. This can occur for example when the track direction of a hadron overlaps with that of a photon. The energy in a pretrigger cluster is generally much higher than the energy of a typical hadron, giving $E/p \gg 1$.

Figure 3.9.13 gives the efficiency and the background rejection as a function of the minimum E/p. The effect of requiring a maximum on E/p of 1.5 is also shown. For a minimum E/p of 0.5, the efficiency for signal electrons is 99.2(1)%, while the efficiency for the background is 43.9(6)%. Increasing this minimum does not give a much higher background rejection. A maximum on E/p of 1.5, however, improves the background rejection by almost a **factor two**, from 43.9(6)% to 28.4(7)%, without any considerable efficiency loss.

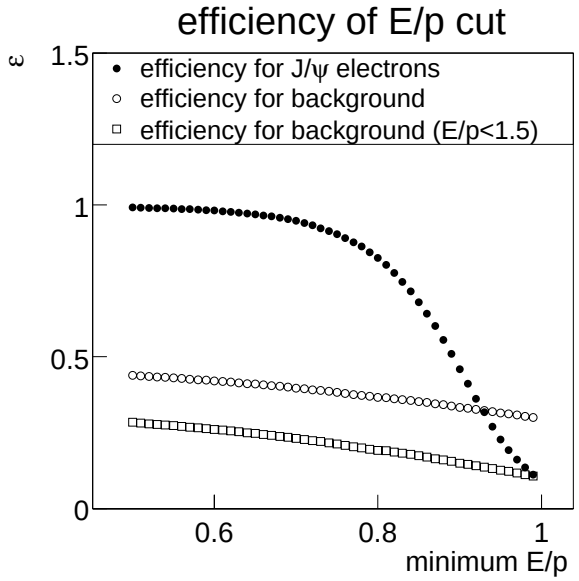

Figure 3.9.13: *Efficiency and background rejection of an E/p cut.*

3.9.5 Efficiency for $J/\psi \to e^+e^-$ decays

The benchmark performance of the ECAL pretrigger is its efficiency to select $J/\psi \to e^+e^-$ decays. The achieved J/ψ efficiency was lower than the design value of 35%. The main reasons are the higher than foreseen E_T threshold (1.0 GeV instead of 0.7 GeV) and the reduced acceptance due to missing or malfunctioning pretrigger boards.

Table 3.9.4 lists the individual contributions to the efficiency that was achieved in 2000, along with the values that can be reached with some improvements to the system.

	achieved in 2000	achievable	improvement
acceptance	37.7	62.3	install missing boards
hardware defects	94.3(1)	100	repair hardware
summation	91 (cross)	100 (nonet)	change LUT program.
$E_T > 1$ GeV	32	41.7(1)	remove magnet chambers
sub-total	10.4(1)	26.0(1)	
extrapolation	92	98	change γ, ρ
E/p cut	99.2	99.2	change cut to $0.5 < E/p < 1.5$
total	9.4(1)	25.2(2)	

Table 3.9.4: *Achieved and achievable pretrigger efficiencies (in %) for* $J/\psi \to e^+e^-$ *decays. The achieved efficiencies correspond to the setup (coverage, pretrigger settings) used in the end of running of 2000.*

An efficiency increase can also be obtained from the removal of magnet chambers. The resulting reduction of unrecoverable electron energy losses, gives an efficiency increase of more than 30%, from 32% to 42%.

The additional background rejection that is obtained from a maximum on E/p allows the reduction of the E_T threshold by 150 MeV. This increases the J/ψ efficiency by another 35%.

At an interaction rate of 10 MHz , the pretrigger would select $J/\psi \to e^+e^-$ decays at a rate of 7100/h, if the achievable J/ψ efficiency is met, and no additional efficiency losses are suffered at the FLT.

3.10 Summary

Although the ECAL installation had not yet been completed, the ECAL pretrigger performed largely as expected. The simulation is able to reproduce the behaviour of the hardware exactly, while locating hardware defects at the level of a few percent.

The dominant limitation of the pretrigger to the resolution are binning effects in the coding of the cluster energy and position. Due to these binning effects, the resolution in x and y is typically 50% worse than the resolution of an off-line reconstruction.

The energy resolution is dominated by electron energy loss effects. Bremsstrahlung, radiated before and inside the magnet, leads to cluster energies that are systematically too low. The energy resolution is more than a factor five worse than if such energy losses were absent. Bremsstrahlung recovery by the pretrigger improves the energy determination by 50%.

The efficiency for $J/\psi \rightarrow e^+e^-$ decays is dominated by the geometrical acceptance (62.3%) and the transverse energy cut (32% for $E_T > 1$ GeV). The removal of the magnet chambers increases the latter to 42%.

The trigger settings used in 2000 can be improved. Requiring $0.5 < E/p < 1.5$, gives an additional background rejection of a factor 2, without efficiency losses. Enlarging the RoI sizes can give an efficiency increase of 10%.

The background rejection power of a Bremsstrahlung requirement is less than the rejection power of an increased E_T threshold.

Chapter 4

Performance of the FLT network

The installation of the FLT network was largely completed in the course of 2000. At the end of the 2000 running period, much of the data taking was dedicated to the commissioning of the FLT.

In this chapter we present an analysis of the performance of the FLT. We first address several aspects of the hardware, such as the performance of the Outer Tracker, data transmission to the FLT, latency and message rates. The behaviour of the FLT network is compared to the results from an FLT emulation on the same events.

Subsequently we study the different contributions to the track parameter and momentum resolution, and compare the expected resolutions with the values obtained from a Monte Carlo simulation. The reliability of the Monte Carlo simulation is verified using the data of 2000. The track finding efficiency is measured from the 2000 data, and different sources of inefficiency are discussed.

We restrict ourselves to tracks initiated by an ECAL pretrigger. A study on the performance of the FLT in the muon channel can be found elsewhere [49].

4.1 Performance of the Outer Tracker in 2000

Electron candidates are reconstructed from ECAL pretrigger messages, confirmed by four space points in the tracking system. In 2000, the Inner Tracker was not available for the FLT, and track finding was restricted to the Outer Tracker stations TC2, TC1, PC4 and PC1 (see figures 2.2.1 and 2.3.2).

A properly working Outer Tracker is essential for the FLT. [1] Considerable problems with the Outer Tracker have precluded efficient FLT operation:

Efficiency

The hit efficiency was only between 85 and 90%, which is considerably lower than the design value of 98%. There are two reasons for this: The chambers were operated at a high voltage that was below the efficiency plateau and the discriminator threshold of

[1] Since the FLT does not use drift time information, the hit resolution of the Outer Tracker is not important for the FLT.

the ASD8[2] readout chip was much higher than foreseen. This gives an upper limit on the FLT track finding efficiency (see Eq. 2.3.7) of approximately 80%.

Dead channels

A considerable part of the Outer Tracker could no be used because of high voltage problems. At a rate of about one per six hours of operation [10], a new short circuit in one of the high voltage groups appeared, leading to a loss of 256 channels. This could only be reduced to 16 channel per HV group after an access to the detector. By the end of the running period of 2000, over 500 high voltage groups were defective, corresponding to more than 10% of the Outer Tracker channels. Problems with detector readout and disconnected cables disabled a few percent more.

Noise

Although the ASD8 threshold values were up to 600 mV higher than foreseen, ASD8 oscillations were still present. This affected specifically the chambers used by the FLT. In total about 10% of the ASD8s showed various degrees of oscillations. The FLT algorithm has no drift time information and can therefore not distinguish noise hits (that usually have impossibly low drift times) from hits of charged particles[3].

Noise hits are generally clustered in one ASD8 group of 16 channels and sometimes in several neighbouring ASD8s. When the FLT searches for a valid space point in such a region it will often find many candidates, for each one of which a new message will be generated. One true track can thus lead to many track clones, as shown in figure 4.1.1.

Hit duplication (after pulsing)

The ASD8 circuitry gave rise to the duplication of hits due to 'after pulsing'. If a strong pulse arrives at the input of the ASD8, the resulting baseline fluctuation can cause additional pulses above the threshold, which are registered as hits in subsequent bunch crossings.

This effect can be observed in the Wire Memory of the TFUs[4], where the Outer Tracker data of 128 consecutive events are stored. Figure 4.1.2 shows the probability for a hit to re-appear in the same channel in the following bunch crossing(s). If there were no after pulsing, this probability should be equal to the channel occupancy. It is significantly higher. The complete event is partially (24% for the MUON system, 10% for the Outer Tracker) copied into the next bunch crossing. This gives an overall occupancy increase and will cause also events without an interaction to be occupied by hits. This is an alternative explanation for the exponentially decreasing occupancy

[2] Amplifier-Shaper-Discriminator, digitises the raw pulses from the drift chambers

[3] Off-line, such oscillations can be identified on an event-by-event basis, since they yield a large number of synchronous hits within one ASD8 group (16 channels). An algorithm that discards all hits with drift times that are within 3 ns (6 TDC counts) identical to the drift times of three or more other hits within the same ASD8, can suppress the noise level by more than 95%. This event-by-event noise suppression rejects only 2% of signal hits and is therefore significantly more efficient than switching noisy channels off for the entire run, as was done by default.

[4] A recent upgrade of the FCS allows this to be studied off-line too

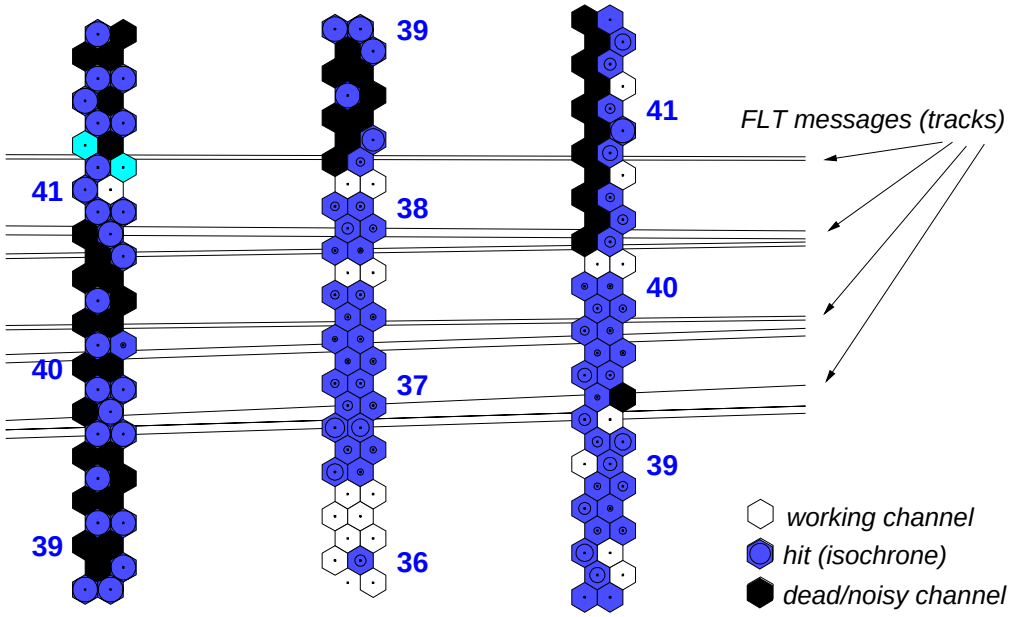

Figure 4.1.1: *Example of FLT message multiplication due to Outer Tracker noise. Shown is a part of superlayer TC1 with FLT messages that were fully propagated in this event. All three stereo angles in this section suffered severely from noise caused by ASD8 oscillations. The ASD8 groups comprise 16 channels and are indicated by a number.*

in the gap of 15 empty proton bunches, that has elsewhere been interpreted as the occurrence of 'thermal neutrons' [50].

Alignment

The performance of the FLT is also affected by misalignment of detector layers. The chamber positions were determined off-line, and then used to define the position of the Wire Memory channels in the TFU. The internal alignment of the Outer Tracker chambers outside the magnet area is expected to be better than 0.5 mm [14]. The global alignment (position of the Outer Tracker w.r.t the ECAL) is accurate to about 1 mm.

If there is a global misalignment of the Outer Tracker with respect to the ECAL (or MUON), the space point of a track may be outside the search window of the incoming message. Based on our previous studies of the extrapolation efficiency of pretrigger messages (see section 3.9.3), we estimate the extrapolation efficiency to be reduced by not more than 1% due to a global misalignment.

A misalignment of three different stereo angles with respect to each other affects the FLT more severely. In such cases, the triple coincidences in the Wire Memory are possibly not of the valid types shown in figure 2.3.9.

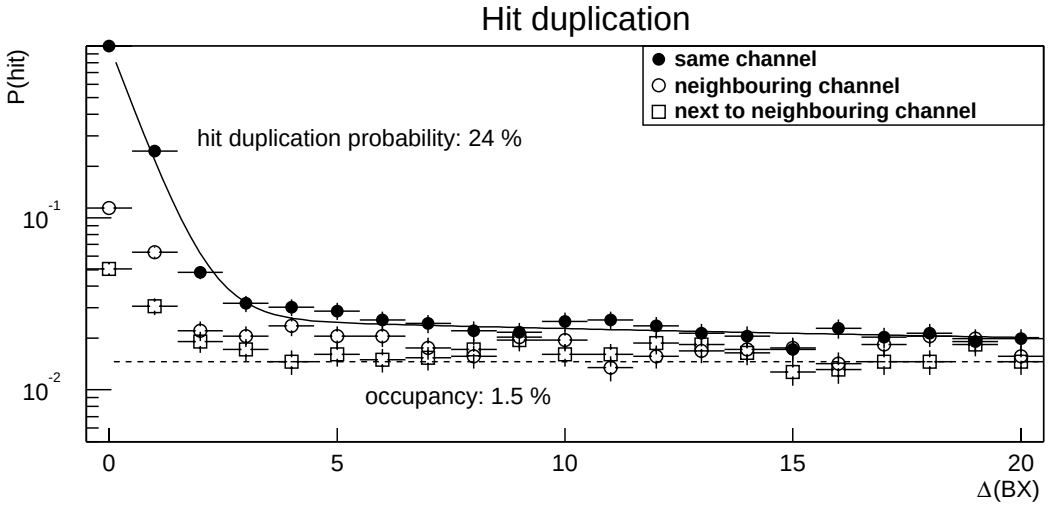

Figure 4.1.2: *Hit duplication in consecutive bunch crossings. Shown is the probability that, given a hit in a certain bunch crossing, the same hit will appear in subsequent bunch crossing. Ideally this probability would not exceed the occupancy of the detector, shown as a dashed line. It is clearly visible that at the first bunch crossings after a recorded hit, there is an increased probability of finding a hit in the same or neighbouring channels. This plot shows the behaviour of the MUON tube system, where there is a 24% probability that a hit will appear again in the next bunch crossing.*

Outer tracker performance at the end of 2000

The performance of the Outer Tracker was continuously monitored during data taking. Figure 4.1.3 summarises the status of the Outer Tracker in the period, during which the FLT was operated. The number of defective channels steadily increased to more than 15% of the total number of channels.

A dead channel cannot be circumvented by the FLT. If one of the twelve required hits is missing, the track will not be reconstructed. To prevent a reduced track finding efficiency, dead Outer Tracker channels were set on in the FLT by unplugging ASD8 cables. This was, however, only possible during an access to the detector: HV failures that appeared during running could not be directly recovered [5].

A hit is present in the Wire Memory if either of the two layers of a double layer registers a hit (see Fig.2.3.11). These two layers are connected to different HV groups. A HV failure in one of the two layers is therefore compensated by the other layer, giving only a reduced hit efficiency of 90% for the corresponding Wire Memory channels. In some cases, however, both layers were affected. Figure 4.1.4 shows that more than 3% of channels was dead. Almost 5% of the channels had been set on, giving an occupancy that exceeds the occupancy due to charged particles.

[5] This will be possible in future data taking.

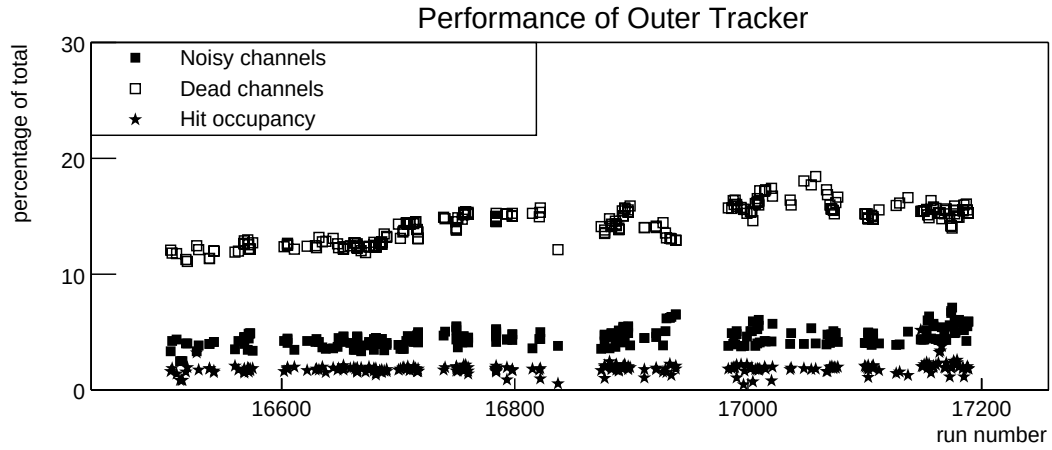

Figure 4.1.3: *Percentage of defective channels in the Outer Tracker at the end of the running period of 2000. Short term fluctuations in the number of dead or noisy channels are an artifact of the analysis, caused by a limited statistical precision in the determination.*

4.2 Performance of the data transmission

The transmission of the detector data to the TFUs of the FLT proved to be particularly problematic in 2000. Figure 4.2.1 shows the data path between the detector and the FLT. The data, collected by the TDC, are sent to the FLTLB via a flat cable, where they are re-mapped, serialised and sent to the FLT network via optical links.

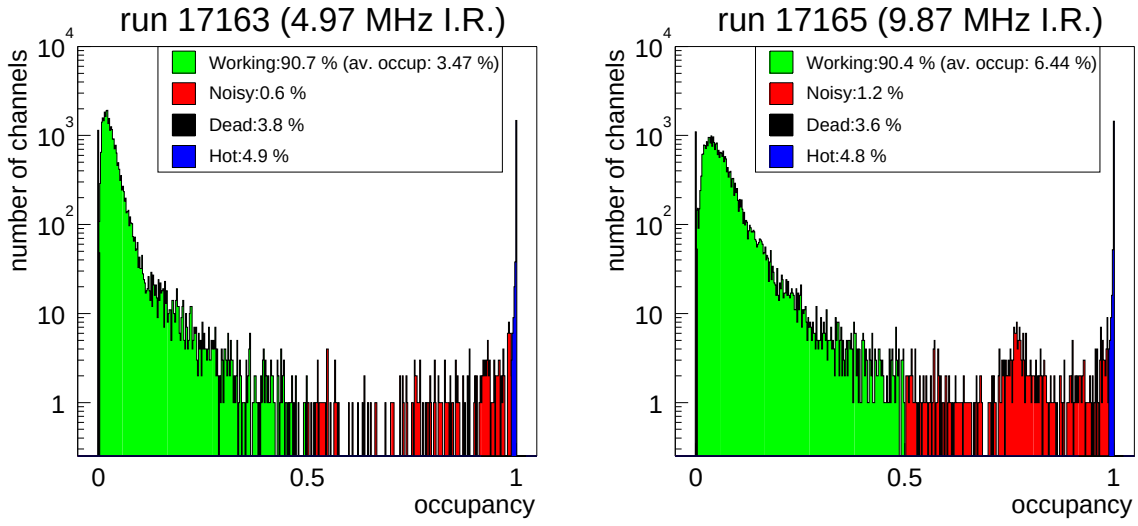

Figure 4.1.4: *Distribution of occupancies for the Wire Memory channels in a 5 MHz (left) and a 10 MHz (right) run. The average occupancy of properly working channels scales with the interaction rate, as expected. Approximately 3.6% of the channels are dead in the Wire Memory (occupancy <0.01%) and almost 5% are set on because of HV failures.*

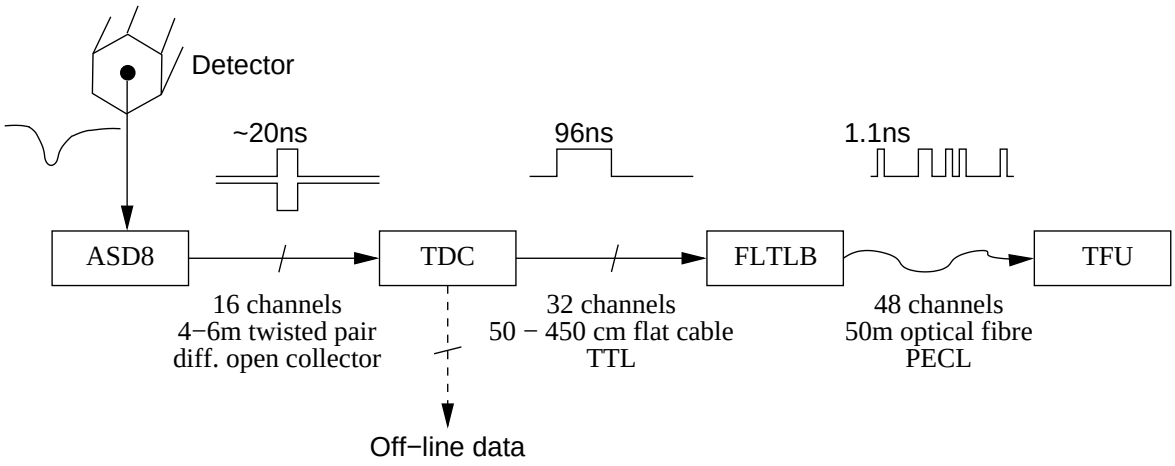

Figure 4.2.1: *Data path of detector channels to the FLT. The pulses from the drift chambers are read out by the ASD8 and then digitised by the TDC. The TDC buffer temporarily stores the drift time information, and sends hit patterns for each event to the FLTLB, where they are re-mapped, serialised and send to one of the TFUs.*

4.2.1 Connection between the TDC and the FLTLB

The TDCs of the Outer Tracker are connected to the FLTLBs by 34 pin flat cables, carrying single line TTL signals. These cables provided insufficient ground lines (only 2 for 32 signal lines) and no appropriate termination was applied. As a result, the signal arrived at the FLTLB severely distorted. The period in which the data could be reliably latched by the FLTLB was therefore small. Nevertheless, after modifying the timing of the FLTLB, the data could be properly received by the FLTLB. In the most severe case, i.e. when the data transmitted was alternating between all 32 channels on and off, all channels were correctly recorded.

However, the resulting ground fluctuations of the TDC coupled back to the analogue input from the ASD8 [51], which induced oscillations. Such noise was partially reduced by ferrite rings on the input cables, but could only be prevented by an increase of the discriminator threshold of up to 600mV.

The TTL drivers have since been removed from the TDCs, which has proven [51] to be an adequate solution for both problems. The MUON system, where no such high power TTL drivers were used, did not suffer from these problems.

4.2.2 Optical transmission

The transmission of data from the front-end of the detector to the FLT network is done by approximately 1000 optical point-to-point connections. The schematic of such a connection is shown in figure 4.2.2.

The transmitted data are normally the hit patterns from the detector, but can also be test patterns generated by the FLTLB. The data are sent in 24-bit packets, labelled with the current BX number, serialised by a Motorola Autobahn [52] IC, and subsequently driven though an optical fibre by a optical transmitter module. An

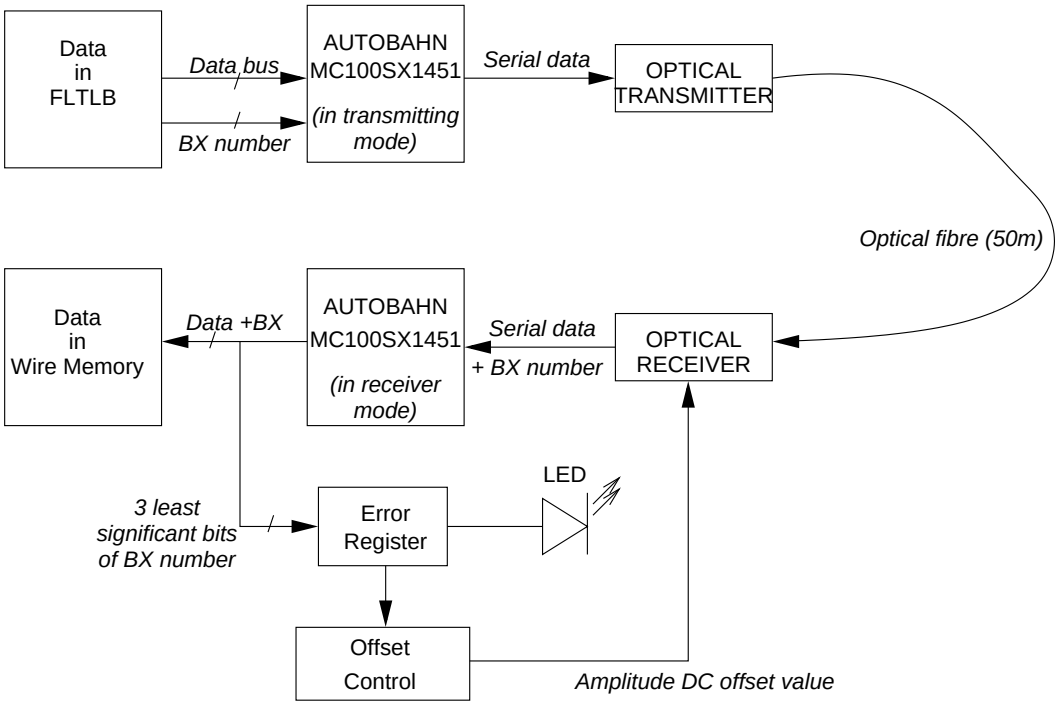

Figure 4.2.2: *Schematic of a optical point-to-point connection between the FLTLB and the TFU. The transfer of detector data to the FLT is done by approximately 1000 of these connections.*

optical receiver converts the light output back to the serial data patterns, which are then parallelised by an Autobahn in receiver mode and stored in the Wire Memory of the TFU.

The receivers are equipped with a comparator that separates the logical low and the logical high values of the signal. The offset voltage, above which the receiver considers the signal to be a logical high, can be adjusted at the receiver. The best separation of the two logical levels is achieved, when this voltage is set to the average of a logical high and a logical low. However, since the duty cycle is generally not equal to 50%, this average value cannot be readily determined. An offset control program, running on the TFU, varies the offset value and determines for each value if the detector data are received without errors[1]. The offset value is then set to the central value of the error-free offset range.

The amplitude and offset of the optical output of the transmitter can also be changed through variable resistors. Before installation of the FLTLBs, these values were tuned to a value that yielded the largest error-free range. The values could not be changed after installation. A recent upgrade [10] enables a remote adjustment of the offset and amplitude of the transmitters too.

[1] An error register counts the number of times that the three least significant bits of the BX number in subsequent data packets are not consecutive and therefore inconsistent. For each offset value the program reads the number of errors recorded by the error register in 100 ms.

Transmission tests

Each of the optical links was tested before and during installation of the FLTLBs. This test included an inspection of the optical signal on a digital oscilloscope of high sampling frequency (see figure 4.2.3) and the optimisation of the offset range. When one of the links had a narrow or no offset range, the FLTLB was not installed. In total about 40 Autobahn ICs had to be replaced due to one of the following problems:

- **Failing PLL**
  A large amount of phase jitter (wide horizontal bands in eye pattern of fig. 4.2.3 and narrow or no offset range) indicated failure of the Phase Lock Loop circuitry of the Autobahn;

- **Too low amplitude**
  The output current of the Autobahn was sometimes too low to generate optical signal of appreciable power, even after tuning or replacing the transmitter;

- **Internal bit errors**
  A few Autobahns showed internal bit errors. In such cases, the quality of the optical transmission was good, but the BX number was corrupted by the Autobahn. The error register showed inconsistent data for each offset value.

For optical links that passed the tests, a bit error rate of less than 10^{-7} was measured by sending test patterns of the FLTLB (counter or constant patterns) and verifying

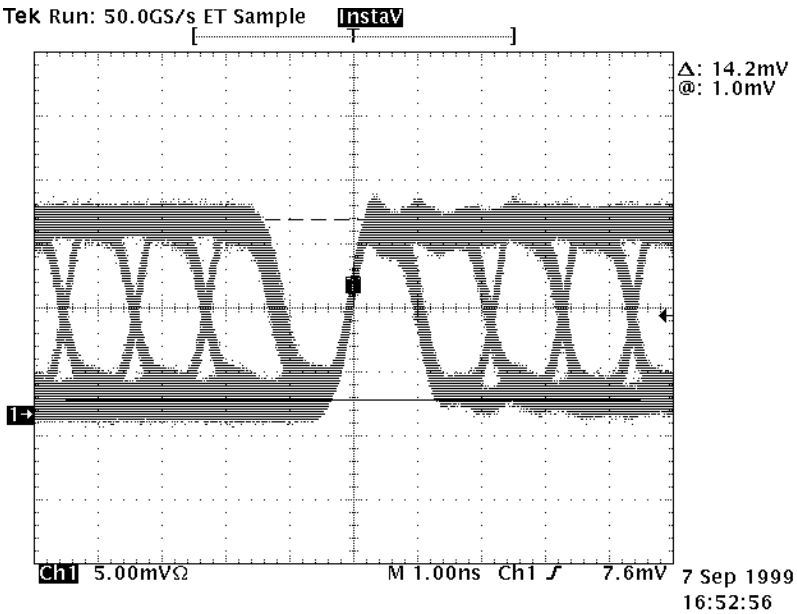

Figure 4.2.3: *Display of optical signal on oscilloscope, or 'eye pattern'. Shown is an overlay of recordings, triggered on a rising edge. The thickness of the bands show the amount of amplitude (vertical band) and phase jitter (horizontal band).*

that these patterns were correctly recorded in the Wire Memory. For links that showed a narrow or no offset range, the bit error rate was typically between 10^{-5} and 10^{-4}.

After installation some the optical connections, that were properly working when installed, became unreliable or faulty. The laser diodes on the optical transmitter were affected by a change of the environmental temperature. This could cause the amplitude of the optical signal to increase to a value that was outside of the dynamic range of the receivers. The DC offset of the signal also showed a significant dependence on the duty cycle of the transmitted data. A few of the Autobahn chips of the FLTLBs stopped working altogether.

Before each run, bad optical links were identified by the offset control program of the TFU. Figure 4.2.4 shows the percentage of malfunctioning optical links in the end of the running period in 2000. This number fluctuated around 4% for the Outer Tracker chambers. The optical connection from the MUON chambers was better, possibly due to a more constant environmental temperature. The corresponding 48 channels in the Wire Memory of malfunctioning links were usually set on. This prevented a reduced FLT efficiency, at the expense of increased occupancies and trigger message rates.

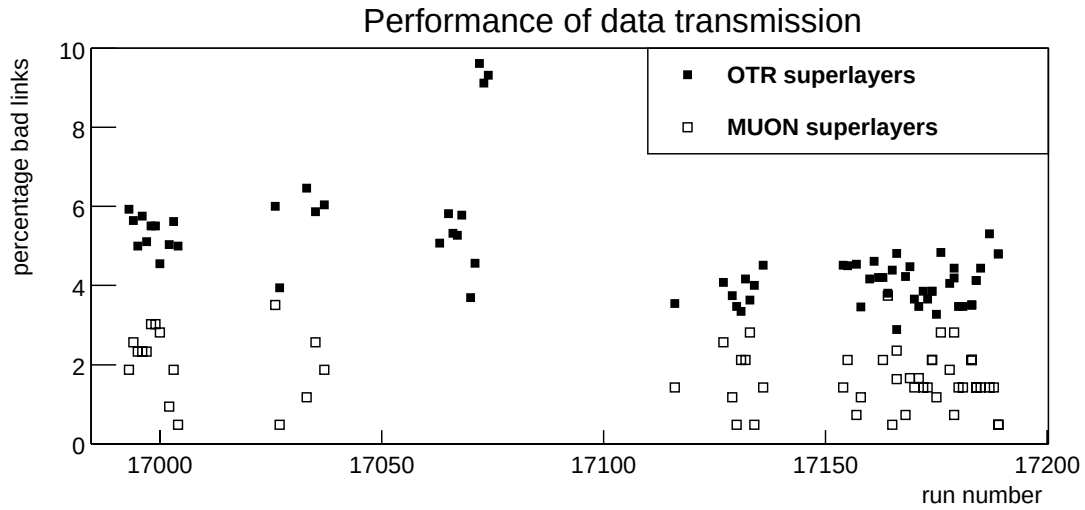

Figure 4.2.4: *Percentage of bad optical links vs. run number, for the MUON system and OTR system separately. The average of 4% corresponds to about 40 links in total. The optical links in the MUON system behaved significantly better than those of the Outer Tracker, possibly due to better cooling conditions.*

4.2.3 Channel mapping

After installation, the transmission of the full data path from TDC to the TFU was tested by comparing the content of the Wire Memory of the TFU to the Wire Memory as reconstructed from off-line data. This comparison not only shows the discussed transmission errors, but also reveals broken pins on TDC or FLTLB connectors, damaged or badly plugged cables, swapped optical fibres and errors in the mapping of OTR channels to Wire Memory channels.

Ideally, such a comparison is done for identical events. The data in the Wire Memory of the TFU should then be exactly the same as those reconstructed off-line. This was not possible in 2000. The comparison was done on a statistical basis, i.e. by checking that the channel occupancy of the Wire Memory is correctly reproduced off-line, an example of which is shown in Fig. 4.2.5.

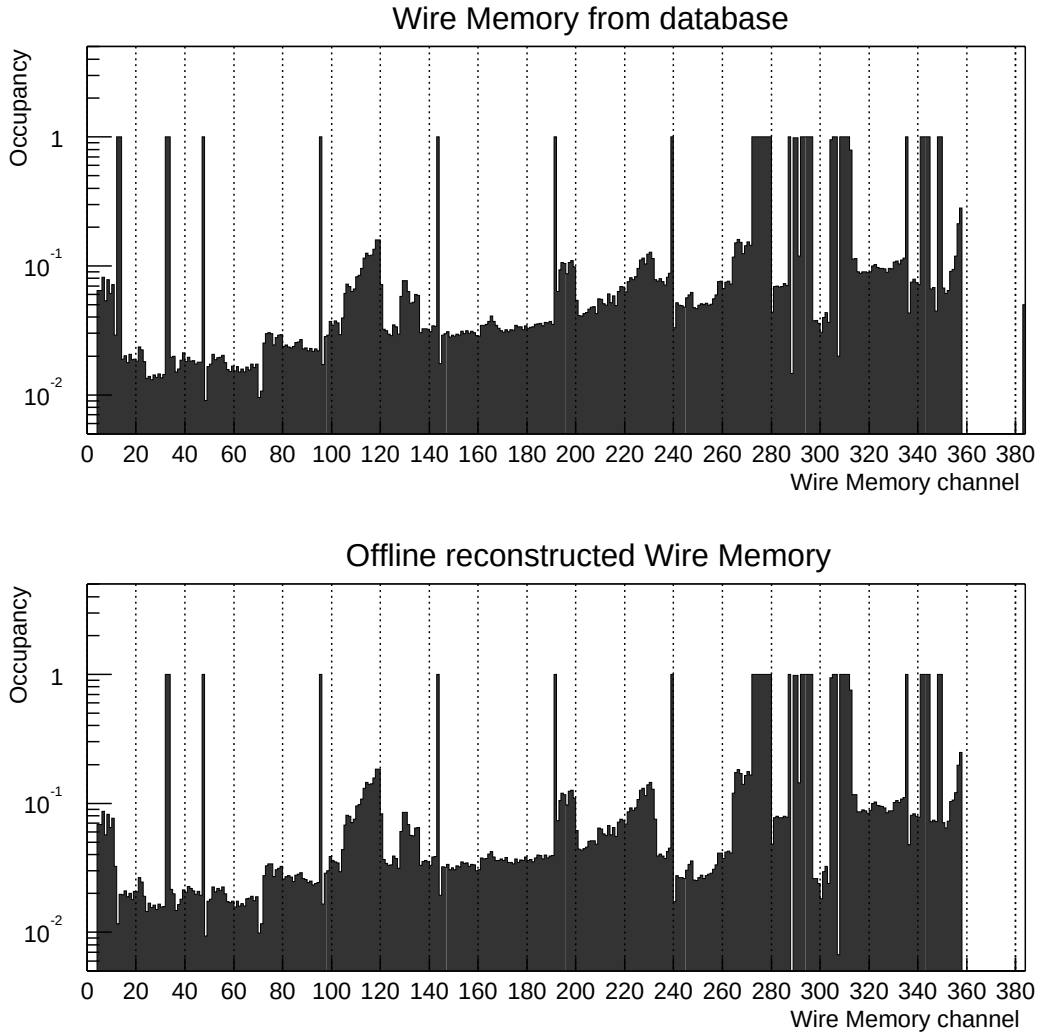

Figure 4.2.5: *Wire Memory channel occupancy in a TFU (TFU 20, positive degree) and reconstructed off-line (below). The occupancy in the TFU is stored in the database in the beginning of each run. To increase the statistical precision, all runs between 17000 and 17200 are used for this plot. The off-line reconstructed Wire Memory occupancy is determined from minimum bias events in a 5 MHz run. A discrepancy is visible for channels 12 and 13. This can be caused by a broken pin on a TDC output or FLTLB input connector.*

This test was performed for all TFUs [10]. Approximately 1.5% of the Outer Tracker channels [10] were not properly stored in the Wire Memory. No errors were found in the MUON system, where the channel mapping is considerably simpler.

The method of comparing occupancies, however, is not sensitive to transmission errors that occur at low frequency, or to corrupted BX numbers. Such errors would directly show up in an event-by-event comparison. In future running the event-by-event comparison will be possible, providing better diagnostics on the performance of the complete data transmission chain.

4.3 Performance of the FLT network

The performance of the FLT processor network is studied in a similar manner as was previously done for the ECAL pretrigger alone (section 3.4). We analyse runs, in which the FLT was operating but not necessarily triggering events. Up to 24 messages found by the FLT network (if any) were stored in the off-line data stream. An emulation of the FLT is executed on the same events, and the messages found by the hardware are compared to the messages reconstructed by the emulation.

We had already observed that 5% of the recorded ECAL pretrigger messages were not reproduced by the simulation exactly. If the pretrigger messages are not equal, then neither will the fully propagated FLT messages be. Problems with data transmission, errors in the mapping or cabling and errors in the FLT network will lead to further dissimilarities.

4.3.1 Emulation of the FLT

The emulation of the FLT, called FasSim, performs operations that are bitwise identical to those of the hardware. It uses the same set of functions that are used to generate the lookup tables for the FLT processors. An arbitrary FLT network can be simulated by defining the TFUs and their connections.

In each event the Wire Memory content of the TFUs is reconstructed from the off-line data. Figure 4.3.1 shows the distribution for the Wire Memory channel occupancy for the runs 17163 and 17165 as reconstructed off-line. These distributions are to be compared with the online occupancies of figure 4.1.4. There are some significant differences between the online and off-line reconstructed Wire Memory:

- **Number of hot channels**
  The setting on of the malfunctioning optical links has increased the number of hot channels in the Wire Memory by 4%. These channels were also set on in the hardware, but not included in figure 4.1.4.

- **Number of dead channels**
  Almost 4% of the channels were found to be dead in the hardware, whereas this is 2.0-2.5% in the off-line reconstructed Wire Memory.

- **Occupancy of working channels**
  The data in these runs were recorded on a SLT accept. Events without an interaction were rejected, and the SLT favoured events with high occupancy, possibly containing multiple interactions. The average occupancy of the working

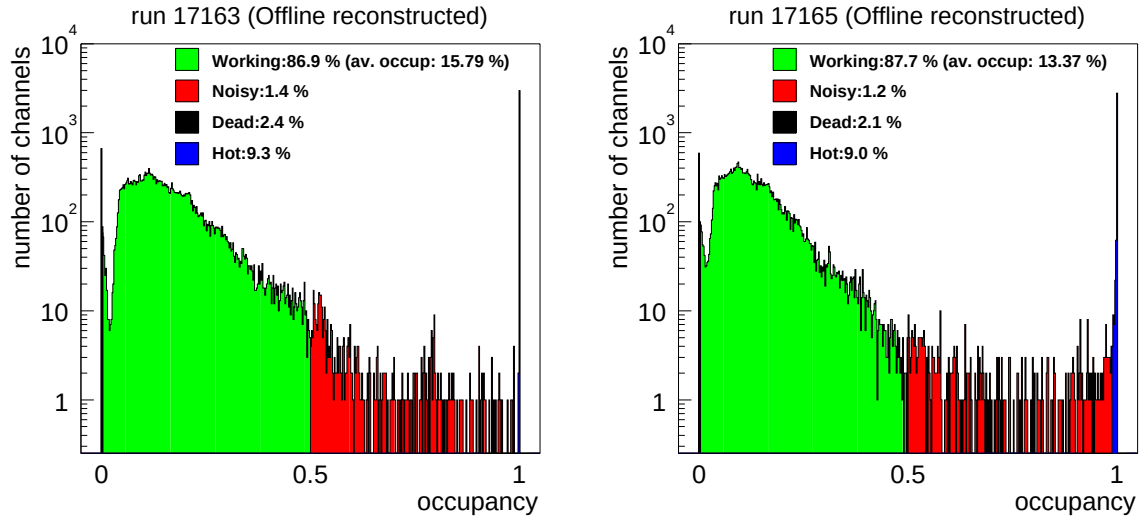

Figure 4.3.1: *Distribution of occupancies for the Wire Memory channels in a 5 MHz (left) and a 10 MHz (right) run. The average occupancy of properly working channels scales with the interaction rate, as expected. Approximately 3.6% of the channels are dead in the Wire Memory (occupancy <0.01%). Channels that were set on because of HV problems give an occupancy increase of almost 5%.*

channels was about 15%. The overall occupancy, including the hot channels was almost 25%, which approximately corresponds to the average occupancy for an interaction rate of 40 MHz. Surprisingly, the occupancy in triggered events is independent of the interaction rate.

Simulated pretrigger messages are processed by the simulation in an identical manner as by the hardware. FasSim keeps track of all messages that are propagated (partway) through the network in a hierarchical structure. These (intermediate) messages can then be analysed further. Even the individual pipeline steps of a given processor board can be executed one at a time, for an in-depth analysis of the FLT performance.

The FLT simulation can also be used on Monte Carlo simulated events, using DAQIF [53] to emulate the readout electronics. In this way, one can determine the efficiency of the FLT for specific decays, such as $J/\psi \rightarrow e^+e^-$.

4.3.2 Comparison of recorded and simulated messages

Figure 4.3.2 shows the results of the comparison between messages from the FLT simulation and the hardware for run 17243. We restrict ourselves to the comparison of the message variables ξ, η, $d\xi$ and P_x: other variables, such as P_y and P_z are directly related to these. We have required not more than one message in both the simulation and the hardware to prevent ambiguities or clones. If there was a message recorded, at least one fully propagated simulated message was always found, provided a pretrigger message was issued by the emulation.

Almost 99% of the simulated messages are at least similar to the message found by

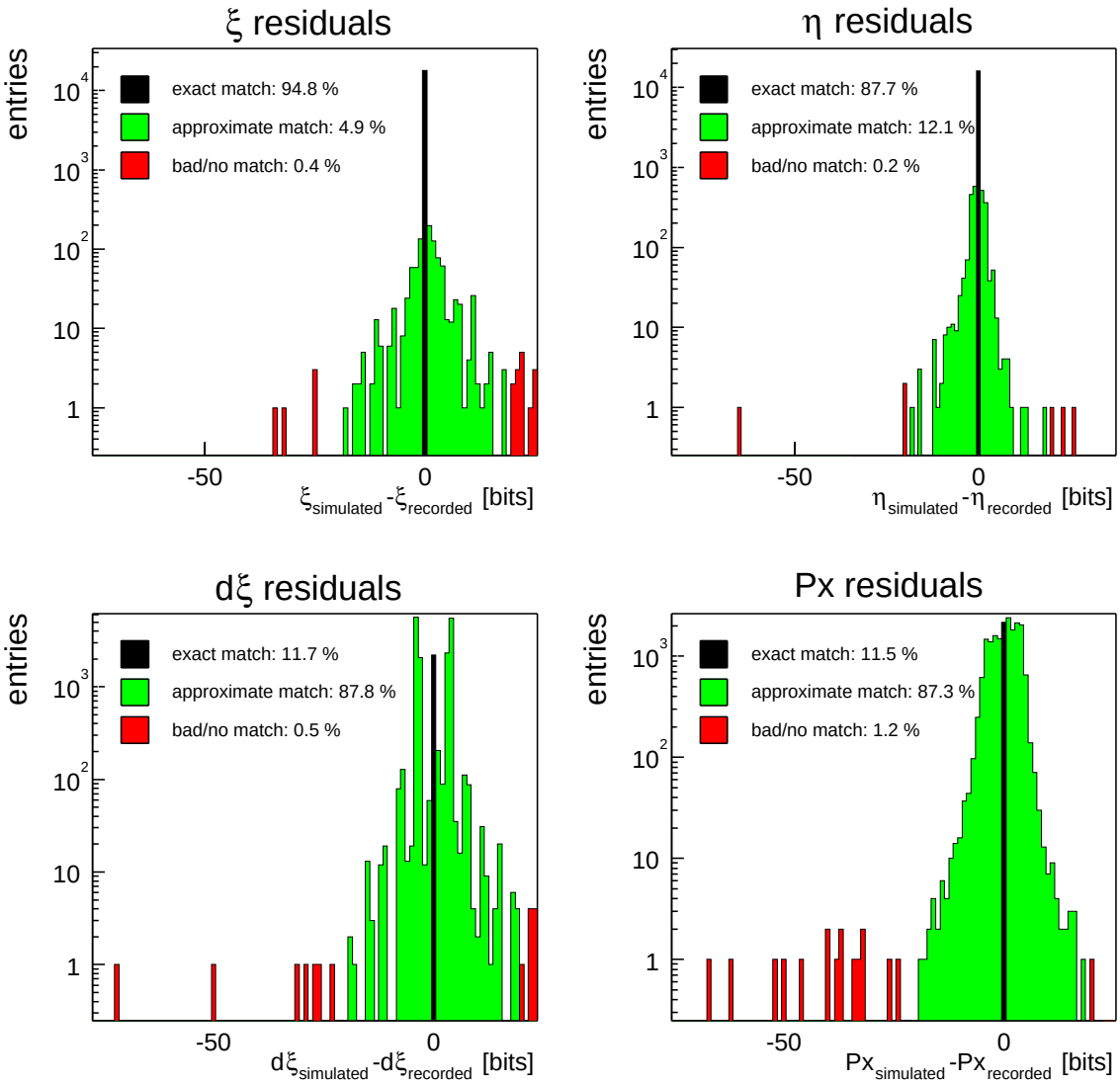

Figure 4.3.2: *Residuals between message variables of recorded messages and simulated messages. The residuals are given in multiples of the least significant bit. The percentage of exact matches (residual= 0), approximate matches (residual< 20) and bad matches (residuals≥ 20) are given for each of the parameters.*

the hardware. A window of 20 in ξ or $d\xi$ corresponds to only few cm or a few mrad, respectively. It is practically excluded that the recorded message and the simulate one did not originate from the same pretrigger cluster if they are so similar. Nevertheless, only 11% of the messages are exactly identical, as they should be.

Any differences in η can only be caused by the ECAL pretrigger, since this variable remains constant in the FLT network. It exceeds the level of errors we expect from our previous measurement of performance of the ECAL pretrigger hardware (see figure

3.4.1). The pretrigger hardware could have behaved worse for the runs studied here. Another explanation is that the ECAL calibration constants used in the simulation were slightly different from those of the hardware.

The differences in ξ, $d\xi$ and P_x are caused by the FLT network. There are several effects that could cause the simulated messages to be different from the recorded ones:

- **Clone rejection by the TPU**
  Since it is not possible to emulate in which order the messages arrive at the TPU, the clone rejection (section 2.3.3) in the simulation may discard a different track than was actually discarded by the hardware. The remaining simulated message will then only be a clone of the recorded one, with differences of typically one or two in message variables P_x and P_y. Since we have required only one simulated and only one recorded message to be found, we expect this effect to be negligible.

- **Differences in the Wire Memory positions**
  The positions of the TFU Wire Memory were regularly updated with improved alignment constants. It is probable that the Wire Memory positions in the simulation were slightly different from the values used in the hardware. Although none of the geometry files used in 2000 brings the simulation and the hardware in exact agreement, some produce clearly better results than others. Moreover, the differences in results between different positions are at least qualitatively similar to the observed discrepancies of figure 4.3.2;

- **Differences in the Wire Memory content**
  Differences in the content of the Wire Memory between the hardware and the simulation, due to cabling or mapping errors (section 4.2.3) can also give small discrepancies if clones of the true track are present. More often, however, the track finding would fail altogether;

- **Bit errors**
  If there are bit errors corrupting the message within the FLT network, it is also unlikely that the subsequent track propagation would still have been successful. The messages can only have been corrupted *after* propagation through the TFU network, for example in the transmission from the TDU to the SLT. In such cases we expect peaks in the residuals of the message variables at even powers of two. This was observed in FLT runs prior to the run under study and is illustrated in figure 4.3.3. In dedicated transmission tests no transmission errors were found within the TFU network [10];

- **Algorithmic differences**
  If the simulation would perform slightly different calculations than the actual hardware, the resulting messages would also differ. The results of a 'Vector Test' [54] practically exclude this possibility: if the Wire Memory of the hardware and that of the simulation is filled with the same hits, and the track finding is initiated with identical pretrigger messages, then the content of each pipeline cycle is identical in hardware and simulation. The resulting messages are always

exactly the same. This is the strongest evidence that the simulation is a correct emulation of the hardware and that the hardware behaves as expected;

Most of the discrepancies can be explained by differences in the Wire Memory positions or content and are not due to algorithmic differences between the simulation and the hardware. We are confident that the simulation accurately emulates the hardware, if the settings and the content of the Wire Memory are identical.

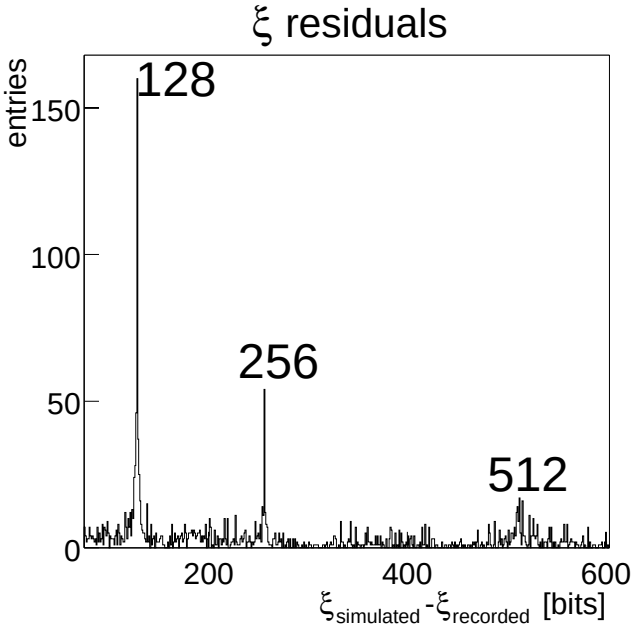

Figure 4.3.3: *Bit errors in the message variable ξ of recorded FLT messages. Clear peaks at residuals of 128 and 256 are visible, indicating bit errors caused after track propagation. The peak at 512 is not necessarily due to bit errors: here only the sign of the simulated message and that of the recorded track is different, which can occur around $x = 0$ due to small alignment differences.*

4.3.3 Efficiency of the FLT hardware

The hardware efficiency, defined as the probability that a simulated message is also found by the hardware, can be measured in runs where the FLT was operating, but not required to deliver a trigger, so-called 'FLT spy runs'. The hardware efficiency indicates to which extent the performance of the FLT has been affected by malfunctioning data transmission, bad cabling, and errors in the processing.

Table 4.3.1 shows the hardware efficiency for several FLT spy runs. We separately determine the probability for finding *any* message in the record, and the probability for finding a message that is approximately the same as that found by the simulation. For an approximate match the message variables ξ, η and $d\xi$ must be the same within a window of 20.

If there is more than one message recorded or simulated, they are usually clones, initiated by the same pretrigger message. To avoid double counting, we restrict ourselves to the first message found by the simulation.

The hardware efficiency of the complete FLT is significantly lower than the efficiency of the ECAL pretrigger alone, which, in turn, is lower than for the run studied in the previous chapter (see table 3.4.2). Furthermore, there are significant fluctuations from run to run, due to the unstable performance of the data transmission.

Run	I.R, comment, conditions	any message	matched message
17036	4 MHz	0.45(1)	0.36(1)
17037	4 MHz	0.54(1)	0.48(1)
17065	5 MHz, only -y	0.42(2)	0.29(3)
17066	5 MHz, only -y	0.55(2)	0.49(2)
17067	5 MHz, only -y	0.51(1)	0.49(1)
17068	5 MHz, pretrigger only	0.87(1)	0.84(1)
17070	5 MHz	0.54(1)	0.49(1)
17071	5 MHz	0.53(1)	0.45(1)
17072	5 MHz	0.57(1)	0.52(1)
17160	5 MHz, FLT triggered	1.00(0)	0.93(1)
17161	5 MHz, FLT triggered	1.00(0)	0.93(1)
17162	5 MHz	0.58(2)	0.54(1)
17163	5 MHz	0.40(1)	0.35(1)
17164	10 MHz		
17165	10 MHz	0.47(1)	0.38(1)
17166	15 MHz	0.40(1)	0.22(1)

Table 4.3.1: *Efficiency of the FLT hardware, defined as the probability that a simulated message was found by the hardware. All runs, except 17160 and 17161, were taken with the FLT running in 'spy mode' - operating, but not triggering. The FLT was in transparent mode for run 17068, which therefore shows the efficiency of the ECAL pretrigger hardware.*

Table 4.3.2 shows the estimated contributions to the hardware efficiency. They indicate that the known sources could account for the measured hardware efficiency of approximately 50%, although the uncertainty on the separate contributions is sizeable. The estimated FLT track finding efficiency is taken the 12th power of the channel efficiency (in "% of total").

4.3.4 Latency measurement

A positive FLT decision must be reached within 10.4 μs [55]. This leaves the Fast Control System sufficient time to notify the readout buffer, before the buffer is overwritten with new data.

The latency of the FLT is measured from the difference between the BX number of the message and the current BX number. The TDU determines this difference for all arriving messages and codes this in the message variable *BXdiff*, which gives the total latency in multiples of 96 ns[1]. It has been found that all messages with a *BXdiff* of more than 103 BX cycles are too late to be used for a trigger decision. Figure

[1]There is a constant offset to *BXdiff*, because the BX number at the TDU was not properly synchronised w.r.t. the detector.

Source	% of total	efficiency	efficiency(cumulative)
pretrigger hardware	-	0.85-0.95	0.85-0.95
mapping/cabling errors	1-2%	0.78-0.89	0.66-0.84
dead channels in hardware	1-2%	0.78-0.89	0.51-0.75
bad optical links, unmasked	0.0-0.5%	0.95-1	0.48-0.75
different geometry	-	0.96-1	0.46-0.75
TPU rejection	-	0.95-1	0.44-0.75
latency (section 4.3.4)	-	0.99-1	0.43-0.75

Table 4.3.2: *Sources contributing to the hardware efficiency of table 4.3.1. The two most important sources of inefficiency are mapping/cabling errors (see section 4.2.3) and channels that are dead in the hardware, but not off-line. The latter has been estimated from the difference between the number of dead channels found in the off-line reconstructed Wire Memory (Fig. 4.3.1) and online (Fig. 4.1.4).*

4.3.4 shows the latency of the ECAL pretrigger, and the latency of the complete FLT network including the ECAL pretrigger.

For the setup with the ECAL pretrigger alone, we estimate that the messages must arrive within a *BXdiff* of less than 60. This leaves sufficient time for subsequent processing by the FLT, and for the time needed for Bremsstrahlung recovery, which was not yet implemented in 2000.

Approximately 0.4% of all electron FLT messages arriving at the TDU have a difference in BX numbers of more than 103 and are therefore too late for triggering. This is significantly less than the 12% loss reported [10] for muon candidates. The variation in the latency is caused by fluctuations in the load of the FLT network. The number of messages processed by the FLT network increases strongly with with the occupancy. The processing of a new message is stalled by the TFU (see section 2.3.3), until each of the coincidences found inside the RoI is processed. Each new coincidence will generate a message that is later in time. Consequently, the average latency and the spread therein increases with occupancy, as shown in figure 4.3.5.

Since the messages that arrive too late are usually clones of a message that arrived in time, a trigger decision can often still be reached in time.

Most of the occupancy in 2000 was due to channels that were permanently set on, to recover HV failures or optical transmission problems. The HV failures have been solved in the meantime and also the optical transmission should be better in future running. Furthermore, there will be a multiplicity veto [41, 42] installed, that will reject events of high occupancy before they are processed by the FLT. Losses due to latency are therefore expected to be negligible for the electron channel in future running.

4.3.5 Message Rates

During data taking, the rate of incoming and outgoing messages for each of the TFUs was continuously monitored and stored in a database for later analysis. Normally,

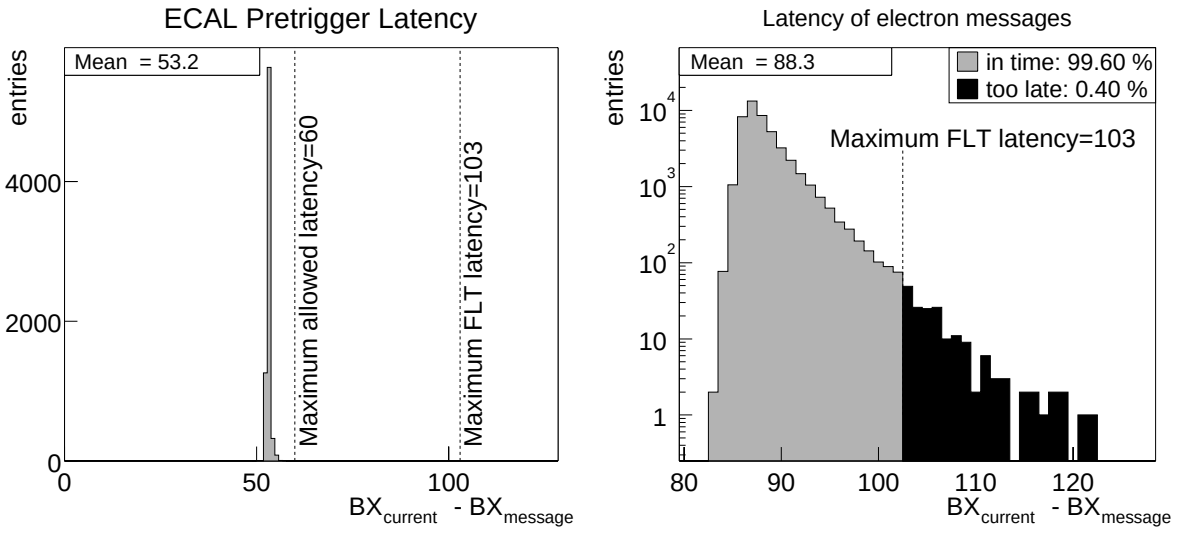

Figure 4.3.4: *Latency (in multiples 96 ns) of all messages arriving at the TDU for a run with 5 MHz interaction rate. The left figure shows the latency for the ECAL pretrigger alone and the right figure shows the latency for the full FLT network. All messages with a difference in BX of less 103 are in time to be used for a positive trigger decision. The ECAL pretrigger messages are issued on time, but a small fraction of the fully propagated FLT messages arrive at the TDU too late.*

the message rate should decrease when going from one tracking superlayer to a more downstream one: the Region of Interest is getting smaller and the probability for creating or confirming a clone of a track decreases.

In 2000, however, there were many hot regions in the Wire Memory, mostly because channels had been set on recover HV failures or malfunctioning data transmission. If a message is to be confirmed by hits near a cluster of hot channels, more than one valid

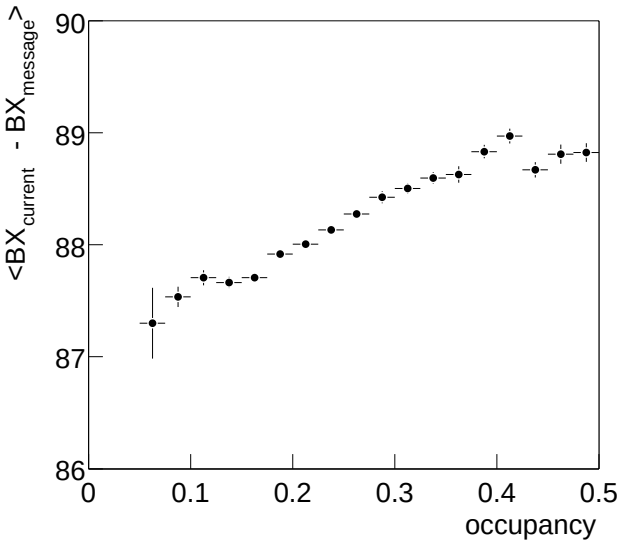

Figure 4.3.5: *Dependence of the average latency on the occupancy of the Wire Memory. The steady increase of the latency with occupancy is caused by the fact that the processing of a new message by the TFU is stalled by 20 ns for each new coincidence found inside the Wire Memory.*

coincidence will usually be found there. For each of these coincidences a new message will be constructed, leading to a multiplication of messages.

Figure 4.3.6 shows the output rate of messages at the different superlayers for three runs of 5, 10 and 15 MHz interaction rate.

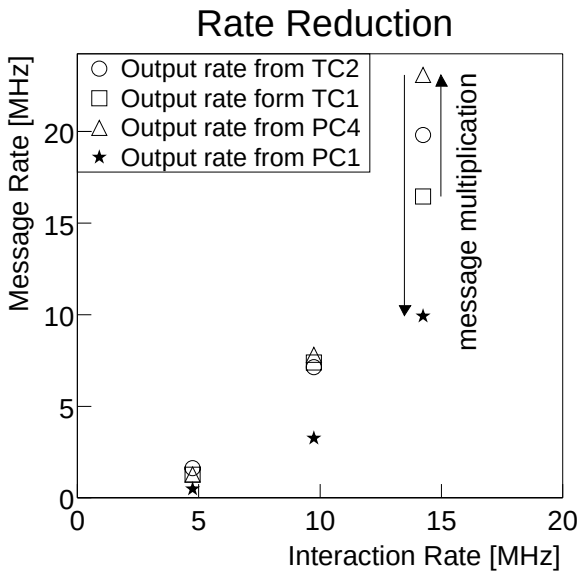

Figure 4.3.6: *Dependence of the FLT message rate on the interaction rate. Shown is the number of valid messages leaving the different superlayers for three runs of different interaction rate.*

The message multiplication exceeds the rejection of ghosts between superlayer TC1 and PC4, for interaction rates higher than 5 MHz. The strongest rate reduction is achieved at the last tracking station PC1. Here, the size of the RoI is too small to have an appreciable message multiplication.

The message rate does not scale with the interaction rate. When the interaction rate increases from 5 to 10 MHz, the rate of messages from PC1 increases from 0.48 MHz to 3.3 MHz. For each true track, there are several clones present, and the probability of creating a clone increases with occupancy. Some of them are discarded by the double track rejection of the TPU, but many are sufficiently different to pass the TPU.

The final trigger rate depends on the cuts imposed at the TPU and the TDU. Merely requiring two or more messages ('count trigger') does not bring about an appreciable rate reduction, since a message is often accompanied by a few clones that passed the TPU. Alternatively, if a mass cut ('pair trigger') is imposed at the TDU, the rate is reduced by more than an order of magnitude [56], giving a trigger rate that is acceptable for the SLT, even at an interaction rate of 20 MHz.

4.4 Resolution of the FLT

In this section we study the track reconstruction algorithm in more detail using the FLT emulation on Monte Carlo simulated events. We study the contributions to the resolution for each of the track parameters and for the momentum vector and compare the estimated resolution to the measured residuals.

4.4.1 Reconstruction of track parameters behind the magnet

A track segment in a field-free region is defined by the (x, y) coordinates at a fixed position in z and the track slopes in two dimensions, $t_x = dx/dz$ and $t_y = dy/dz$. In the FLT, the fixed z-plane is taken to be the position of the Outer Tracker superlayer TC2, $z = Z_{\mathrm{TC2}} = 1305\mathrm{cm}$.

The y position and direction t_y are not independent parameters for the FLT. The FLT assumes all tracks to have originated from a fixed point before the magnet at (0,0,0). It also assumes that the magnetic field causes no deflection in the vertical direction. The value of t_y is then determined from the y position of the ECAL pretrigger cluster,

$$t_y = \frac{y_{\mathrm{ECAL}}}{Z_{\mathrm{ECAL}}}, \tag{4.4.1}$$

and remains constant during the track reconstruction.

The purpose of the TFU network is therefore the reconstruction of x and t_x. The x position of the track is defined as the position of the hit in the zero degree layer of superlayer TC2. After a coincidence of hits is found at TC2, its value remains fixed in the further processing of the track.

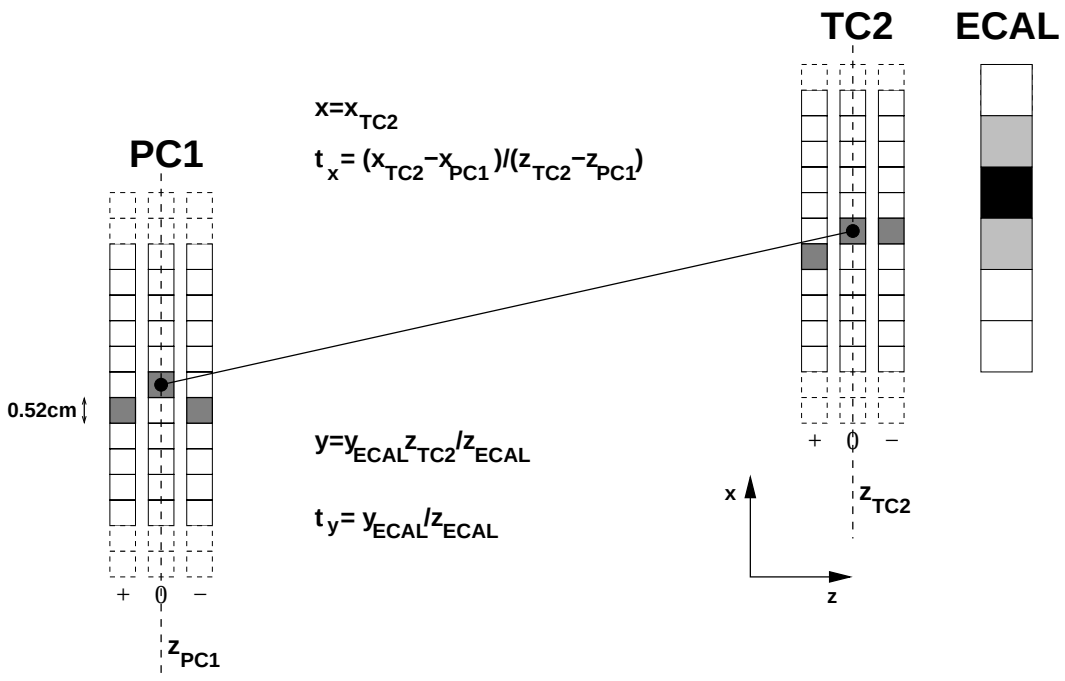

Figure 4.4.1: *Reconstruction of track parameters by the FLT. For electron candidates, the vertical position and track slope are fixed by the ECAL pretrigger cluster. The x position is the wire position of the hit in the zero degree layer of TC2. The slope is determined from this x position and the x position of a hit in PC1.*

The value for t_x is updated at each superlayer using the x position of the hit in that

superlayer. When the track is ultimately confirmed at PC1, the slope t_x is given by:

$$t_x = \frac{x_{\mathrm{TC2}} - x_{\mathrm{PC1}}}{Z_{\mathrm{TC2}} - Z_{\mathrm{PC1}}}. \tag{4.4.2}$$

Calculation of the momentum vector

For all fully propagated tracks, the TPU calculates the momentum vector at the origin from the track parameters behind the magnet. This momentum vector is given by the longitudinal momentum p_z, and the track slopes before the magnet:

$$\hat{p}_x \equiv \frac{p_x}{p_z}; \tag{4.4.3}$$

$$\hat{p}_y \equiv \frac{p_y}{p_z}. \tag{4.4.4}$$

Since the tracks are assumed not to have been deflected in the vertical direction:

$$\hat{p}_y = t_y. \tag{4.4.5}$$

In the horizontal (bending) plane, the extrapolation of the track segment before the magnet and that of the track segment behind the magnet coincide in the middle of the magnet[1], $z_{\mathrm{MAGNET}} = 450$ cm . The slope before the magnet $\hat{p}_x$ is therefore given by:

$$\hat{p}_x = \frac{x_{\mathrm{TC2}} - t_x(Z_{\mathrm{TC2}} - Z_{\mathrm{MAGNET}})}{Z_{\mathrm{MAGNET}}}. \tag{4.4.6}$$

The longitudinal momentum p_z is determined from the deflection angle $t_x - \hat{p}_x$. The HERA-B magnetic field is approximately uniform and attributes a p_T kick of 0.640 GeV/c in horizontal direction:

$$p_z \approx \frac{0.640 \text{ GeV/c}}{t_x - \hat{p}_x}. \tag{4.4.7}$$

The TPU takes into account small corrections to this relation due to non-uniformities of the HERA-B magnetic field. A measured field map is used to relate p_z to values for x and t_x,

$$p_z = p_z(x, t_x). \tag{4.4.8}$$

4.4.2 Contributions to the track resolution

The necessary simplifications of the track reconstruction algorithm leads to

- **Hit resolution**
  Since the FLT does not use drift times, the uncertainty in the x position is given

[1] The middle of the magnet is the z position for which the particle has traversed half of the integrated magnetic field

by the spatial extent of the Wire Memory channel, which corresponds to the size of one Outer Tracker cell or four Inner Tracker strips:

$$\sigma_x^{\text{cell}} = \begin{cases} 0.12 \text{ cm } /\sqrt{12} & = & 0.035 \text{ cm} & \text{(Inner Tracker)} \\ 0.52 \text{ cm } /\sqrt{12} & = & 0.15 \text{ cm} & \text{(Outer Tracker, 5mm)} \\ 1.04 \text{ cm } /\sqrt{12} & = & 0.30 \text{ cm} & \text{(Outer Tracker, 10mm)} \end{cases} . \quad (4.4.9)$$

This resolution is better than the spatial resolution of the ECAL pretrigger cluster (table 3.6.2), which is the reason that the FLT uses the hit at TC2 and not the cluster coordinate to determine x.

- **Binning effects**
  Depending on the required precision, 7 to 10 bits are used to encode a track parameter in one of the message variables of table 2.3.1. Each of the coding functions is adjusted to the cell resolution.

- **Alignment**
  The FLT is more sensitive to misalignment of detector chambers than an off-line track reconstruction. Off-line, each Outer Tracker or MUON chamber module of 32 cells can be individually positioned. This is not possible in the FLT, which assumes all channels within one TFU to be contiguous and equidistant. A non-uniform cell spacing can arise from gaps between two Outer Tracker or MUON modules.[2]

The resolution also depends on external influences, which would equally affect any track reconstruction algorithm:

- **Multiple scattering**
  A particle, traversing a medium of thickness X and radiation length X_0, is deflected due to Coulomb scattering off the nuclei. The average deflection $\Delta\theta$ is inversely proportional to the momentum of the particle[6]:

$$\Delta\theta^{\text{M.S.}} = \frac{0.0136 \text{ GeV}}{p}\sqrt{\frac{X}{X_0}}\left[1 + 0.038 \ln\left(\frac{X}{X_0}\right)\right] \quad (4.4.10)$$

  The horizontal slope of an FLT track (Eq. 4.4.2) is affected by the material in between PC1 and TC2, summarised in table 4.4.2. The vertical slope is affected by the material between the target and the ECAL, amounting to approximately a full radiation length.

- **Energy loss**
  Energy losses due to Bremsstrahlung before or inside the magnet, which were discussed in section 3.8, lead to a systematic underestimation of the momentum of electrons. The spread in this energy loss worsens the momentum resolution.

[2]Such gaps can be corrected by enlarging the cell pitch of the Wire Memory, spreading the total size of the gaps over all Wire Memory cells. In the MUON system such gaps were identified and pitch corrections of up to 5 percent were applied[57]. No such corrections have been done for the Outer Tracker TFUs.

PC1	PC2	PC3	PC4	RICH	TC1	TC2
0.0418	0.0391	0.0391	0.0417	0.1804	0.0355	0.0355

Table 4.4.1: *Thickness of detector superlayers (in X_0) between the first (PC1) and the last (TC2) point of an (electron) FLT track.*

4.4.3 Monte Carlo simulation

For the measurement of the resolution and efficiency of the FLT a sample of 50000 Monte Carlo generated $J/\psi \rightarrow e^+e^-$ decays is used. We have simulated two different detector setups, which are summarised in table 4.4.2.

	2000 Monte Carlo	2002 Monte Carlo
ECAL pretrigger coverage	run 17163	complete ECAL
ECAL calibration	run 17163	ideal
OTR cell efficiency	90%	98 %
OTR noise	0.5%	0.1 %
OTR cross talk	2%	1 %
Inner Tracker included	no	yes
FLT links, masked on	37 (run 17163)	0

Table 4.4.2: *Parameters used for the digitisation of Monte Carlo events. We have defined two setups: the 2000 setup is a simulation of the achieved detector performance; the 2002 setup reflects expectations for future running.*

The '2000 Monte Carlo' is a simulation of the achieved detector performance, which takes into account detector coverage, cell efficiencies, noise, link masking, etc. The '2002 Monte Carlo' is an estimate of the detector performance that could be achieved in the next data taking period.

We have simulated chamber misalignment implicitly by generating the hits at the nominal (Monte Carlo) positions and filling these hits on Wire Memory positions used for data. The difference between the two positions is a typical value for the measured chamber displacements. Since a TFU sector comprises a large area of the detector coverage, the uncertainty in a cell position is of the same order of magnitude as these displacements. We will later confirm the accuracy of the simulated misalignment by comparing the residuals between off-line tracks and FLT tracks in data and in Monte Carlo.

The resolution is measured from residuals of reconstructed track parameters and the values of the Monte Carlo 'truth'. The Monte Carlo reference values of the momentum vector before the magnet ($\hat{p}_x$, $\hat{p}_y$, p_z) are the values generated by PYTHIA. The reference track parameters behind the magnet (x, t_x, y, t_y) are obtained from an impact point of the track at superlayer TC2. The latter are therefore also affected by interactions with the detector material, such as energy loss and multiple scattering.

The Monte Carlo events were processed by the ECAL pretrigger and FLT emulations. The track parameters and momentum vector of the FLT are obtained by de-coding the message found by the simulation. The track parameters behind the magnet are obtained from the variables ξ, η, $d\xi$ and $dd\xi$. The momentum vector $(\hat{p}_x, \hat{p}_y, p_z)$ is obtained from the TPU message variables P_z, $\hat{P}_x$ and $\hat{P}_y$.

4.4.4 Track parameter resolution

Resolution of the x position at TC2

The resolution of the x coordinate at the reference position $z = \mathrm{Z_{TC2}}$ consists of three independent contributions:

$$\sigma_x = \sigma_x^{\mathrm{cell}} \oplus \sigma_x^{\mathrm{binning}} \oplus \sigma_x^{\mathrm{align}}. \tag{4.4.11}$$

(i) σ_x^{cell}
The hit resolution of a FLT channel is given by Eq. 4.4.9.

(ii) $\sigma_x^{\mathrm{binning}}$
The x position at TC2 is coded in the message variable ξ, for which 10 bits are allocated. The granularity for this coding reflects the cell sizes. It is shown in figure 4.4.2 with the resulting resolutions.

Region	#bins	bin size	resolution
|x|<23.0 cm	192	0.12 cm/bit	0.035 cm
23.0<|x|<78.5 cm	320	0.433 cm/bit	0.125 cm
78.5<|x|<189.3 cm	448	0.866 cm/bit	0.250 cm
189.3<|x|<300.2 cm	512	1.732 cm/bit	0.500 cm

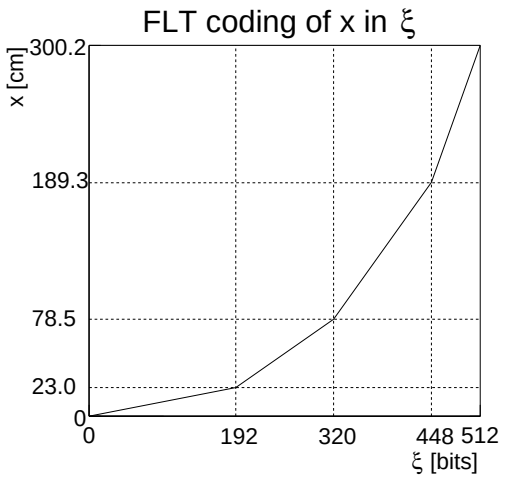

Figure 4.4.2: *Coding of x coordinate at TC2 in the message variable ξ. Once determined by a TFU at TC2, ξ remains fixed in the tracking. Here only positive values for x are shown; the sign of x is given by the most significant bit of ξ.*

(iii) $\sigma_x^{\mathrm{align}}$
This gives the uncertainty in the x position due to detector misalignment. As discussed in section 4.4.3, we have simulated a detector misalignment in the Monte Carlo. As x is completely determined by the position of one hit in TC2, any

misalignment will directly enter in the measurement of x. A misalignment causes a shift of the average residuals. Since the different regions (quadrants) will have different shifts, they will give also a broader residual distribution when added. We can estimate the contribution of misalignment by comparing the residual distributions for one quadrant of the detector to those for all four quadrants combined.

Figure 4.4.3 shows the residual distributions for only the ($+x$,$+y$) quadrant for each of the regions in x. The resolutions, summarised in table, 4.4.3 are in agreement with the expectations from binning and cell sizes. The results for all four quadrants combined are also given.

The contribution to the resolution from misalignment is estimated in Monte Carlo as the quadratic difference between this resolution and the resolution measured in one quadrant. It is seen that the average chamber displacements and gaps between chambers give a dominant contribution to the resolution in x, except in the outermost ($|x| > 189.3$cm) region.

	|x|<23.04 cm	23.04<|x|<78.5 cm	78.5<|x|<189.3 cm	|x|>189.3 cm
$\sigma_x^{\text{binning}}$	0.035 cm	0.125 cm	0.25 cm	0.5 cm
σ_x^{cell}	0.15 cm	0.15 cm	0.15 cm	0.3 cm
total	0.15 cm	0.20 cm	0.29 cm	0.58 cm
1 q.	0.19(2) cm	0.20(1) cm	0.30(2) cm	0.58(3) cm
all q.	0.36(2) cm	0.31(1) cm	0.49(1) cm	0.69(4) cm
σ_x^{align}	0.31(3) cm	0.23(1) cm	0.39(2) cm	0.37(5) cm

Table 4.4.3: *Contributions to the resolution in x (at TC2) of FLT tracks. The contribution from misalignment σ_x^{align} is the quadratic difference between the measured resolution in all four (x,y) quadrants, and the resolution in one quadrant.*

Resolution of t_x

After finding a space point in TC2, the purpose of subsequent tracking by the FLT is the determination of t_x. From the definition of t_x of Eq. 4.4.2 follows:

$$\sigma_{t_x} = \frac{(\sigma_{x,\text{PC1}} \oplus \sigma_{x,\text{TC2}})}{z_{\text{TC2}} - z_{\text{PC1}}} \oplus t_x \frac{(\sigma_{z,\text{TC2}} \oplus \sigma_{z,\text{PC1}})}{z_{\text{TC2}} - z_{\text{PC1}}} \oplus \sigma_{t_x}^{\text{binning}} \oplus \sigma_{t_x}^{\text{M.S.}}. \tag{4.4.12}$$

(i) $\sigma_{t_x}^{\text{binning}}$
The slope t_x is coded into the message variable $d\xi$, for which eight bits are used. The coding function has two different bin sizes:

$$t_x - x/z = \begin{cases} 0.0002 d\xi & d\xi < 96 \\ 0.0015(d\xi - 96) + 0.0192 & 96 \le d\xi < 128 \end{cases}. \tag{4.4.13}$$

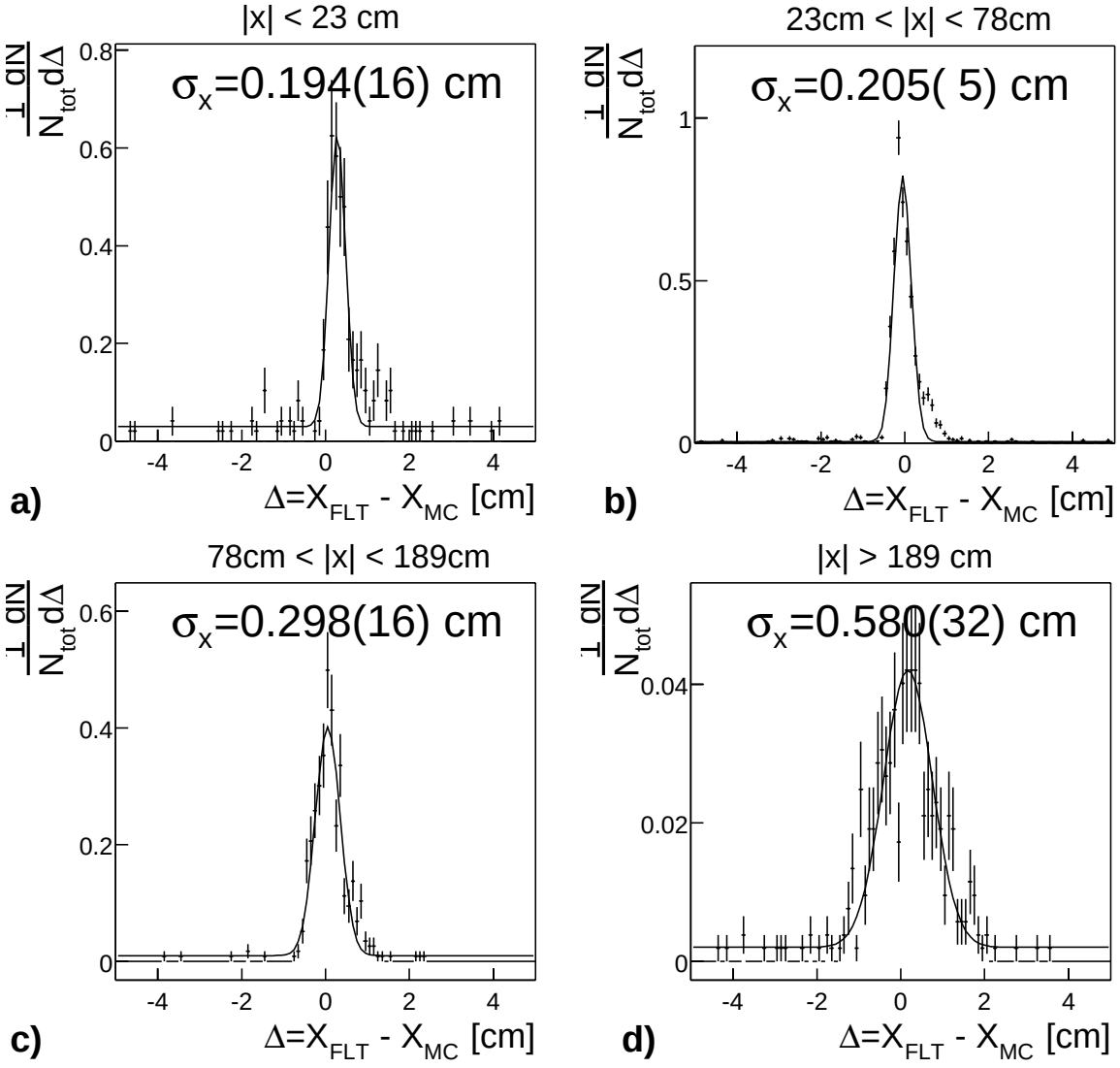

Figure 4.4.3: *Residual distributions between the x position at TC2 of FLT tracks and Monte Carlo truth. The resolution is separately measured in four regions of x.The quoted resolutions are the widths of Gaussians fitted to the distributions. For each of these distributions, only one quadrant of the detector was used, to avoid misalignment effects.*

For 95% of the messages the value of $d\xi$ is below 96, where it has a binning resolution of 0.057 mrad.

(ii) $\sigma_{t_x}^{\text{M.S.}}$
Multiple scattering in the material between PC1 and TC2 gives a momentum dependent contribution to σ_{t_x}. The slope t_x as measured from the x coordinates at PC1 and TC2 can be considered as the average direction of the track between

PC1 and TC2, so that

$$\sigma_{t_x}^{\text{M.S.}} = \Delta\theta^{\text{M.S.}}/\sqrt{2}. \tag{4.4.14}$$

Assuming that half of the material in PC1 and TC2 contributes to the resolution, we obtain a total thickness between PC1 and TC2 (see table 4.4.2) of $X = 0.3745X_0$ and consequently

$$\sigma_{t_x}^{\text{M.S.}} = \frac{0.00566 \text{ GeV}}{p} \tag{4.4.15}$$

The resolution in t_x is the quadratic sum of a constant term C and a momentum dependent term from multiple scattering:

$$\sigma_{t_x} = \frac{0.00566 \text{ GeV}}{p} \oplus C. \tag{4.4.16}$$

Since σ_x depends on x, C has different values for the different x regions of table 4.4.3.

The value of C is measured by fitting Eq.4.4.16 to the momentum dependence of the resolution. Figure 4.4.4 shows the measurement in the region $23.04 < |x| < 78.5$ as an example. The results for all four regions of x are shown in table 4.4.4 and compared to the expectations.

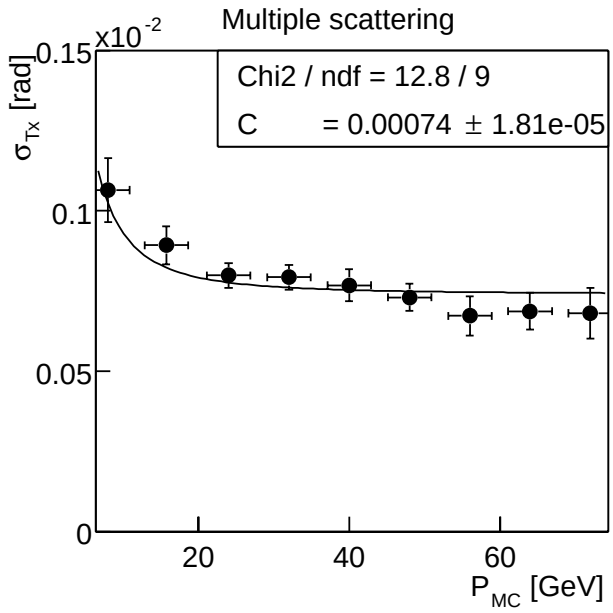

Figure 4.4.4: *Dependence of σ_{t_x} on the momentum of electron. The dependence is fitted with Eq. 4.4.16, where C was left as a free parameter. It can be seen that multiple scattering is insignificant for momenta above 20* GeV.

It is clear that σ_{t_x} is dominated by the uncertainty in the x position of the hits. Binning effects and the uncertainty in the z position of the superlayers give no significant contribution.

The simulation allows the study of the gradual improvement of the track parameter resolution during the FLT tracking. Whereas the track parameters x,y and t_y are fixed after passing TC2, t_x is constantly updated. The resolution in σ_{t_x} is inversely proportional to the distance in z to the last superlayer to TC2. Figure 4.4.5 shows that σ_{t_x} improves by approximately a factor of two at each superlayer.

	$\|x\|<23.04$	$23.04<\|x\|<78.5$	$78.5<\|x\|<189.3$	$\|x\|>189.3$
from σ_x	0.73(4) mrad	0.63(2) mrad	0.99(2) mrad	1.39(8) mrad
from σ_z	0.03 mrad	0.08 mrad	0.20 mrad	0.40 mrad
$\sigma_{t_x}^{\text{binning}}$	$\gtrsim$0.06 mrad	$\gtrsim$0.06 mrad	$\gtrsim$0.06 mrad	$\gtrsim$0.06 mrad
resulting C	0.73(4) mrad	0.64(2) mrad	1.02(2) mrad	1.5(2) mrad
measured C	0.71(3) mrad	0.74(2) mrad	1.03(2) mrad	1.6(2) mrad

Table 4.4.4: *Measurement and expectation for the momentum independent part C of σ_{t_x} (Eq.4.4.16) in different regions of x. The resolution due to the uncertainty in the x and z position of the space-points and binning effects are shown separately.*

Resolution in y and t_y

The resolution in y, and consequently for t_y, is given by:

$$\sigma_y = \sigma_y^{\text{pretrigger}} \oplus \sigma_y^{\text{FLT binning}} \oplus \sigma_y^{\Delta Z} \oplus \sigma_y^{\text{M.S.}} \tag{4.4.17}$$

(i) $\sigma_y^{\text{pretrigger}}$
The spatial resolution of the pretrigger $\sigma_y^{\text{pretrigger}}$ has been evaluated in the previous chapter (table 3.6.2).

(ii) $\sigma_y^{\text{FLT binning}}$
Although t_y (y) is not measured by the FLT network, its value is re-binned by the FLT, which affects the resolution. The coding function used for this has two different bin sizes:

$$\begin{aligned} \eta &= 20/11.15 \times y_{\text{ECAL}} \quad y < 66.9 \\ \eta &= 128 + 8/11.15 \times y_{\text{ECAL}} \quad y > 66.9 \end{aligned} \tag{4.4.18}$$

(4.4.19)

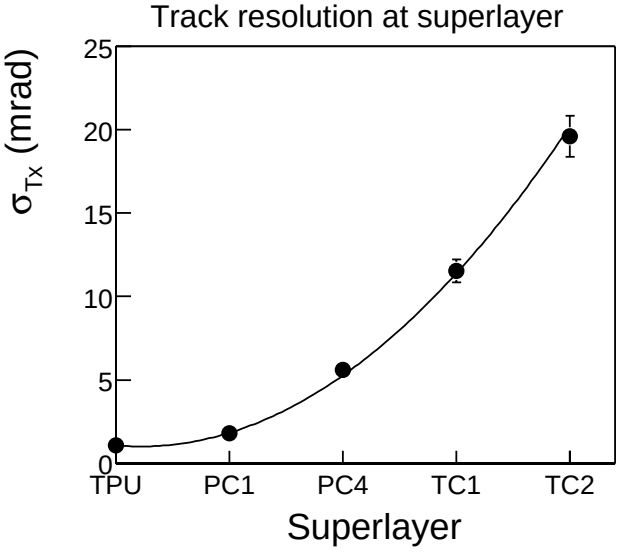

Figure 4.4.5: *Resolution of the horizontal slope of FLT for electron candidates at the various superlayers. For the messages at TC2 the uncertainty in the slope also incorporates the uncertainty in the charge of the particle.*

The most significant bit in η gives the sign of t_y. This coding function is not optimal, since values for η between 120 and 128 are not used. It has the advantage, however, that the vertical row of the central cell of the ECAL pretrigger cluster can be easily determined. The resulting resolutions are 0.16 cm (0.12 mrad) and 0.40 cm (0.30 mrad).

(iii) $\sigma_y^{\text{M.S.}}$
The contribution of multiple scattering has been evaluated for the average momentum of the electron in each of the three ECAL regions, assuming a full radiation length between the target and the ECAL (see Fig. 3.8.1).

(iv) $\sigma_y^{\Delta Z}$
The assumption that the particle originated from $(0, 0, 0)$ and that the z position of the pretrigger cluster was fixed at $z = Z_{\text{ECAL}} = 1350$ cm is the source of an additional uncertainty. It gives an error on the slope t_y of $\Delta Z / Z_{\text{ECAL}} \approx 5/1350 = 0.4\%$.

The resolutions in y and t_y for the three different regions of the ECAL are given in table 4.4.5. The quadratic sum of all contributions in y is approximately equal to the resolution measured from the residuals. In t_y, there could be an additional contribution from a non-zero deflection in the vertical direction, which was assumed to be non-existent. This could account for the fact that the measured resolution in t_y is slightly worse than expected.

	σ_y [cm]			σ_{t_y} [mrad]		
	Inner	Middle	Outer	Inner	Middle	Outer
$\sigma^{\text{pretrigger}}$	0.23(1)	0.45(1)	0.74(5)	0.17(1)	0.35(1)	0.55(4)
$\sigma^{\text{FLT binning}}$	0.16	0.40	0.40	0.12	0.30	0.30
$\sigma^{\Delta Z}$	0.04(1)	0.23(2)	0.41(2)	0.07	0.14	0.31
$\sigma^{\text{M.S.}}$	-	-	-	0.18	0.45	0.97
total	0.28(1)	0.64(3)	0.94(6)	0.29	0.66	1.20
measured	0.32(1)	0.57(3)	0.85(9)	0.39(1)	0.82(2)	1.40(4)

Table 4.4.5: *Contributions to the resolution in y and t_y of FLT tracks. The effect of multiple scattering on σ^{t_y} has been evaluated at the average momenta in that region, assuming a full radiation length of material between the target and the ECAL.*

4.4.5 Momentum and mass resolution

Resolution of $\hat{p}_x$

The horizontal slope $\hat{p}_x$ is obtained from the extrapolation of the track to the middle of the magnet (Eq. 4.4.6). The resolution in $\hat{p}_x$ consists of the following terms:

$$\sigma_{\hat{p}_x} = \frac{\sigma_x}{Z_{\mathrm{MAGNET}}} \oplus \sigma_{t_x} \oplus \sigma_{\hat{p}_x}^{\mathrm{binning}} \oplus \sigma_{\hat{p}_x}^{\mathrm{M.S.}} \oplus \sigma_{\hat{p}_x}^{\mathrm{extrapol.}} \oplus \sigma_{\hat{p}_x}^{\mathrm{E-loss}}. \tag{4.4.20}$$

(i) $\sigma_{\hat{p}_x}^{\mathrm{extrapol}}$
This is the uncertainty from the assumption that the extrapolations of the track before and after the magnet coincide at the middle of the integrated magnetic field of $Z_{\mathrm{MAGNET}} = 450$ cm . This includes also the uncertainty in the z position of the target, which is assumed by the FLT at $Z_{\mathrm{TARGET}} = 0$. We estimate the total uncertainty in the z position of the matching plane at 5 cm , which gives

$$\sigma_{\hat{p}_x}^{\mathrm{extrapol}} = \frac{5 \text{ cm}}{450 \text{ cm}} \times \langle \hat{p}_x \rangle \approx 0.4 \,\mathrm{mrad}. \tag{4.4.21}$$

(ii) $\sigma_{\hat{p}_x}^{\mathrm{E-loss}}$
Bremsstrahlung inside the magnet causes the FLT to systematically overestimate p_x/p_z. We have addressed this issue in section 3.8, where we estimated the average energy loss of electrons inside the magnet at 20%. The deflection is typically 10% less than estimated, with an uncertainty of approximately 5%, and therefore:

$$\sigma_{\hat{p}_x}^{\mathrm{E-loss}} \approx 0.05 \times (t_x - \hat{p}_x) = 0.032 \text{ GeV}/p_z. \tag{4.4.22}$$

This is actually an upper limit for $\sigma_{\hat{p}_x}^{\mathrm{E-loss}}$, since electrons that have suffered too large energy losses are implicitly rejected by the ECAL pretrigger.

(iii) $\sigma_{\hat{p}_x}^{\mathrm{M.S.}}$
The measurement of $\hat{p}_x$ is affected by multiple scattering in the material between the target and the RICH, which corresponds to $X = 0.65 X_0$ and therefore (see Eq. 4.4.10)

$$\sigma_{\hat{p}_x}^{\mathrm{M.S.}} = 0.011 \text{ GeV}/p. \tag{4.4.23}$$

(iv) $\sigma_{\hat{p}_x}^{\mathrm{binning}}$
The coding function for $\hat{p}_x$ is derived from the coding function for ξ and adjusted by a factor 0.91/300.16. Figure 4.4.6 shows this function and the resulting resolutions.

All contributions to $\sigma_{\hat{p}_x}$ are summarised in table 4.4.6. The estimated values for C are slightly larger than the measured values. This could be caused by an improper treatment of the correlations of the misalignment contributions to the resolution of x and t_x.

The combined effect of Bremsstrahlung and multiple scattering is measured from the momentum dependence of $\sigma_{\hat{p}_x}$, which is shown in figure 4.4.7. From this dependence we estimate $\sigma_{\hat{p}_x}^{\mathrm{E-loss}} = 0.017$ GeV/p.

Region	#bins	bin size	resolution
|px/pz|<0.07	192	0.36mrad/bit	0.10 mrad
0.07<|px/pz|<0.24	320	1.31mrad/bit	0.38 mrad
0.24<|px/pz|<0.57	448	2.63mrad/bit	0.76 mrad
0.57<|px/pz|<0.91	512	5.25mrad/bit	1.51 mrad

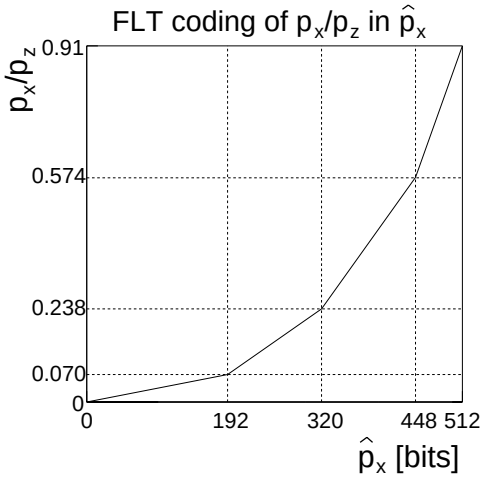

Figure 4.4.6: *Coding of the horizontal slope of the track at the target p_x/p_z in the FLT message variable $\hat{p}_x$. This function is derived from the function for ξ, shown in figure 4.4.2. The maximum of 910 mrad was not well chosen and should be set to ∼300 mrad.*

Resolution of p_z

The momentum in longitudinal direction p_z is obtained from the deflection of the particle in the magnetic field (Eq. 4.4.7). The terms contributing to the resolution in p_z are:

$$\sigma_{p_z} = \sigma_{p_z}^{\text{binning}} \oplus \sigma_{p_z}^{\text{E-loss}} \oplus \sigma_{p_z}^{\text{extrapol.}} \oplus \sigma_{p_z}^{\text{defl.angle}} \tag{4.4.24}$$

(i) $\sigma_{p_z}^{\text{defl.angle}}$
The uncertainty in t_x and $\hat{p}_x$ lead to an uncertainty in the deflection angle and,

	|x|<23.04	23.04<|x|<78.5	78.5<|x|<189.3	|x|>189.3
$\sigma_x/Z_{\text{MAGNET}}$	0.82(4) mrad	0.69(1) mrad	1.1(1) mrad	1.5(1) mrad
σ_{t_x}	0.71(3) mrad	0.74(2) mrad	1.03(2) mrad	1.6(2) mrad
$\sigma_{\hat{p}_x}^{\text{binning}}$	0.1 mrad	0.38 mrad	0.76 mrad	1.51 mrad
$\sigma_{\hat{p}_x}^{\text{extrapol}}$	0.15(1) mrad	0.21(1) mrad	0.43(1) mrad	0.72(2) mrad
$\sigma_{\hat{p}_x}^{\text{E-loss}}$	<0.032 GeV/p_z	<0.032 GeV/p_z	<0.032 GeV/p_z	<0.032 GeV/p_z
$\sigma_{\hat{p}_x}^{\text{M.S.}}$	0.011 GeV/p	0.011 GeV/p	0.011 GeV/p	0.011 GeV/p
estimated C	1.10(5) mrad	1.10(3) mrad	1.7(2) mrad	2.8(2) mrad
measured C	1.01(1)mrad	1.06(1) mrad	1.3(1)mrad	2.4(1) mrad

Table 4.4.6: *Contributions to the resolution in $\hat{p}_x$. The momentum-independent terms add up to give the estimated C. This term is measured in the Monte Carlo simulation from the residuals by requiring $p > 40$ GeV/c.*

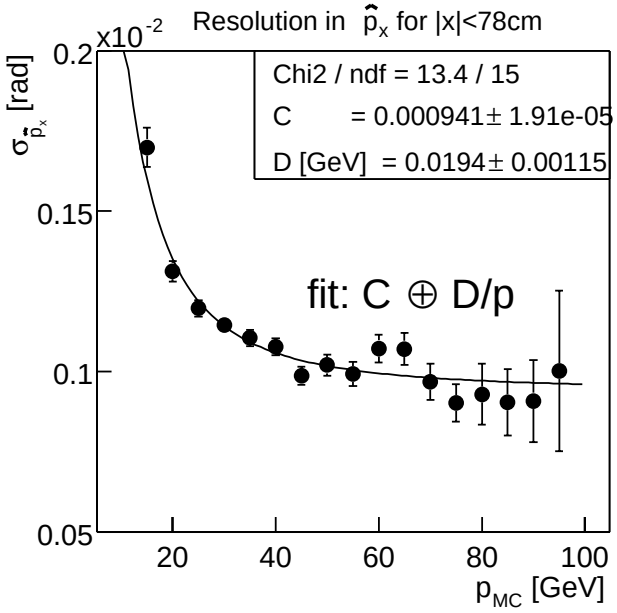

Figure 4.4.7: *Resolution in $\hat{p}_x$ as a function of the momentum. We restrict ourselves to the region $|x| < 78.5$ cm , where the momentum-independent resolution term is smallest. The momentum dependence is due to multiple scattering and Bremsstrahlung in the magnet and given by a term D/p, which is obtained from the fit.*

consequently, to an uncertainty in the momentum estimate:

$$\frac{\sigma_{p_z}^{\text{defl.angle}}}{p_z} = \frac{p_z}{0.640}\left[\sigma_{t_x} \oplus \sigma_{\hat{p}_x}\right]. \tag{4.4.25}$$

The uncertainty in the deflection angle is given in table 4.4.7 for each of the four regions in x, together with the resulting contribution to σ_{p_z}.

	$\|x\|<23.04$	$23.04<\|x\|<78.5$	$78.5<\|x\|<189.3$	$\|x\|>189.3$
σ_{t_x} [mrad]	0.71(3)	0.74(2)	1.03(2)	1.6(2)
$\sigma_{\hat{p}_x}$ [mrad]	1.01(1)	1.06(1)	1.3(1)	2.4(1)
$\frac{\sigma_{p_z}^{\text{defl.angle}}}{p_z^2}$ [10^{-3} GeV^{-1}]	1.9(1)	2.0(1)	2.6(2)	4.5

Table 4.4.7: *Momentum resolution due to the uncertainty in t_x and $\hat{p}_x$. The uncertainty in the deflection $\hat{p}_x - t_x$ leads to a term in the momentum resolution, that increases proportionally to the momentum, given in the last row.*

(ii) $\sigma_{p_z}^{\text{binning}}$

The resolution due to binning effects follows from the coding function for p_z, which reads:

$$p_z(\text{in GeV}) = \begin{cases} 200/(45-p_z) & 0 < P_z < 25 \\ 400/(65-p_z) & 25 \le P_z < 45 \\ 1600/(125-p_z) & 45 \le P_z < 125 \\ 1600 & P_z > 125 \end{cases}. \tag{4.4.26}$$

The average values of $\sigma_{p_z}^{\text{binning}}/p_z$ for the different regions of p_z are 0.785%, 1.02% and 1.4% respectively.

(iii) $\sigma_{\mathbf{p_z}}^{\text{E-loss}}$: Whereas $\hat{p}_x$ was only affected by energy losses *inside* the magnet, p_z is also affected by energy losses *before* the magnet. The vertex detector layers and the exit window of the vertex detector tank, amount to a thickness of approximately $X = 0.16X_0$. The energy loss spectrum for electrons before and inside the magnet are shown in figure 3.8.2.

(iv) $\sigma_{\mathbf{p_z}}^{\text{extrapol.}}$: This term gives the uncertainty in the relation between the momentum and the deflection in the magnet, which is measured from the track direction behind the magnet by assuming the track to have originated from (x, y, z) =(0,0,0).

We estimate this uncertainty in a Monte Carlo simulation, by measuring the width of the distribution of $p_z(\hat{p}_x - t_x)$ as shown in figure 4.4.8. We take only Monte Carlo truth values and require that the electron did not suffer any energy loss due to Bremsstrahlung. If we take the RMS of this distribution as the uncertainty in the extrapolation, it gives

$$\sigma_{p_z}^{\text{extrapol.}}/p_z = \frac{0.0355}{0.636} = 0.056. \tag{4.4.27}$$

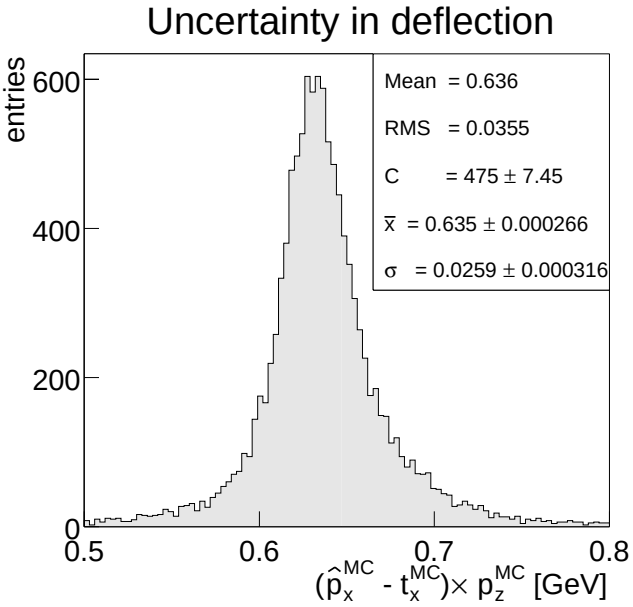

Figure 4.4.8: *Uncertainty in the relation between the deflection angle and the momentum. The momentum is inversely proportional to the deflection in the magnet, which is estimated as* $t_x - \hat{p}_x$. *The width of this distribution is a measure of the uncertainty of this momentum estimate.*

Combining all contributions, σ_{p_z}/p_z consists of a constant term, which is dominated by $\sigma_{p_z}^{\text{extrapol.}}$, plus a term that rises linearly with the momentum, which is due to the uncertainty in the deflection angle. Figure 4.4.9 shows the measured σ_{p_z}/p_z as a function of p_z for the region $x < 78$ cm. Both the constant and the slope are in agreement with the values expected from Eq. 4.4.27, respectively table 4.4.7.

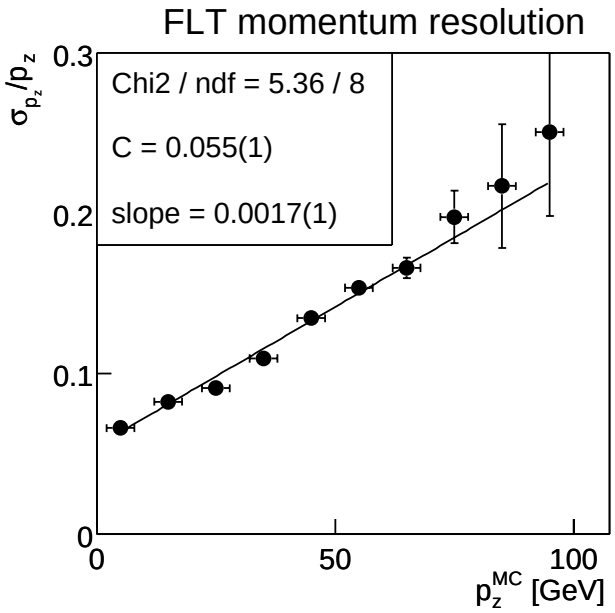

Figure 4.4.9: *Momentum dependence of σ_{p_z}. The measurement is restricted to the region $|x| < 78$ cm, where we expect the resolution to be $\sigma_{p_z}/p_z = 0.056 + 1.9(1) \times 10^{-3} p_z$, in reasonable agreement with these results.*

Mass resolution

Ultimately, the FLT calculates the invariant mass of all possible pairs of tracks of opposite charge. A mass cut would typically be executed at 2 GeV/c^2, which imposes a mild constraint on the required J/ψ-mass resolution. The momentum resolution, determined before, gives an expected resolution on the J/ψ mass of typically 200-300 MeV/c^2, which is sufficient to impose an efficient mass cut. However, in the absence of Bremsstrahlung recovery, a significant tail is present, which could lead to efficiency losses. Figure 4.4.10 shows the distribution of the J/ψ mass as reconstructed by the FLT, both with and without energy losses. Without Bremsstrahlung recovery, the efficiency of a mass cut of 2 GeV/c^2 is approximately 90%.

4.5 Track finding efficiency

The track reconstruction efficiency of the FLT is measured in data and in a Monte Carlo simulation as the probability to reconstruct an external reference track. For each external reference track a matching-χ^2 is determined from the measured track parameter residuals with all FLT tracks:

$$\chi^2 = \frac{(x^{\mathrm{FLT}} - x^{\mathrm{Ref}})^2}{\sigma_x^2} + \frac{(t_x^{\mathrm{FLT}} - t_x^{\mathrm{Ref}})^2}{\sigma_{t_x}^2} + \frac{(t_y^{\mathrm{FLT}} - t_y^{\mathrm{Ref}})^2}{\sigma_{t_y}^2}. \tag{4.5.1}$$

The optimally matching FLT track is taken to be the one with the minimum χ^2.

4.5.1 Construction of external reference tracks

The external reference tracks are constructed from clusters in the ECAL and track segments in the vertex detector. The Outer Tracker is not used, so that we are fully

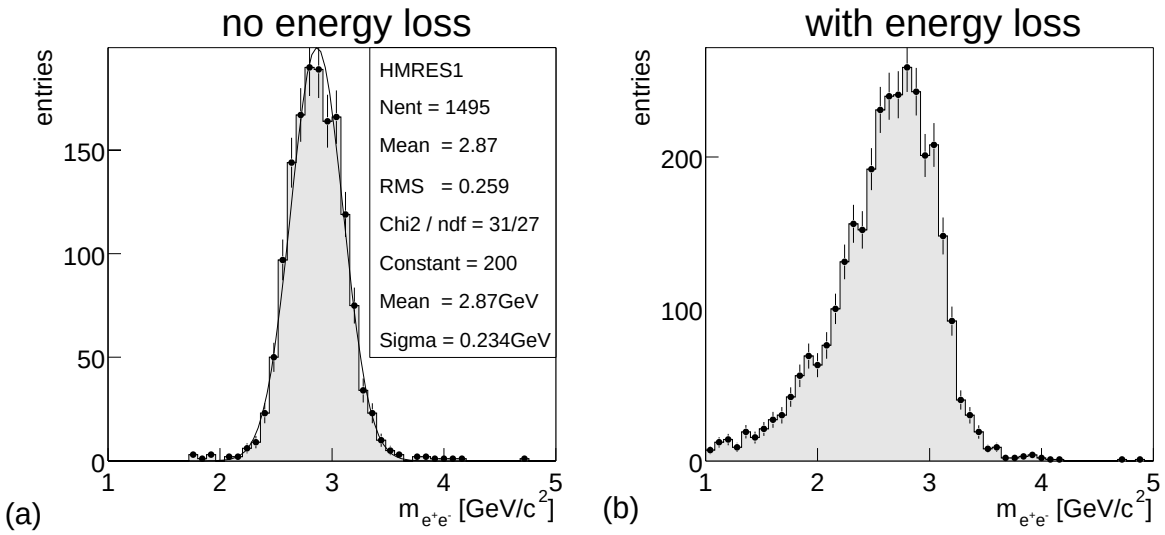

Figure 4.4.10: *Invariant di-electron mass as reconstructed by the FLT.*

sensitive (and unbiased) to the cell efficiencies of the Outer Tracker.

Track segments in the vertex detector are matched to clusters in the ECAL by requiring the difference in y between the cluster and the extrapolated vertex segment to be less than 2 cm. Furthermore, the vertex segment is extrapolated in x through the magnet, taking the reconstructed cluster energy as a momentum estimate. The residuals in x should then be less than 7 cm.

To remove possible fake matches, we also require a ring reconstructed in the RICH, for which the corresponding track directions are within 2 mrad equal to the slopes of the extrapolated track segment. The clusters must have a transverse energy of more than 1 GeV, a cut that is identical to the one imposed on pretrigger clusters.

The track parameters behind the magnet (x, y, t_x, t_y) are the parameters from the extrapolated vertex segment at tracking station TC2. The total momentum is determined as the momentum for which the extrapolated vertex segment coincides with the x coordinate of the ECAL cluster. The momentum vector is calculated from the total momentum and the direction of the track segment in the vertex detector.

Track parameters residuals

The track parameter resolution of the external tracks, measured from the residuals with the Monte Carlo reference, is shown in table 4.5.1

σ_x(cm)	σ_y(cm)	σ_{t_x} (mrad)	σ_{t_y} (mrad)	σ_{p_z}/p_z	$\sigma_{\hat{p}_x}$ (mrad)	$\sigma_{\hat{p}_y}$ (mrad)
0.259(4)	0.239(4)	0.611(9)	0.565(19)	0.0355(5)	0.378(9)	0.295(5)

Table 4.5.1: *Track parameter and momentum resolution of reference tracks. To avoid multiple scattering effects, the tracks are required to have a momentum of more than 40* GeV.

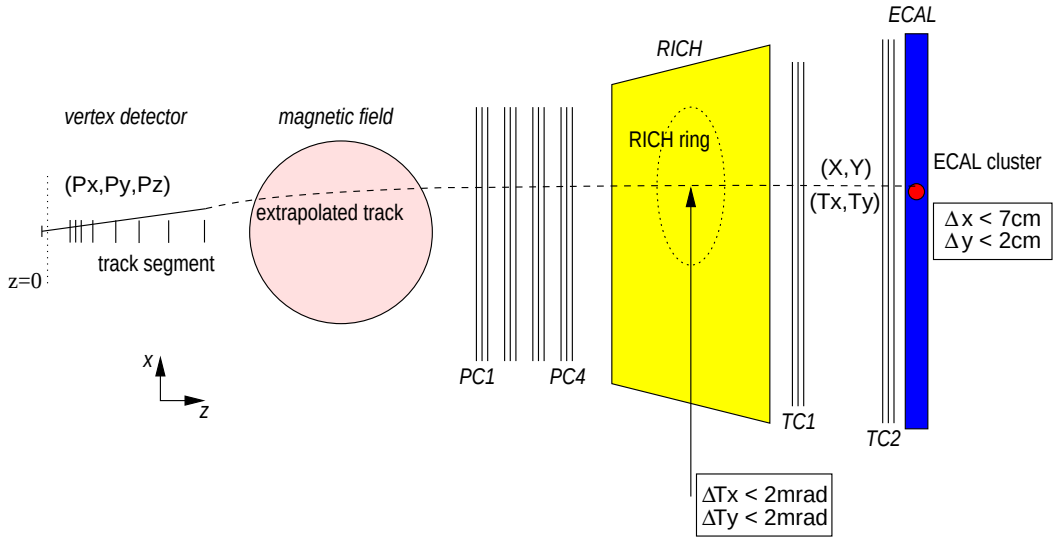

Figure 4.5.1: *Construction of external reference tracks for measurement of FLT track parameter resolution and track finding efficiency. A vertex segment is extrapolated through the magnetic field with a Runge-Kutta integration and required to point to the ECAL cluster. This cluster must have a transverse energy of more than 1 GeV. In addition, a RICH ring is required, for which the track slopes in both directions are within 2 mrad equal to those of the extrapolated track.*

Since these external reference tracks can be constructed both in data and in the Monte Carlo simulation, we can use them to verify that the Monte Carlo simulation provides an accurate description of the detector. Figure 4.5.2 shows the distribution of the residuals of the three components of the momentum vector. The residual distributions of the Monte Carlo simulation and those of the data of 2000 are in agreement.

4.5.2 Results

The FLT track finding efficiency is measured from the distribution of the χ^2-probability of the match, an example of which is shown in figure 4.5.3. If the track finding efficiency would be 100% and there would no clones present, the distribution of the χ^2-probability would be flat. Mismatches or bad matches show up as entries with a χ^2-probability of approximately zero.

We consider a reference tracks for which the closest FLT track has a χ^2-probability of less than 1% as unmatched. The FLT track finding efficiency is then:

$$\epsilon_{\text{FLT track}} = 0.01 + \frac{\int_{0.01}^{1} P(p)dp}{\int_{0}^{1} P(p)dp}, \tag{4.5.2}$$

where $P(p)$ is the probability of the χ^2-probability of the match.

Table 4.5.2 gives $\epsilon_{\text{FLTtrack}}$ for the FLT efficiency runs of 2000. The results from the Monte Carlo simulation, both in the 2000 and 2002 setups (see table 4.4.2), are also

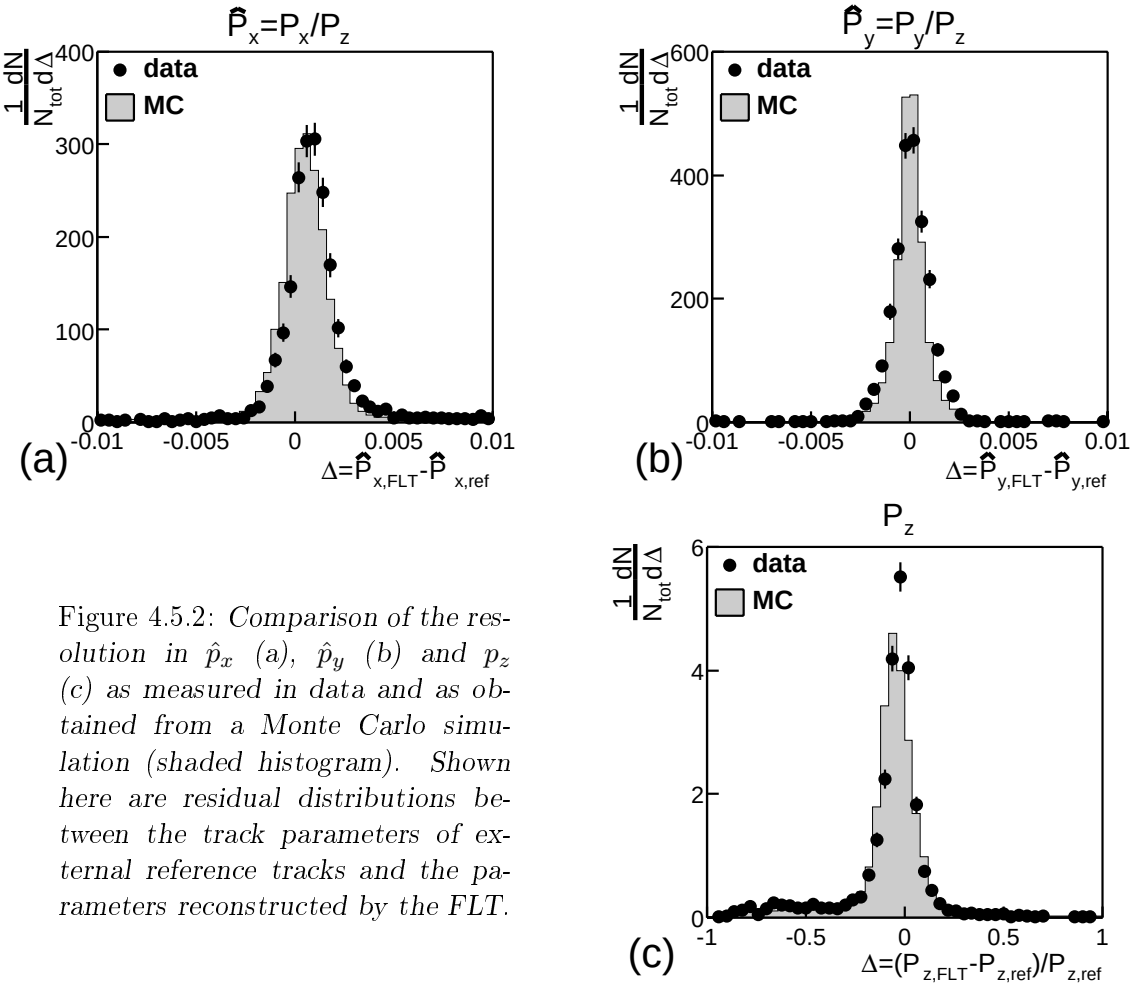

Figure 4.5.2: *Comparison of the resolution in $\hat{p}_x$ (a), $\hat{p}_y$ (b) and p_z (c) as measured in data and as obtained from a Monte Carlo simulation (shaded histogram). Shown here are residual distributions between the track parameters of external reference tracks and the parameters reconstructed by the FLT.*

shown. The track finding efficiency fluctuates around 50% and is significantly different for the two data run periods (17036-17067, 17163-17166), indicating the sensitivity to data taking conditions. The results of the Monte Carlo simulation of 2000, which was based on the detector performance of run 17163, are in good agreement with the data.

The contributions to the overall track finding efficiency are given in table 4.5.3. The main sources of inefficiency are the low Outer Tracker cell efficiency and the dead or wrongly mapped channels.

Misalignment

The effect of a global and an internal misalignment is estimated by re-determining the efficiencies after correcting the x positions of the channels in the Wire Memory by the measured displacements. The displacements have been measured for each of the three angles of all Outer Tracker TFUs from the residuals between the x position of offline reconstructed reference tracks and the nominal x position of hits in the Wire Memory.

The reference tracks are candidates for photon-conversions behind the magnet. Since such conversions passed the magnetic field as photons, they give track segments

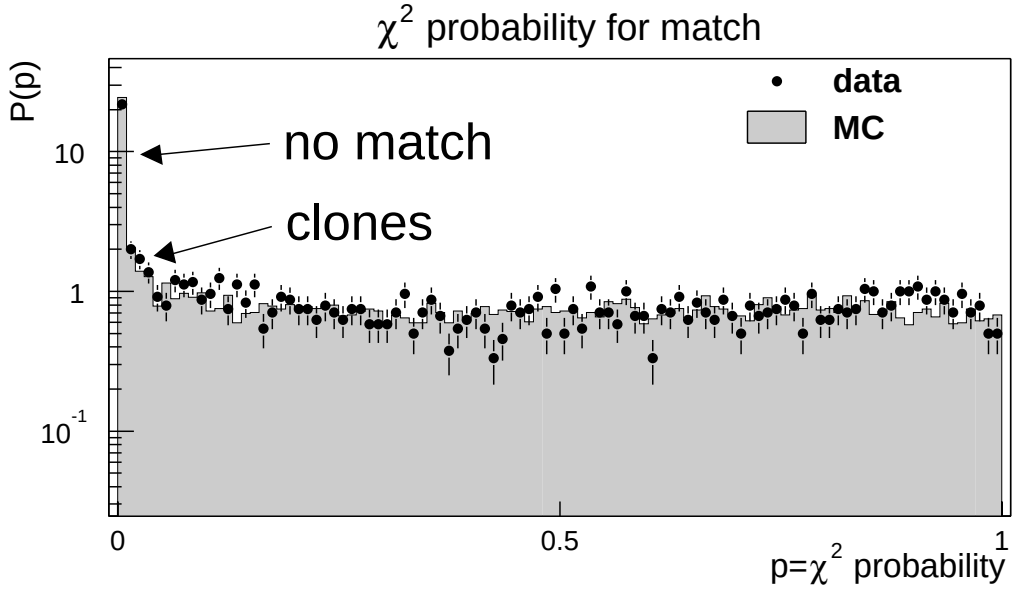

Figure 4.5.3: *Distribution of the matching-χ^2 probability. This probability measures the quality of the match between external reference tracks and FLT messages. Bad matches or no matches all end up in the first bin of the histogram. The distribution is reasonably flat, indicating that the residuals between the different track parameters are practically uncorrelated. A small rise near low probabilities is due to track clones.*

that point directly to the target.

They are selected as ECAL clusters that cannot be matched to a reconstructed track segment in the Vertex Detector. Moreover, a reconstructed ring in the RICH must exist for which the track slopes are within 1 mrad the same as that of an unbent track pointing from the target to the cluster. The track parameters are derived from the cluster coordinates, where $p_x/p_z = x/z_{\mathrm{ECAL}}$ and $p_y/p_z = y/z_{\mathrm{ECAL}}$.

With conversions we directly measure global alignment constants. Figure 4.5.4 shows the residual distribution for one TFU as an example. After the re-alignment of the Wire Memories channel positions, the FLT track finding efficiency is observed to increase by 2-4%, depending on the run used.

4.6 Summary and Outlook

During the commissioning of the First Level Trigger in 2000, a strong sensitivity to the performance of the tracking chambers was observed. Whereas the FLT network behaves largely as expected, the quality of the incoming data was much worse than needed for an efficient operation. Problems with the transmission and mapping of Outer Tracker data have caused the FLT network to find only half of the tracks it should find.

Since then, the Outer Tracker chambers and the data transmission electronics have been upgraded or repaired [10]. Cell efficiencies are expected to reach design specifica-

Run	$\epsilon_{\text{FLT track}}$ (matched message)	$\epsilon_{\text{FLT track}}$ (any message)
17036	0.45(1)	0.49(1)
17065	0.45(2)	0.50(2)
17067	0.43(1)	0.49(2)
17163	0.53(1)	0.59(1)
17164	0.50(2)	0.60(2)
17165	0.50(3)	0.59(3)
17166	0.49(2)	0.61(2)
2000 MC	0.491(8)	0.578(8)
2002 MC	0.785(8)	0.841(7)

Table 4.5.2: *FLT track finding efficiencies measured for runs taken in 2000, and obtained from a Monte Carlo simulation. The '2000 MC' gives the results of a simulation of detector performance of 2000. The '2002 MC' is an estimate for future data taking.*

tions and the dead regions of the Outer Tracker have been repaired. The performance of the FLT will benefit greatly from these improvements.

The inclusion of a multiplicity veto in future running will prevent the processing of events that put a disproportionate load on the FLT network. The probability that the network becomes congested due to message multiplication will be greatly reduced. This will be essential if the Bremsstrahlung recovery by the ECAL pretrigger is included, since this would otherwise lead to considerable efficiency losses due to increased latency.

We have determined the individual contributions to the resolution of the FLT for

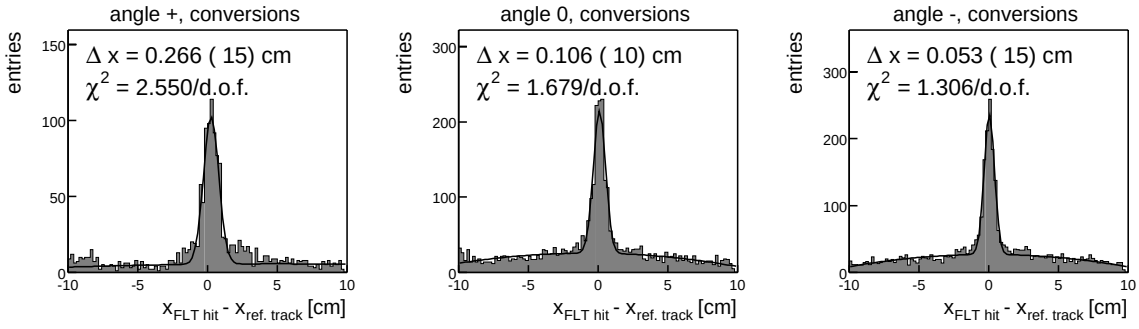

Figure 4.5.4: *Example of the determination of Wire Memory alignment constants from residual distributions in x between offline reconstructed reference tracks and hits in the three angles of the Wire Memory of TFU 15 (sector 5 in PC4). The reference tracks are conversions behind the magnet, selected by requiring a match between a RICH ring and an ECAL cluster, without a matching track segment in the vertex detector. The residual distributions are fitted with a Gaussian for the signal and a Gaussian for the background.*

	2000	2002	achievable
pretrigger extrapolation (ϵ_{RoI})	0.92(1)	0.92(1)	0.98
OTR cell efficiency	0.89(1)	0.99(1)	0.99
Dead channels	0.78(3)	-	1
Wrongly mapped channels	0.83(3)	-	1
Global misalignment	0.98(1)	0.98(1)	0.98(1)
Internal misalignment	0.95(3)	0.95(3)	0.97(3)
FLT algorithmic efficiency	0.97(1)	0.97(1)	0.98
Total	0.48(5)	0.82(4)	0.90

Table 4.5.3: *Sources of inefficiency for track finding by the FLT. The estimates are based on an Outer Tracker cell efficiency of 90%. The number of wrongly mapped and dead Wire Memory channels were taken to be 1.5% and 2%, respectively. These numbers are based on the performance measured in the previous chapter (see Fig. 4.3.1). The FLT algorithmic efficiency refers to the efficiency measured in a toy simulation[10], when all hits belonging to some fiducial track are set on at the expected location in the Wire Memory. The efficiency for extrapolating the pretrigger message has been measured in section 3.9.3).*

each of the track parameters x, t_x and $y(t_y)$ and for the momentum vector $(\hat{p_x}, \hat{p_y}, p_z)$. We have shown that the track parameter and momentum resolutions, measured using a Monte Carlo simulation, are in reasonable agreement with expectations.

Limitations of the FLT track reconstruction algorithm, binning effects in the coding and the neglect of drift times, lead to a marginal reduction of the resolution, compared to extrinsic effects such a misalignment, multiple scattering and energy losses.

The mass resolution of the J/ψ, reconstructed in the decay $\mathrm{J}/\psi \rightarrow \mathrm{e}^+\mathrm{e}^-$ is 234(4) MeV/c^2, if energy losses are absent. This is approximately equal to the mass resolution for $\mathrm{J}/\psi \rightarrow \mu^+\mu^-$ decays. In future running, the reduced amount of detector material in the magnet, and the recovery of Bremsstrahlung emitted before the magnet, will permit a mass cut at 2 GeV/c^2 with an efficiency for J/ψ well above 90%.

The FLT track finding efficiency was approximately 50%. This result can be reproduced in a Monte Carlo simulation. With repairs and upgrades that have since been done on the detector, the efficiency can increase to 80%.

An important issue for the performance of the FLT is the alignment and the mapping of the Wire Memory channels. The Wire Memories can be aligned using conversions behind the magnet. The improved alignment gives an increase of the FLT track finding efficiency of up to 4%.

Part II

Nuclear effects in J/ψ production

Chapter 5

J/ψ production in pA collisions

In this chapter, an overview of the theory of J/ψ production in proton-nucleus collisions is given. We first describe the hadroproduction of charm quarks and present several models for the formation of charmonium. The proton-nucleus interaction is discussed within the framework of the Glauber model. An overview of (proposed) nuclear effects is given. The chapter is concluded with a discussion of existing experimental data and with a short summary of the potential of HERA-B.

5.1 Charm hadroproduction

5.1.1 Kinematics of hard parton scattering

The QCD improved parton model (see e.g. [58]) describes a scattering process between two hadrons as the result of an interaction between the partons, the quarks and gluons that make up the hadrons. The cross section for a process initiated by two hadrons, labelled 1 and 2, can be written as a convolution between their parton densities $f_{i,j}$ and the partonic cross sections $\hat{\sigma}_{ij}$:

$$\sigma(P_1, P_2) = \sum_{i,j} \int dx_1 dx_2 f_i^{(1)}(x_1) f_j^{(2)}(x_2) \hat{\sigma}_{ij}(p_1, p_2, \alpha_S) + \mathcal{O}(\frac{\Lambda^2_{\rm QCD}}{Q^2}), \tag{5.1.1}$$

where i and j indicate a quark, an anti-quark or a gluon and Q^2 the hard scale of the process. The four-momenta of the partons $p_{1,2}$ are fractions $x_{1,2}$ of the total hadron four-momenta $P_{1,2}$:

$$p_1 = x_1 P_1, \tag{5.1.2}$$
$$p_2 = x_2 P_2. \tag{5.1.3}$$

The difference between the partonic momentum fractions gives a net longitudinal momentum p_z in the centre-of-mass frame ($\vec{P}_1 = -\vec{P}_2$):

$$x_1 - x_2 \approx \frac{2p_{z,\rm c.m.}}{\sqrt{s}} \equiv x_F, \tag{5.1.4}$$

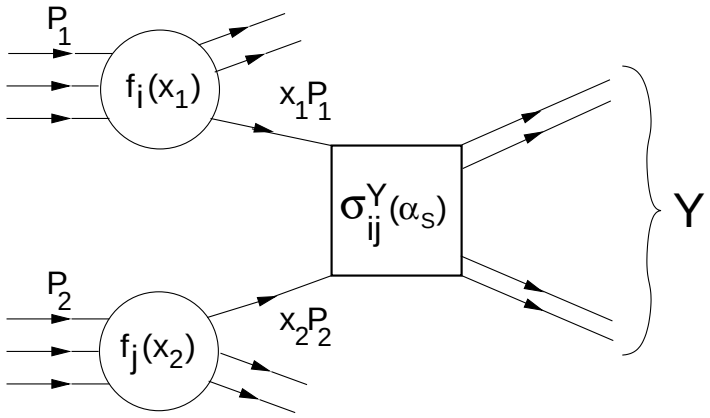

Figure 5.1.1: *Description of hadron-hadron scattering in the parton model. The hadrons 1 and 2, with four-momenta P_1 and P_2 interact with each other through the partons with four-momentum fractions x_1 and x_2 to create Y in the final state. The parton scattering is factorised in the partonic cross section σ_{ij}^Y.*

where $s = (P_1 + P_2)^2$ is the centre-of-mass energy squared. The variable x_F ('Feynman x') and the transverse momentum p_T are commonly used to describe the kinematics of the produced particles.

For J/ψ production, the momentum fractions x_1 and x_2 must be sufficiently large to produce the invariant mass of the J/ψ, $m_{\mathrm{J}/\psi} \approx 3.1$ GeV/c^2 :

$$m^2 = (p_1 + p_2)^2 \approx x_1 x_2 s > m^2_{\mathrm{J}/\psi}. \tag{5.1.5}$$

In fixed target J/ψ production $pA \to \mathrm{J}/\psi X$, where in the laboratory frame $p_2 = (x_2 m_N, 0, 0, 0)$ and $p_1 = (x_1 E_{\mathrm{beam}}, 0, 0, x_1 E_{\mathrm{beam}})$, the system has a forward Lorentz boost γ_z that is related to x_F:

$$\begin{aligned} \gamma_z &= \frac{p^{\mathrm{J}/\psi}_{z,\mathrm{lab.}}}{m_{\mathrm{J}/\psi}} = \frac{x_1 E_{\mathrm{beam}}}{\sqrt{2 x_1 x_2 m_N E_{\mathrm{beam}}}} = \frac{m_{\mathrm{J}/\psi}}{2 x_2 m_N} \\ &= \frac{m_{\mathrm{J}/\psi}}{m_N} \frac{1}{-x_F + \sqrt{x_F^2 + 4 m^2_{\mathrm{J}/\psi}/s}}. \end{aligned} \tag{5.1.6}$$

Figure 5.1.2 shows $\gamma_z(x_F)$ for HERA-B, where $\sqrt{s} = 41.6$ GeV.

5.1.2 Factorisation and renormalisation

When the partonic cross section for a strong interaction is calculated as a power series in α_S, two types of divergences appear: infrared divergences and ultraviolet divergences.

Ultraviolet divergences occur in loop-diagrams when the momenta $p \to \infty$. These divergences are removed by a renormalisation procedure. This introduces a scale, μ_R, at which the subtractions that remove these divergences are performed. The 'bare' coupling constant α_S, is then replaced by a renormalised coupling constant $\alpha_S(\mu_R)$, which depends on the choice made for μ_R.

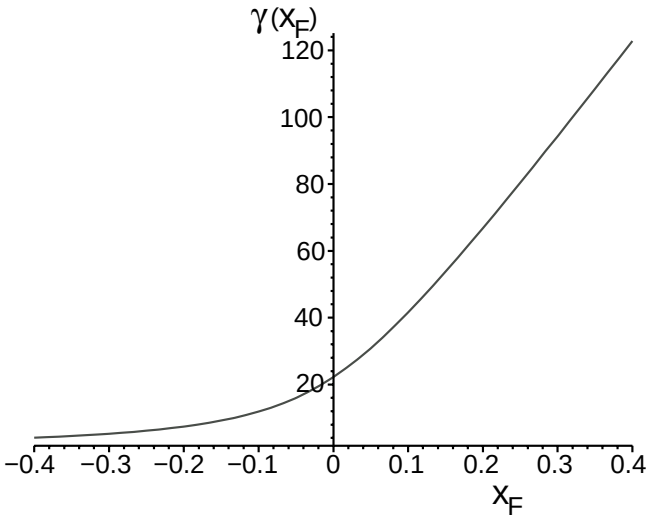

Figure 5.1.2: *Dependence of the Lorentz factor γ_z on the x_F of J/ψ at* HERA-B. *The geometrical acceptance of the* HERA-B *detector covers an x_F range of $[-0.4, 0.3]$.*

The infrared divergences ($p \to 0$) are factorised into a universal non-perturbative part of the cross section. The QCD factorisation theorem allows a separation of the long distance ('soft') and short distance ('hard') part of the interaction. The hard and soft processes are separated by a factorisation scale μ_F.

In the short distance part of the cross section the four-momentum transfers $|Q|$ are sufficiently large to ensure that the perturbative expansion of the cross section converges. The values of $|Q|$ must be a few times $\Lambda_{\mathrm{QCD}}(\approx 0.2$ GeV), if a truncation of the perturbation series is to produce reliable results.

In contrast, processes with low momentum transfers cannot be calculated perturbatively. Since they are universal, however, they can be measured separately, e.g. in deep-inelastic scattering experiments.

Both the renormalisation scale μ_R and the factorisation scale μ_F are arbitrary parameters. Their values are typically chosen to be of the order of the scale of the hard interaction Q.

$$\mu_F = \mu_R = Q. \tag{5.1.7}$$

The two scales are usually varied to estimate the uncertainty associated with the truncation of the perturbative expansion. The higher the order of the perturbative calculation, the weaker the dependence on the exact values of μ_R and μ_F will be. After factorising all processes with scales $Q^2 < \mu_F$ into the parton densities, the production cross section for a hard scattering process, calculated to order α_S^n is written as:

$$\sigma(P_1, P_2) = \sum_{i,j} \int dx_1 dx_2 f_i^{(1)}(x_1, \mu_F^2) f_j^{(2)}(x_2, \mu_F^2) \sum_{m=2}^{n} \hat{\sigma}_{ij}^m(p_1, p_2, \alpha_S^m(\mu_R^2), \frac{Q^2}{\mu_F^2}, \frac{Q^2}{\mu_R^2}). \tag{5.1.8}$$

5.1.3 Partonic cross sections for charm production

At leading order (LO) in α_S, the production of a $c\bar{c}$ pair has contributions from gluon fusion and quark-anti-quark annihilation. All propagators in the corresponding Feynman diagrams (see figure 5.1.3) are off-shell by at least m_c^2. The charm quark mass

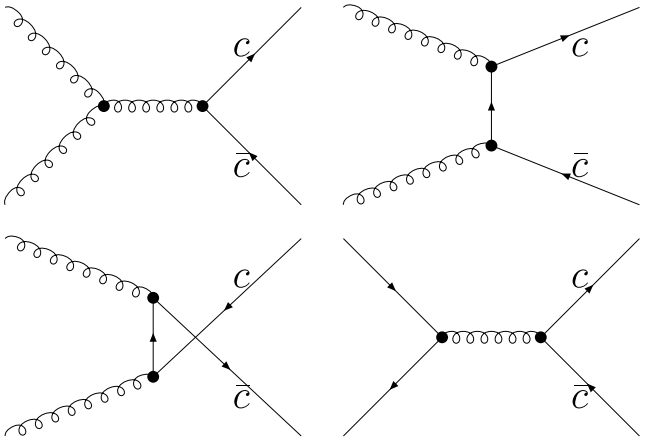

Figure 5.1.3: *Leading order Feynman diagrams for $c\bar{c}$ production. The minimum virtuality of an s-channel gluon is $4m_c^2$, which is commonly used as value for the factorisation scale μ_F.*

provides a natural choice for the scale of the process, which is generally taken to be the minimum virtuality of an s-channel exchange:

$$\mu_F^2 = Q^2 = 4m_c^2. \tag{5.1.9}$$

To estimate the theoretical uncertainty of the calculated cross section, the charm quark mass m_c is generally varied between the lower and upper limits of 1.2 and 1.8 GeV/c^2, respectively.

Since $m_c > \Lambda_{\rm QCD}$, a perturbative approach should give reasonable results for the partonic cross section for charm production, which is not the case for the lighter flavours. The LO partonic cross sections are [59]:

$$\sigma_{gg}^{c\bar{c}}(m^2) = \frac{\pi\alpha_S^2}{3m^2}\left[(1+4\frac{m_c^2}{m^2}+\frac{m_c^4}{m^4})\ln(\frac{1+\lambda}{1-\lambda}) - \frac{1}{4}(7+\frac{31m_c^2}{m^2})\lambda\right], \tag{5.1.10}$$

$$\sigma_{q\bar{q}}^{c\bar{c}}(m^2) = \frac{8\pi\alpha_S^2}{27m^2}(1+\frac{2m_c^2}{m^2})\lambda, \tag{5.1.11}$$

where $\lambda \equiv \sqrt{1-4m_c^2/m^2}$ and $m^2 = x_1x_2s$.

5.1.4 Parton densities

The parton densities $f_i(x,Q^2)$ cannot be calculated perturbatively. There are many parametrisations available that have been fit to data from various experiments, spanning large regions in both x and Q^2. Figure 5.1.4 shows the CTEQ5L [60] quark, anti-quark and gluon densities of the proton, evaluated at the scale $Q^2 = 4m_c^2$.

An important property of the parton densities is approximate scaling $f_i(x,Q^2) \approx f_i(x)$, so that the dependence on the factorisation scale is weak. In contrast, the variation with x is strong: the dependence of the production cross section on m_c is dominated by the parton density, and not by the partonic cross section. Since the gluon density rapidly decreases with increasing x, the $c\bar{c}$ pairs are generally produced with an invariant mass near the threshold of $2m_c$ and therefore we have (see 5.1.5):

$$x_1x_2s \approx m_{\rm J/\psi}^2. \tag{5.1.12}$$

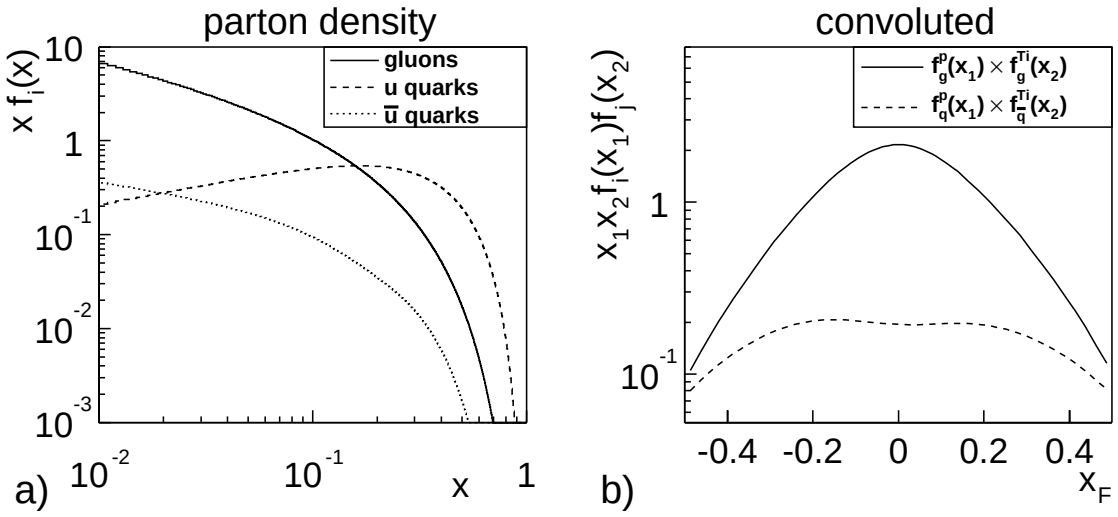

Figure 5.1.4: *Quark and gluon densities of the proton, evaluated at an appropriate scale for charm production of $Q^2 = 4m_c^2$. (a) shows the CTEQ5L density function for u, $\bar{u}$ and gluons. (b) shows a convolution of the parton densities of the proton with the densities in a Titanium nucleus (from parametrisation A-EKS [61]) as a function of x_F, assuming $x_1 x_2 s = m^2_{J/\psi}$. The $q\bar{q}$ convolution is the sum of all flavours. The parton densities are obtained from pdflib version 8.04 [62].*

5.1.5 Charm production at higher orders

The cross sections for charm and beauty hadroproduction have been calculated at next-to-leading order [63, 64, 65, 66, 67] which includes the effects of real and virtual gluons. Figure 5.1.5 shows the results for charm quark masses of 1.2, 1.5 and 1.8 GeV/c^2 in a comparison with experimental data at fixed target energies.

A full next-to-next-to-leading order calculation for heavy quark production does not yet exist. First steps in this calculation have recently been taken [68].

5.1.6 Transverse momentum

There are various approaches to describe the transverse momentum of the $c\bar{c}$ pairs:

- **Perturbative**
  In Feynman graphs beyond LO, one or more recoiling gluons lead to a non-zero p_T of the $c\bar{c}$. A pertubative approach, however, can only give reliable results for sufficiently large p_T.

- **Intrinsic transverse momentum**
  The description of the creation of low p_T particles cannot be handled in a perturbative manner. Such processes are part of the higher twist corrections to the factorisation formula (Eq. 5.1.1). One can effectively reproduce the observed p_T spectra by attributing an intrinsic transverse momentum $\vec{k}_T$ to the partons. The

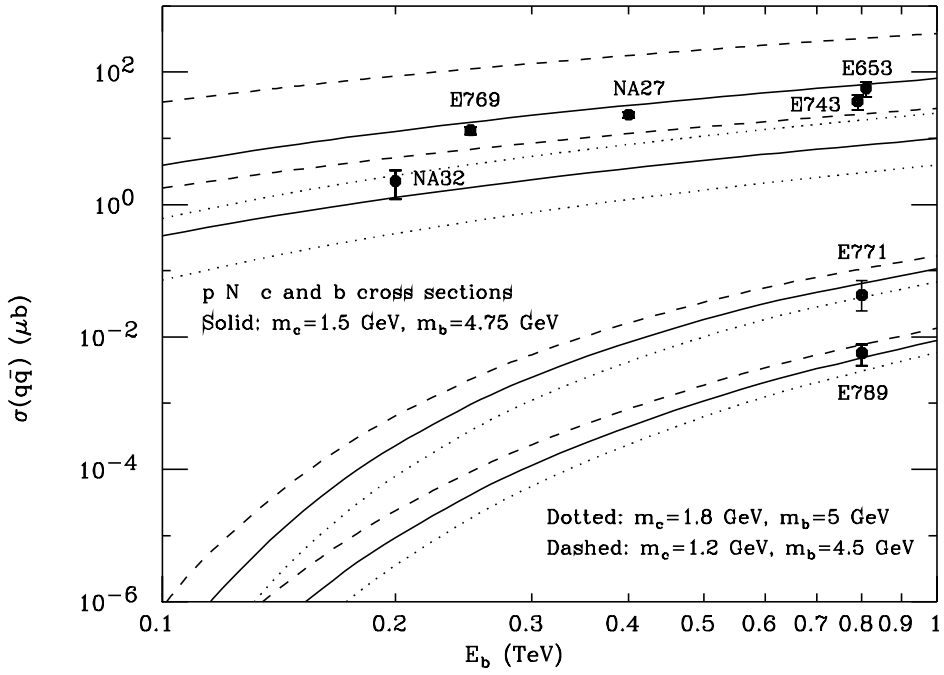

Figure 5.1.5: *Heavy quark production cross section as a function of the proton beam energy in pA collisions, calculated to NLO for various values of m_c and m_b. The top curves show the charm production cross section, the bottom curves give the beauty cross section. The upper and lower limit are obtained by varying the factorisation scale μ_F between $m_Q/2$ and $2m_Q$. Experimental data, mainly from Fermilab fixed target experiments, are also shown.*

p_T of the $c\bar{c}$ pair is then inherited from the $\vec{k}_T$ of the partons. One generally assumes $\vec{k}_T$ to be distributed according to a Gaussian distribution:

$$P(\vec{k}_T) = \frac{b}{\pi} \exp(-2bk_T^2), \tag{5.1.13}$$

where $k_T = |\vec{k}_T|$. This intrinsic transverse momentum gives rise to a total p_T in the final state, which is distributed according to:

$$\frac{d\sigma}{dp_T^2} \propto \exp(-bp_T^2). \tag{5.1.14}$$

The p_T distributions at fixed target energies are reproduced if one assigns to the partons $\langle k_T \rangle = \sqrt{\pi/4b}$ of the order of 1 GeV/c.

- **Fragmentation**
  The production of $c\bar{c}$ pairs of very high p_T ($p_T > 10$ GeV/c) is generally described by the fragmentation of hard gluons. For $c\bar{c}$ production at HERA-B, we can disregard this mechanism, since here $p_T < 5$ GeV/c.

5.2 Charmonium production

5.2.1 The charmonium spectrum

Charmonium, a bound state of a $c\bar{c}$ pair, is approximately a non-relativistic system: the average velocity β of a c quark is estimated at $\beta_c^2 \approx 0.23$ [58].

The $c\bar{c}$ pair is tightly bound, and the $c\bar{c}$ interaction is dominated by the exchange of single gluons. In analogy to positronium, a good description of the spectrum of charmonium states (see figure 5.2.1) can be obtained from non-relativistic quantum mechanics, using a Coulomb-like binding potential, but adding a term that ensures confinement a large distances

$$V(r) = -\frac{4}{3}\frac{\alpha_S(1/r^2)}{r} + K^2 r. \tag{5.2.1}$$

Here, r is the distance between the two c quarks and $K(\approx 430$ MeV) is called the string tension.

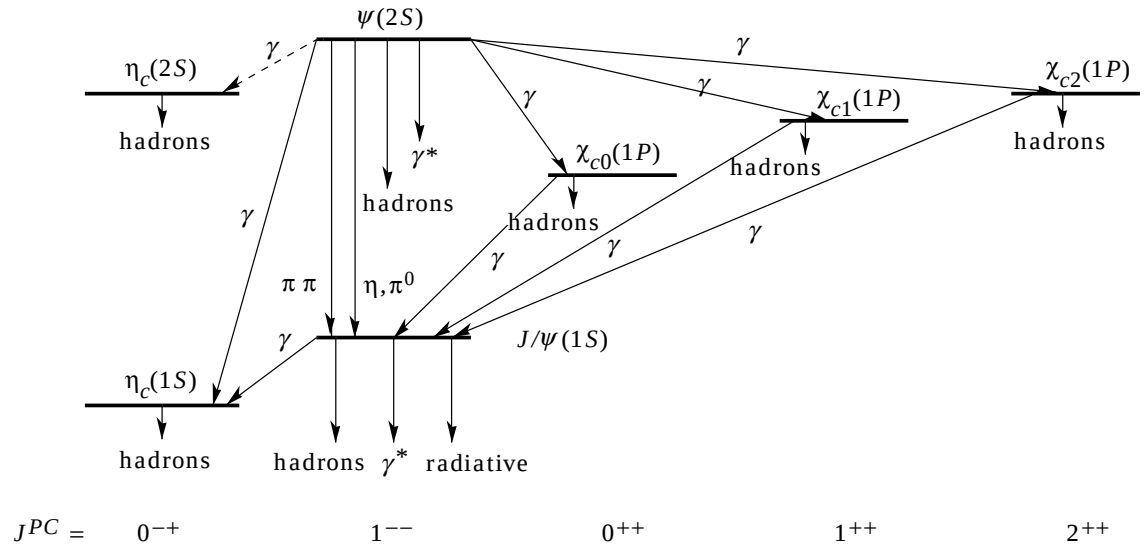

Figure 5.2.1: *The spectrum of charmonium states, indicating the radiative transitions between different charmonium states and the dominant decay modes. Only well-established states below the open charm threshold are shown. The total measured* J/ψ *yield includes feed-down from both* ψ' *and* χ_c*. The notation* γ^* *refers to decay processes involving an intermediate virtual photon, which includes the decays to* e^+e^- *and* $\mu^+\mu^-$*.*

5.2.2 Charmonium decays - indirect and direct J/ψ production

All states with masses above the open charm threshold $m_{D\bar{D}} = 2M_D$ decay strongly to a $D\bar{D}$ pair and therefore should not be considered as truly bound states. The sub-threshold charmonium states can decay electro-magnetically or hadronically. Such decays are subject to conservation laws:

- **Colour SU(3) symmetry**
  Since bound states are colour singlet states, they cannot annihilate into a single (colour octet) gluon.

- **C parity conservation**
  The quantity $C = (-1)^{L+S}$ must be conserved in the decay. The states η_c, χ_{c0} and χ_{c2} have C=+1, and can decay via two gluons or two photons (C(γ)=-1). Such a decay is forbidden for J/ψ and ψ', since for these states C=-1.

- **Yang's theorem**
  A massive spin-1 particle may not decay to two identical massless spin-1 particles. This forbids the decay of a χ_{c1} into two photons or two gluons, although such a decay conserves C parity.

- **OZI rule**
  The Okubo-Zweig-Izuka rule states that decays, that are mediated by one or more hard gluons, have reduced rates. This makes a bound $c\bar{c}$ states with a mass below the D$\overline{\text{D}}$ threshold relatively stable.

The states J/ψ and ψ' have the same quantum numbers as the photon. They can decay into a lepton pair via a virtual photon. Since the strong decay rate is suppressed because of the OZI rule, the leptonic branching ratio of a J/ψ is an appreciable 12%. This makes the J/ψ relatively easy to detect experimentally.

An excited charmonium state can make a radiative transition to a charmonium state of lower mass, as illustrated in figure 5.2.1. Since it is experimentally difficult to separate a directly produced J/ψ from a J/ψ, that originated from an excited state, the common definition of the J/ψ production cross section includes such feed-down processes:

$$\sigma^{\mathrm{J}/\psi} = \sigma^{\mathrm{J}/\psi}_{\mathrm{direct}} + \sum \sigma^{\chi_{cJ}} \times \mathrm{Br}(\chi_{cJ} \to \mathrm{J}/\psi\gamma) + \sigma^{\psi'} \times \mathrm{Br}(\psi' \to \mathrm{J}/\psi X), \qquad (5.2.2)$$

where Br() indicates the branching ratio for the transition. Measurements show that approximately 55% of the J/ψ are directly produced (see e.g. [69] and references therein). The indirect production is predominantly from $\chi_{c1,2}$ (35%) and ψ' (10%).

5.2.3 Charmonium formation

Most of the $c\bar{c}$ pairs created in a proton-nucleus interaction will fragment into a $D\bar{D}$ pair. Only a small fraction (~5%) will bind together and form a charmonium state. A firm understanding of the formation of charmonium is still lacking. The key issue is whether or not the c$\bar{c}$ pair must have been created in the same colour neutral state as the charmonium state. The following three models have been proposed to describe charmonium formation:

Colour evaporation model (CEM)

In the colour evaporation model [70] a coloured $c\bar{c}$ pair can become colour neutral by radiating a soft gluon. Each $c\bar{c}$ pair (coloured or not) with a mass below the $D\bar{D}$ threshold has a certain probability A_H to form a bound state H:

$$\sigma^H = A_H \int_{2m_c}^{2M_D} dm \frac{d\sigma(m)}{dm}, \tag{5.2.3}$$

where $m^2 = x_1 x_2 s$. Since the probabilities A_H cannot be calculated, this model cannot predict absolute cross sections. Nevertheless, two predictions can be made: differential production cross sections should be the same of for all charmonium states, except for an absolute normalisation factor A_H. Furthermore, cross section ratios should not depend on the centre-of-mass energy. Both predictions are in reasonable agreement with observations [69].

Colour singlet model (CSM)

A more rigorous and predictive description of charmonium formation is the colour singlet model [71, 72]. It assumes that the $c\bar{c}$ pair is created in a colour neutral state with the same quantum numbers as the charmonium state. The rules for the decay are equally applicable to the production of the charmonium state. It implies that only a subset of the diagrams for $c\bar{c}$ production can contribute to the production of a charmonium state: no charmonium state can be produced from an s-channel gluon because of colour neutrality; C-parity conservation forbids the creation of a J/ψ from gluon fusion at leading order. Therefore, the lowest order diagrams are $\mathcal{O}(\alpha_S^3)$ for the production of J/ψ, and $\mathcal{O}(\alpha_S^2)$ for the production of η_c (fig. 5.2.2).

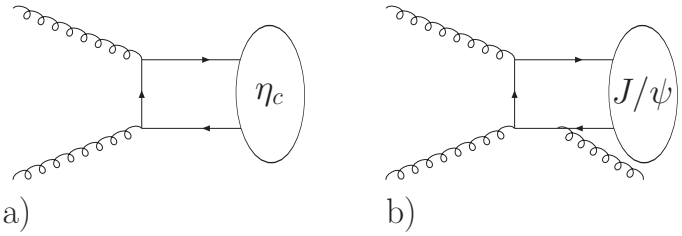

Figure 5.2.2: *Leading order diagrams in the Colour Singlet Model for the production of η_c (a) and J/ψ (b). In the CSM, the leading order J/ψ production is $\mathcal{O}(\alpha_S^3)$ as a consequence of C parity conservation.*

The probability that a $c\bar{c}$ pair with correct quantum numbers will bind into a charmonium state H is given by the square of the radial wave function at the origin:

$$\sigma(H(^{2S+1}L_J)) = \left| \frac{d^l}{dr^l} R_{nl}(0) \right|^2 \sigma(c\bar{c}(^{2S+1}L_J). \tag{5.2.4}$$

The wave function R_{nl} can be calculated from Schrödingers equation with a potential $V(r)$ as given in Eq. 5.2.1. Its value at the origin can be obtained from the leptonic decay width [69], e.g.

$$\Gamma(\psi(nS) \to l^+l^-) = \frac{16\alpha^2}{9M^2_{\psi(nS)}} |R_{nS}(0)|^2 \left[1 - \frac{16}{3}\frac{\alpha_S}{\pi}\right]. \tag{5.2.5}$$

The CSM prediction for the ratio of (direct) J/ψ and ψ' production

$$\frac{\sigma^{\psi'}}{\sigma^{\mathrm{J}/\psi}} = \frac{\Gamma(\psi' \to l^+l^-)}{\Gamma(\mathrm{J}/\psi \to l^+l^-)} \frac{M^3_{\mathrm{J}/\psi}}{M^3_{\psi'}} \approx 0.24, \tag{5.2.6}$$

is in good agreement with the measured value of 0.23 [73]. However, the prediction that $\sigma^{\mathrm{J}/\psi}$ should be one order in $\alpha_S(m_c^2) \approx 0.20$ smaller than σ^{χ_c} is at variance with observations at fixed target energies, where similar rates are observed. Moreover, the colour singlet model fails to describe the data on J/ψ and ψ' production at high p_T. Such high p_T J/ψ production is dominated by gluon fragmentation, which, in the CSM, can only occur in association with two hard gluons, and is therefore suppressed by α_S^2.

Colour octet model - NRQCD factorisation

A recent approach to charmonium formation is the colour octet model, based on an effective theory called Non-Relativistic QCD (NRQCD) [74]. It is similar to the colour evaporation model in that it allows for non-perturbative transitions from coloured $c\bar{c}$ pairs to charmonium states, but it is built on more solid theoretical foundations.

For each $c\bar{c}$ pair in a colour octet (8) or colour single (1) state n (in spectroscopic notation $n = {}^{2S+1}L_J$), there is a transition probability $\langle O^H_{1,8}(n)\rangle$ to become a charmonium state H. The NRQCD factorisation formula for the production cross section of state H then includes the contributions from these transitions:

$$\sigma^H = \sum_n \sigma^{c\bar{c}}_{1,8}(n) \langle O^H_{1,8}(n)\rangle \tag{5.2.7}$$

In contrast to the factors A_H of the colour evaporation model, the non-perturbative matrix elements $\langle O^H_{1,8}(n)\rangle$ can (in principle) be calculated in NRQCD. The singlet contributions are the same as those of the CSM:

$$\langle O^H_1(n)\rangle = \frac{9}{2\pi} \left|\frac{d^l}{dr^l} R_{nl}(0)\right|^2. \tag{5.2.8}$$

The value for the octet matrix elements $\langle O^H_8(n)\rangle$ could be determined using lattice NRQCD calculations. In practice, however, they are extracted from fits to data. An order-of-magnitude estimate for $\langle O^H_8(n)\rangle$ in powers of the heavy quark velocity v and the mass m can be obtained from the NRQCD Lagrangian. One generally takes into account only the leading order matrix elements in the fit.

For the direct J/ψ production, the dominant matrix elements are [75]:

$$\langle O_1^{\mathrm{J}/\psi}(^3S1)\rangle = \frac{9}{2\pi}\left|R(0)\right|^2 = 1.16\ \mathrm{GeV}^3 \quad (5.2.9)$$

$$\langle O_8^{\mathrm{J}/\psi}(^3S1)\rangle = 6.6\times10^{-3}\ \mathrm{GeV}^3(\text{from fit}) \quad (5.2.10)$$

$$\Delta_8^{\mathrm{J}/\psi} \equiv \langle O_8^{\mathrm{J}/\psi}(^1S0)\rangle + \frac{7}{m_c^2}\langle O_8^{\mathrm{J}/\psi}(^3P0)\rangle = 3.0\times10^{-2}\ \mathrm{GeV}^3(\text{from fit}) \quad (5.2.11)$$

The high-p_T J/ψ data can be well described by NRQCD factorisation, in combination with gluon fragmentation. However, it remains to be seen how successful NRQCD will be in predicting other measurements. In the absence of reliable results from Lattice calculations, NRQCD is a model with a disconcertingly large number of free parameters. Different fits give values for the matrix elements, that can differ by up to an order of magnitude. Moreover, one of the (very few) true predictions of NRQCD, namely that, at high p_T, the J/ψ should be predominantly produced in a transversely polarised state, is at variance with data from CDF. More data are needed to determine the values of the matrix elements to a precision, sufficient for meaningful predictions.

5.3 Nuclear effects in J/ψ production

5.3.1 A-dependence of production cross sections

Proton-nucleus (and nucleus-nucleus) interactions are commonly described by the Glauber model. Within the Glauber model, such an interaction is considered as a series of binary sub-collisions between the incident proton and individual nucleons. These sub-collisions are assumed to be incoherent, so that, after one sub-collision, the proton is unaffected and interacts with other nucleons with the same cross section. The total number of sub-collisions N_{pN} then depends on the proton-nucleon cross section $\sigma_{pN}^{\mathrm{inel}}$, and on the amount of nuclear matter encountered by the proton. The latter depends on the impact parameter $b = |\vec{b}|$, and is proportional to the nuclear density $\rho(b,z)$:

$$N_{pN} \propto \int d^2\vec{b} \int dz \rho(b,z)\sigma_{pN}. \quad (5.3.1)$$

An effective path length $L(b)$ is defined as the amount of nuclear matter encountered by a proton, incident with impact parameter b,

$$L(b) = \int dz \rho(b,z). \quad (5.3.2)$$

If we normalise the path length, we obtain the nuclear thickness function t_A:

$$t_A(b) \equiv \frac{L(b)}{\int d^2\vec{b} L(b)}. \quad (5.3.3)$$

This function is a probability density for the number of participating nucleons, so that $t_A(b)d^2\vec{b}$ gives the probability to have an inelastic collision within the transverse area

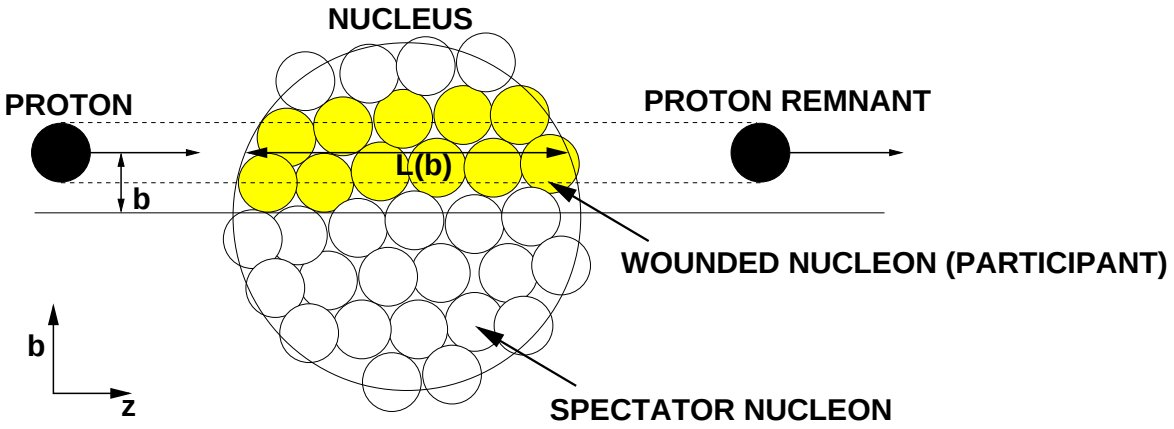

Figure 5.3.1: *Description of a proton-nucleus collision in the Glauber model. The incoming proton propagates through the nucleus in a straight line and collides with the nucleons. The number of wounded nucleons (also called participants) is proportional to the path length inside the nucleus.*

element $d^2\vec{b}$. The probability that a proton, incident with impact parameter b on a target nucleus with A nucleons, undergoes exactly n inelastic sub-collisions is then

$$P(n;b)d^2\vec{b} = \binom{A}{n}[t_A(b)\sigma_{pN}]^n[1-t_A(b)\sigma_{pN}]^{A-n}d^2\vec{b}. \tag{5.3.4}$$

To determine the total cross section for a certain process, we replace σ_{pN} by the cross section for that process and integrate over all impact parameters b.

The inclusive inelastic cross section is the probability of at least one inelastic sub-collision:

$$\sigma_{pA}^{\text{inel}} = \int d^2\vec{b}\left[1-[1-t_A(b)\sigma_{pN}^{\text{inel}}]^A\right]. \tag{5.3.5}$$

If we consider the nucleus as a black sphere, with unit probability for causing one or more inelastic sub-collisions when b is smaller than the radius R,

$$t_A(b) = \begin{cases} 1/\sigma_{pN}^{inel} & b \le R; \\ 0 & b > R \end{cases}, \tag{5.3.6}$$

then the inelastic cross section is simply the surface of a disk with radius R:

$$\sigma_{pA}^{\text{inel}} = \int d^2\vec{b} = \pi R^2 = \sigma_{pN}A^{2/3}. \tag{5.3.7}$$

In contrast, for a hard process such as the creation of a $c\bar{c}$ pair, the cross section is several orders of magnitude smaller than σ_{pN}^{inel}. Replacing σ_{pN} in Eq. 5.3.5 with $\sigma_{pN}^{c\bar{c}} \ll 1$, and taking only the leading order contribution, we obtain

$$\sigma_{pA}^{c\bar{c}}(b) = t_A(b)\sigma_{pN}^{c\bar{c}}A \tag{5.3.8}$$

$$\sigma_{pA}^{c\bar{c}} = \sigma_{pN}^{c\bar{c}}A. \tag{5.3.9}$$

This scaling with A is expected to hold for any process for which the cross section is much smaller than $\sigma_{pN}^{\text{inel}}$.

In general, the A-dependence of the production cross section for some particle X is parametrised as

$$\sigma_{pA}^{X} = \sigma_{pN}^{X} A^{\alpha^X}. \tag{5.3.10}$$

If $\alpha^X < 1$, the production is suppressed by the nuclear environment. Our naive estimate for inelastic interactions of $\alpha = 2/3$ can be considered as a lower limit for α.

In the next chapters we present a measurement of the A-dependence of J/ψ production, parametrised by $\alpha^{\mathrm{J}/\psi}$. A value of $\alpha^{\mathrm{J}/\psi} < 1$ indicates a nuclear suppression of J/ψ production, or 'J/ψ suppression'. Various mechanisms have been proposed that can cause J/ψ suppression. They can be subdivided in 'initial state effects' (nuclear effects on the partons that form a $c\bar{c}$ pair) and 'final state effects' (effects occurring during the formation of a J/ψ).

5.3.2 Initial state effects

Shadowing

Deep-inelastic scattering experiments have shown that the parton densities $f_i^A(x, Q^2)$ in nuclei are different from the parton densities in single protons (see [76] and references therein). The parton density can be depleted or enhanced in a nucleus, depending on the value of x. This effect is commonly referred to as 'shadowing'[1]. The nuclear structure functions are usually given by the ratio of the parton density per nucleon in the nucleus and the density in a proton:

$$R_i^A(x, Q^2) = \frac{f_i^A(x, Q^2)}{f_i^p(x, Q^2)} \tag{5.3.11}$$

The production of $c\bar{c}$ at HERA-B is predominantly due to gluon fusion (see Fig. 5.1.4b). The behaviour of $R_g^A(x, Q^2)$ is not well known yet, but it is expected to be similar to $R_q^A(x, Q^2)$, which has been measured to reasonable precision. Figure 5.3.2 shows a parametrisation for $R_g^A(x, Q^2 = 9\ \text{GeV}^2\ )$ for some of the target materials used at HERA-B.

In the kinematic region where at HERA-B most of the J/ψ are produced and detected ($x_F \approx 0$), we have $x \approx 0.15$. Figure 5.3.2 shows that the gluon density for this x is enhanced by the nuclear environment. If shadowing were the only effect present, we expect $\alpha^{\mathrm{J}/\psi} > 1$ at HERA-B.

Parton energy loss

The parton flux of the incident proton can also be affected by the nuclear environment. Partons are expected to loose energy when traversing matter, leading to depletion of partons of high energy (or x). Several energy loss mechanisms have been proposed,

[1] With 'shadowing' we indicate the overall modification of the parton densities, including the enhancement.

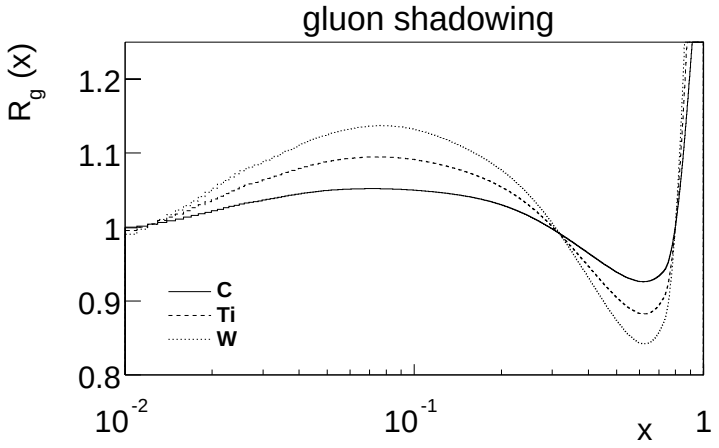

Figure 5.3.2: *Nuclear modification of the gluon structure function as parametrised by the parton density function A-EKS [61] from pdflib version 8.04 [62]. $R_g(x)$ is the ratio of the gluon density in the nucleus over the gluon density in the proton. The scale of $Q^2 = 9GeV^2$ is applicable to open charm production.*

each of which can be characterised by $\Delta x = x'_p - x_p$, the modification of the parton flux of the projectile proton:

$$\begin{array}{lcll} \Delta x & = & \varepsilon_i x A^{1/3} & \text{(from [77])}; \\ \Delta x & \leq & \kappa L(b)/(xs) \quad \propto A^{1/3}/(xs) & \text{(from [78])}; \\ \Delta x & = & CL(b)A^{1/3}/(xs) \quad \propto A^{2/3}/(xs) & \text{(from [79])}, \end{array} \tag{5.3.12}$$

where $L(b)$ is the path length, s the centre-of-mass energy squared, and ε_i, C and κ model dependent constants.

Parton energy loss gives a nuclear suppression at high values of $x_1 = x_p$ (or x_F), where the parton density is strongly reduced. Conversely, the production cross section is enhanced ($\alpha > 1$) at low or negative values of x_F. For a quantitative evaluation of the effect of energy loss mechanisms on J/ψ production, see [80].

Transverse momentum broadening

An effect that is correlated with the nuclear modifications of the parton densities, is an increase in the intrinsic transverse momentum k_T of the partons. The partons of the incident proton are subject to a multiple-scattering-like interactions with the nuclear matter. Besides leading to a reduction of x of the partons, it causes a broadening of the k_T distribution, which is proportional to the path length $L(b)$:

$$\langle k_T^2 \rangle_{pA} = \langle k_T^2 \rangle_{pp} + cL(b). \tag{5.3.13}$$

As a consequence, the p_T spectrum of the J/ψ grows broader with the size of the target nucleus:

$$\langle p_T^2 \rangle_{pA}^{J/\psi} = \langle p_T^2 \rangle_{pp}^{J/\psi} + \lambda A^{1/3}. \tag{5.3.14}$$

Measurements by NA50 [81] and its predecessors of the dependence of $\langle p_T^2 \rangle^{J/\psi}$ on the average path length $\bar{L}$, shown in figure 5.3.3, show the following behaviour:

$$\langle p_T^2 \rangle^{J/\psi} = 1.20(2)\ \mathrm{GeV}^2/c^2 + 0.080(1)\ \mathrm{GeV}^2/c^2\mathrm{fm} \times \bar{L}, \tag{5.3.15}$$

where $\bar{L}$ is the average path length inside the nucleus. It has also been observed that the proportionality with $\bar{L}$ is independent of the centre-of-mass energy.

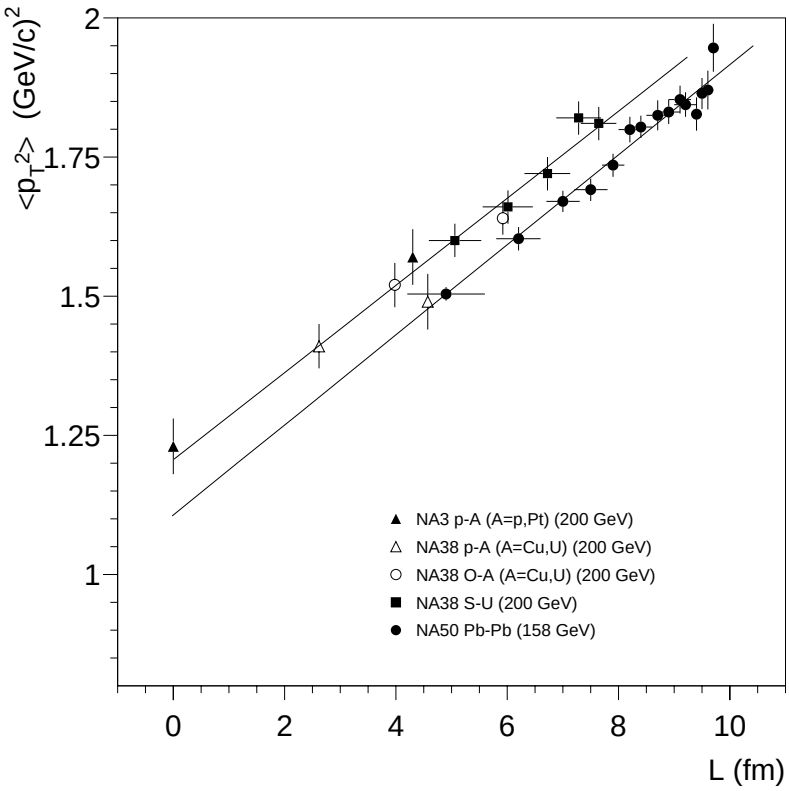

Figure 5.3.3: *Mean transverse momentum of* J/ψ *as a function of the mean path length* $\bar{L}$ *in the nucleus [81]. The mean path length is determined from the total transverse energy produced in the nucleus-nucleus collision. The lower beam energy of NA50 gives values for* $\langle p_T^2 \rangle$ *that are approximately 0.1* GeV^2/c^2 *lower than the data at 200 GeV. The proportionality with L is the same for both data sets.*

5.3.3 Final state effects

Nuclear absorption

The formation of a J/ψ can be thought to occur on a time-scale related to the energy-difference between the various charmonium states. An order of magnitude estimate for the proper distance travelled before the formation of any charmonium state is:

$$\tau_F^{J/\psi} \gtrsim \frac{\hbar}{\Delta E} \approx \frac{2\hbar}{m_{\psi'} - m_{J/\psi}} = 0.6\ \ \mathrm{fm/c} \tag{5.3.16}$$

A similar result is obtained from a fit to data [82].

This formation time must be multiplied by a Lorentz factor $\gamma(x_F)$ as shown in figure 5.1.2. Most of the J/ψ are produced with an $x_F \approx 0$ and a corresponding $\gamma \approx 20$. Since the typical radius of a nucleus is a few fm, this implies that most of the J/ψ are only fully formed outside the nucleus.

Inside the nucleus, they travel as pre-meson $c\bar{c}$ states through the nuclear environment. We expect $c\bar{c}$ pairs to be subject to interactions, similar to those that affect the parton flux of the incident proton. Such interactions reduce the probability that the pre-meson state will ultimately form a J/ψ. Since the individual c quarks experience small p_T kicks from surrounding gluons, the effective mass of the pre-meson state will gradually increase, and may thus rise above the $D\bar{D}$ threshold, preventing a J/ψ from being formed. An alternative interpretation is that the $c\bar{c}$ pair is dissociated, and subsequently escapes the nucleus as separate open-charm hadrons.

The Glauber model, which was used to describe proton-nucleus interactions, can also be used to describe interactions of a $c\bar{c}$ pair with the nuclear matter in which it was formed [83]. One can introduce an 'absorption' cross section, $\sigma_{\rm abs}^{\rm J/\psi}$, and a 'survival probability', $S^{\rm surv}$, and express the production cross section in pA collisions (see also fig. 5.3.4) as:

$$\sigma_{pA}^{\rm J/\psi} = \sigma_{pN}^{\rm J/\psi} \int d^2\vec{b}dz\rho(b,z)S^{\rm surv}(b,z) \tag{5.3.17}$$

$$S^{\rm surv}(b,z) = \exp\left[-\int_z^\infty dz'\rho(b,z')\sigma_{\rm abs}^{c\bar{c}}\right] \tag{5.3.18}$$

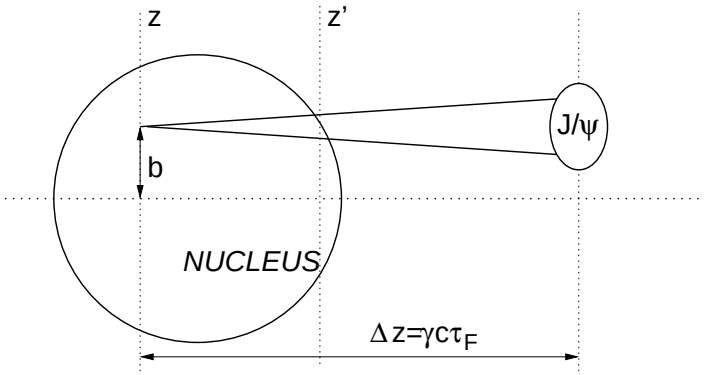

Figure 5.3.4: *Geometrical picture of* J/ψ *formation in a nucleus. The formation of a* J/ψ *takes place on a time scale that is dilated by a factor* $\gamma(x_F)$*. For negative values of* x_F *the* J/ψ *can be fully formed inside the nucleus. While inside the nucleus, the* $c\bar{c}$ *pair interacts with the nuclear matter, which reduces the probability for forming a* J/ψ*.*

For a uniform spherical nuclear density $\rho(b,z) = \rho_0 = 3A/(4\pi R^3)$, and assuming small values for $\sigma_{\rm abs}^{c\bar{c}}$ and for $(\alpha - 1)$, so that

$$\frac{\sigma_{pA}}{\sigma_{pN}} \equiv A^\alpha \approx A - A\ln(A)(1-\alpha), \tag{5.3.19}$$

we can expand Eq. 5.3.17 to obtain:

$$\begin{aligned} \alpha &= 1 - \frac{9}{16}\frac{A\sigma_{\rm abs}^{c\bar{c}}}{\ln(A)\pi R^2} \\ &= 1 - \frac{9}{16}\frac{A^{1/3}}{\ln(A)}\frac{\sigma_{\rm abs}^{c\bar{c}}}{\pi r_0^2}, \end{aligned} \tag{5.3.20}$$

where $r_0 = 1.1$ fm . The dependence on A is weak: for A between 50 and 200, the factor $A^{1/3}/\ln(A)$ differs from unity by up to 10 %. Using this approximation we can write:

$$\sigma_{\rm abs}^{c\bar{c}} = \frac{16\pi r_0^2}{9}(1 - \alpha^{\rm J/\psi}). \tag{5.3.21}$$

If we neglect initial state effects at values of $x_F \leq 0$, the measured value of $\alpha^{\rm J/\psi} \approx 0.95$ [84] corresponds to an absorption cross section of about 3.4 mb.

Here we have assumed a constant absorption cross section. One can also consider the $c\bar{c}$ pair to expand until it reaches the size of the charmonium state. $\sigma_{\rm abs}^{\rm J/\psi}$ is then proportional to the size of the $c\bar{c}$ pair and increases until the J/ψ is formed:

$$\sigma_{\rm abs}^{\rm J/\psi}(z'-z) = \begin{cases} \sigma_{\rm abs}^{c\bar{c}}(t/\tau_F)^2 & t < \gamma\tau_F \\ \sigma_{\rm abs}^{\rm J/\psi} & t > \gamma\tau_F \end{cases} . \tag{5.3.22}$$

The probability of dissociating a fully formed charmonium state at $t > \gamma\tau_F$ can be different for the different states. One may expect the deeply bound J/ψ to be essentially unaffected by the nuclear environment, thus $\sigma_{\rm abs}^{\rm J/\psi} \approx 0$. Weakly bound states such as χ_c and ψ' could still be broken up, leading to a suppression at low values of x_F. In this model one expects nuclear suppression of ψ' to be stronger than J/ψ suppression. This is agreement with data [84].

If the J/ψ production is described by the colour octet model, one can assume colour neutral charmonium states to have been preceded by coloured $c\bar{c}$ states. A colour octet $c\bar{c}$ state would interact with the nuclear environment with a larger absorption cross section [80]:

$$\sigma_{\rm abs}^{c\bar{c}\ \rm octet} > \sigma_{\rm abs}^{c\bar{c}\ \rm singlet}. \tag{5.3.23}$$

This would imply that J/ψ and ψ', mostly produced via a colour octet states, are more strongly suppressed than χ_c, which are mainly produced in a colour singlet state [85]. No data on χ_c suppression exist to date, but HERA-B is expected to measure this in 2002.

Co-mover suppression

Another possible mechanism for nuclear suppression is due to the scattering of $c\bar{c}$ states or fully formed charmonium states with other particles produced in the interaction. If such associated particles are close in phase space they can interact with the charmonium, causing a dissociation of the charmonium state into open charm, before it can decay.

It is generally assumed that fully formed J/ψ states are too deeply bound to be broken up by co-mover interactions. This is not the case for excited charmonium states such as ψ' and χ_c, that are barely below the open charm threshold. The production of ψ' and χ_c is therefore more strongly suppressed by co-movers than the (direct) production of J/ψ.

Colour screening in a quark-gluon plasma

In energetic and central nucleus-nucleus collisions one expects energy densities sufficient for the formation of a de-confined state of matter or 'quark-gluon-plasma'(QGP). The production of J/ψ is expected to be strongly suppressed in a QGP because of colour screening [86]. In fact, an anomalously reduced J/ψ yield is possibly the clearest indication that such a quark-gluon-plasma (QGP) has formed [87].

Colour screening indicates that the $c\bar{c}$ binding potential of Eq.5.2.1 is affected by the medium of freely moving colour charges of the QGP. The string tension K in the term Kr decreases with the density of free colour charges, or equivalently, with the temperature T of the medium:

$$Kr \rightarrow \frac{K}{\mu(T)}(1 - e^{-\mu(T)r}) \tag{5.3.24}$$

where $\mu(T)$, called the screening mass, increases with the temperature T. The results of Lattice QCD simulation [86] can be parametrised as:

$$\mu(T) \approx \frac{1}{4}\frac{T}{T_c}. \tag{5.3.25}$$

The critical temperature T_c is the temperature at which the phase transition from hadronic matter to a QGP occurs. It is estimated at $T_c \approx 260$ MeV [88].

In a QGP, the colour charge of the charm quarks are effectively reduced, due to the Debye screening by the colour-conducting medium. Consequently, the Coulomb-type potential becomes a Yukawa-type potential:

$$-\frac{4}{3}\frac{\alpha_S(1/r^2)}{r} \rightarrow -\frac{4}{3}\frac{\alpha_S(1/r^2)}{r}e^{-\mu(T)r}, \tag{5.3.26}$$

so that the $c\bar{c}$ binding potential in a QGP becomes:

$$V(r) = \frac{K}{\mu(T)}(1 - e^{-\mu(T)r}) - \frac{4}{3}\frac{\alpha_S(1/r^2)}{r}e^{-\mu(T)r} \tag{5.3.27}$$

At sufficiently high temperature $T > T_c$, the $c\bar{c}$ binding potential becomes ineffective and the charmonium state therefore dissociates into open charm before it can decay.

Since the binding energy of the excited charmonium states ψ' and χ_c is much less than that of the J/ψ, these states can be broken up more easily and 'melt' at lower temperatures. The production of J/ψ, including the feed-down from these excited states, is suppressed stepwise with increasing temperature. When the QGP temperature is sufficient for the melting of (direct) J/ψ, no more J/ψ should be visible.

A recent measurement by NA50 [89], presented in figure 5.3.5, shows an abrupt decrease of the J/ψ yield in central Pb-Pb collisions. At energy densities above 3 GeV/fm^3, the number of produced J/ψ is 60%-70% of what is expected. This decrease is in agreement with the disappearance of the contribution from excited states to the total J/ψ yield.

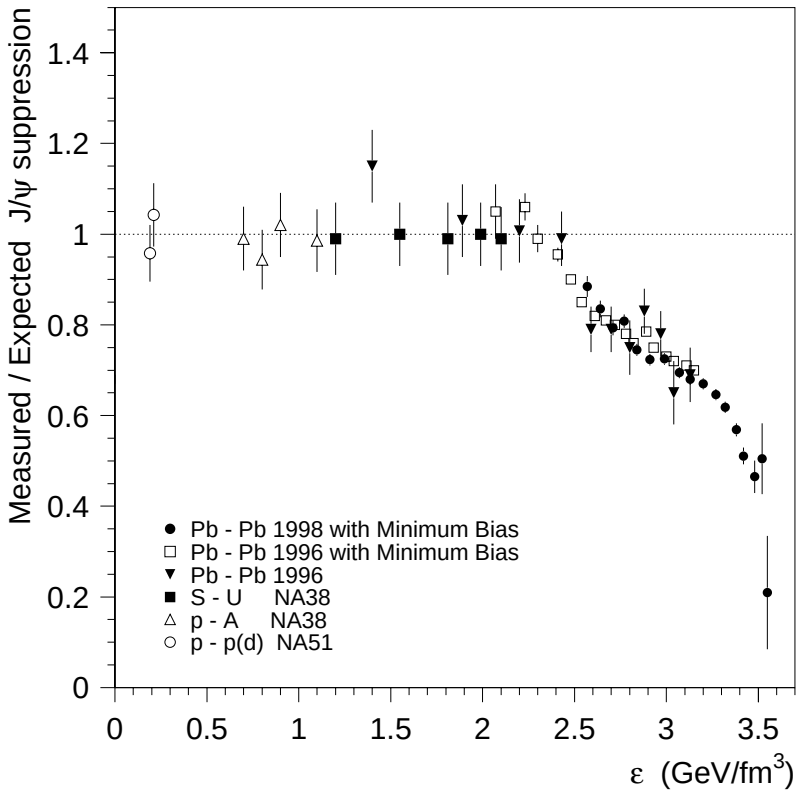

Figure 5.3.5: *Measured J/ψ production yields, normalised to the yields expected from a constant nuclear absorption by the nuclear medium. The ratio is shown as a function of the energy density reached in the nucleus-nucleus collision [89].*

Summary on nuclear effects

The complete mechanism for J/ψ suppression is far from being understood. Whether or not the anomalously large suppression in central Pb-Pb collisions is due to a QGP, is a subject of lively debate. The data of NA50 can equally be explained by a co-mover suppression mechanism [90]. The co-mover suppression mechanism, however, has not been established in pA collisions yet. With the full reconstruction of particles associated with a J/ψ, HERA-B could provide evidence for this mechanism for the first time.

5.4 Measuring nuclear effects in J/ψ production

The experimental data on J/ψ suppression can be subdivided into three types of measurements:

(i) **Dependence on A**
Nuclear effects in J/ψ production lead to a deviation from the scaling of the cross section with the atomic number A of the target, as discussed in section 5.3.1. The suppression parameter $\alpha^{J/\psi}$ can be determined from the cross section ratio for targets with different atomic numbers A_1 and A_2:

$$\alpha^{J/\psi} = \frac{\ln\left[\sigma^{J/\psi}_{pA_1}/\sigma^{J/\psi}_{pA_2}\right]}{\ln[A_1/A_2]}. \tag{5.4.1}$$

(ii) **Dependence on number of tracks or E_T**
The effective proton path length $L(b)$ can be measured indirectly from event variables, such as the charged track multiplicity or the total transverse energy in the event. Within the Glauber model, the number of wounded nucleons scales with the path length and each of these wounded nucleons will independently produce hadrons, which can be observed as charged tracks or energy deposits in a detector.

The spread in these quantities for a fixed path length is however sizable. Consequently, the correspondence to the path length L is diluted, especially for interactions with a small number of participants.

(iii) **Dependence on x_F**
With a measurement of the longitudinal momentum, or, equivalently, the x_F of the J/ψ, the parton momentum fractions x_1 and x_2 can be determined. The parton densities for the incoming proton and the target nucleus are modified due to the nuclear environment and consequently lead to different suppression for different values of x_F.

In addition, the nucleus appears Lorentz contracted by a factor γ, which is directly related to x_F (Fig. 5.1.2). For positive values of x_F, ($\gamma > 22$), the formation of a J/ψ takes place on a scale that is larger than the size of the nucleus. Conversely, for values of $x_F < -0.3$ and sufficiently large nuclei, the J/ψ can be fully formed inside the nucleus.

The x_F dependence of J/ψ and ψ' suppression in pA collisions has recently been measured by the E866 experiment [84]. This measurement surpasses all previous measurements in precision. Figure 5.4.1 shows the dependence of α on x_F and p_T for J/ψ and ψ'. The E866 data show that the more loosely bound ψ' is more strongly suppressed than J/ψ at low x_F, as expected from a size-dependent absorption mechanism. The high x_F data indicate a stronger suppression than expected from only shadowing effects and therefore suggest the presence of parton energy loss mechanisms.

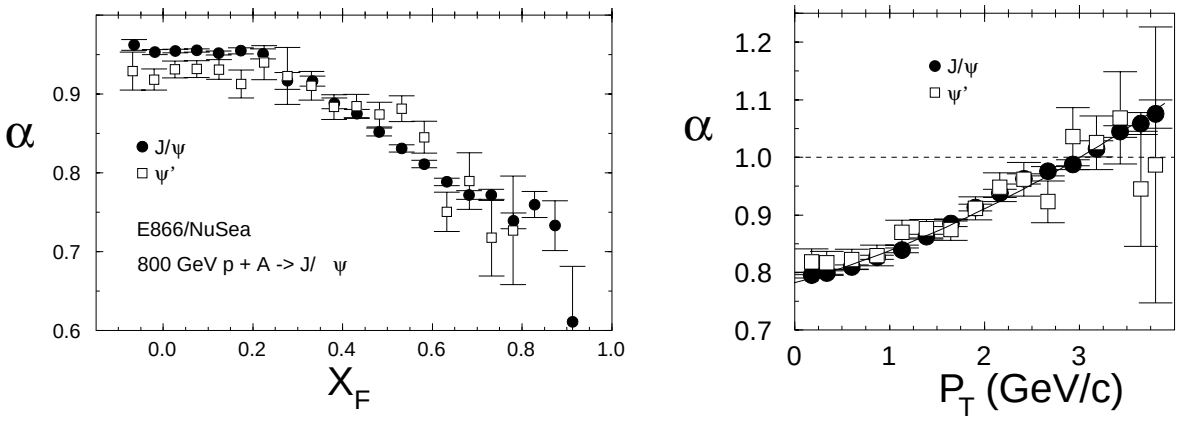

Figure 5.4.1: *Suppression parameter α for J/ψ and ψ' as a function of x_F as measured by E866 [84] in 800 GeV pBe, pFe and pW interactions. The final state effects, which are dominant at low x_F, lead to a stronger suppression for ψ' than for J/ψ. The high x_F behaviour is predominantly due to initial state effects (shadowing and parton energy loss), which are the same for ψ' and J/ψ. The increase of α with p_T is a direct consequence of the broadening of the p_T spectrum.*

5.4.1 Separating initial state effects

Initial state effects can be disentangled from final state effects such as (co-mover) absorption. Two production processes can be used for this that are both sensitive only to the initial state effects: Drell-Yan production and open charm production.

Drell-Yan production

A process that is often used to identify initial state effects is the production of Drell-Yan $\mu^+\mu^-$ pairs. Such pairs contribute to the continuum in the di-muon mass spectrum in which the J/ψ appears as a peak around 3.1 GeV/c^2. In the absence of other contributions to the continuum, they can be readily selected as di-muons in the mass range outside the range of charmonium or bottomium resonances.

Heavy ion experiments such as NA50 measure the ratio of the J/ψ yield over the Drell-Yan yield as a function of the E_T in the event. At HERA-B, such a measurement is difficult since the Drell-Yan contribution to the di-muon continuum is small compared to the contribution of random combinations of muons from decaying pions and kaons: in contrast to NA50 or E866, HERA-B does not immediately filter out these hadrons by a hadron absorber near the target.

A recent measurement of Drell-Yan production in pA collisions [91] shows some evidence for initial state effects beyond the modified nuclear parton densities.

A drawback of using Drell-Yan lepton pairs is that it is only sensitive to modified (anti-)quark densities, whereas J/ψ production is predominantly due to gluon fusion. Although they are expected to be similar, this must be experimentally verified.

Open charm production

Approximately 95% of the $c\bar{c}$ pairs do not bind into charmonium, but form separate charmed mesons. Initial state effects in open charm production are by definition the same as those of charmonium, because they are created with the same partonic cross sections. Open charm production is therefore optimally suited for measuring the modification of the gluon flux in pA or AA collisions. No sufficiently accurate data on the A dependence of open charm production exists.

5.4.2 The potential of HERA-B

The HERA-B experiment is well suited for measuring nuclear effects in J/ψ production, even though it was not designed for this purpose. Compared to most of the experiments that have performed similar measurements in the past, there are some favourable characteristics:

- **Simultaneous use of different target materials**
  The synchronous operation of different target wires has the particular advantage that detector performance and data taking conditions are at all times identical. Systematic uncertainties in measurements of the A dependence are therefore greatly reduced.

- **New kinematic acceptance**
  The HERA-B spectrometer covers angles between 10 and 220 mrad. This angular acceptance includes a large part of the backward hemisphere in the centre-of-mass and corresponds to an x_F acceptance of $-0.4 < x_F < 0.3$. Present measurements are predominantly in the positive x_F region.

- **Reconstruction of the complete event**
  In contrast to experiments such as NA50 and E866, HERA-B reconstructs a large fraction of the charged particles in the event. Furthermore, the presence of a calorimeter enables an efficient reconstruction of χ_c states through their radiative decay $\chi_c \to \mathrm{J}/\psi\gamma$.

In the following chapters we present a measurement of the A-dependence of the J/ψ production cross section, integrated over x_F. In the future, with a fully operational detector, HERA-B can address the following open questions on nuclear effects in charmonium production:

- **What is the suppression at negative x_F ?**
  At negative x_F, the initial state suppression effects (shadowing and parton energy loss) are small. Therefore this kinematic region provides a relatively pure measurement of the nuclear absorption cross section of J/ψ.

- **Is there suppression due to scattering with co-movers ?**
  Co-mover absorption is experimentally not established. The theoretical calculations suffer from large uncertainties in the assumed co-mover absorption cross

section. HERA-B, with its large phase-space coverage and full event reconstruction, is in a unique position to verify this mechanism, which would reveal itself in a relative depletion of particles close in phase space to the charmonium state.

- **Is there a difference between the suppression if J/ψ, ψ' and χ_c?**
  The E866 data indicate that the ψ' is more strongly suppressed than the J/ψ. These differences should become more pronounced at negative x_F. A surprising prediction [85] of the colour octet absorption mechanism is that both J/ψ and ψ' are more strongly suppressed than χ_c. HERA-B will be able to do a first measurement of χ_c suppression.

- **What is the A dependence of open charm production ?**
  With the use of a special trigger, HERA-B can collect and reconstruct a sizeable sample D mesons and measure for the first time the A dependence of open charm production. Gluon shadowing and energy loss effects can then be cleanly separated from other effects present in charmonium production.

Chapter 6

Measurement of the luminosity ratio

In July and August of 2000, HERA-B accumulated data for physics analysis. Part of the data sample taken during physics running in July and August of 2000 used both a carbon and a titanium target wire simultaneously. This allows a determination of the A-dependence of the J/ψ production cross section.

A measurement of the ratio of J/ψ yields is presented in the next chapter. In this chapter we determine the luminosity ratio with three different approaches, all using inclusive inelastic interactions as a control channel.

6.1 Measurement method

6.1.1 Luminosity ratio from inelastic interactions

The A dependence of the J/ψ production cross section, as parametrised by $\alpha^{J/\psi}$, is measured from the ratio of J/ψ yields and the ratio of luminosities of the two target wires:

$$\alpha^{J/\psi} = \frac{1}{\ln(A_{Ti}/A_C)} \ln \left[\frac{N_{Ti}^{J/\psi}}{N_C^{J/\psi}} \frac{\epsilon_C^{J/\psi}}{\epsilon_{Ti}^{J/\psi}} \frac{\mathcal{L}_C}{\mathcal{L}_{Ti}} \right]. \tag{6.1.1}$$

A direct determination of the total luminosity requires knowledge of the number of protons in the halo passing through the target wire. This is not possible at HERA-B. The luminosity can, however, be determined indirectly with a suitable control channel: a production process for which the cross section is well known and for which the efficiency can be well determined (and is preferably large). A suitable control channel is the production of inclusive inelastic interactions:

$$\frac{\mathcal{L}_{Ti}}{\mathcal{L}_C} = \frac{N_{Ti}^{inel}}{\sigma_{pTi}^{inel}} \frac{\sigma_{pC}^{inel}}{N_C^{inel}}, \tag{6.1.2}$$

where N_{Ti}^{inel} and N_C^{inel} are the yields of inelastic interactions. We will present three different approaches to determine the ratio of inelastic yields

$$R^{inel} \equiv \frac{N_C^{inel}}{N_{Ti}^{inel}} \tag{6.1.3}$$

of the two target wires. This essentially means counting the observed number of inelastic interactions and correcting for the reconstruction efficiency, which is determined using a Monte Carlo simulation.

We can easily identify inclusive inelastic interactions by the occurrence of hits in the tracking chambers, photons in the RICH, or one or more reconstructed primary vertices. Both the inelastic yield and the efficiency can be determined with sufficient accuracy. Moreover, since we measure a *ratio*, many systematic uncertainties cancel.

6.1.2 Dependence of inelastic production cross section on A

The A dependence of the inclusive inelastic cross section is parametrised as

$$\sigma_{pA}^{\text{inel}} = \sigma_{pN} A^{\alpha^{\text{inel}}}. \tag{6.1.4}$$

Based on the opacity of the nucleus (see section 5.3.1) we estimated $\alpha^{\text{inel}} = 2/3$. A compilation of all pA data [92] shows that the average value is $\alpha^{\text{inel}} = 0.71$ for incident proton momenta up to 300 GeV/c, slightly higher than naively expected. This value is observed to increase slowly with the momentum of the incident proton.

The inelastic cross section deviates from a simple power law when one includes very light targets such as Be. An empirical parametrisation [8] which gives a reasonable description of the data in a large range of A is:

$$\sigma_{pA}^{\text{inel}} = \sigma_{pN}^{\text{inel}} A^{2/3}[1.3 + 0.15 \log_{10} A]. \tag{6.1.5}$$

For a carbon-titanium combination, this corresponds to $\alpha^{\text{inel}} = 0.71$ when parametrised as a simple power law. The data used in this fit are, however, also at proton momenta that are systematically lower that the 920 GeV/c of HERA-B.

For this measurement we take $\alpha^{\text{inel}} = 0.72$, which is estimated by extrapolating the momentum dependence of α^{inel} [92], to p=920 GeV/c. For the carbon-titanium combination this then gives:

$$\frac{\sigma_{\text{pTi}}^{\text{inel}}}{\sigma_{\text{pC}}^{\text{inel}}} = \left[\frac{A_{\text{Ti}}}{A_{\text{C}}}\right]^{\alpha^{\text{inel}}} = \left[\frac{47.88}{12.01}\right]^{0.72} = 2.71. \tag{6.1.6}$$

The uncertainty in α^{inel} is an irreducible systematic uncertainty in the measurement of $\alpha^{\text{J}/\psi}$. Based on the data [92] we estimate the allowed values for α^{inel} to be between 0.71 and 0.73. This gives a systematic uncertainty to the ratio of inelastic cross sections of 1.5%.

We have assumed here that the inelastic cross section ratio can be parametrised with a power law. Without this assumption and using only the measured values of $\sigma_{\text{pC}}^{\text{inel}}$ and $\sigma_{\text{pTi}}^{\text{inel}}$ (table 1.3.1), we would obtain a ratio of 2.75 with an uncertainty of 4 %.

6.1.3 Monte Carlo generation of inelastic interactions

For the determination of acceptance corrections we make use of a Monte Carlo simulation. Inelastic interactions are simulated by the event generator FRITIOF [38]. The creation of an inelastic pA collision by FRITIOF is based on the Glauber model, and comprises the following steps:

(i) **Generation of collision geometry**
The nucleus is built up by placing nucleons one after the other, according to the Woods-Saxon density profile and requiring that the centre of each nucleon is separated from the centre of any other by at least 1 fm . A random impact parameter b is subsequently generated for the incident proton. The nucleons that overlap with the path of the proton inside the nucleus are considered wounded.

(ii) **String creation and fragmentation**
Each of the wounded nucleons constitutes an independent proton-nucleus collision in which two colour strings are generated. These strings subsequently fragment into the final state particles according to the LUND [93] fragmentation model.

(iii) **Generation of hard parton scattering**
The latest version of FRITIOF includes the generation of hard scattering processes, that describe the creation of particles at high p_T. Each proton-nucleon collision has a small probability to involve a hard scattering of the partons. The hard interactions are generated by PYTHIA [37] and give rise to extra fragmenting strings.

FRITIOF uses a number of tunable parameters such as the distribution of impact parameters, the transverse momentum distribution of (soft) strings, cross sections, nucleon-nucleon overlap functions, etc. The values for these parameters have been tuned to describe a large amount of experimental data.

In this analysis we will assume that the generation of inelastic interactions is accurate and does not lead to additional systematic uncertainties. In support of this assumption is the observation that the multiplicity distribution in the data of HERA-B is well described by the Monte Carlo simulation, as will be shown later. We assume that interactions with low multiplicities such as diffractive processes, which cannot be observed by the HERA-B detector and therefore play an important role in the acceptance corrections, are also correctly simulated.

We make use of two samples of 50.000 Monte Carlo generated inelastic pTi and pC interactions. Secondary interactions of the generated particles with the detector material were simulated by GEANT [39]. The Monte Carlo events were subsequently digitised, taking into account hit efficiencies. The event reconstruction was identical to the one used for data.

6.2 Data set

6.2.1 Runs

The data used in this analysis were taken between 24th of July 2000 and the 16th of August 2000. In total about 1.5 million events were written to tape. In the runs selected for this analysis, the interaction rate was continuously shared between two target wires: Inner II (carbon) and Below I (titanium). For almost the complete data set the interaction rate was 5 MHz .

6.2.2 Random triggers and J/ψ triggers

The ratio of inelastic interactions is determined in events, that are recorded with a random trigger. Upon a random trigger, the detector data was recorded for a randomly chosen bunch crossing, without any requirement on the content of the data. These events may contain an interaction, but this was not required. They are therefore free of any bias (efficiency, dead-times, etc.) that a trigger might otherwise induce.

During data taking, random triggers were continuously issued at a rate of typically 4 Hz, amounting to approximately 30% of the total output event rate. In total 480796 random trigger events were recorded in the runs used. All other recorded events were accepted by a J/ψ trigger, the criteria of which are described in the next chapter.

6.2.3 Event reconstruction

All events accepted by the SLT, either on a random trigger or on a J/ψ-trigger, were reconstructed online by the 4LT/FARM, using the HERA-B reconstruction software ARTE. The event reconstruction was independent of the type of trigger issued.

For each of the sub-detectors a stand-alone reconstruction program was executed, as summarised in table 6.2.1. A matching package was used to combine track segments, ECAL clusters and RICH rings into long tracks, that were subsequently re-fitted. Tracks in the vertex detector, containing momentum information (if matched) or otherwise with an estimated average momentum, were used by a vertex reconstruction package to reconstruct primary and secondary vertices.

Sub-detector	Package	Description
VDS	CATS [94]	Cellular automata based pattern recognition, clone removal, track fit.
Main Tracker	RANGER [40]	Kalman filter pattern recognition and track fit.
ECAL	CARE [47]	Hierarchical cluster reconstruction method.
RICH	RISE [95]/RITER [96]	Stand alone (RISE) or external track based (RITER) ring search.
MUON	MUREC-A [97]	Track finding/fit (Kalman filter).
Matching	MARPLE [98]	Makes 3σ cut on track parameter differences.
Vertexing	GROVER [99]	Topological vertex finding and Kalman filter fit.

Table 6.2.1: *Reconstruction packages in the Hera-B reconstruction framework ARTE.*

After the track and vertex reconstruction, several modules were invoked to reconstruct decays. These include the J/ψ candidates through their leptonic decays, but also Λ and K^0_S, in which case the RICH was used for particle identification.

All reconstructed events were stored on tape (DST). A sub-selection of the event data, comprising vertex detector tracks, calorimeter clusters and reconstructed decays, was stored in the smaller mini-DST format. This enabled a faster access and processing of the events.

After data taking, several improvements were made in the reconstruction software and in the alignment of the detector. This made a new reconstruction of events beneficial. The complete physics data set of 2000 has undergone several iterations of re-processing during the shutdown that followed data taking in 2000. This analysis uses the data, that had been reprocessed in February and March 2001 (rp0002).

6.2.4 Event selection

The random trigger also records events in bunch crossings that are nominally empty, whereas these bunches are masked out in the J/ψ trigger. These bunches sometimes yield an interaction, and, as can be seen in figure 6.2.1, do so more often on the titanium wire than on the carbon wire. We mask them out also in the selection of random trigger events, since we would otherwise systematically overestimate the contribution from the titanium wire.

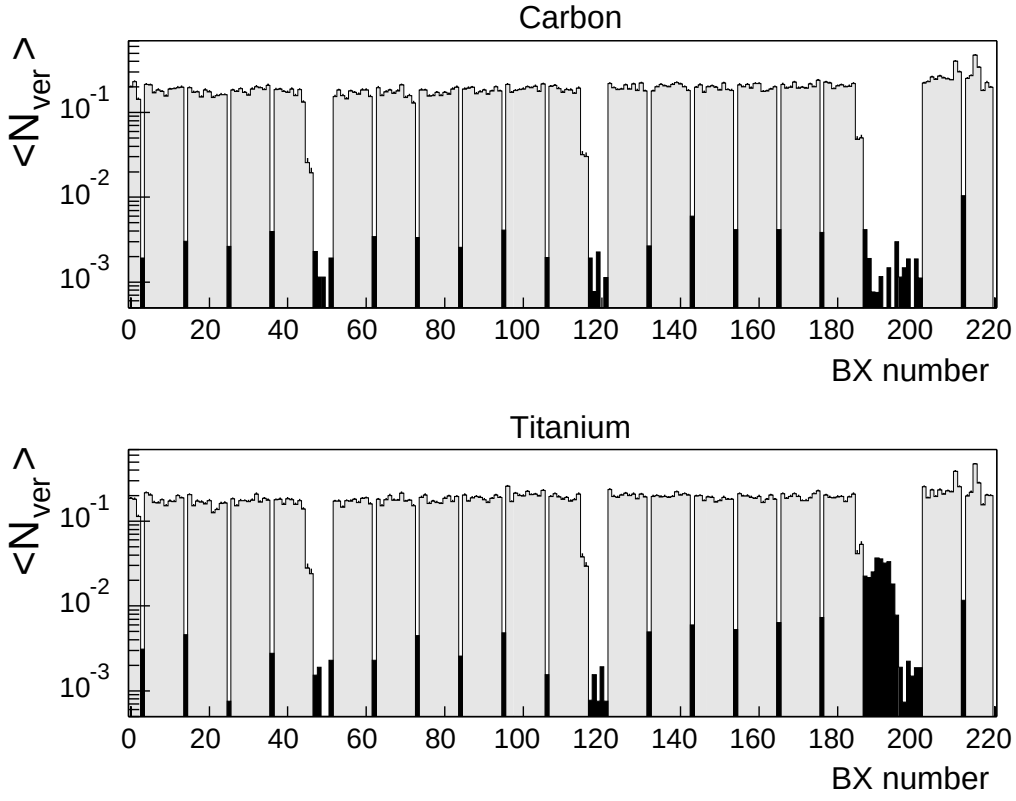

Figure 6.2.1: *Contribution of the individual bunches to the total interaction rate. The nominally empty bunches are indicated in black. They are discarded for the measurement of* R^{inel}.

The final analysis is done within the object oriented analysis framework ROOT [100]. Information for determining R^{inel} is stored for all random trigger events. This includes the total energy deposit in the calorimeter, the total numbers of hits in the outer tracker, vertex detector and RICH, and the parameters of reconstructed vertices.

6.3 Event weighting

The efficiency to trigger and reconstruct a J/ψ was not constant during the period, in which the data of this analysis were taken. The performance of sub-detectors, especially the Outer Tracker and the ECAL, was not stable. Fluctuations in the trigger efficiency and dead-times were of the order of 20 %. The distribution of inelastic interactions was also not constant (see Fig. 1.3.2), and neither was the total interaction rate. Furthermore, the bandwidth allotted to random trigger events had not always been set to the typical value of 4 Hz. Consequently, the ratio of the number of inelastic interactions to the number of J/ψ varied in time:

$$R(t) = \frac{\dot{N}^{\mathrm{J}/\psi}(t)}{\dot{N}^{\text{inel}}(t)}. \tag{6.3.1}$$

Unfortunately, the small J/ψ yield does not permit a time dependent measurement. However, since the trigger *criteria* did not change in the period under study, we may assume the number of recorded (true) J/ψ at any moment to be proportional to the number of candidates passing the J/ψ-trigger:

$$\dot{N}^{\mathrm{J}/\psi} = \epsilon^{\mathrm{J}/\psi}(t)\mathcal{L}(t)\sigma^{\mathrm{J}/\psi} = C\sigma^{\mathrm{J}/\psi}\dot{T}^{\mathrm{J}/\psi}(t), \tag{6.3.2}$$

where $\dot{T}^{\mathrm{J}/\psi}(t)$ is the rate of J/ψ-triggers. This means that the non-J/ψ background, which dominates the J/ψ-trigger rate, is equally affected by the fluctuating detector performance.

The time dependence of the number of recorded inelastic interactions is:

$$\dot{N}^{\text{inel}}(t) = \dot{T}^{\text{rnd}}(t)\mathcal{L}(t)\sigma^{\text{inel}}, \tag{6.3.3}$$

where $\dot{T}^{\text{rnd}}(t)$ is the rate of random triggers.

We take these fluctuations into account by including time-dependent weights in the determination of the luminosity ratio. If $\epsilon^{\mathrm{J}/\psi}(t)$ was lower than average at some point in time t, then the importance of the relative luminosity, measured at that moment, is accordingly tuned down. Similarly, if the rate of random triggers was high, the importance of the measured luminosity ratio is reduced.

The importance weighting equalises the *random trigger density*, i.e. the ratio of random triggered events and J/ψ-triggered events. This is achieved by time dependent event weights:

$$\begin{aligned} w(t) &= \frac{\dot{T}^{\mathrm{J}/\psi}(t)}{\dot{T}^{\text{rnd}}(t)} \\ &= \frac{\text{Number of J}/\psi\text{-triggered events}}{\text{Number of random triggered events}}. \end{aligned} \tag{6.3.4}$$

The weights $w(t)$ are determined in time bins of 1000 sequentially recorded events, corresponding to a new weight per minute. The distribution of the random trigger density and the time dependence of $w(t)$ are shown in figure 6.3.1.

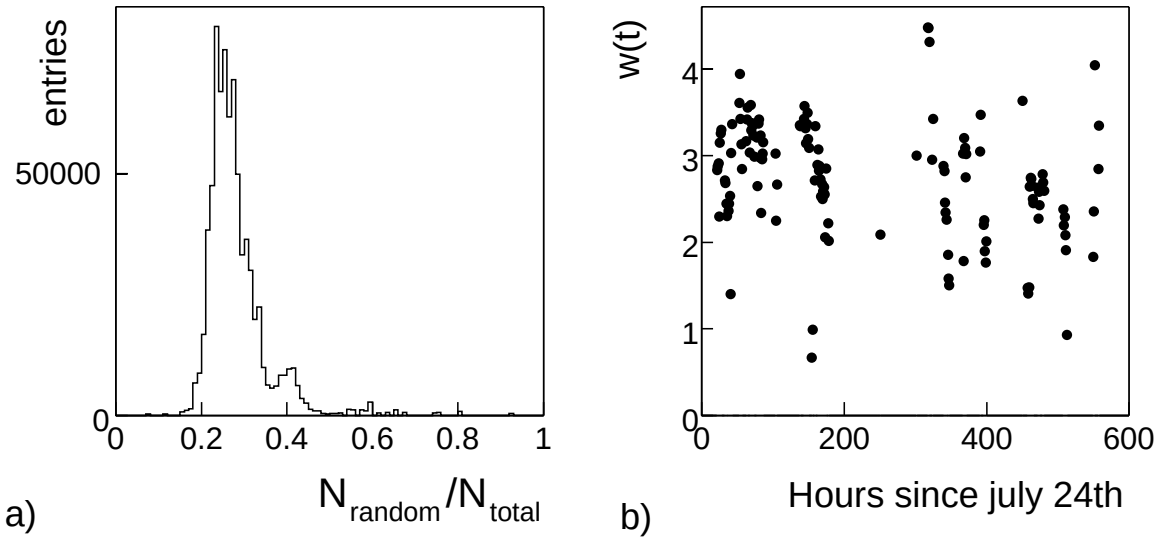

Figure 6.3.1: *Distribution of the random trigger density (figure a) and the time dependence of the event weights $w(t)$ (figure b). A low value of $w(t)$ indicates a low trigger efficiency or large dead-times.*

There is a systematic uncertainty associated with the arbitrariness of the size of the time bin. This uncertainty is estimated by comparing the results for a weight per 1000 events, with the results obtained using a single event weight for each run. The difference is observed to be negligible.

6.4 Measuring R^{inel} with reconstructed vertices

A straightforward method of counting interactions is by determining the number of primary vertices. If we know the vertex reconstruction efficiency for both wires, the number of inelastic interactions can be directly extracted.

The vertex finding algorithm [99] uses the position of the inserted wires in a pre-selection of the vertex tracks. The tracks are required to be compatible with one of the wires within $3.5\sigma_t$, where σ_t is the estimated uncertainty on the impact parameter of the tracks in the z-plane of the wire. After this pre-selection, a Kalman filter is used for the fit. For a primary vertex to be found at least three tracks must be compatible with the wire.

6.4.1 Vertex reconstruction efficiency

The vertex reconstruction efficiency is defined as the probability to find a reconstructed primary vertex if there was one inelastic interaction. We expect this efficiency to be different for the two target wires. An inelastic interaction on the titanium wire produces on average about 28% more tracks from the primary interaction point than an interaction on the carbon wire, which is confirmed by figure 6.4.1. The reconstruction efficiency is therefore larger for the titanium wire. Secondly, the two wires are 3.5 cm apart, which implies a different geometrical acceptance in the vertex detector.

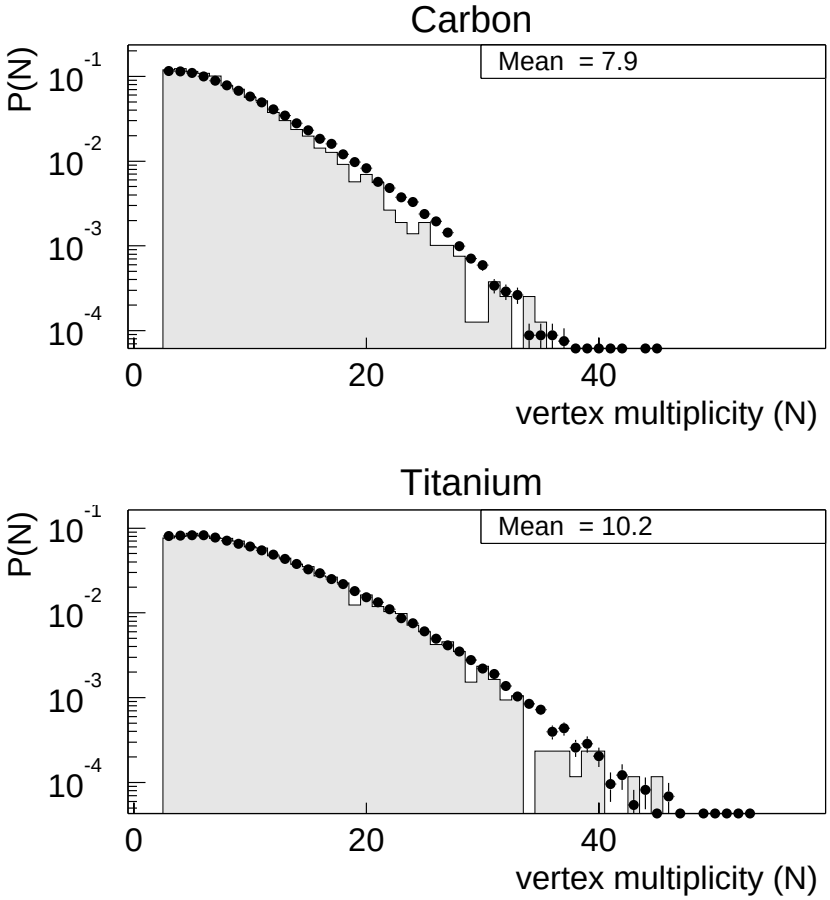

Figure 6.4.1: *Number of tracks per reconstructed primary vertex on the carbon wire and the titanium wire. Solid circles show the data and the hatched histogram show the Monte Carlo simulation.*

From figure 6.4.1 we see that nuclear effects on the charged track multiplicity are reasonably well simulated by FRITIOF. In the data, there is a small but significant excess in the region of high vertex multiplicity. This has been observed for all target materials in HERA-B [7] and agrees with previous observations of the E814 collaboration [101]. We expect this discrepancy to have a negligible effect, since here the vertex reconstruction efficiency is practically 100% regardless of the target wire material.

Misalignment and noise have not been taken into account in the Monte Carlo simula-

tion. These effects have a significant impact on the vertex resolution and reconstruction efficiency. Figure 6.4.2 summarises the performance of the primary vertex reconstruction in data and in a Monte Carlo simulation. The top plot gives the reconstructed z position, from which the primary vertex resolution is measured. The lower two plots give the average number of track segments used to reconstruct this primary vertex, as a function of the total number of track segments in the vertex detector.

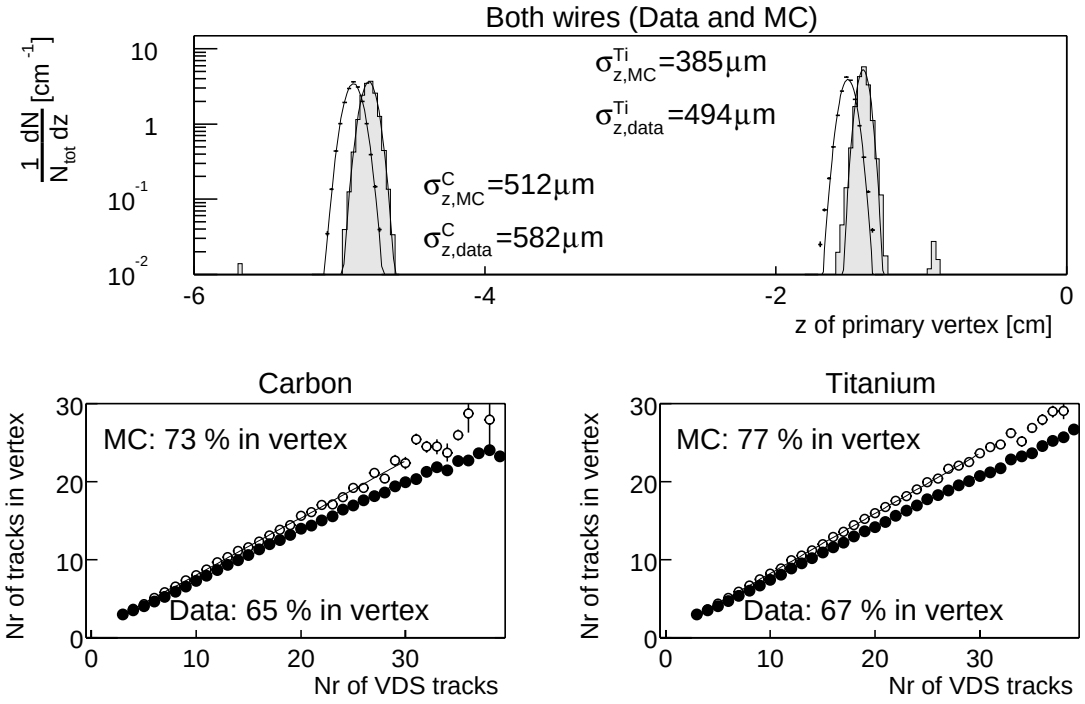

Figure 6.4.2: *Comparison of the vertex reconstruction performance in data and from a Monte Carlo simulation. The upper plot shows the reconstructed z coordinate of the primary vertex and the vertex resolutions obtained from Gaussian fits. The Monte Carlo result is indicated by the shaded histogram. The lower two plots show the fractions of tracks reconstructed by the vertex detector that is compatible with the primary vertex, for data (solid) and Monte Carlo (open circles), and for both wires separately.*

There are small but significant differences between the data and the Monte Carlo simulation. The fact that in the Monte Carlo simulation the target wires are slightly displaced w.r.t. their real position should not worry us too much, since these displacements are small compared to the distance to the vertex detector modules, and therefore they have a negligible effect on the estimated difference in geometrical acceptance.

The lacking description of misalignment in the Monte Carlo overestimates the precision with which tracks in the vertex detector are reconstructed. This causes an overestimated resolution, and, more importantly, an overestimated number of tracks that are compatible with the primary vertex. The vertex reconstruction efficiency obtained from our Monte Carlo simulation is therefore expected to be systematically higher than the actual performance. Since the carbon wire has on average fewer tracks

per interaction, the efficiency for this wire is more affected by this than that for the titanium wire.

Preferably one would incorporate misalignment and noise effects in the Monte Carlo simulation. This was not feasible for the data of 2000. However, we can perform an effective correction. We determine the probability p that a track, found to be compatible with the primary vertex in Monte Carlo, would also be so in reality. This probability is estimated as the fraction of the track segments that is used for the primary vertex in the Monte Carlo simulation, divided by the same fraction in data (0.73/0.65 and 0.77/0.67 for carbon and titanium respectively). Since a primary vertex should contain at least three tracks, the corrected reconstruction efficiency for a vertex of N tracks then reads:

$$\epsilon^N_{\mathrm{ver,corr}} = \sum_{n\geq 3}^{N} \binom{N}{n} p^n (1-p)^{N-n} \epsilon^N_{\mathrm{ver}}. \tag{6.4.1}$$

Interactions with a large number of charged tracks can lead to vertex splitting, i.e. the reconstruction of two primary vertices for a single interaction. Furthermore, there is a small probability that a vertex will actually be found on a wire different from the one where the interaction took place. While events were generated on one of the two wires exclusively, we have assumed both of them to be inserted in the event reconstruction. This allows an estimate for the probability of a wrong target assignment.

The vertex reconstruction efficiencies are summarised in table 6.4.1. To illustrate the importance of misalignment and noise we also show the uncorrected values.

Wire	ϵ_0	ϵ_1	ϵ_2	ϵ_w
C (uncorrected)	19.77 %	79.09 %	0.72 %	0.42%
Ti (uncorrected)	13.00 %	85.25 %	1.61%	0.14%
C (corrected)	24.13 %	74.87 %	0.74 %	0.26%
Ti (corrected)	15.90 %	82.56 %	1.45 %	0.09 %

Table 6.4.1: *Vertex reconstruction efficiency for single inelastic interactions before and after applying the correction given by Eq. 6.4.1.* $\epsilon_{i=\{0,1,2\}}$ *are the probabilities of reconstructing* i *vertices, and* ϵ_w *is the probability that the vertex is reconstructed on the wrong target wire.*

The higher average vertex multiplicity of the titanium wire leads both to a larger probability of vertex splitting, and a smaller probability to have the primary vertex reconstructed on the wrong target wire. It has been checked that wrongly assigned vertices have a larger χ^2_{ver} per degree of freedom and a lower than average track multiplicity, as expected.

Taking into account vertex splitting and wrong assignments, the number of interactions on the titanium wire N^{Ti} can now be related to the number of reconstructed vertices $N^{\mathrm{Ti}}_{\mathrm{ver}}$ and $N^{\mathrm{C}}_{\mathrm{ver}}$ as

$$N_{\mathrm{Ti}} = \left[\frac{N^{\mathrm{Ti}}_{\mathrm{ver}}}{\eta^{\mathrm{Ti}}} - \epsilon^{\mathrm{C}}_w \frac{N^{\mathrm{C}}_{\mathrm{ver}}}{\eta^{\mathrm{Ti}}\eta^{\mathrm{C}}}\right] \Big/ \left[1 - \frac{\epsilon^{\mathrm{C}}_w \epsilon^{\mathrm{Ti}}_w}{\eta^{\mathrm{C}}\eta^{\mathrm{Ti}}}\right] \tag{6.4.2}$$

where $\eta^A = \epsilon_1^A + 2\epsilon_2^A$. Another effect that should be considered is the occurrence of vertex *merging*, i.e. two inelastic interactions on the same target wire leading to a single primary vertex. A Monte Carlo analysis [7] estimates this probability at 54 %. If we assume this number to be identical for the titanium and the carbon wires at the 20% level, it leads to a systematic error of less than 0.2% for the data of this analysis. Here this effect is neglected, but it may become significant when this method is applied to data with a larger interaction rate.

6.4.2 Results

The number of interactions is determined by counting the number of primary vertices on either side of $z = -3$ cm, and using equation 6.4.2. The results, both with and without the event weighting described in section 6.3, are presented in table 6.4.2.

Target	$N^{\text{inel}}_{\text{uncorr.}}$	$N^{\text{inel}}_{\text{corr.run}}$	$N^{\text{inel}}_{\text{corr.1000}}$
C	117374 (89707)	121063 (92526)	121154 (92595)
Ti	102018 (87490)	105074 (90110)	105117 (90148)
R^{inel}	**1.151**	**1.152**	**1.153**

Table 6.4.2: *Number of inelastic interactions as determined from the number of reconstructed vertices, before and after efficiency corrections. The values* $N^{\text{inel}}_{\text{uncorr.}}$ *,* $N^{\text{inel}}_{\text{corr.run}}$ *and* $N^{\text{inel}}_{\text{corr.1000}}$ *refer to the number of inelastic interactions without luminosity weighting, with an average weight per run and with weights determined per 1000 events respectively.*

The luminosity weights have only a small influence on the measured fraction of inelastic interactions. This indicates that the combined influence of rate sharing fluctuations (Fig 1.3.2) and variations of the random trigger density (Fig 6.3.1) is small. Apparently, in periods when rate sharing deviated from the mean, the random trigger density has been conform the average of the entire period.

The main uncertainty in these fractions is a possible inaccuracy in the reconstruction efficiencies obtained from the Monte Carlo simulation. If no correction for misalignment effects would have been applied, the relative luminosity would have been lower by less than 2%. The statistical uncertainty for the determined vertex reconstruction efficiencies are 0.6%. The total uncertainty on the fraction is estimated at 1%.

6.5 Measuring R^{inel} by the response in sub-detectors

To verify the estimated systematic uncertainty in R^{inel}, we determine this ratio also with two other approaches. The first of these is by measuring the total response in a sub-detector due to one or more inelastic interactions. Such an approach has been used to determine the luminosity in data with one wire inserted [102]. In principle any sub-detector can be used for this, but the most suitable are those, that record many hits for a single interaction and have a large acceptance.

One of the main advantages of this method is that we are able to determine the number of interactions also at high target rates, where the method previously described may be inaccurate due to the merging of overlapping vertices.

6.5.1 Selecting interactions

Although this method does not require a vertex to be reconstructed, we still need the vertex detector to determine on which of the two wires the interaction(s) took place.

For all reconstructed track segments in the vertex detector, we determine if it can be assigned to one of the two target wires. A vertex segment is assumed to originate from a certain target wire if the distance of closest approach (DCA) of the track segment to this target wire is less than 2 mm and less than half the DCA to the other target wire.

To select interactions on one of the two target wires only, we require two or more tracks segments pointing to this wire, and no segments pointing to the other. In the Monte Carlo simulation we observe that such a requirement effectively discards interactions on the other target wire. The efficiency of these cuts is again different for the two target wires and determined from Monte Carlo. To estimate the systematic uncertainty, we vary the number of tracks required.

Events where interactions took place on both targets are rejected, since here we are no longer able to determine the exact number of interactions by this method. The number of rejected interactions is estimated from data, and added to the total.

6.5.2 Sub-detector response per interaction

First the average response of a sub-detector to a *single* inelastic interaction must be determined. The number of interactions is then the total response in all random triggered events, divided by this average. Since the typical number of hits in the OTR, VDS and RICH is much smaller than the total number of channels (at least for the interaction rates in the studied data set), we can neglect nonlinearity due to saturation. The calorimeter energy deposit does not suffer from such saturation effects even at high target rates.

The average response per single interaction is determined in runs where the interaction rate was very low. Here we can assume the probability of having more than one interaction to be negligible. A suitable run with only 2 MHz interaction rate, part of the data set, was chosen for this. In addition, the two pilot bunches of each of the three trains (bunches 45,46,115,116,185 and 186) are used. They have a contribution to the total target rate that is systematically much lower than average (see figure 6.2.1). As a cross-check, the response resulting from the Monte Carlo simulation is also used.

In this analysis we use the response of four sub-detectors: hits in the Outer Tracker, photons in the RICH, hits in the vertex detector and total deposited energy in the calorimeter. For the ECAL we use here the total transverse energy, deposited in clusters, corrected for bending in the magnet:

$$K_T = \sum_{\text{clusters}} E_{\text{cl}} / \left(\frac{1}{\sqrt{x_{\text{cl}}^2 + y_{\text{cl}}^2}} + \frac{1}{\sqrt{x_{\text{cl}}^2 + |y|_{\text{cl}}^3}} \right). \tag{6.5.1}$$

To avoid nonlinearities due to noise, we restrict ourselves to hits in the vertex detector or the Outer Tracker that were used in a reconstructed track.

The method is applied to each of the four sub-detectors separately. The differences in the results are used to estimate the systematic uncertainty of this method.

The average detector response per interaction for the low target rate data and Monte Carlo are shown in table 6.5.1. Since the low target rate data had quite limited statistics (about 1000 interactions) the uncertainty in the response per interaction thus obtained is rather large (2%).

Target	K_T	K_T(mc)	N_{otr}	N_{otr}(mc)	N_{vds}	N_{vds}(mc)	N_{rich}	N_{rich}(mc)
C	3409	3500	353.4	380.1	103.8	92.9	593.2	383.9
Ti	4066	4245	437.3	467.6	131.1	117.6	668.3	447.7
fraction	1.193	1.212	1.237	1.230	1.263	1.266	1.127	1.166

Table 6.5.1: *Average response per single interaction for the different subdetectors from data (pilot bunches and low target-rate run) and from Monte Carlo (mc). The uncertainty in the fraction extracted from data is estimated at 2 %. The statistical uncertainty in the Monte Carlo values is less than 0.5%.*

6.5.3 Total sub-detector response

In figure 6.5.1 the total response in the random triggered events for different sub-detectors in shown.

To the detector response from the Monte Carlo simulation we have added the response from multiple interactions, assuming Poisson statistics with a mean of 0.25 interactions per event for each target wire. We can see that the simulation gives a reasonable description of the response of the ECAL, OTR and VDS. It fails to accurately describe the response of the RICH. This is believed to be caused by a lower amount of detector material upstream from the RICH in the detector description of the Monte Carlo simulation. The extra material causes additional conversions ($\gamma \rightarrow e^+e^-$), that yield extra photons in the RICH.

6.5.4 Results

The number of interactions is now determined by dividing this total by the average of a single interaction from table 6.5.1. The results, including the corrections for acceptance and rejected events with interactions on both wires, are presented in table 6.5.2.

6.5.5 Systematic uncertainty

The systematic uncertainty in the relative luminosities obtained with this method is dominated by the uncertainty in the response per interaction from data, amounting to about 2 %. The acceptance corrections are accurate up to 0.5 %. The total uncertainty

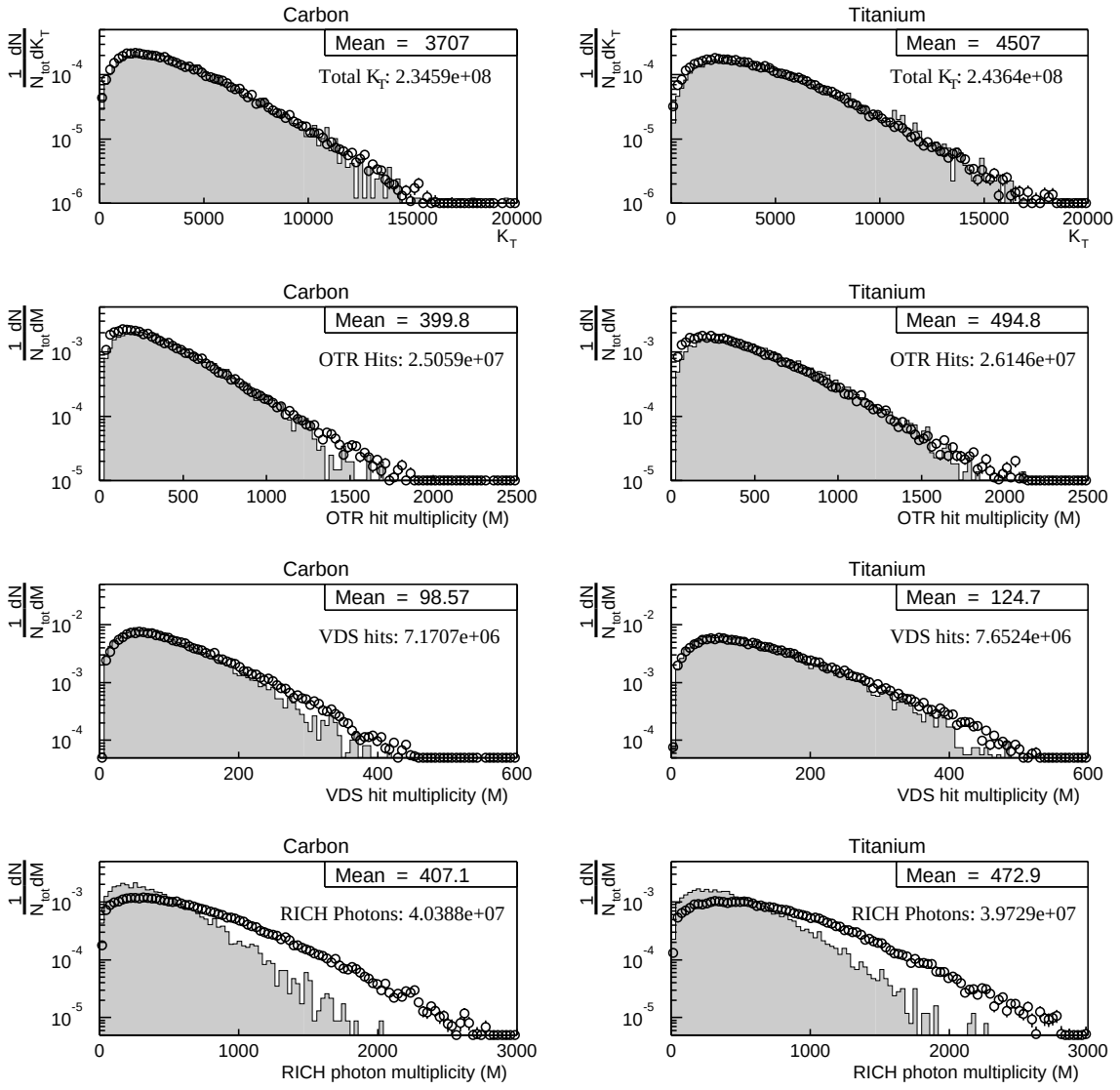

Figure 6.5.1: *Detector response due to inelastic interactions singled out on either of the two wires. The open circles show the data, the hatched histogram shows the Monte Carlo*

is therefore larger than in the previous method. If a larger sample of data with low interaction rate will be available in upcoming data taking, this method could become of comparable precision.

The measured luminosity ratio is reasonably stable under the variation of the criteria to select an interaction. If we vary the minimum number of track segments pointing to a certain target wire from one to three, the ratio of inelastic interaction changes by typically 1%, as shown in table 6.5.3

	carbon			titanium			
	Sum	N_{tot}	$N_{tot,corr}$	Sum	N_{tot}	$N_{tot,corr}$	R^{inel}
$K_{T,tot}$	2.346E+8	97403	116863	2.436E+8	88513	100975	1.157 (1.169)
$N_{otr,tot}$	2.506E+7	99496	119374	2.615E+7	88377	100819	1.184 (1.176)
$N_{svd,tot}$	7.170E+6	97653	117163	7.652E+6	86942	99183	1.181 (1.188)
$N_{rich,tot}$	4.039E+7	96673	115987	3.973E+7	88028	100421	1.155 (1.199)

Table 6.5.2: *Total response in the different subdetectors due to inelastic interactions and extracted ratio of inelastic interactions. N_{tot} is the number of interactions obtained by dividing the total energy or number of hits by the average per interaction and adding the number of events with interactions on both target wires (28584)). $N_{tot,corr}$ is the number of interactions after applying the acceptance correction as obtained from Monte Carlo (1.200 for carbon and 1.141 for titanium). The fraction given shows the relative luminosity if we use the values for the response per interaction from data (Monte Carlo in brackets), as given in table 6.5.1.*

6.6 Measuring R^{inel} by counting empty events

A third approach to determine the number of interactions makes use of the assumption that the number of interactions follows a Poisson distribution (Eq.1.3.1). We extract the expectation value of the number of interactions from the probability of having no interaction $P(0)$ in a random triggered event:

$$E(N) = \overline{\mu} = -\frac{1}{a}\ln P(0), \tag{6.6.1}$$

where a is the acceptance for finding a single interaction. This acceptance is again different for the two target wires and estimated from Monte Carlo.

We have assumed here that the acceptance for finding N interactions is simply $1-(1-a)^N$, i.e. that the acceptances factorise. In reality, the probability to detect N interactions is more than this, since they can partly overlap in the detector. This bias has been determined elsewhere [14], and gives an error of less than 0.01% in the ratio, which we can comfortably neglect.

For the measurement of $P(0)$ of one target wire, we require that no tracks in the vertex detector point to the other target wire, using the same assignment criteria as

cut	ECAL	OTR	SVD	RICH
$n > 0$	1.154	1.177	1.173	1.151
$n > 1$	1.157	1.184	1.181	1.155
$n > 2$	1.169	1.186	1.185	1.166

Table 6.5.3: *Values of R^{inel} for different selection criteria. The column 'cut' indicates the number of tracks required to point to the target wire. Note that all of these criteria are less stringent than the requirement of a reconstructed vertex, and that consequently the acceptance corrections are smaller than when requiring a vertex.*

described previously. $P(0)$ is then determined as the probability that no interaction is seen in the other subdetectors.

We use reconstructed OTR hits, photons in the RICH, and the total transverse energy in the ECAL to define the occurrence of one or more interactions. The cuts are based on the measured detector response in the low end region, shown in figure 6.6.1. The occurrence of one or more interactions is defined in each of the subdetectors by

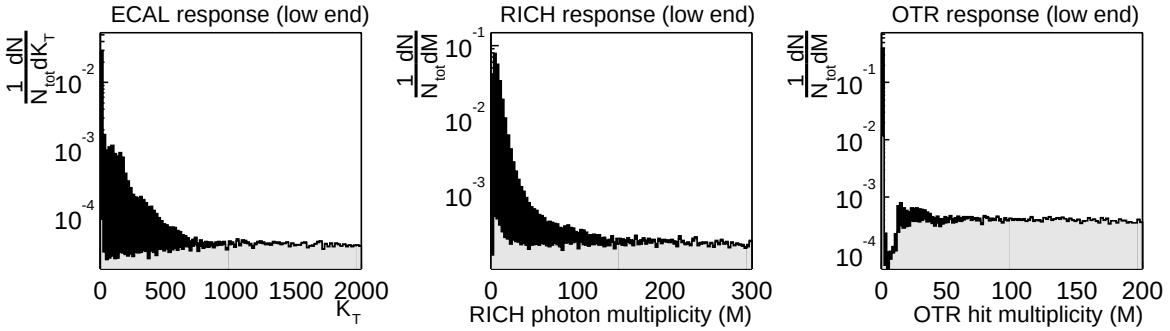

Figure 6.6.1: *Detector response for various subdetectors near the cut values. The black histogram shows the inclusive distribution without cuts, the shaded histogram shows the detector response when the event satisfies the cuts used to identify an interaction in the other two detectors. The difference between these two histograms shows empty events and detector noise.*

more than 20 OTR hits, more than 50 photons in the RICH or a total K_T of more than 500 GeV cm in the ECAL. It must be confirmed by at least two detectors, which eliminates the possibility that an interaction is faked by noise.

In this method we have assumed that the number of interactions follows Poisson statistics. We have seen already that this does not hold exactly since not all bunches contribute equally to the total interaction rate. However, the *ratio* of inelastic interactions is not affected by this, since both target wires are equally affected by these bunch-to-bunch fluctuations (see figure 6.6.2).

This does not hold however for fluctuations in time, which are caused by baseline shifts of the charge integrators, because such fluctuations are uncorrelated. We therefore determine $P(0)$ separately in time as shown in figure 6.6.3.

The mean value of the ratio is obtained from a minimisation of χ^2 of the fit. The weight of a data point to this fitted mean is inversely proportional to its uncertainty squared, or, equivalently, with the total statistics used for the measurement of the data point. Table 6.6.1 gives the results for the different combinations of sub-detectors.

A systematic uncertainty, introduced by assuming the number of interactions to be Poisson distributed at least for a small time period, is estimated by varying the size of time bins. We obtain an uncertainty on the measured fraction of less than a percent. The uncertainty in the acceptance determined from Monte Carlo is 0.5%. We estimate the total uncertainty of this method at 1.2%.

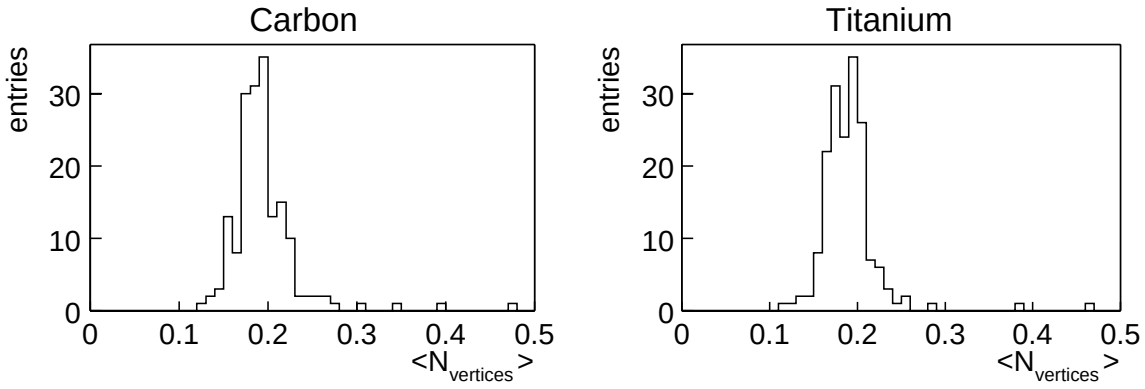

Figure 6.6.2: *Bunch to bunch fluctuations to the total inelastic interaction rate for both target wires. The entries in the histograms are the average number of reconstructed vertices for each of the bunches, as shown in figure 6.2.1.*

6.7 Conclusions

Three different methods to determine the ratio of inelastic interactions on two target wires have been presented, each of which is based on different assumptions. The first method relies on a good understanding of the vertex reconstruction efficiency. This method will become inaccurate at high interaction rates, when vertices start to overlap.

Under these circumstances the second method will give the most accurate results. This method, though, requires the response per single interaction to be well known, for which sufficient statistics of data at low target rate needs to be taken. In addition, this method assumes a stable performance of the sub-detectors, so that the response per interaction does not vary in time.

The third method has the advantage that it relies less on the accuracy of the Monte Carlo simulation than the first one. However, it will become inaccurate when the target rate fluctuates strongly, so that the Poisson assumption no longer holds.

The value for R^{inel} that we will use for the determination of $\alpha^{\text{J}/\psi}$ is the one measured

	carbon			titanium			
	$P(0)$	a	μ	$P(0)$	a	μ	ratio
OTR&RICH	0.8085(7)	0.8769	0.2424	0.8248(6)	0.9186	0.2097	**1.156(2)**
ECAL&RICH	0.8156(6)	0.8611	0.2367	0.8311(6)	0.9077	0.2038	**1.161(2)**
OTR&ECAL	0.8140(6)	0.8933	0.2304	0.8299(6)	0.9310	0.2003	**1.150(2)**
ALL	0.8185(6)	0.8574	0.2336	0.8337(6)	0.9050	0.2007	**1.164(2)**

Table 6.6.1: *Ratio of inelastic interactions of the two target wires as determined by counting empty events. The indicated errors are statistical.*

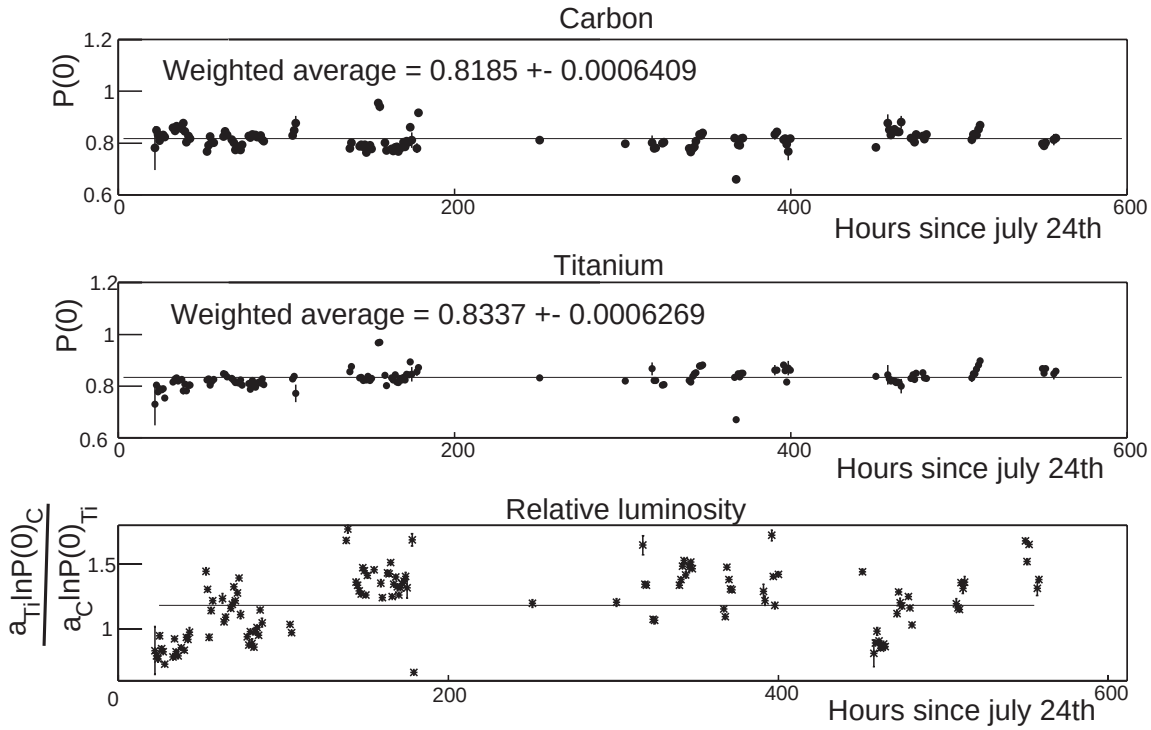

Figure 6.6.3: *Ratio of inelastic interactions measured by counting events without interactions. The mean value and the uncertainty therein are obtained from a fit.*

by counting vertices, with an event weighting based on 1000 events (see table 6.4.2):

$$R^{\text{inel}} = \frac{N_{\text{C}}^{\text{inel}}}{N_{\text{Ti}}^{\text{inel}}} = 1.153 \pm 0.0052(\text{stat.}) \pm 0.012(\text{syst.}). \tag{6.7.1}$$

The other two methods give results that are in agreement with this, but they have slightly larger uncertainties.

Chapter 7

Measurement of J/ψ yields

In this chapter we determine the yields of J/ψ, which are reconstructed through the decays J/$\psi \to \mu^+\mu^-$ and J/$\psi \to e^+e^-$. For each of the two channels a suitable description of the invariant mass spectrum will be presented. We will tune several cuts to obtain the most significant signal. The observed ratio of J/ψ yields is then corrected for the difference in the trigger and reconstruction efficiency for the two target wires. The ratio is then divided by the luminosity ratio, determined in the previous chapter, to determine $\alpha^{J/\psi}$. The chapter is concluded with a comparison of this measurement to existing data and a discussion of the potential of HERA-B for future data taking.

7.1 Introduction

Knowing the luminosity ratio, $\alpha^{J/\psi}$ can be determined by measuring the ratio of J/ψ yields from the two different targets (see Eq. 6.1.1),

$$R_{J/\psi} = \frac{N_{\mathrm{Ti}}^{J/\psi}}{N_{\mathrm{C}}^{J/\psi}} \frac{\epsilon_{\mathrm{C}}^{J/\psi}}{\epsilon_{\mathrm{Ti}}^{J/\psi}}. \tag{7.1.1}$$

The J/ψ are reconstructed through the decays J/$\psi \to e^+e^-$ or J/$\psi \to \mu^+\mu^-$. Since the background conditions for these two channels are very different, we treat them separately.

The efficiency $\epsilon_A^{J/\psi}$ is the product of the geometrical acceptance, of the trigger efficiencies including dead-times, and of the efficiency for the off-line reconstruction and selection. It is difficult to determine them precisely. They require a detailed and accurate Monte Carlo simulation of all trigger levels and good understanding of data taking conditions. The attainable accuracy on $\epsilon_A^{J/\psi}$ is of the order of 20%.

However, all these contributions, except the geometrical acceptance, are equal for the two wires and therefore cancel in the ratio. The difference in geometrical acceptance can be determined accurately.

7.2 Trigger and reconstruction

7.2.1 J/ψ-trigger criteria

Throughout 2000, the First Level Trigger network was tested and commissioned. It was not used for data taking. The MUON and ECAL pretrigger systems were available, but had smaller than design acceptance. The FLT decision was the occurrence of two MUON or two ECAL pretrigger messages. Part of the functionality that would have been covered by the FLT was emulated by the Second Level Trigger, using additional modules FLTe and FLTm. The criteria for the J/ψ-trigger in 2000 were:

ECAL Pretrigger: A message is generated for each cluster with $E_T > 1$ GeV.

MUON Pretrigger: A message is generated for each pad coincidence.

TDU: Accept the event if there are two or more ECAL pretrigger messages or two or more MUON pretrigger messages.

FLTe: Re-evaluate the ECAL clusters found by the FLT and require two or more clusters with $E_T > 1$ GeV. If the event satisfies this cut, the invariant mass of each of the pairs is calculated, assuming that the particles have been bent outwards in the magnet. The event is accepted if there is a combination with $m_{e^+e^-} > 2$ GeV/c^2.

FLTm: For each pad coincidence found, compatible hits in the zero-degree layers of MU1 and MU2 are required. From the x position of the hits a transverse momentum is estimated, which is required to be in the range $0.7 < p_T < 2.5$ GeV/c.

Slicer: All electron and muon candidates found by FLTe or FLTm are required to have at least one hit in each of the OTR superlayers PC1, PC2, PC3, PC4, TC1 and TC2.

RefitX and RefitY: Using the hits found by the slicer a track fit is performed. A cut on the quality and the number of hits used in the track is executed and only the best five track candidates are kept.

L2Sili: Each of the tracks found downstream from the magnet is extrapolated through the magnet to the vertex detector. These tracks are used to determine the search window for track finding and fitting in the VDS, using an approximate Kalman filter. Each of the tracks is required to have at least three hits in at least two superlayers.

The magnet propagation module of the SLT (L2Magnet) was not executed because the tracking chambers inside the magnet were not aligned. Furthermore, no common vertex was required (L2Vertex) for the lepton pair.

The inclusive efficiencies of the 2000 trigger chain for J/ψ reconstruction, has been estimated using a Monte Carlo simulation to be 1.3 % for J/$\psi \to e^+e^-$ and 1.4% for J/$\psi \to \mu^+\mu^-$ [10]. The rate, at which J/ψ were recorded, was up to 100 per hour of data taking in each channel.

7.2.2 Off-line reconstruction of J/ψ candidates

After passing the J/ψ-trigger, the events were reconstructed by the 4LT/FARM using the reconstruction packages described in section 6.2.3. The two SLT lepton tracks that formed the J/ψ candidate were used as track seeds for the off-line track reconstruction. The efficiency to reconstruct these tracks was practically 100%.

A pre-selection of $J/\psi \to e^+e^-$ decays was constructed from electron and positron candidates, that satisfied the following criteria:

- $p > 5$ GeV/c. This reduces the number of combinations made.
- $|E/p - 1| < 0.36$. The cluster energy should match the momentum.
- $E_T > 0.9$ GeV. The trigger cuts are redone with updated calibration.
- $\Delta_{y,\mathrm{ECAL}} < 3$ cm. The track and the cluster are required to match in y.
- $E_{\mathrm{brem}} > 0$ OR $L_{\mathrm{rich}} > L_{\mathrm{min}}(p)$. The particle must have radiated Bremsstrahlung or have a ring in the RICH compatible with an electron.

The electron and positron tracks must also form a common vertex and give an invariant mass $m_{e^+e^-} > 2$ GeV/c^2.

A pre-selection of $J/\psi \to \mu^+\mu^-$ decays was made from pairs of oppositely charged tracks, seeded by the MUON SLT tracks. They also must form a common vertex with mass $m_{\mu^+\mu^-} > 2$ GeV/c^2.

Events that contain a J/ψ candidate were further analysed in ROOT. Besides general information on the nature of the event, the track and vertex parameters of the J/ψ candidates were stored. For $J/\psi \to \mu^+\mu^-$ candidates, all tracks reconstructed in the vertex detector were also saved. These tracks are used in the analysis of associated particle production, presented in the next chapter.

7.2.3 Monte Carlo simulation

For cross checks we use two samples samples of 100000 Monte Carlo generated $J/\psi \to \mu^+\mu^-$ events. The J/ψ itself is generated by PYTHIA. The remaining energy, $E_{\mathrm{beam}} - E_{J/\psi}$, is subsequently passed to FRITIOF as the energy of an incident proton to generate the underlying proton-nucleus interaction. The Monte Carlo generation is described in more detail elsewhere [103].

After a detector simulation and digitisation, the Monte Carlo events are processed through a detailed simulation of the trigger chain. The events that passed this trigger chain, which was approximately 1.5% of the generated sample, were reconstructed in the same way as the data.

7.3 Ratio of yields in the decay $J/\psi \to \mu^+\mu^-$

7.3.1 Signal optimisation

A clean $J/\psi \to \mu^+\mu^-$ signal is already obtained by the pre-selection. Nonetheless, some small improvements in the significance of the signal can still be obtained by additional selection criteria. We consider the following cuts, that we will later optimise:

- **muon likelihood in RICH**
  If the muon crosses the acceptance of the RICH, the angle of the emitted Cherenkov radiation should be compatible with a muon hypothesis. The likelihoods are obtained by the stand-alone ring search (RISE) or from the track based particle identification program (RITER).

- **number of hits in VDS, OTR or MUON sub-detectors**
  The invariant mass spectrum can be contaminated by ghost tracks: random coincidences of hits that are erroneously regarded as a track of a physical particle. Such tracks have a smaller than average number of hits per track and can thus be rejected by demanding this number to be above a certain value.

- **χ^2 of dimuon vertex**
  If the two tracks forming the J/ψ candidate would not have originated from a common point, or if one of the tracks was a ghost track, any vertex, still reconstructed, will generally have a large χ^2. Such combinations can thus be rejected by setting an upper limit on the χ^2 of the dimuon vertex.

- **Polarisation angle**
  If the J/ψ is not polarised, which is approximately[1] the case, the cosine of the decay angle λ is uniformly distributed. Background to the J/ψ however, is more asymmetric, giving rise to small decay angles. A cut on $|\cos(\lambda)|$ can therefore reduce this background.

The cut values are varied, and for each value we fit the di-muon invariant mass spectrum to a functional form, which consists of a Gaussian to describe the signal, plus a exponential for the background:

$$N(m) = C_{\text{bgnd.}} e^{-bm} + C_{\text{signal}} e^{\frac{-(m-m_\psi)^2}{2\sigma_\psi^2}}. \tag{7.3.1}$$

The J/ψ yield and the uncertainty therein are extracted from the fit. The significance is determined as the number of the J/ψ, divided by the uncertainty.

Figure 7.3.1 shows the invariant mass spectra for three different values of the minimum MUON likelihood in the RICH. The dependence of the signal significance on the value of this cut and on the value of the vertex-χ^2 cut are shown in figure 7.3.2.

The vertex cut, the likelihood cut, and the cut on the number of hits in the MUON chambers give some small improvements to the significance of the signal. Although we

[1] It has been shown that, dependent on both the x_F and p_T, the J/ψ are either longitudinally or transversely polarised [104]. The average polarisation however is small.

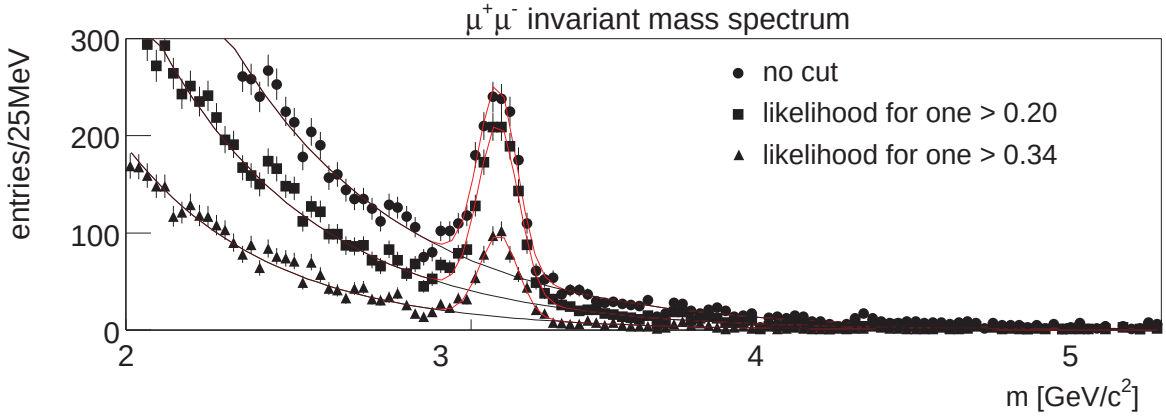

Figure 7.3.1: *$\mu^+\mu^-$ invariant mass spectra for three different values of the minimum muon-likelihood for the ring reconstructed in the RICH.*

have also found a significant difference in polarisation angles between J/ψ candidates and background, this background is already removed by the vertex and likelihood cuts. The fact that track quality requirements on the muon tracks (such as the number of hits) improve the signal only marginally, indicates that ghost tracks do not contribute significantly to the background.

The optimal cut values are summarised in table 7.3.1. Note that these values of the cuts in table 7.3.1 are optimal values only for *this* analysis. The cuts give the most significant J/ψ signals, given the statistics in this data set. They are approximately the maximum in signal/$\sqrt{\text{background}}$. For larger statistical samples with identical background conditions the optimal cut values will become more stringent than the values used here.

Figure 7.3.3 shows the invariant mass spectra before and after the combined cuts. There are some noticeable effects visible in the invariant mass spectra for the two different wires:

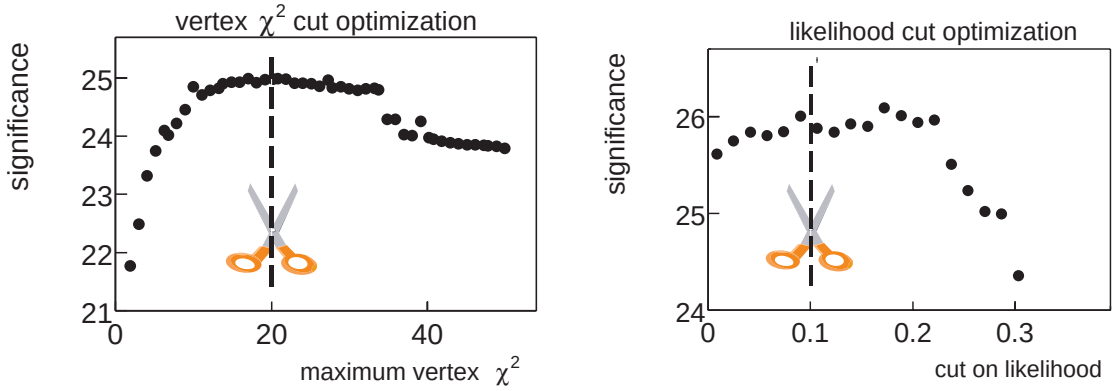

Figure 7.3.2: *Dependence of the significance of the $J/\psi \to \mu^+\mu^-$ signal on the value of cuts. The left plot shows the variation with the χ^2 of the di-muon vertex. The right plot gives the dependence on the muon likelihood of the RICH.*

cut	value	improvement	efficiency
vertex χ^2	$\chi^2 < 20$	$\approx 5\%$	99.3 %
μ likelihood in RICH	$L_\mu > 0.1$ (for one track)	$\approx 2\%$	99.5 %
hits in muon system	$N_{MUON} > 10$ (for both tracks)	$\approx 2\%$	97.3 %

Table 7.3.1: *Selection criteria for J/ψ candidates in the decay to muons. The improvement refers to the increased significance as obtained from the fit, with respect to no additional cut. The efficiencies are determined from a sample of 3000 Monte Carlo J/ψ events.*

- **mass shift**
  The reconstructed mass of 3.077 GeV/c^2 is significantly off the nominal J/ψ mass of 3.097 GeV/c^2. It is not fully clear what causes this effect. A possible explanation is detector misalignment, which can explain such a mass shift at least qualitatively;

- **resolution differences.**
  The resolution of the J/ψ signal is slightly better on the carbon wire (σ = 51 MeV/c^2) than on the titanium wire (σ = 56 MeV/c^2). The Monte Carlo simulation gives a resolution of 45 MeV/c^2 for both target wires. The differences can be caused by the incorporation of wrong hits in the vertex track segments. The mass resolution has been found to worsen with track multiplicity. Interactions on the titanium wire have a 28 % higher track multiplicity. The present Monte Carlo simulation underestimates the multiplicity in J/ψ events (see section 8.1.6) and does not simulate noise;

- **different background level.**
  The background level is larger for titanium than for carbon. This is a direct consequence of the higher average track multiplicity, that causes a higher probability for (non-J/ψ) interactions on the titanium wire to pass the trigger requirements. The track multiplicity in triggered events is further studied in section 8.1.

The J/ψ yields are extracted from the fit, using two different bin-sizes for the mass spectrum, 25 MeV/c^{2}and 50 MeV/c^2. As a check on the sensitivity to low statistics, the fit has been performed by minimising the total χ^2 and by maximising the likelihood. The J/ψ yields and the ratios are given in table 7.3.2. The ratio does not depend

Target	χ^2 fit		likelihood fit	
	$N_{25\ \mathrm{MeV/c^2}}$	$N_{50\ \mathrm{MeV/c^2}}$	$N_{25\ \mathrm{MeV/c^2}}$	$N_{50\ \mathrm{MeV/c^2}}$
C	777 ± 34	782 ± 34	772 ± 33	775 ± 34
Ti	1028 ± 41	1033 ± 41	1011 ± 40	1025 ± 41
ratio	**1.323±0.078**	**1.321±0.078**	**1.310±0.078**	**1.322±0.078**

Table 7.3.2: J/ψ *yields as extracted from a χ^2 minimisation or a likelihood maximisation fit of Eq. 7.3.1 to the invariant di-muon mass spectrum, using two different bin sizes.*

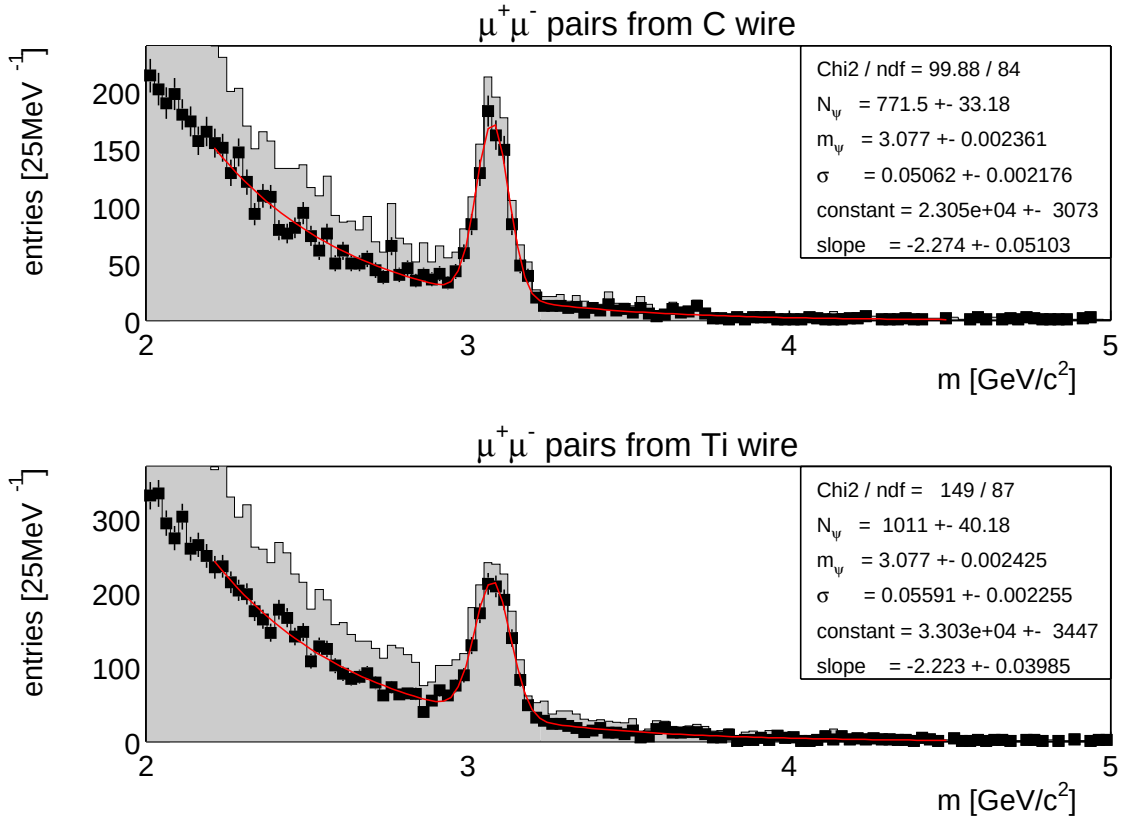

Figure 7.3.3: *Invariant mass spectra for $\mu^+\mu^-$ pairs from the carbon ($z_{vertex} < -3$ cm) and titanium ($z_{vertex} > -3$ cm) wires. The hatched histograms show the invariant mass spectrum before the cuts, the data points and the fit show the spectrums after the cuts.*

significantly on the bin-sizes or the fitting method. For the determination of $\alpha^{J/\psi}$ we will take the results from the χ^2 fit using a bin-size of 25 MeV/c^2:

$$\frac{N_{\mathrm{Ti}}^{J/\psi \rightarrow \mu^+\mu^-}}{N_{\mathrm{C}}^{J/\psi \rightarrow \mu^+\mu^-}} = 1.323 \pm 0.078(\mathrm{stat}). \tag{7.3.2}$$

7.3.2 Ratio of trigger efficiencies

To obtain the ratio of produced J/ψ from the observed yields, any differences in trigger efficiency must be taken into account. The only difference in trigger efficiency is a geometrical acceptance difference between the two wires.

The carbon wire is installed more upstream ($z = -4.9$ cm) than the titanium wire ($z - 1.6$ cm). As a result, the carbon wire has a larger inner acceptance for J/ψ and the titanium wire has a larger outer acceptance. The acceptance differences cancel at least partially. Since the differences are small compared to the total acceptance, we can expect the ratio of efficiencies to be close to unity.

Monte Carlo estimates of the trigger efficiency ratio

The number of Monte Carlo events that pass the trigger simulation and the off-line requirements directly gives the absolute trigger efficiency[2] for both wires.

We expect dead detector regions (mainly in the Outer Tracker) to have only a small effect on the net acceptance differences. Therefore we also study the case where the dead regions in the Outer Tracker have not been masked out in the simulation, to increase the statistical precision. The results are given in table 7.3.3.

	with masking		without masking	
target	events passing trigger	efficiency	events passing trigger	efficiency
C	1532	1.53(4)%	5275	5.28(7)%
Ti	1564	1.56(4)%	5448	5.45(7)%
$\epsilon_{\rm Ti}^{\rm J/\psi}/\epsilon_{\rm C}^{\rm J/\psi}$	**1.021(36)**		**1.033(19)**	

Table 7.3.3: *Trigger and reconstruction efficiencies as determined from Monte Carlo.*

The Monte Carlo results suggest that the net acceptance for the titanium wire is slightly larger than for the carbon wire. However, even in the sample that does not include the masking, the (statistical) uncertainty is almost 2%. If we would take this relative acceptance, its uncertainty would dominate our overall systematic uncertainty. Moreover, one would have to include an additional systematic uncertainty related to an imperfect detector description in the Monte Carlo, which is difficult to estimate.

Determination of the trigger efficiency ratio from data

There are important advantages in obtaining the acceptance corrections from data. To this end, we measure the probability that a J/ψ, produced on one wire, would also have been accepted, had it been produced on the other wire. This will be the case if both muons are still inside the sensitive area of our detector. This area is described by two rectangles at the position $z = 60$ cm: a small rectangle that covers the inner acceptance hole, and a large rectangle that gives the outer acceptance. The two acceptance rectangles are determined from data, as shown in figure 7.3.4.

We study the effect of the inner and the outer acceptances separately. For the inner (outer) acceptance we will only consider the impact point of the muon track that has the smallest (largest) opening angle[3].

Such 'decisive' muon tracks are translated to the other target wire. They are then extrapolated to $z = 60$ cm. The J/ψ is considered accepted if the impact points of the translated tracks at are still within the detector acceptance, parametrised by two rectangles.

If these rectangles would be defined to cover the true detector coverage, we would never be able to take into account events that moved *into* the acceptance. Any translation could only cause a loss of events. The rectangle should allow for migration *into*

[2]Barring specific hardware related effects and dead-times induced at the different trigger levels.

[3]More precisely, since we are dealing with a rectangular inner acceptance, it is the muon track for which the maximum of $|\frac{p_x}{p_z}|$ and $|\frac{p_y}{p_z}|$ is smaller than this maximum for the other muon track.

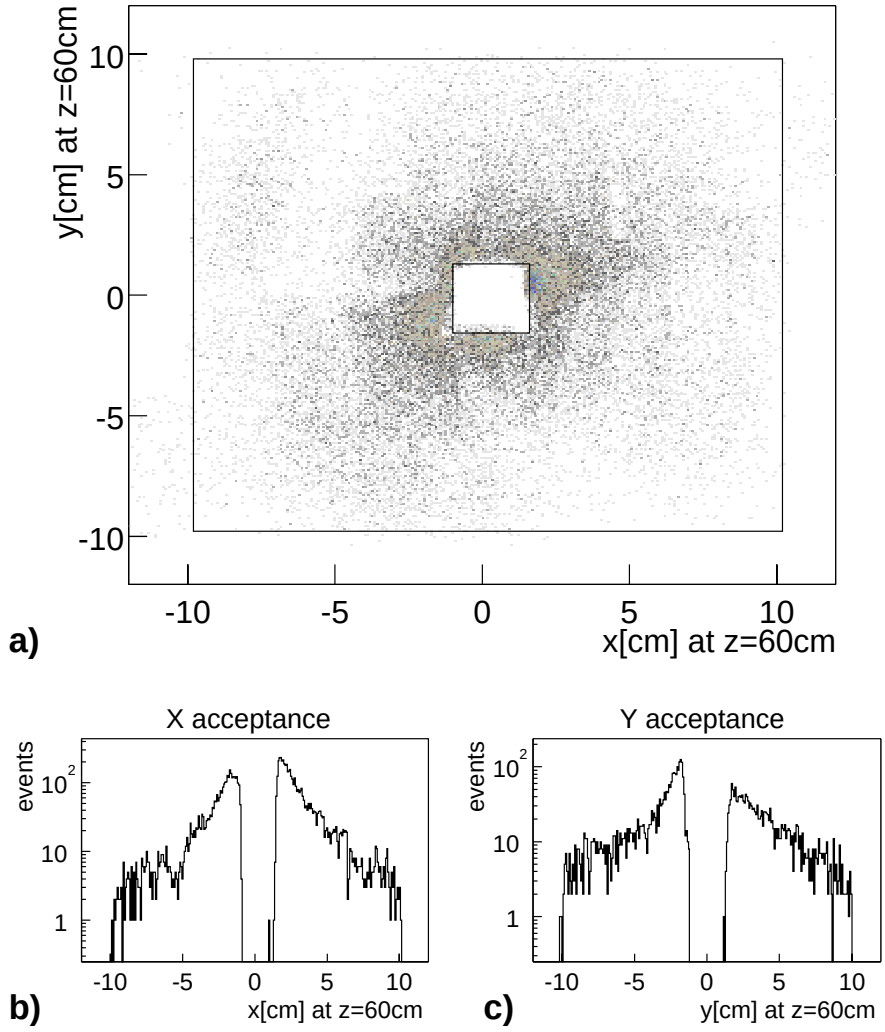

Figure 7.3.4: *Determination of the geometrical acceptance of the detector from the impact points of all muon J/ψ tracks at $z = 60$ cm (fig. a). Below slices are shown for x and y separately around $|y|_{(z=60\text{ cm})} < 1$ cm (fig. b) and $|x|_{(z=60\text{ cm})} < 1$ cm (fig. c) respectively.*

the acceptance, too. We define the acceptance boxes as the true acceptance of figure 7.3.4, plus an additional margin Δ_{xy} on all sides (see figure 7.3.5). The ratio of the geometrical acceptance is then obtained by extrapolating $\Delta_{xy} \to 0$.

We determine the acceptance both with and without (i.e. applying only a shift in z of 3.5 cm) the transverse translations. The method is also applied to the Monte Carlo sample as a systematic check.

In figure 7.3.6 the dependence on Δ_{xy} is shown. The extrapolation to $\Delta_{xy} = 0$ is done by a straight line, fitted in the region where full migration is still possible.

The final results are shown in table 7.3.4. The difference in the inner acceptance

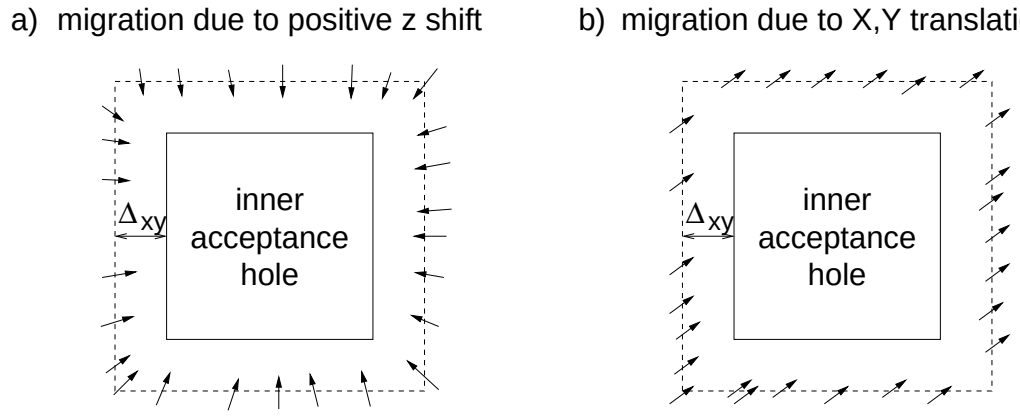

Figure 7.3.5: *Illustration of the determination of the relative inner acceptance corrections by means of marginal migration. Indicated is the effect of moving J/ψ muon tracks from the carbon to the titanium wire. For the movement from titanium to carbon, the arrows point in the opposite direction. The acceptance is determined for rectangular boxes that are Δ_{xy} larger than the true inner acceptance hole. This allows for migration into the acceptance too.*

and the outer acceptance are both of the order of 1-2%. They cancel and give no significant difference in the J/ψ efficiency for the two target wires. The inclusion of transverse translations does not give significantly different results, indicating that the acceptance is largely symmetric under rotations of 90 degrees.

There are two sources of uncertainty in the relative geometrical acceptance. The first is the uncertainty of the true detector coverage as determined from the impact points. The other is an uncertainty due to the possible contamination by non-J/ψ events. They are estimated by varying the box sizes and the J/ψ mass cut, and found to be below 1.5%. Taking the average from table 7.3.4 (data, including translations)

No transverse translations						
	Data			MC		
Migration	Inner	Outer	$\epsilon_{\mathrm{Ti}}^{\mathrm{J}/\psi}/\epsilon_{\mathrm{C}}^{\mathrm{J}/\psi}$	Inner	Outer	$\epsilon_{\mathrm{Ti}}^{\mathrm{J}/\psi}/\epsilon_{\mathrm{C}}^{\mathrm{J}/\psi}$
C $\rightarrow$ Ti	0.987(4)	1.028(5)	**1.015(7)**	0.980(3)	1.029(2)	**1.013(4)**
Ti $\rightarrow$ C	0.986(4)	1.022(6)	**1.008(7)**	0.979(2)	1.025(3)	**1.012(3)**
Including transverse translations						
	Data			MC		
Migration	Inner	Outer	$\epsilon_{\mathrm{Ti}}^{\mathrm{J}/\psi}/\epsilon_{\mathrm{C}}^{\mathrm{J}/\psi}$	Inner	Outer	$\epsilon_{\mathrm{Ti}}^{\mathrm{J}/\psi}/\epsilon_{\mathrm{C}}^{\mathrm{J}/\psi}$
C $\rightarrow$ Ti	0.978(5)	1.028(5)	**1.005(8)**	0.978(3)	1.032(3)	**1.009(4)**
Ti $\rightarrow$ C	0.983(5)	1.021(6)	**1.004(8)**	0.985(3)	1.029(3)	**1.014(4)**

Table 7.3.4: *Ratio of geometrical acceptances for J/ψ from the two target wires, measured by means of marginal migration. Indicated uncertainties are statistical.*

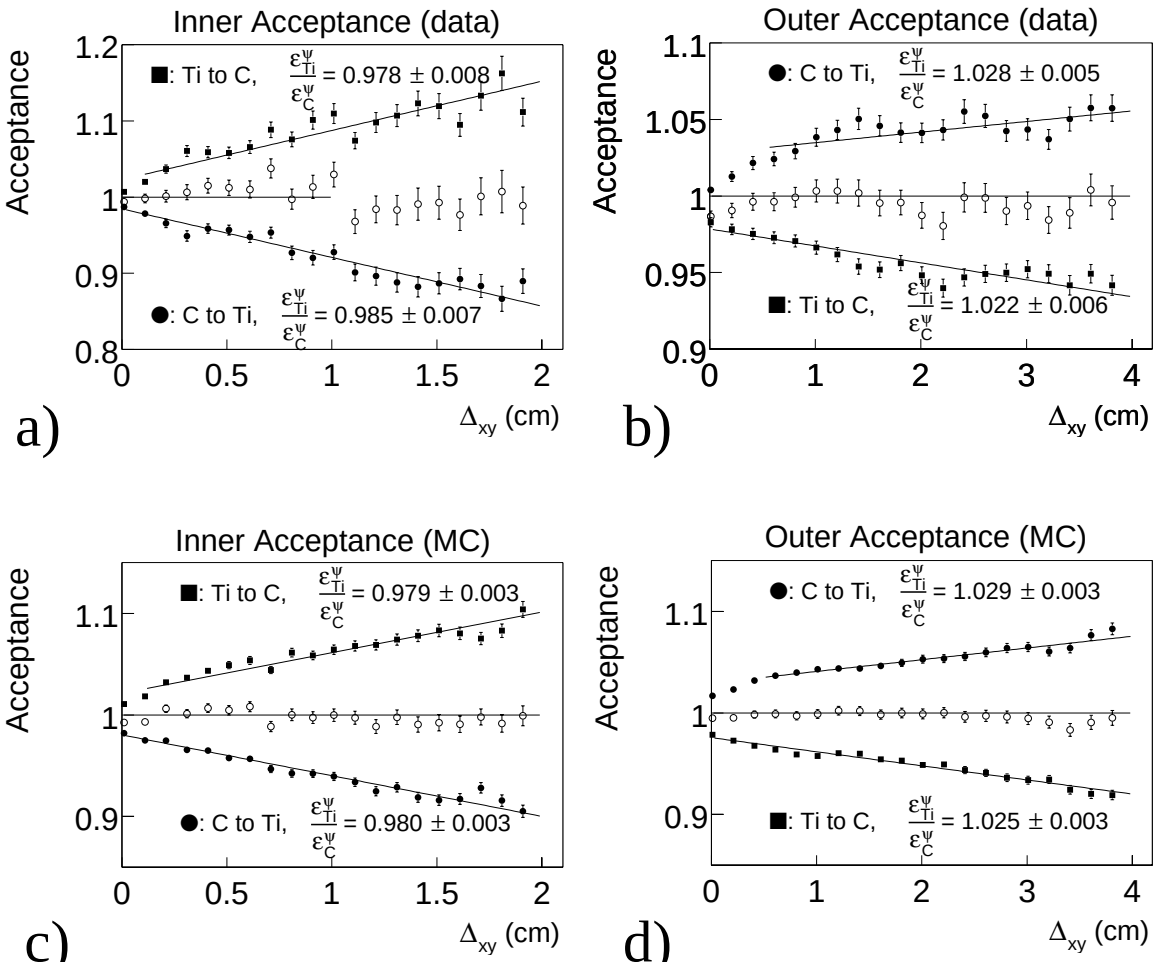

Figure 7.3.6: *Extraction of relative geometrical acceptances by marginal migration of a shift in z by 3.1 cm. The inner and outer acceptance corrections are separately determined, using both Monte Carlo and real data. The open circles show the product of the two independent relative efficiencies, corresponding to migrations from the carbon to the titanium wire and vice versa. As long as the acceptance is large enough to include full migration, this product should be equal to one.*

we obtain:

$$\frac{\epsilon^{J/\psi}_{Ti}}{\epsilon^{J/\psi}_{C}} = 1.005 \pm 0.015. \tag{7.3.3}$$

7.3.3 Kinematical acceptance

p_T acceptance

The p_T acceptance is determined from Monte Carlo by dividing the measured p_T distribution by the generated distribution. The Monte Carlo generator PYTHIA , which

is used to generate the J/ψ, has an intrinsic p_T cutoff at the parton level, required to regularise the scattering amplitudes. As a consequence, the generator fails to describe the spectrum at low p_T correctly. This has been compensated through the inclusion of weights [103], that are tuned to fit a parametrisation of the p_T spectrum as measured by E789 [105]. This parametrisation deviates from the simple exponential behaviour of Eq.5.1.14 and reads:

$$\frac{d\sigma}{dp_T^2} \propto \left(1 + \frac{p_T^2}{a}\right)^{-6}. \tag{7.3.4}$$

After inclusion of weights, we observe a flat acceptance in p_T, as shown in figure 7.3.7.

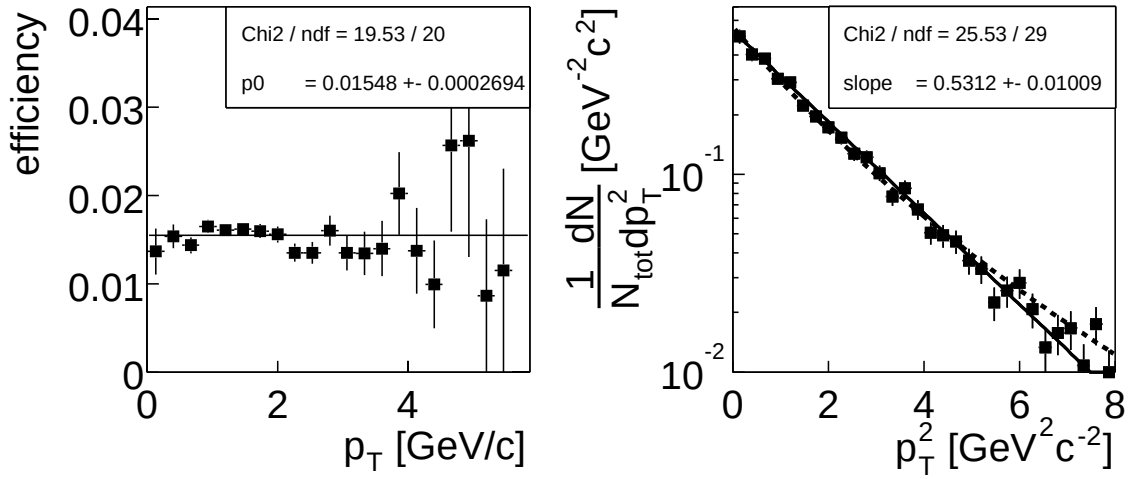

Figure 7.3.7: *p_T acceptance as determined in Monte Carlo from a comparison of the reconstructed and the generated p_T spectrum (left) and the inclusive distribution fitted with an exponential (solid line, Eq. 5.1.14) and the E789 parametrisation (dashed line, Eq.7.3.4).*

x_F acceptance

The acceptance for x_F is not uniform. The inner and outer acceptance hole renders the detector insensitive to large and small values of x_F, respectively.

An intuitive estimate of the acceptance of the detector can be obtained by relating the minimum and maximum angles of the detector to x_F, via $\gamma(x_F)$ (Fig.5.1.2). A J/ψ has the highest probability to be accepted if the decay angle in the centre-of-mass frame is perpendicular to the beam axis. This angle corresponds approximately to an angle of $1/\gamma$ in the laboratory frame. The minimum opening angle of the HERA-B detector is designed to be 10 mrad, and consequently γ cannot exceed 100. The corresponding value of x_F is approximately 0.35. Similarly, since the maximum decay angle is about 250 mrad, γ must be larger than 4, and $x_F > -0.4$. Therefore, for a full detector as designed, the x_F acceptance will approximately be $-0.4 < x_F < 0.35$.

In 2000, however, the detector was not fully installed according to design specifications. The distance of the Vertex Detector planes to the beam was larger than originally planned, to reduce radiation damage. Moreover, the Inner Tracker was not available in the trigger. Consequently, we expect the acceptance at positive x_F to be largely lost.

The x_F acceptance is determined from a Monte Carlo simulation, similar to the p_T acceptance done previously. The distribution obtained after all trigger cuts is divided by the generated distribution. This generated x_F distribution is also re-weighted to match the spectrum measured by E789, which is given by [103]:

$$\frac{d\sigma}{dx_F} \propto (1 - |x_F|)^{4.9}. \tag{7.3.5}$$

The x_F acceptance and the resulting distributions are shown in figure 7.3.8. The acceptance is indeed predominantly at negative x_F, corresponding to the backward hemisphere in the centre-of-mass frame. The minimum of -0.4 is in agreement with our expectation. Since near the acceptance limit only a narrow range of decay angles are accepted, the rise is not steep.

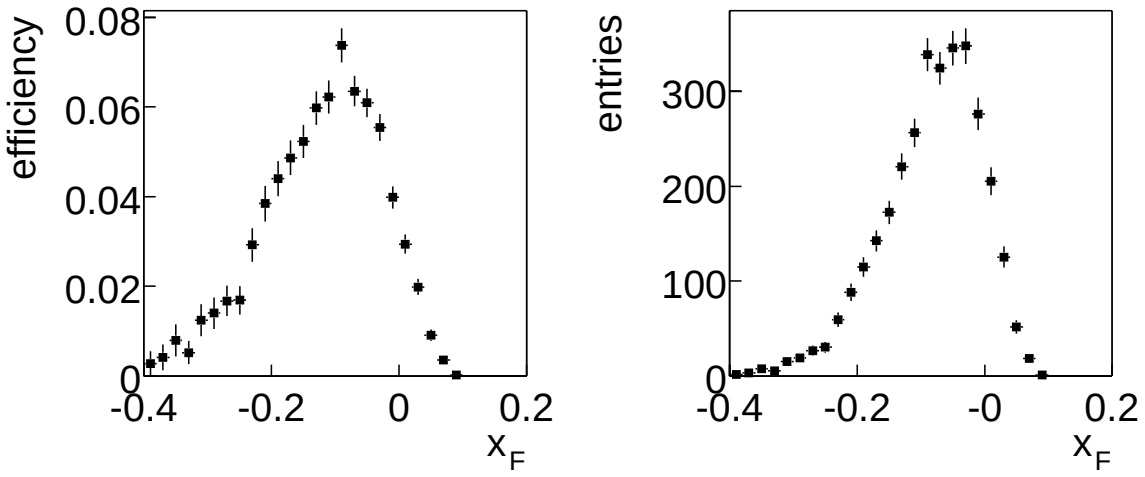

Figure 7.3.8: *x_F acceptance as determined from a comparison of reconstructed and generated x_F spectra (left) and the resulting distribution in Monte Carlo.*

The acceptance-corrected x_F spectra are determined for both wires separately. The x_F spectrum from the continuum background is estimated from the side-bins, and subtracted from the distribution measured in a window of 150 MeV/c^{2}around the J/ψ mass. Figure 7.3.9 shows the results, fitted with the parametrisation

$$\frac{d\sigma}{dx_F} \propto (1 - |x_F|)^{p_0}. \tag{7.3.6}$$

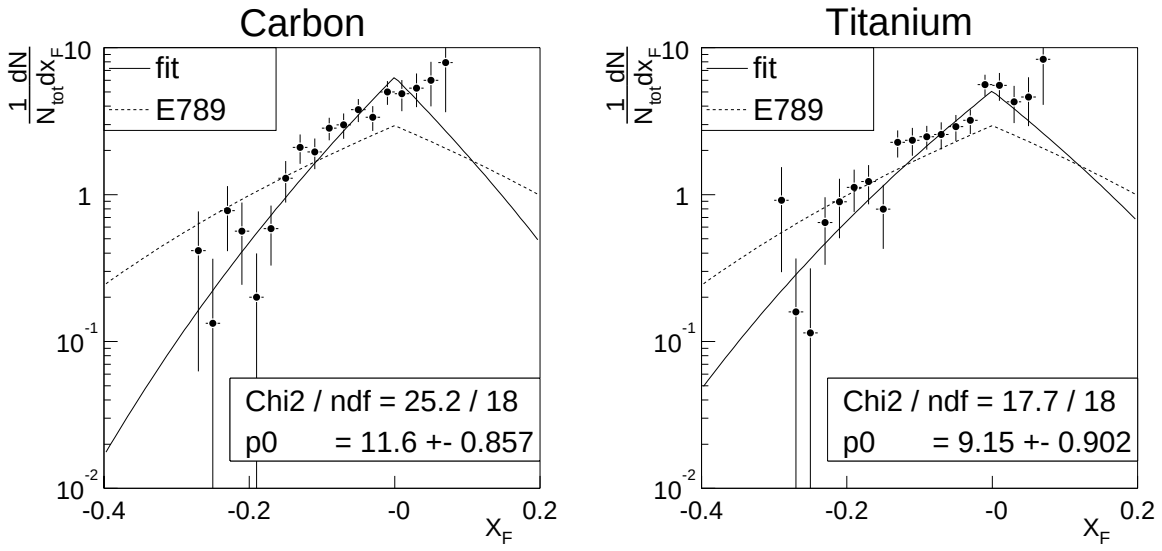

Figure 7.3.9: *Acceptance corrected differential x_F distributions for both targets. The distributions are fitted with the parametrisation of Eq. 7.3.6. Also shown is a parametrisation of the E789 data, given by Eq. 7.3.5.*

The two target wires give similar x_F distributions, indicating that we are not sensitive to x_F-dependent nuclear effects, at least in this range. We obtain an average $x_F = -0.061$ for both wires and a width (RMS) of 0.044. There is a significant difference with the parametrisation of E789, which was based on measurements in the region of positive x_F. This can partly be explained by the difference in centre-of-mass energies.

7.4 Ratio of yields in the decay J/$\psi \rightarrow e^+e^-$

7.4.1 Mass spectrum

Where the raw di-muon mass spectrum already showed a clear J/ψ signal, such is not the case for the raw di-electron mass spectrum. The trigger criteria for J/$\psi \rightarrow e^+e^-$ are not selective enough to reduce the background sufficiently. This background is dominated by the more abundant pions that deposit enough of their energy to pass the energy and mass cuts of the trigger.

The invariant mass of J/$\psi \rightarrow e^+e^-$ candidates at the Second Level Trigger is not calculated from the momenta of the reconstructed tracks. Instead, the SLT uses the energies in the corresponding pretrigger clusters, assuming a common origin at a fixed point near the target wires. This incorporates an implicit E/p electron identification, since pions generally leave clusters that are less energetic than electrons. From the two charge combinations, it will take the one that leads to the lowest mass.

The final mass spectrum, that uses the momenta of the reconstructed tracks, is therefore different from that of the SLT. Since the reconstructed momentum is usually larger than the deposited energy, masses are shifted towards higher values. The

SLT mass cut of 2 GeV/c^2 becomes diluted and results in a slow rise, that reaches a maximum at about 2.5 GeV/c^2, as shown in figure 7.4.1. Furthermore, the off-line reconstructed invariant masses are corrected by the Bremsstrahlung energy, if recovered, which also shifts the masses towards higher values.

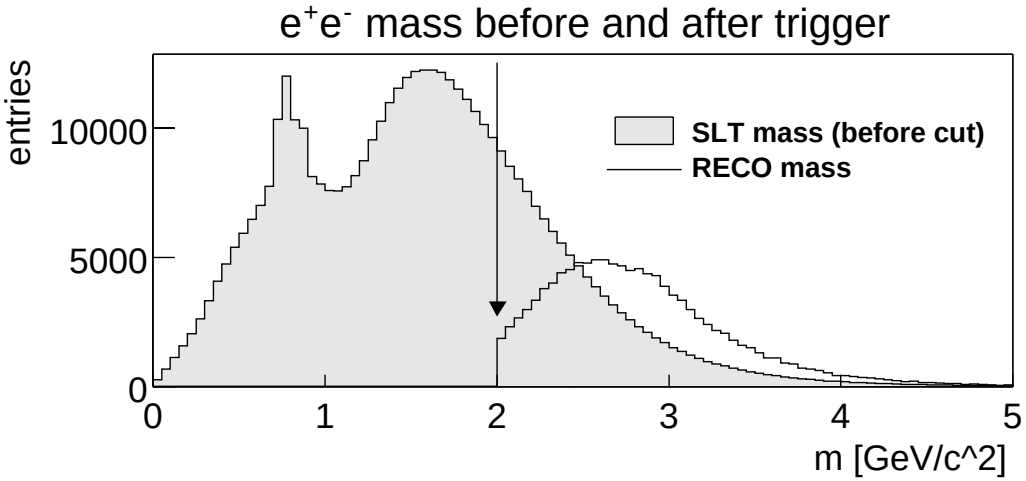

Figure 7.4.1: *Di-electron mass spectra before cuts. The open histogram shows the reconstructed invariant mass of* e^+e^- *pairs using the momenta of the tracks. The shaded histogram shows the mass spectrum reconstructed at the SLT from the energies of the calorimeter clusters.*

7.4.2 Fitting

In the muon channel our background was described by an exponential in the mass region above 2 GeV/c^2. This is not possible in the electron channel. Due to the dilution of the SLT mass cut, only at high masses should we expect this background to fall off exponentially. Restricting the fit of the background to a region well above 2 GeV/c^2, however, yields unstable results, and, consequently, a large uncertainty in the extracted number of J/ψ. It is therefore beneficial to model the background over the full mass region above 2 GeV/c^2, including the slow rise around 2 GeV/c^2.

We may expect the raw SLT mass spectrum, on which the cut is performed, to follow an exponential behaviour above values of 2 GeV/c^2. One difference between the SLT mass spectrum and the off-line reconstructed mass spectrum is due to the difference between energy E (used for the SLT mass calculation) and momentum p (used for the off-line mass calculation). This is essentially a multiplicative factor to the masses of

$$\sqrt{\frac{E_1 E_2}{p_1 p_2}}, \tag{7.4.1}$$

where $E_{1,2}$ and $p_{1,2}$ are the cluster energies and the momenta of the two tracks. As shown in figure 7.4.2, these mass-dilution factors are approximately distributed according to a Gaussian.

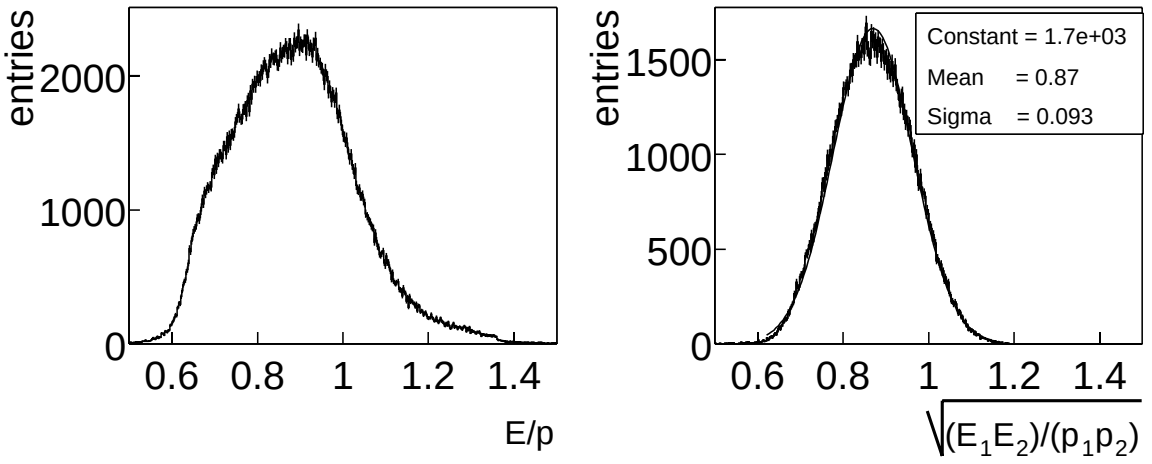

Figure 7.4.2: *Distribution of ECAL cluster energy (E) divided by the track momentum (p) (left) and the mass dilution factors (right). The latter determines the difference between the mass spectrum determined from the energies and the mass spectrum using reconstructed momenta.*

Consequently, we expect that the background can be described by an exponential, convoluted with a Gaussian:

$$\begin{aligned} \frac{dN_{\text{bgnd.}}}{dm} &= \int_2^\infty e^{-(x/a)} e^{\frac{-(m-x-l_{\text{dil}})^2}{2\sigma_{\text{dil}}^2}} dx, \\ &\propto e^{-\frac{m}{a}} \left[1 + \text{erf}\left[\frac{am - al_{\text{dil}} - 2a - \sigma_{\text{dil}}^2}{a\sigma_{\text{dil}}\sqrt{2}}\right]\right]. \end{aligned} \tag{7.4.2}$$

The parameters σ_{dil} (spread of the dilution), l_{dil} (shift in the dilution) and a (slope of the exponential) are used as free parameters in the fit of the background. The J/ψ signal is described by a Gaussian. In figure 7.4.3 we confront the raw di-electron mass with this fit. Our description of the background in the invariant mass spectrum is a posteriori justified by the χ^2 of the fit, which is practically one per degree of freedom. The values of σ_{dil} and l_{dil} obtained from the fit are in good agreement with the values expected from the measured dilution factors.

7.4.3 Signal optimisation

In the raw mass spectrum (Fig. 7.4.3) no clear J/ψ signal can be observed and additional cuts are necessary. The signal is again optimised by varying the cuts and maximising the significance, as was done for the muon channel. Given the worse background conditions, these cuts will be relatively strict.

We consider similar cuts as for the muons, concerning track and vertex quality and RICH likelihood, but the most powerful way to select electrons is by a cut on E/p. We determine a window for E/p by separately optimising minimum and maximum values,

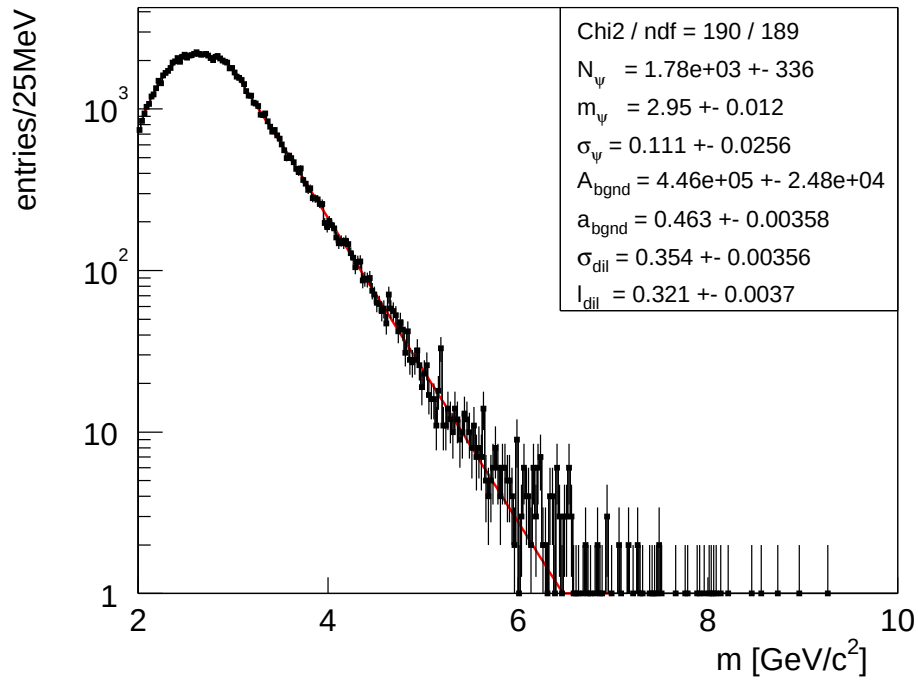

Figure 7.4.3: *Raw di-electron mass spectrum fitted with background parametrisation (7.4.2) and a Gaussian signal.*

since, due to energy loss and miscalibration, E/p of electrons need not be centred around unity. The dependence of the significance on the minimum and maximum E/p are shown in figure 7.4.4. Table 7.4.1 summarises the cut values that give the most significant $J/\psi \to e^+e^-$ signal.

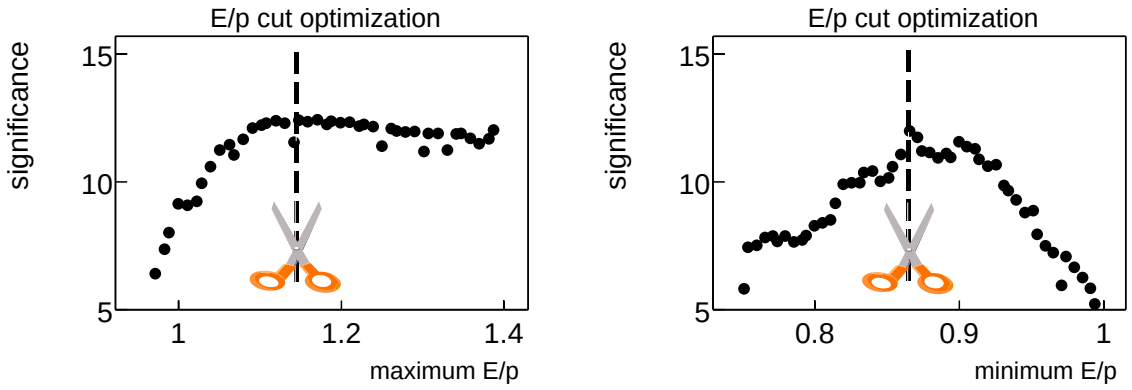

Figure 7.4.4: *Dependence of the significance of the $J/\psi \to e^+e^-$ signal on the value of cuts. The left plot shows the variation with the χ^2 of the di-muon vertex. The right plot gives the dependence on the muon likelihood of the RICH.*

Another method for selecting electrons is by requiring the electron candidates to have emitted one or more Bremstrahlungs photons before the magnet. These photons yield calorimeter clusters at the position of the straight-line extrapolation of the track

cut	value	improvement
minimum E/p	0.87 (both tracks)	$\approx 140\%$
maximum E/p	1.15 (both tracks)	$\approx 5\%$
vertex χ^2	$\chi^2 < 4$	$\approx 7\%$
$e^{\pm}$ likelihood in RICH	$L_e > 0.025$ (both tracks)	$\approx 4\%$

Table 7.4.1: *Optimal selection criteria for* $J/\psi \to e^+e^-$ *decays. The improvement refers to the increase in significance with respect to no additional cut.*

segment in the vertex detector. The requirement of one or two Bremsstrahlung clusters result in a relatively clean J/ψ signal, as shown in figure 7.4.5.

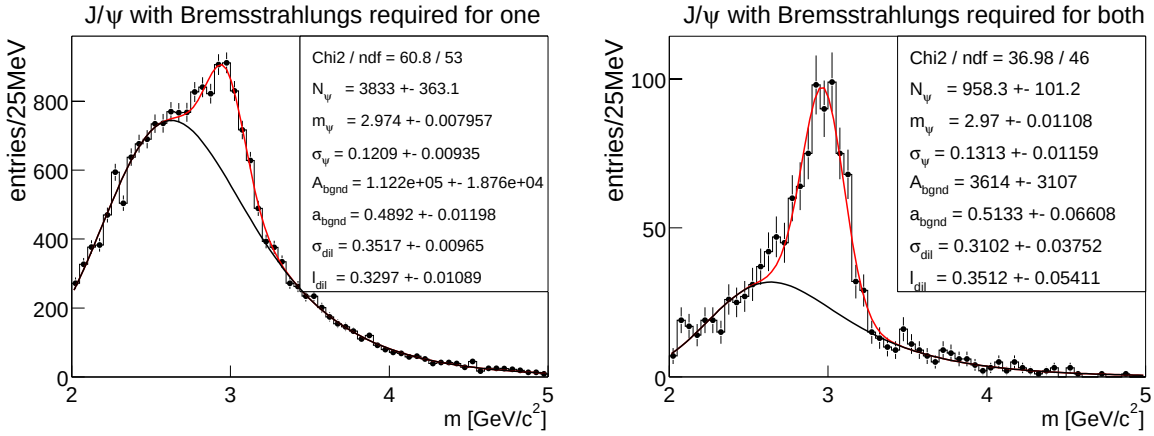

Figure 7.4.5: *Di-electron mass spectra for both target wires combined, with a Bremsstrahlung requirement. The left figure shows the spectrum, when either the electron or the positron candidate has emitted Bremsstrahlung before the magnet. For the mass spectrum on the right, both candidates must have radiated Bremsstrahlung. Note that we can still describe the background with our parametrisation (Eq. 7.4.2).*

However, only about 30% of electrons radiate Bremsstrahlung before the magnet, and this makes this requirement too restrictive. For the selection of J/ψ, we require either a Bremsstrahlung photon, or the combination of cuts in table 7.4.1. The Bremsstrahlung correction shifts the background towards higher values (or higher l_{dil}). In contrast, the E/p cut reduces this mass dilution. Although the background shape is different from that of the raw di-electron spectrum (Fig. 7.4.3), it can still be described by our parametrisation, as can be seen in figure 7.4.6.

Relative J/ψ yield

Even after applying the cuts, the level of background is much larger than observed in the muon channel. And even more than was the case there, the invariant mass is below the nominal J/ψ mass. Here it is caused by a lacking treatment of energy loss effects (predominantly Bremsstrahlung) in the track reconstruction.

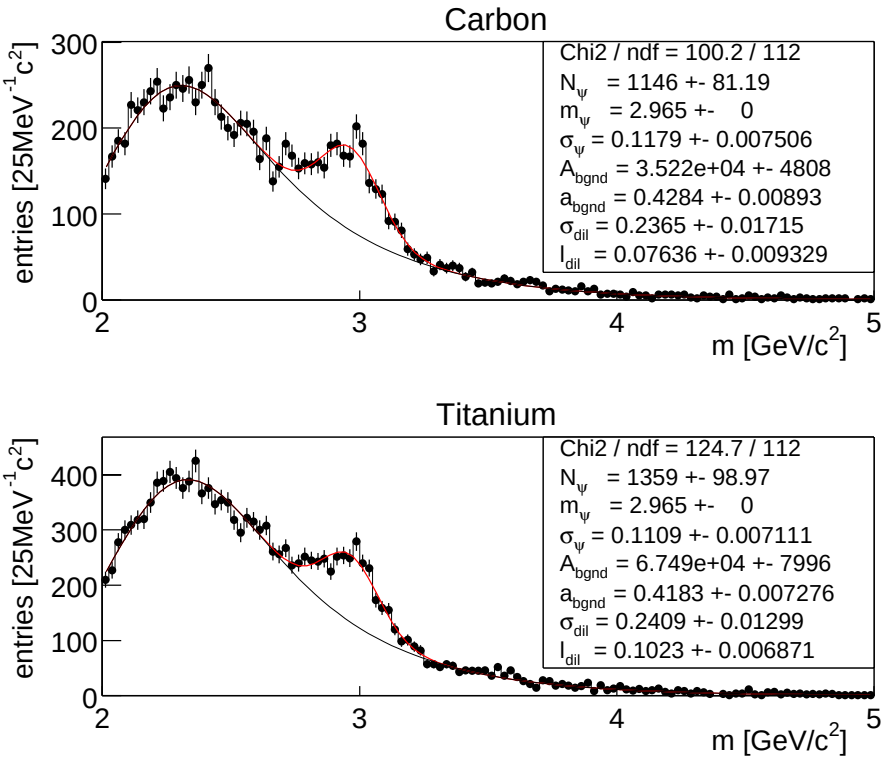

Figure 7.4.6: *Di-electron mass spectra for both target wires after optimisation of cuts. The width of the signal has been fixed to the average value obtained from the separate fits of the two target materials.*

The electron energy losses also cause the width of the J/ψ signal to be twice as large as in the muon channel. This effect is much larger than the mass resolution differences between target materials. It is therefore justified to fix the J/ψ width to a common value for both target wires.

Table 7.4.2 gives the J/ψ yields as obtained from the fits, using different bin-sizes for the histogram as a systematic check. For the measurement of $\alpha^{J/\psi}$ we use:

Target	χ^2 fit		likelihood fit	
	$N_{25\ \mathrm{MeV/c^2}}$	$N_{50\ \mathrm{MeV/c^2}}$	$N_{25\ \mathrm{MeV/c^2}}$	$N_{50\ \mathrm{MeV/c^2}}$
C	1146 ± 81	1134 ± 79	1114 ± 78	1110 ± 78
Ti	1359 ± 99	1349 ± 98	1328 ± 93	1324 ± 94
ratio	**1.19(12)**	**1.19(12)**	**1.19(12)**	**1.19(12)**

Table 7.4.2: *Numbers of reconstructed $J/\psi \to e^+e^-$ decays, obtained from a χ^2-minimisation or a likelihood-maximisation fit on the di-electron mass spectrum, using two different bin-sizes.*

$$\frac{N_{\mathrm{Ti}}^{\mathrm{J}/\psi \rightarrow \mathrm{e}^+\mathrm{e}^-}}{N_{\mathrm{C}}^{\mathrm{J}/\psi \rightarrow \mathrm{e}^+\mathrm{e}^-}} = 1.19 \pm 0.12(\mathrm{stat.}). \tag{7.4.3}$$

The selection criteria of table 7.4.1 reduce the background level by a factor six, while 69% of the J/ψ signal was retained. Nonetheless, the background level remains far worse than in the muon channel. The worse mass resolution also increases the sensitivity to background fluctuations. Even though the J/ψ yield is larger in the electron channel, the significance of the signal is about 60% less.

7.4.4 Relative trigger efficiency

The trigger efficiencies are not separately determined for the electronic channel, since no sufficiently large, clean sample of $\mathrm{J}/\psi \rightarrow \mathrm{e}^+\mathrm{e}^-$ decays can be obtained from data. We can, however, obtain a reasonable estimate by determining the geometrical acceptance.

The inner acceptance is practically equal to that for $\mathrm{J}/\psi \rightarrow \mu^+\mu^-$, since the dominant factor here is the angular coverage of the Outer Tracker and the Vertex Detector. The outer acceptance is limited by the ECAL pretrigger coverage. From the impact points of the $\mathrm{e}^+\mathrm{e}^-$ tracks at $z = 60$ cm, we estimate it to be smaller than that for $\mathrm{J}/\psi \rightarrow \mu^+\mu^-$ decays by approximately 1.5cm at $z = 60$ cm. The resulting (outer) acceptance correction is taken from figure 7.3.6, with $\Delta_{xy} = 1.5$ cm, which we estimate at 1.040(15). This then gives for the ratio of the trigger efficiency:

$$\frac{\epsilon_{\mathrm{Ti}}^{\mathrm{J}/\psi}}{\epsilon_{\mathrm{C}}^{\mathrm{J}/\psi}} = 1.02(2). \tag{7.4.4}$$

7.4.5 Kinematical acceptance

The geometrical acceptance of our detector gave a uniform p_T acceptance for $\mathrm{J}/\psi \rightarrow \mu^+\mu^-$. We assume that this holds for the electron channel too.

The x_F of our $\mathrm{J}/\psi \rightarrow \mathrm{e}^+\mathrm{e}^-$ candidates must be corrected for the background. Figure 7.4.7 shows that the x_F distribution of the signal (defined as $2.8 < m < 3.1$ GeV/c^2) does not differ much from that of the background, which is estimated from the side-bins to the J/ψ. If the estimated contribution of the background is subtracted from the signal, the resulting x_F distribution has an average of -0.012 and a width (RMS) of 0.044.

7.5 Summary and Conclusions

7.5.1 Calculation of $\alpha^{\mathrm{J}/\psi}$

We have presented a measurement of the ratio of J/ψ produced in pC and pTi interactions and reconstructed in the decays through $\mathrm{J}/\psi \rightarrow \mu^+\mu^-$ and $\mathrm{J}/\psi \rightarrow \mathrm{e}^+\mathrm{e}^-$ decays. The suppression parameter $\alpha^{\mathrm{J}/\psi}$ can be calculated by normalising this ratio to the relative luminosity, which was determined in the previous chapter. Table 7.5.1 summarises the values neccesary to determine $\alpha^{\mathrm{J}/\psi}$, together with their uncertainty.

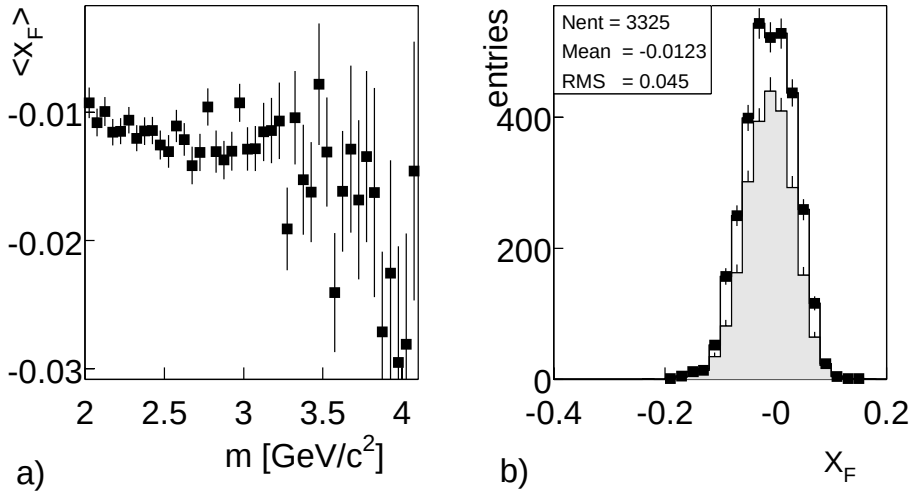

Figure 7.4.7: *Mass dependence of $\langle x_F \rangle$ (a) and x_F distribution inside and outside (shaded) J/ψ mass region (b).*

Inserting these values in Eq. 6.1.1 with the statistical and systematic uncertainties separately added in quadrature, we obtain

$$\alpha^{\mathrm{J}/\psi}(x_F = -0.062(60)) = 1.02 \pm 0.04(\mathrm{stat.}) \pm 0.017(\mathrm{syst.}); \quad (7.5.1)$$
$$\alpha^{\mathrm{J}/\psi}(x_F = -0.012(44)) = 0.93 \pm 0.07(\mathrm{stat.}) \pm 0.020(\mathrm{syst.}). \quad (7.5.2)$$

Both values are consistent with one and therefore with the absence of J/ψ suppression in this region of x_F. The results can also be presented as a measurement, relative to α^{inel}, which eliminates the systematic uncertainty associated to the assumed value

quantity	$\mathrm{J}/\psi \to \mu^+\mu^-$	$\mathrm{J}/\psi \to \mathrm{e}^+\mathrm{e}^-$
$\frac{\sigma^{\mathrm{inel}}_{\mathrm{Ti}}}{\sigma^{\mathrm{inel}}_{\mathrm{C}}}$	$2.71 \pm 1.5\%$ (Eq.6.1.6)	
$\frac{N^{\mathrm{inel}}_{\mathrm{C}}}{N^{\mathrm{inel}}_{\mathrm{Ti}}}$	$1.152 \pm 0.45\%(\mathrm{stat.}) \pm 1\%(\mathrm{syst.})$ (Eq.6.7.1)	
$\frac{N^{\mathrm{J}/\psi}_{\mathrm{Ti}}}{N^{\mathrm{J}/\psi}_{\mathrm{C}}}$	1.32(8) (Eq.7.3.2)	1.19(12) (Eq.7.4.3)
$\frac{\epsilon^{\mathrm{J}/\psi}_{\mathrm{Ti}}}{\epsilon^{\mathrm{J}/\psi}_{\mathrm{C}}}$	1.005(15) (Eq.7.3.3)	1.02(2)
x_F	$-0.105 < x_F < -0.0171$	$-0.056 < x_F < 0.032$
p_T	$p_T < 5$ GeV	$p_T < 5$ GeV

Table 7.5.1: *Summary of parameters for the determination of $\alpha^{\mathrm{J}/\psi}$ in both decay channels.*

of α^{inel}:

$$\begin{aligned} \text{J}/\psi \to \mu^+\mu^- : \quad \alpha^{\text{J}/\psi}(x_F = -0.062(60)) &= \alpha^{\text{inel}} + 0.30 \pm 0.04(\text{stat.}) \pm 0.013(\text{syst.}); \\ \text{J}/\psi \to \text{e}^+\text{e}^- : \quad \alpha^{\text{J}/\psi}(x_F = -0.012(44)) &= \alpha^{\text{inel}} + 0.21 \pm 0.07(\text{stat.}) \pm 0.016(\text{syst.}). \end{aligned}$$

The measurement is also in agreement with the data of E866 [84], that showed a significant suppression of $\alpha = 0.96(1)$ in this region of x_F. A comparison of the results is shown in figure 7.5.1.

It is clear that the E866 data are more precise. This is however only due to the larger statistics of 3 million J/ψ and due to the fact that E866 used target materials that differed more in atomic weight. Both the statistical and the systematic uncertainty in $\alpha^{\text{J}/\psi}$ are scaled down by a factor $\ln(A'/A)$. E866 measured $\alpha^{\text{J}/\psi}$ using berillium ($A = 9$) and tungsten ($A = 184$) targets, the ratio of which is five times larger than that of the carbon-titanium combination used here. If one disregards this trivial atomic weight dependence, the systematic uncertainty of the measurement presented here is equal (if not better) than that of E866 (2.3% vs. 2.5% [106] and 3.0% in [84]).

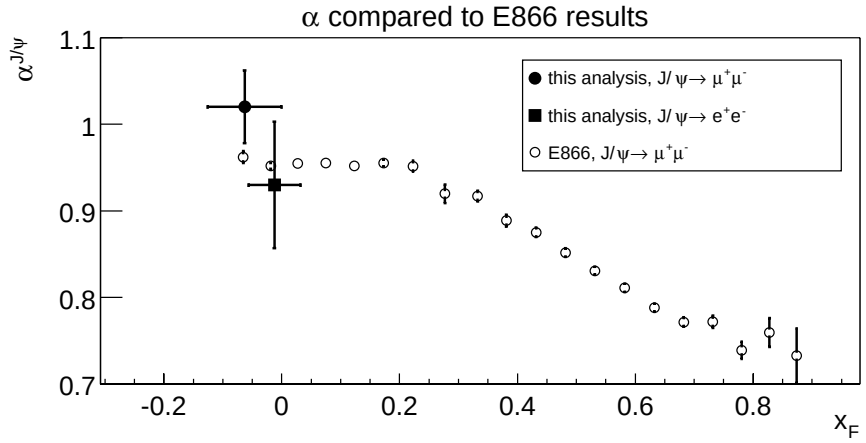

Figure 7.5.1: *Comparison of the results from this analysis to a measurement by E866 [84]. The vertical error bars give the statistical uncertainty only. The horizontal error bar for the results of this analysis is the width of the x_F distribution. The absolute systematic uncertainty of the E866 results is 1%. [84].*

7.6 Future prospects

The measurement of nuclear effects in charmonium production has become one of the primary goals for future data taking [17] for HERA-B, together with a measurement of the b production cross section. In comparison to other experiments, HERA-B offers some distinct advantages, such as the complete reconstruction of the associated event and an x_F acceptance that extends to negative values.

The absence of an early hadron absorber will allow for measurements of nuclear suppression of χ_c states for the first time. The difference in suppression between χ_c

and ψ provides a test [85] of the interplay between the production mechanism (NRQCD) and nuclear absorption effects.

Data taking will re-start in May 2002. A sample of 1.5 million J/ψ, 25.000 ψ' and 100.000 χ_c is expected to be recorded. The usage of tungsten and carbon as target materials will reduce the systematic uncertainty in α by an additional factor two. With these statistics and these target materials, HERA-B can measure $\alpha^{J/\psi}$, $\alpha^{\psi'}$ and α^{χ_c} to the precision shown in figure 7.6.1.

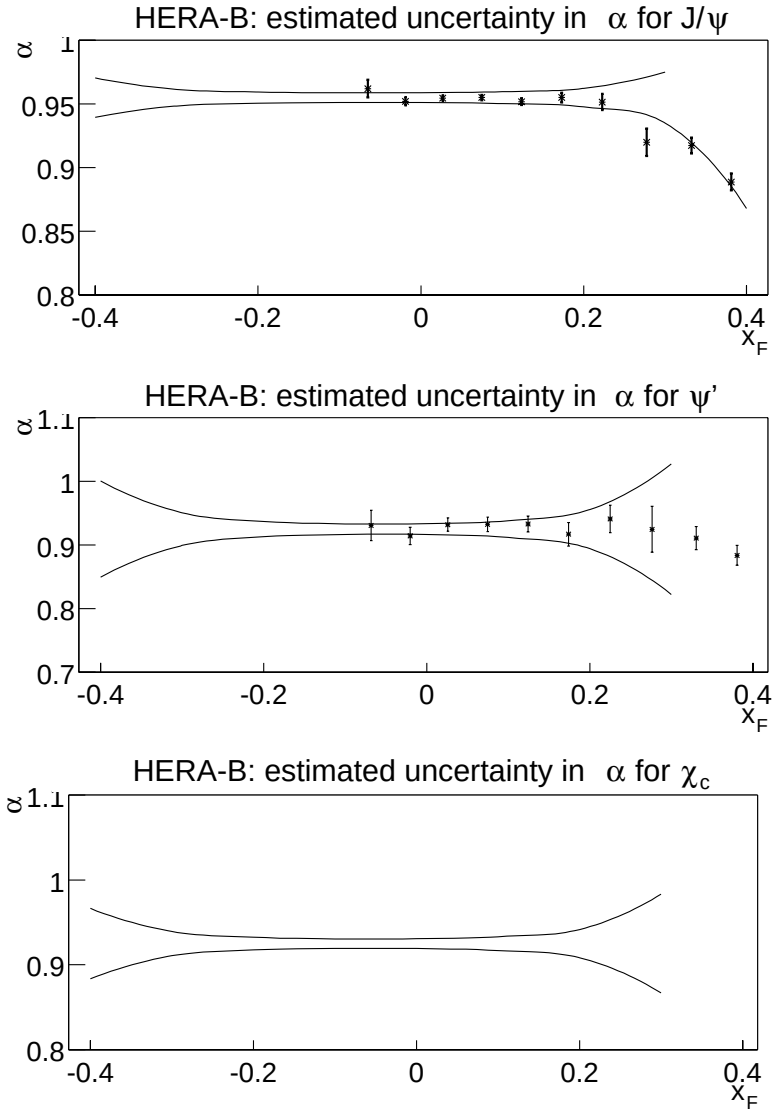

Figure 7.6.1: *Expected accuracy in $\alpha^{J/\psi}$, $\alpha^{\psi'}$ and α^{χ_c} for the data of 2002. The lines indicate the combined statistical and systematic uncertainty (based on this analysis) in bins of 0.1 in x_F, around some fiducial measured value of α. The E866 data points for $\alpha^{J/\psi}$ and $\alpha^{\psi'}$ are included for comparison.*

Chapter 8

Associated particle production

Approximately 80% of the charged particles produced in the proton-nucleus interaction are reconstructed in the HERA-B detector. The multiplicity of charged particles and their kinematic properties give valuable information on the nature of the collision.

In this chapter we study the multiplicity and pseudo-rapidity distributions of particles produced in association with a J/ψ. This provides essential input to models that describe nuclear suppression of J/ψ production through interactions with such co-movers [107]. We will argue that two wrong assumptions have commonly been made to estimate the co-movers density, which, fortuitously, largely cancel. The chapter is concluded with a measurement of the dependence of the p_T of J/ψ on the multiplicity.

8.1 Multiplicity distributions

8.1.1 Introduction

The charged particle multiplicity is among the most easily determined observables in particle physics. A vast amount of data, from e^+e^-, pp, pA and AA collisions, have revealed the following properties:

- **Increase with $\sqrt{s}$**
  The mean multiplicity of particles $\bar{n}_{\rm tot}$, created in a proton-nucleon collision, slowly increases with centre-of-mass energy $\sqrt{s}$. Several parametrisations exist that describe this dependence[108, 109, 110, 92].

- **KNO scaling [111]**
  The shape of the multiplicity distribution $P(n)$ depends only on the mean multiplicity $\bar{n}$:

$$P(n) = \frac{1}{\bar{n}}\psi(\frac{n}{\bar{n}}), \tag{8.1.1}$$

  where $\bar{n} = \bar{n}(s)$ and $\psi(\frac{n}{\bar{n}})$ is a universal function called the KNO scaling function. Small deviations from KNO scaling have been observed by UA5 at high centre-of-mass energies [109].

- **Charge/neutral ratio**
  As expected from isospin conservation, the ratio of charged hadrons over neutral hadrons is approximately two.

- **Dependence on A**
  In the Glauber model, each proton-nucleon sub-collision acts as an independent source of particle production. The total multiplicity is then the sum of the multiplicities generated by these sub-collisions. The multiplicity in pA collisions then scales with the number of participating nucleons, or, equivalently, with the average path length of the proton inside the nucleus $\bar{L}$:

$$\bar{n} \propto N_{\text{participants}} \propto \bar{L} \propto A^{1/3}. \tag{8.1.2}$$

  Energy-momentum conservation implies, however, that the multiplicity reaches an asymptotic limit for infinite path lengths:

$$\bar{n}_{\max} \approx \frac{\sqrt{s}}{m_\pi}. \tag{8.1.3}$$

  The proton loses part of its energy due to interactions, as it traverses the nucleus. Consequently, the average multiplicity does not exactly scale with the number of pN sub-collisions. Figure 8.1.1 shows the dependence of the mean multiplicity on the number of pN sub-collisions, as simulated in FRITIOF.

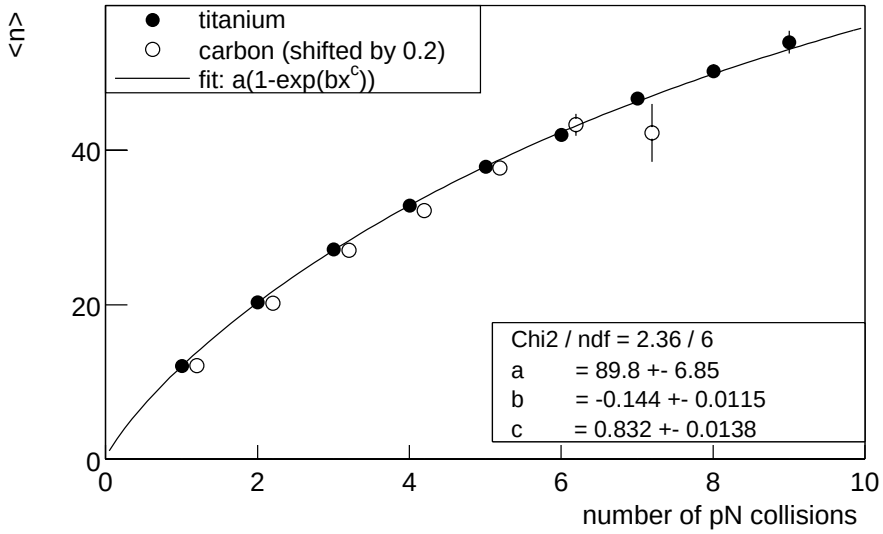

Figure 8.1.1: *Charged particle multiplicity as a function of the number of wounded nuclei, as determined by the event generator FRITIOF. For visibility, the points for the carbon target are shifted to the right by 0.2.*

The A dependence is therefore weaker than given by Eq. 8.1.2. A measurement at HERA-B for four different target materials gives [7]:

$$\bar{n} \propto A^{0.180(23)}, \tag{8.1.4}$$

which was found to agree with the simulation. Our previously determined multiplicities (Fig. 6.4.1) showed $\bar{n}$ to be 28% higher for titanium than for carbon, which agrees with this result.

8.1.2 Parametrisation of the multiplicity distribution

A parametrisation that has been successfully confronted with a wealth of data is the negative binomial (NB) distribution[1] :

$$P(n) = \binom{n+k-1}{n} p^k (1-p)^n. \tag{8.1.5}$$

with values for the mean and the dispersion D :

$$\bar{n} = \sum_n nP(n) = k(1-p)/p. \tag{8.1.6}$$

$$\frac{D^2}{\bar{n}^2} \equiv \frac{\bar{n^2} - \bar{n}^2}{\bar{n}^2} = \frac{1}{\bar{n}} + \frac{1}{k}. \tag{8.1.7}$$

Various interpretations as to why the multiplicity is distributed according to a NB have been presented (see e.g. [110] and references therein). An intuitive interpretation is provided by the clan model [113]. In the clan model, one considers the interaction to be the source of randomly produced clusters or 'clans', which are distributed according to Poisson statistics. Each of these clans decays into n final particles with probability:

$$P'(n) \propto b^n/n. \tag{8.1.8}$$

The number of clans and the average number of final particles per clan are directly related to the parameters of the NB:

$$\begin{aligned} N_{\text{clans}} &= k\ln(1/p), \\ \frac{\bar{n}}{N_{\text{clans}}} &= \frac{1-p}{p\ln(1/p)}. \end{aligned} \tag{8.1.9}$$

The NB obeys KNO scaling if k is independent of $\sqrt{s}$. However, a slow increase of k with $\sqrt{s}$ has been observed by UA5 [109]. We will use the negative binomial to fit the multiplicity distributions and characterise them through the parameters k and p.

8.1.3 Multiplicity of inelastic interactions

Most detectors, including HERA-B, measure multiplicity as the number of tracks of charged particles within a limited acceptance range. Also then, the multiplicity can be described by a NB [110].

[1] More recently it has been found that a better description is obtained with the modified negative binomial distribution [112]

The distribution observed in HERA-B is a convolution of the Poisson distribution for the number of interactions N, and the NB distributions for each of the single pA interaction:

$$P(n) = \sum_N \frac{e^{-\mu}\mu^N}{N!} \prod_{i=0}^{N} P(n_i)\delta(n - \sum_i n_i). \tag{8.1.10}$$

Figure 8.1.2 shows the measured multiplicity distributions of inclusive inelastic pC and pTi interactions. The above convolution, truncated to N=4, has been fit to the data. The values of μ were measured in chapter 6 to be 0.24 and 0.21, respectively, and kept fixed in this fit.

The convolution gives a reasonable description of the data. The average multiplicity per interaction, following from the fitted values of p and k, $\bar{n}^{\mathrm{Ti}} = 10.5$ and $\bar{n}^{\mathrm{C}} = 7.92$, are in agreement with the multiplicities in single primary vertices (Fig. 6.4.1).

The A-dependence of the multiplicities seems to be governed by the value of p: the values for k are not significantly different for the two different target materials. This is in disagreement with the expectation based on Eq. 8.1.9 that the number of particles per clan does not change, and that only the number of clans is different for the two target materials.

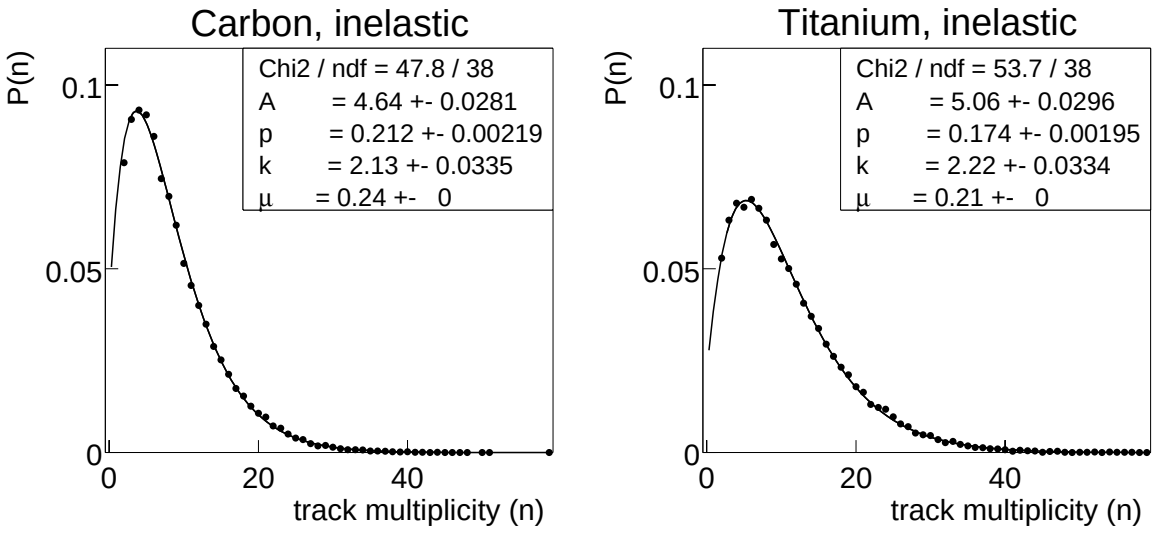

Figure 8.1.2: *Charged track multiplicity in inelastic interactions of carbon and titanium. This distribution is described by a negative binomial with parameters p and k, convoluted with a Poisson distribution for the number of interactions. We have fixed the expectation value μ of the Poisson distribution to the values obtained previously (see e.g. table 6.6.1).*

8.1.4 Multiplicity of particles associated with a J/ψ

We now focus our attention on the associated multiplicity, the number of particles that are produced in association with a J/ψ. This comprises all reconstructed vertex tracks, except those of the leptons from the J/ψ itself.

Figure 8.1.3 show the distribution of the multiplicity in J/ψ events. It can clearly be seen that the average associated multiplicity is significantly higher than the average multiplicity of inclusive inelastic interactions, which is shown as a shaded histogram.

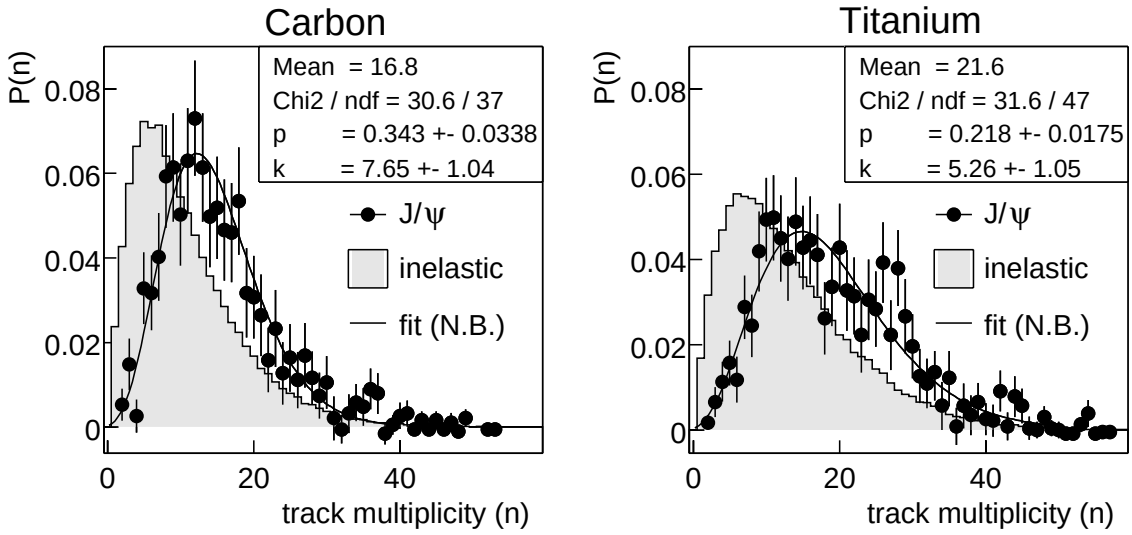

Figure 8.1.3: *Charged track multiplicity in interactions containing a* J/ψ. *The* J/ψ *are selected as muon pairs with a mass that is within 75 MeV/*c^2 *equal to the nominal* J/ψ *mass. The contribution from the background is estimated from the side-bands around the* J/ψ *mass and subtracted. A negative binomial (Eq. 8.1.5) is fit to the distribution. The multiplicity in inelastic interactions is shown as a shaded histogram for comparison.*

This effect can be understood if one takes into account the bias, that is introduced by requiring a J/ψ to be found in the event. The probability to produce a J/ψ – or anything sufficiently rare – is proportional to the number of elementary interactions N_{elem} in the proton-nucleus collision:

$$\mathcal{P}(\text{J}/\psi) \propto N_{\text{elem}} \tag{8.1.11}$$

In the Glauber model, such elementary interactions are identified as wounded nucleons. Alternatively, they can be considered to be the clans in the model that gives rise to the negative binomial multiplicity distribution. In this case, each proton-nucleon sub-collision consists of one or more elementary interactions.

Each of these elementary interactions is an independent source of charged particles. Therefore, N_{elem} is proportional to the charged track multiplicity n, and so is the probability to produce a J/ψ:

$$\mathcal{P}(\text{J}/\psi) \propto N_{\text{elem}} \propto n. \tag{8.1.12}$$

The multiplicity distribution of particles associated with the production of a J/ψ, $P(n|\text{J}/\psi)$, is then related to the distribution for inclusive inelastic interactions $P(n)$ as:

$$P(n|\text{J}/\psi) = \frac{n}{\bar{n}} P(n). \tag{8.1.13}$$

This hypothesis can be easily verified by comparing the associated multiplicity $P(n|\mathrm{J}/\psi)$ to $P(n)$, re-weighted by n. The resulting distributions, shown in figure 8.1.4, are indeed similar.

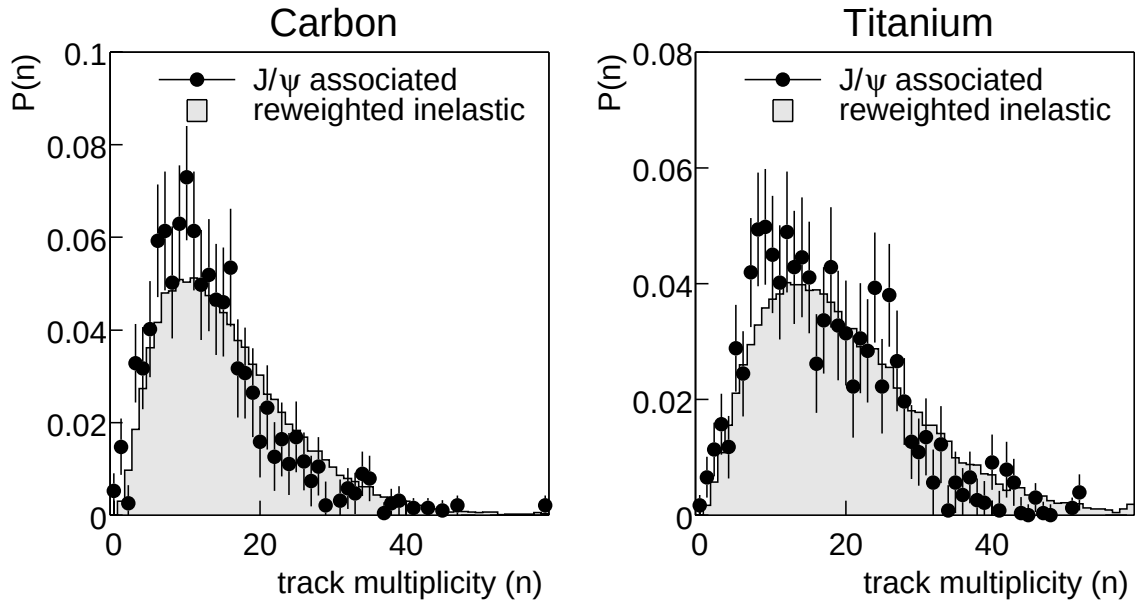

Figure 8.1.4: *Charged particle multiplicity in* J/ψ *events compared to re-weighted multiplicity in inclusive inelastic interactions. The two lepton tracks from the* J/ψ *have been subtracted.*

If $P(n)$ is distributed according to a NB, then so is $P(n|\mathrm{J}/\psi)$. The value for p, that governs the multiplicity per clan, is the same for both distributions, but $k \to k+1$ and $n \to n-1$. The expectation value for $P(n|\mathrm{J}/\psi)$ is related to $\bar{n}$, expectation value for $P(n)$, as

$$\bar{n}_{\mathrm{J}/\psi} = \bar{n} + \frac{1}{p} - 1. \tag{8.1.14}$$

Multiplicity in the triggered background events

At HERA-B, the non-J/ψ background in the J/ψ-triggered events, as observed in the di-muon or di-electron invariant mass spectrum, is predominantly combinatorial. Physical contributions, such as Drell-Yan production or $c\bar{c} \to \mu^+\mu^-$ decays are at least an order of magnitude lower. For the di-muon spectrum, the background is mainly due to random combinations of muons from in-flight pion and kaon decays.

The probability to trigger on a random combination is, however, small ($\ll 1$), and it is proportional to the number of combinations possible:

$$\mathcal{P}(\text{random } \mu^+\mu^-) \propto n(n-1). \tag{8.1.15}$$

where n is the number of charged pions or kaons, which we identify as charged tracks. As a result, the charged particle multiplicity in the triggered background follows the

multiplicity for inelastic interactions, weighted by $n(n-1)$.

$$P(n|\text{random } \mu^+\mu^-) = \frac{n(n-1)}{\bar{n}_{\mathrm{J}/\psi}} P(n). \tag{8.1.16}$$

If $P(n)$ is a NB distribution with expectation value $\bar{n}$, then the expectation value of $P(n|\text{random } \mu^+\mu^-)$ is:

$$\bar{n}_{\text{bgnd.}} = \bar{n}_{\mathrm{J}/\psi} + \frac{1}{p} - 1 = \bar{n} + \frac{2}{p} - 2. \tag{8.1.17}$$

One can make a straightforward generalisation of the multiplicity bias of the trigger. If the trigger for $\mathcal{X}$ requires t rare tracks, so that

$$\mathcal{P}(\mathcal{X}) \propto n(n-1)\ldots(n+1-t), \tag{8.1.18}$$

then the multiplicity is distributed according to a NB, with an expectation value that is related to the average multiplicity of inclusive inelastic interactions $\bar{n}$ as

$$\bar{n}_{\mathcal{X}} = \bar{n} + \frac{t}{p} - t. \tag{8.1.19}$$

Figure 8.1.5 shows the dependence of the average track multiplicity on the mass of the di-muon pair for both target materials separately. The average multiplicity around the J/ψ mass is up to 25 percent lower than outside this region. The mass dependence of the multiplicity is fit with the expected dependence:

$$\bar{n}(m) = \frac{N^{\text{bgnd}}(m)}{N_{\text{tot}}(m)}(\bar{n}_{\text{min.bias}} + 2/p - 2) + \frac{N^{\mathrm{J}/\psi}(m)}{N_{\text{tot}}(m)}(\bar{n}_{\text{min.bias}} + 1/p - 1), \tag{8.1.20}$$

where $\bar{n}_{\text{min.bias}}$ is the average multiplicity in inclusive inelastic interactions and p the parameter of the NB distribution. The signal and background levels are obtained from the di-muon mass spectra, shown in figure 7.3.3. It can be seen that the model gives a reasonable description of the mass dependence of the multiplicity. The average multiplicity is constant outside the J/ψ mass region, indicating that the random combinations dominate the continuum in the entire mass region shown.

8.1.5 Summary and conclusions

We have shown that the requirement of having a J/ψ in the event leads to a bias of the multiplicity distribution. For the combinatorial triggered background this bias is stronger than for the J/ψ event, leading to a mass dependence of the charged track multiplicity. Table 8.1.1 summarises the values of $\bar{n}$ for minimum-bias inelastic interactions, J/ψ associated and triggered background. To estimate the uncertainty related to the assignment of tracks to target wires, we have used four different track definitions.

The results show that, regardless of the definition of a charged track, the measured values for $\bar{n}_{\mathrm{J}/\psi}$ are in good agreement with the values for $\langle nP(n)\rangle$, which are obtained from the minimum bias data. They indicate that the multiplicities can be understood as arising from the mentioned biases.

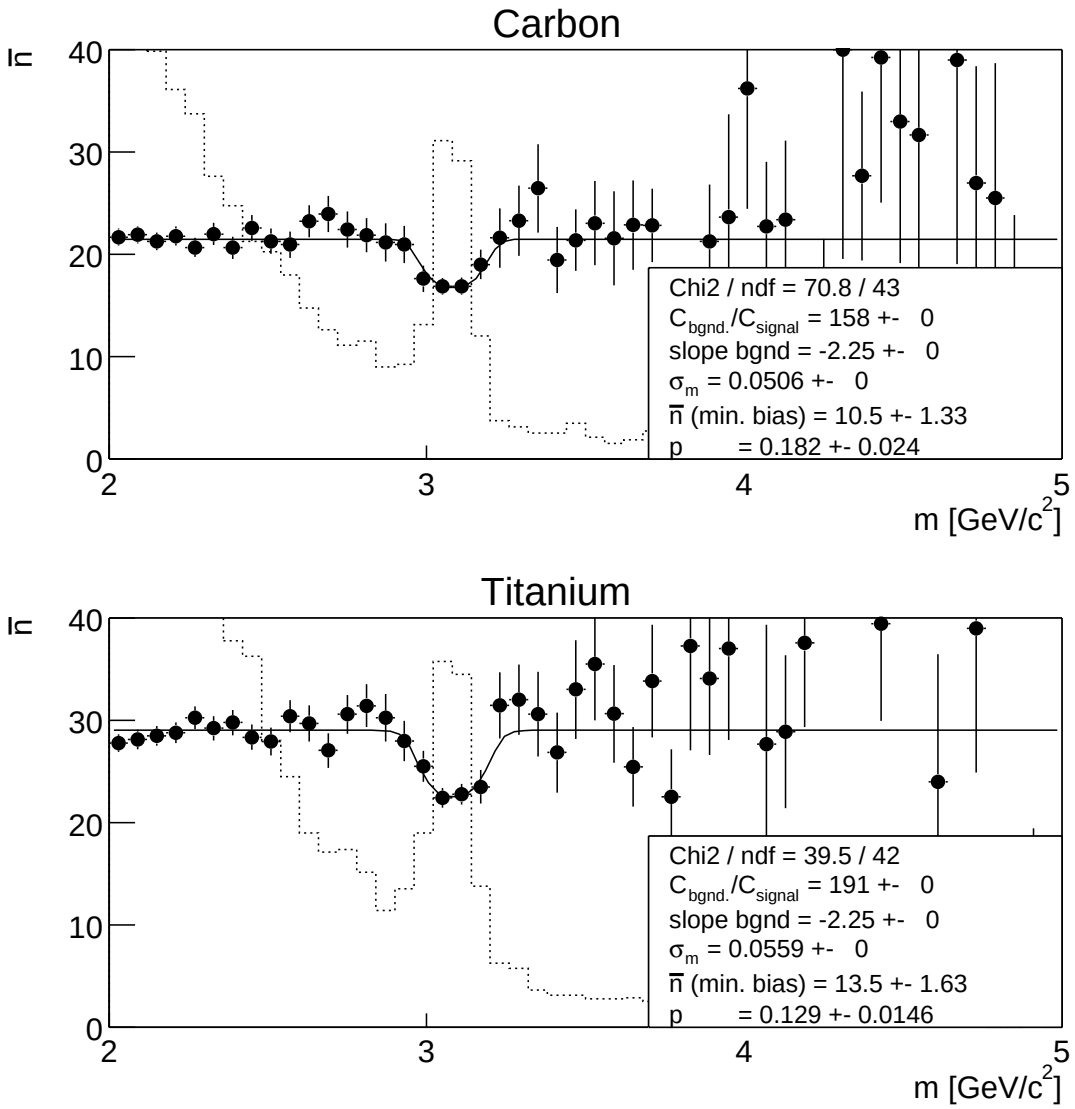

Figure 8.1.5: *Mass dependence of the average charged track multiplicity in triggered di-muon events. The weaker multiplicity bias for a J/ψ causes a clear drop in $\langle n \rangle$ at a mass of 3.1 GeV. For reference, the mass spectrum is also shown.*

There are two possible refinements to this model, the significance of which may have been obscured by the limited precision of the measurement. Both of these refinements lead to a slightly lower associated multiplicity than $\langle nP(n) \rangle$.

The first is the fact that the energy needed to form the J/ψ is no longer available for the production of associated particles. At the HERA-B beam energy of 920 GeV, J/ψ are produced with an average momentum of 56 GeV/c. Based on the $\sqrt{s}$ dependence of associated particle production, we expect an average correction of a few percent.

The second, and possibly more significant effect, is that the charged track multiplicity is only an indirect measure of the true bias, which is given by N_{elem}. Equation 8.1.11 is then only an approximation. The correlation is weaker than assumed (100%),

TITANIUM				
track definition	inelastic $\bar{n}$	J/ψ assoc. $\bar{n}_{J/\psi}$(ratio)	re-weighted inel. $\langle nP(n)\rangle$	triggered bgnd. $\bar{n}_{\rm bgnd.}$(ratio)
all, 1 vertex	14.4	18.9(1.31)	19.5	23.4(1.24)
all, >0 vertex	15.7	22.1(1.41)	22.0	27.4(1.24)
assigned, >0 vertex	12.2	17.5(1.43)	17.2	21.9(1.25)
assigned, 1 vertex	11.1	14.7(1.43)	15.0	18.0(1.22)
negative binomial	10.5	15.2(1.45)		20.0(1.31)
CARBON				
track definition	inelastic $\bar{n}$	J/ψ assoc. $\bar{n}_{J/\psi}$(ratio)	re-weighted inel. $\langle nP(n)\rangle$	triggered bgnd. $\bar{n}_{\rm bgnd}$(ratio)
all, 1 vertex	10.7	14.9(1.39)	15.7	19.9(1.27)
all, >0 vertex	11.5	17.2(1.49)	17.4	21.8(1.27)
assigned, >0 vertex	8.77	13.0(1.43)	13.1	16.6(1.28)
assigned, 1 vertex	8.15	11.4(1.40)	12.0	14.4(1.26)
negative binomial	7.92	11.6(1.46)		15.35(1.32)

Table 8.1.1: *Average multiplicity in inelastic interactions, interactions with a* J/ψ*, and random triggered background for titanium and carbon targets. The fourth column shows the results of the minimum bias distribution that has been re-weighted with the multiplicity itself. They reflect the expectations for the multiplicity in* J/ψ *events. The* $\mu^+\mu^-$ *tracks of the* J/ψ *are not counted in the multiplicity. The number in brackets are the ratio w.r.t the values in the previous column. We have adopted four different definitions of a charged track to estimate the systematic uncertainty in these ratios. The last row for each material gives the results based on the negative binomial with parameters determined in Fig. 8.1.2 and related expectation values as given in Eq. 8.1.14 and Eq. 8.1.17.*

and consequently the bias for the multiplicity is not as strong as assumed. Other candidates for $N_{\rm elem}$ will be studied in a Monte Carlo simulation in the next section.

It has been argued that the difference between the multiplicity of inclusive inelastic interactions and J/ψ events is predominantly caused by the hard scale involved in the production of the heavy charm quarks. If this were the case, then one would expect the difference in track multiplicities between carbon and titanium to become smaller, since then the multiplicity increase is independent of the target material. This is in disagreement with data: the absolute increase in $\bar{n}$ is higher for titanium that for carbon. This implies that the bulk of associated particles is produced independently of the J/ψ itself.

This multiplicity bias has not been reported before, possibly since most other experiments used an early hadron absorber and were therefore not able to observe this. It has been overlooked in co-mover absorption calculations, that assumed the associated particle densities to be equal to what is observed in inclusive inelastic interactions. Fortuitously, this error is largely compensated by another wrong assumption, that will

be discussed section 8.2.

8.1.6 Monte Carlo simulation of the associated event

The Monte Carlo generation of HERA-B (section 7.2.3) does not take into account this bias and, as a consequence, fails to describe the multiplicity in J/ψ events. The underlying event is basically a minimum-bias inelastic interaction, generated at a proton momentum $E_{\rm beam} - E_{\rm J/\psi}$. Since the energy dependence of the multiplicity is weak, the resulting associated particle multiplicity is within a few percent equal to the multiplicity of inclusive inelastic interactions. They differ from the data by more than 40%.

The Monte Carlo generation of the associated event should take into account the bias of Eq. 8.1.11. In data, we observed that the charged particle multiplicity is a reasonable measure of the true bias (the number of elementary sub-collisions $N_{\rm elem}$), but could possibly lead to an overestimate of the multiplicity.

In the Monte Carlo simulation one can study alternative quantities, with which the minimum bias event should be re-weighted to obtain the event associated to a J/ψ. The optimal quantity is the one for which the correlation with $N_{\rm elem}$ is strongest. We have tried several candidates: the number of charged tracks, the number of wounded nuclei, the number of gluons and the number of fragmenting strings [2]. The improved Monte Carlo generation of a J/ψ consists of the following steps:

(i) Generate a J/ψ using PYTHIA ;

(ii) Create a collision geometry and let FRITIOF generate an inelastic interaction;

(iii) Calculate the importance sampling quantity m;

(iv) Accept event if $m/m_{\rm max}$ larger than a random number between 0 and 1, else reject associated event and return to step (ii).

The resulting associated multiplicities in pC interactions for the different candidates are given in table 8.1.2. They indicate that the number of charged tracks and the number of gluons are both a good measure for $N_{\rm elem}$. The other two significantly underestimate the multiplicity increase, which was observed to be approximately 43% percent in data. This importance sampling procedure has now been implemented in the Monte Carlo generation of HERA-B.

8.2 Pseudo-rapidity distributions

In this section we study the pseudo-rapidity distributions of stable charged particles and of hadronic co-movers. We will show that the densities of the two are approximately

[2] One may think that the discrepancy could also be resolved by an importance sampling on the impact parameter b. In FRITIOF , b can be fixed before the determination of the collision geometry. This collision geometry, however, varies from event to event, even for a fixed b. Therefore there is not a unique path length (or $N_{\rm elem}$) for a given b, and, consequently, such a procedure does not successfully bring Monte Carlo and data in agreement.

	$\bar{n}$	$\bar{n}$ after re-weighting	ratio
Nr of charged tracks	8.26	12.1	1.46
Nr of wounded nuclei	8.26	10.6	1.28
Nr of gluons in event	8.26	12.2	1.48
Nr of strings	8.26	10.1	1.22

Table 8.1.2: *Mean multiplicity (Monte Carlo) of the inelastic interaction associated with a J/ψ before and after importance sampling. The ratios are to be compared to the ratios observed in data (table 8.1.1), the average of which is 1.43 for carbon. Both the re-weighting with the number of charged tracks and the re-weighting with the number of gluons in the event give a reasonable description of the data.*

equal, in contrast to the common assumption that they differ by 50%. This is the only existing measurement of the pseudo-rapidity distribution of associated particles in pA collisions.

8.2.1 Rapidity and pseudo-rapidity

In calculations of J/ψ suppression due to interactions with co-movers, the hadronic environment is described by the distribution of the rapidity y of other particles produced in the interaction:

$$y = \frac{1}{2} \ln \frac{E + p_z}{E - p_z}, \tag{8.2.1}$$

where E and p_z are the energy of the particle and its longitudinal momentum respectively. Rapidity differences are Lorentz invariant, and therefore the shape of the rapidity distribution does not change under Lorentz transformations. Such distributions are defined w.r.t. mid-rapidity, which is about 3.5 at HERA-B.

The rapidity requires both knowledge of momentum and mass, which is not available for all charged particles. Under these circumstances a good alternative is pseudo-rapidity:

$$\begin{aligned} \eta &= \frac{1}{2} \ln \frac{p + p_z}{p - p_z}, \\ &= -\ln(\tan \frac{\theta}{2}), \end{aligned}$$

where θ is the angle between the particle and the beam axis. The pseudo-rapidity is equal to the rapidity for massless particles, or generally when $p_T \gg m$. It can be determined from the slopes (p_x/p_z and p_y/p_z) of the tracks in the vertex detector, and requires neither the mass nor the momentum of the particle to be known.

8.2.2 Pseudo-rapidity distribution of stable charged particles

To relate the observed pseudo-rapidity distributions to the distribution produced in the primary interactions one needs to correct for the acceptance. The acceptance is determined with a Monte Carlo simulation as the ratio of the pseudo-rapidity distribution

of stable, charged particles, and that of tracks reconstructed in the vertex detector, as shown in figure 8.2.1.

This acceptance does not only take into account the geometrical acceptance and the track reconstruction efficiency of the vertex detector, but also includes the production of secondary particles due to interactions with detector material. Since the production of secondary particles over-compensates the track reconstruction efficiency and geometrical acceptance at mid-rapidity, the acceptance is larger than unity there.

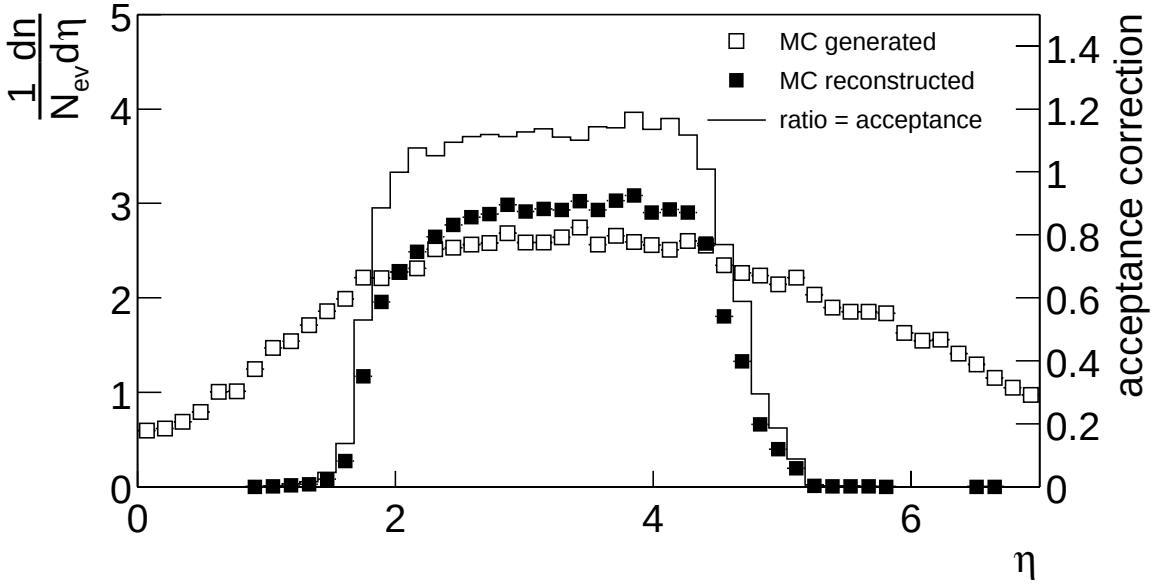

Figure 8.2.1: *Determination of the acceptance in pseudo-rapidity from Monte Carlo simulated inelastic interactions. The open squares show the distribution of generated stable charged particles. The solid squares show the resulting distribution of charged tracks in the vertex detector. The acceptance correction factor is the ratio of the two distributions.*

Figure 8.2.2 shows the measured pseudo-rapidity distributions of stable, charged particles, produced in association with a J/ψ for both target materials separately. For comparison, the distributions before acceptance corrections, and the results from the (improved) Monte Carlo simulation, are also shown.

There is a small but significant discrepancy between the data and the Monte Carlo simulation. This has also been observed in minimum bias events, but it is not completely understood. The discrepancy is predominantly in the tails of the distribution, that correspond to the boundaries of the acceptance. The Monte Carlo simulation overestimates the reconstruction efficiency there. This could be caused by the fact that the efficiency of the strips at the edges of a vertex detector plane is significantly lower than in the middle of the plane. This effect was not taken into account in the simulation.

The density at forward ($\eta > 4$) rapidity of associated particles is less than observed in inclusive inelastic interactions. This is a consequence of the 40% higher track multiplicity: the total available energy is shared by more particles, that each have a lower forward momentum, and, consequently, a lower pseudo-rapidity. For the same

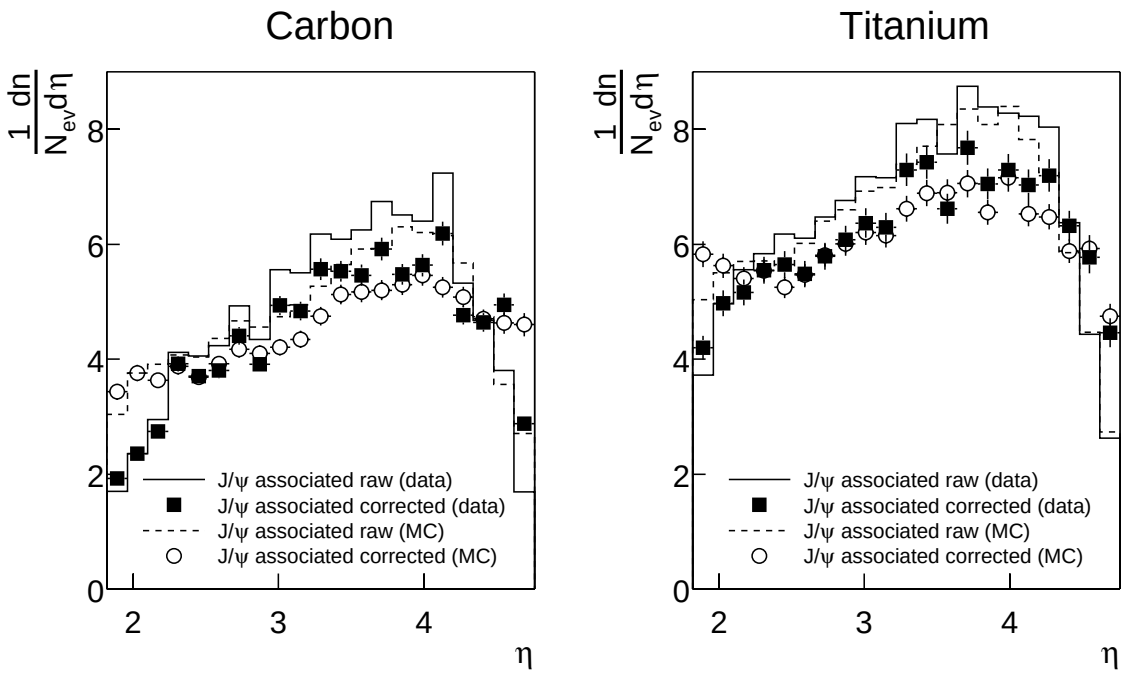

Figure 8.2.2: *Pseudo-rapidity distributions of charged particles produced in association with a* J/ψ. *The uncorrected distributions are shown both for data (solid) and Monte Carlo (dashed). The solid squares and open circles indicate the distributions corrected for the acceptance (Fig. 8.2.1).*

reason, the average pseudo-rapidity decreases with the atomic weight of the target material [92].

8.2.3 Pseudo-rapidity distribution of hadronic co-movers

The distributions of figure 8.2.2 were restricted to charged stable particles, since these are directly observed as tracks in the detector. However, the particles that could possibly break up the J/ψ are not necessarily of this nature. The J/ψ may interact with any hadron that is present in its vicinity within its short lifetime. These co-movers, defined as hadrons present during the formation and lifetime of the J/ψ, may be neutral and/or unstable. The lifetime of particles such as ρ, η, ω is larger than the effective proper time in which co-movers interact with the J/ψ [80].

For calculations of co-mover suppression one should use the density of the hadrons that are present at this small time scale. The determination of this density involves a large dependence on the production model. Here, FRITIOF is used to relate the measured charged tracks to the initial co-mover density. A co-mover is assumed to be any hadron directly produced from a fragmenting string. An acceptance profile, similar to the one shown in figure 8.2.1 is used for this. In figure 8.2.3 we show the pseudo-rapidity distributions of both primary stable hadronic particles and co-movers in inelastic interactions.

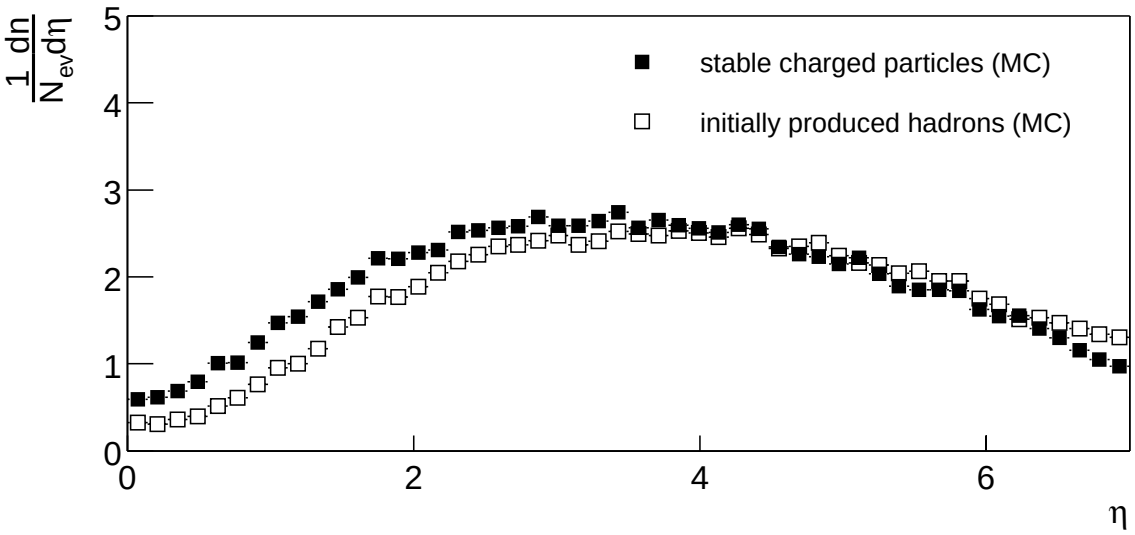

Figure 8.2.3: *Pseudo-rapidity distributions of hadronic co-movers and primary stable charged particles. In the acceptance of* HERA-B, $2 < \eta < 4.5$, *the density of co-movers is similar to that of the (measured) hadrons.*

Compared to stable particles in the final state, the co-movers are slightly enhanced at high η and depleted at low η. This is to be expected since the co-movers have a higher momentum than the stable particles into which they decay. In the region that corresponds to the geometrical acceptance of the detector ($2 < \eta < 4.5$) the differences are small. In the HERA-B acceptance, the pseudo-rapidity distribution of J/ψ co-movers (Fig. 8.2.4), does not differ much from that of stable charged tracks (Fig. 8.2.2).

It implies that the co-mover densities used in theoretical calculations, commonly taken to be 1.5 times the number of charged stable particles, is an overestimate of the true density. This overestimate is however compensated by the other effect that was overlooked, namely the multiplicity bias. This multiplicity bias causes the J/ψ event to have a multiplicity, that is 45% higher than general inelastic interactions. As a result, the co-mover densities taken in these calculations should be approximately correct, accidentally.

8.3 Transverse momentum broadening

As discussed in section 5.3.2, the p_T spectrum of J/ψ has been observed to grow broader with the atomic weight of the target. The average value of p_T^2 rises linearly with the amount of matter the proton encountered in the nucleus before producing the J/ψ.

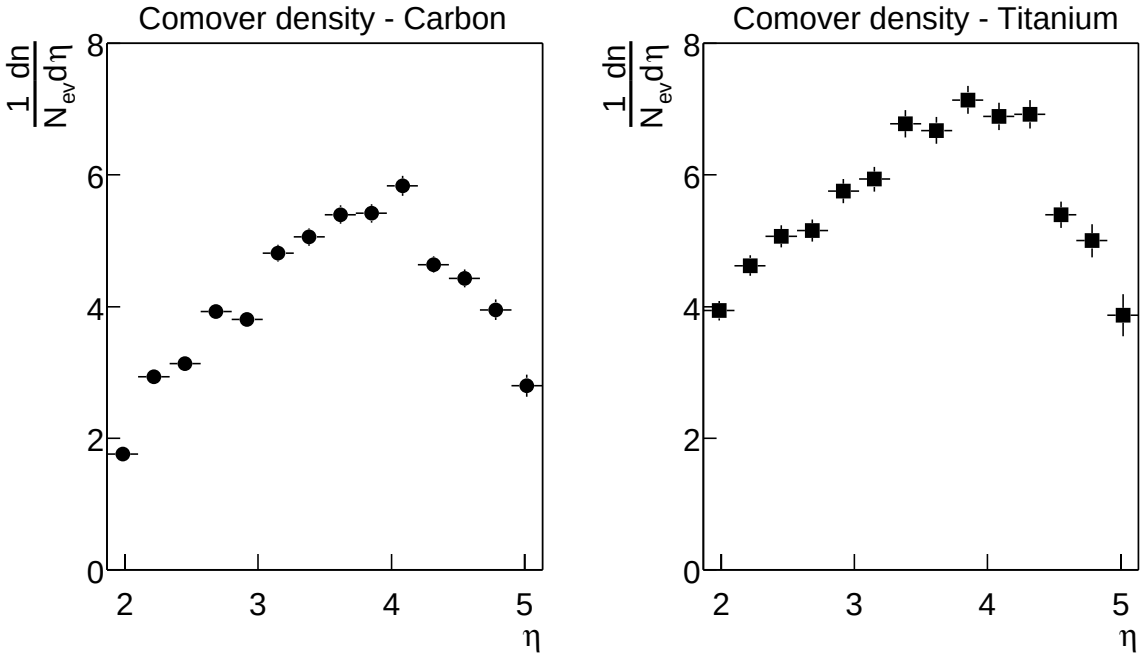

Figure 8.2.4: *Measurement of the pseudo-rapidity distributions of* J/ψ *co-movers. A co-mover is defined as a hadron present during the formation of the* J/ψ*. Co-movers can break up charmonium states, leading to an observable reduction of the* J/ψ *yield.*

A-dependence of the p_T spectrum of J/ψ

Figure 8.3.1 shows the distributions of p_T^2 of the J/ψ from the carbon wire and from the titanium wire separately. The J/ψ are selected as muon pairs that are within 75 MeV/c^2 ($\approx 1.5\sigma_m$) of the nominal mass. We have again corrected for the contribution from the background by subtracting the p_T^2 spectrum of the sidebands ($2.45 < m < 2.95$ GeV/c^2 and $3.1 < m < 2.95$ GeV/c^2) in the correct proportion.

The distributions are fitted with an exponential (Eq. 5.1.14), for which the inverse slope ($1/b$) is equal to the mean value of $\langle p_T^2 \rangle^{\mathrm{J}/\psi}$. The results indeed seem to indicate that the p_T spectrum of titanium is broader than that of carbon, but the (statistical) significance is too small to permit a conclusive statement.

The expected A dependence can be obtained from the path length dependence in the NA50 data (Fig. 5.3.3):

$$\langle p_T^2 \rangle^{\mathrm{J}/\psi} = 1.20(2)\ \mathrm{GeV}^2/\mathrm{c}^2 + 0.080(1)\ \mathrm{GeV}^2/\mathrm{c}^2\mathrm{fm} \times \bar{L} \qquad (8.3.1)$$

Assuming a uniform spherical density, the average path length of a proton in a nucleus with radius R is $\bar{L} = \frac{4}{3}R$ for minimum bias events. If a J/ψ is produced, however, it is

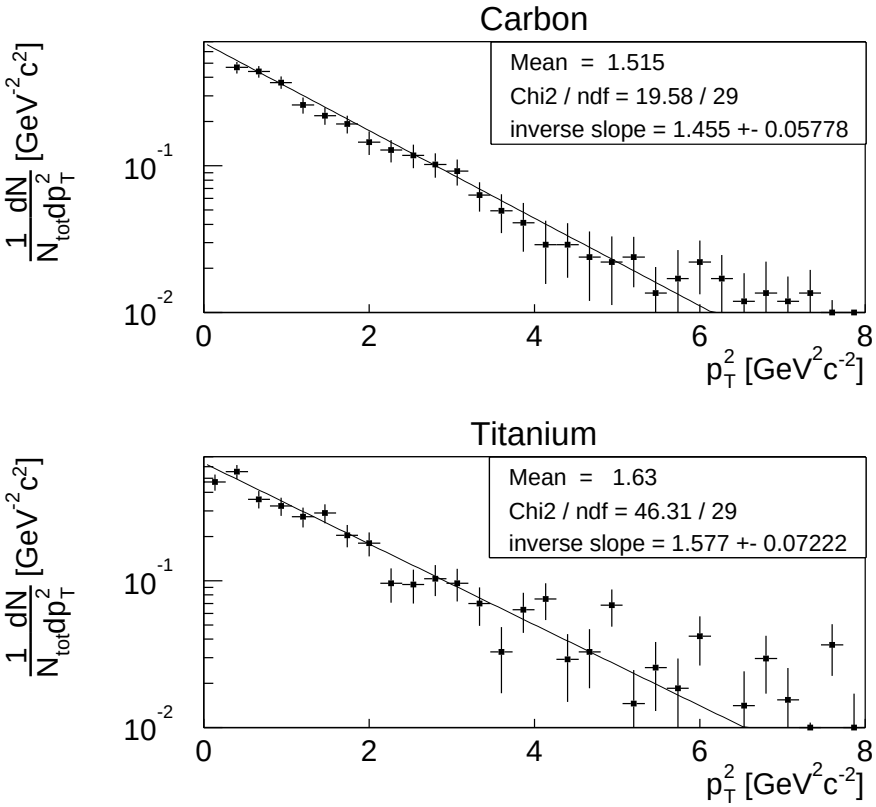

Figure 8.3.1: *p_T^2 spectra for J/ψ from carbon and titanium. The data are fitted with an exponential distribution (Eq. 5.1.14), with a single free parameter.*

higher, because the probability to find a J/ψ is proportional to the path length itself[1]:

$$\begin{aligned} \bar{L}_{J/\psi} &= \frac{\int_0^R dr(R^2-r^2)}{\bar{L}\int_0^R dr\sqrt{R^2-r^2}} \\ &= \frac{3}{2}R = \frac{3}{2}r_0 A^{1/3}. \end{aligned} \tag{8.3.2}$$

This then gives the predicted dependence on A, with $r_0 = 1.1$ fm ,

$$\langle p_T^2\rangle^{J/\psi} = 1.20(2)\ \mathrm{GeV}^2/\mathrm{c}^2 + 0.048(1)\ \mathrm{GeV}^2/\mathrm{c}^2\mathrm{fm} \times A^{1/3}\frac{A-1}{A}, \tag{8.3.3}$$

where the factor $(A-1)/(A)$ accounts for the fact that we do not expect any p_T broadening for a proton target. This dependence is in good agreement with data, shown in figure 8.3.2.

A linear fit to this data gives for beam energies of 200 GeV

$$\langle p_T^2\rangle_{pA} = 1.209(3)\ \mathrm{GeV}^2/\mathrm{c}^2 + 0.0525(47)A^{1/3}(A-1)/A. \tag{8.3.4}$$

[1]This is the *proton* path length. The mean path length of the J/ψ is half of this.

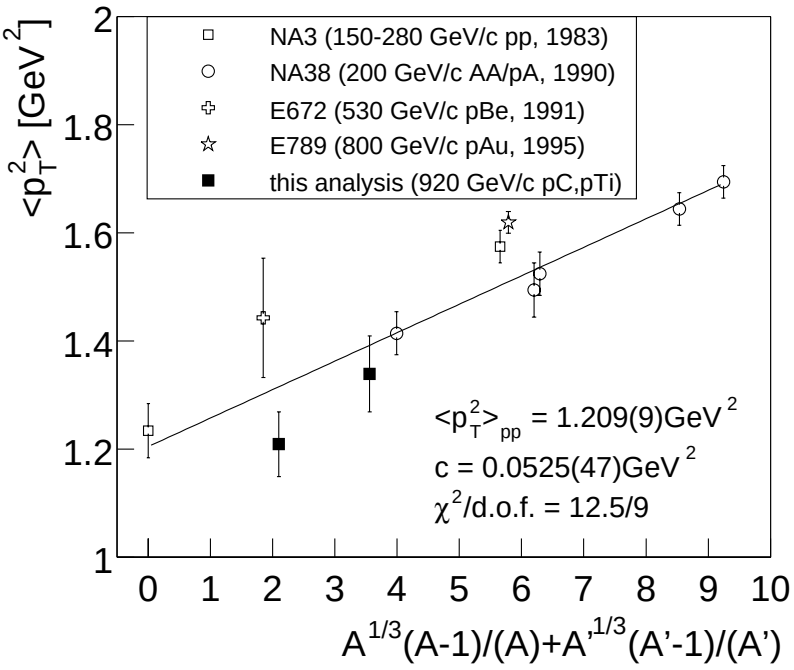

Figure 8.3.2: *Nuclear dependence of $\langle p_T^2 \rangle$. A and A′ refer to the atomic numbers of projectile and target. The E789 data is not used in the fit since their parametrisation (Eq.7.3.4) is different from the one used in the other measurements, and may lead to systematically higher values of $\langle p_T^2 \rangle$. All data points are re-scaled to the NA38 beam energy of 200* GeV *using Eq. 8.3.5.*

The value of the slope 0.0525(47) is slightly less than previously obtained by Gerschel and Hüfner [114], most likely mainly due to a wrong inclusion of one of the NA38 data points on their part.

In figure 8.3.2, we have included data from various fixed target experiments, which have beam energies different from that of NA38. These data have been corrected for the centre-of-mass energy dependence of $\langle p_T^2 \rangle$, taken from [83]:

$$\langle p_T^2 \rangle_{pp}(s) = 1.17 \text{ GeV}^2 \ + 1.81 \times 10^{-4} s. \tag{8.3.5}$$

Whereas this formula yields incredible results for high centre-of-mass energies, it gives a reasonable description of the data at fixed target energies ($\sqrt{s} < 40$ GeV).

The HERA-B data have also been corrected to a beam energy of 200 GeV. This gives a subtraction of

$$\Delta\langle p_T^2 \rangle = 1.81 \times 10^{-4} \times 2m_p \times (920 \text{ GeV} - 200 \text{ GeV}) = 0.21 \text{ GeV}^2/\text{c}^2 \tag{8.3.6}$$

for both data points. The uncertainty in 8.3.5 was not given, but based on the difference between Eq. 8.3.5 and a similar fit to data of pion-induced J/ψ production we estimate this to be of the order of 30%. This gives an additional uncertainty for the HERA-B data points of 0.06 GeV^2 .

Dependence on the multiplicity

According to Eq. 8.3.1, the $\langle p_T^2 \rangle$ of J/ψ is proportional to the path length L traversed by the incident proton before the hard interaction. As discussed in section 5.4, indirect measures of this path length are the charged track multiplicity and the total (transverse) energy deposited in the calorimeter.

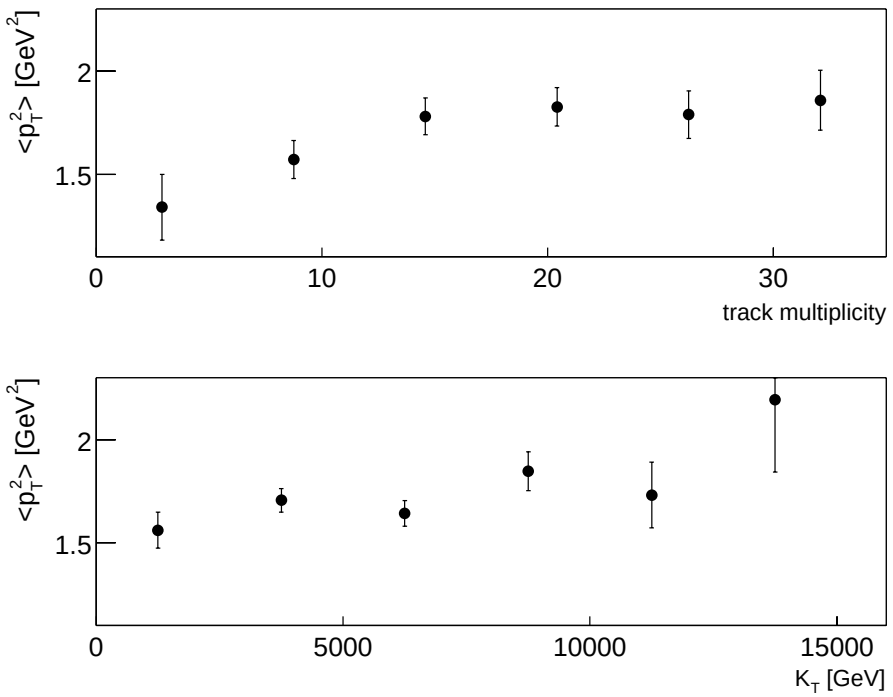

Figure 8.3.3: *Dependence of the $\langle p_T^2 \rangle$ of J/ψ on total charged track multiplicity (above) and on the magnet corrected transverse energy(below). Both quantities are expected to scale with the path length L traversed by the proton through the nucleus.*

In figure 8.3.3 we show the dependence of $\langle p_T^2 \rangle$ of J/ψ on the multiplicity and on the total magnet-corrected transverse energy K_T (see Eq.6.5.1) in the event. The J/ψ are selected to be within 100 MeV/c^2 of the nominal mass. We also require that the event does not contain more than a single primary vertex. This reduces the dilution due to multiple interactions, that would otherwise fake an interaction with large path length.

Indeed the dependence on these quantities suggest a broadening of the p_T^2 spectrum with path length. This qualitatively confirms the result of NA50 [81], shown in figure 5.3.3, although with poorer statistical precision.

The increase of $\langle p_T^2 \rangle$ is more significant if the track multiplicity is taken as a measure of the path length, than if the transverse energy is used. The correlation between the transverse energy and the path length is weaker than the correlation between the multiplicity and the path length. This was already shown in the relative increase of the detector response with target material (see table 6.5.1): the track multiplicity was

27 percent higher for titanium than for carbon, whereas the total energy was only 20 percent more.

Nuclear suppression as a function of p_T

The broadening of the p_T spectrum implies that the suppression factor $\alpha^{J/\psi}$ must rise with p_T. The production of J/ψ of high p_T is enhanced by nuclear matter. Separate measurements of the relative J/ψ yield in the low p_T ($p_T < 1$ GeV/c) and in the high p_T ($p_T > 1$ GeV/c) domain indeed suggest a rise with p_T, although statistical uncertainty is too large to permit any conclusive statement. In table 8.3.1 the results of this measurement are summarised.

	$N_{\mathrm{C}}^{J/\psi}$	$N_{\mathrm{Ti}}^{J/\psi}$	$\alpha^{J/\psi}$
$p_T^{J/\psi} < 1$ GeV/c	405 ± 24	497 ± 29	0.974 ± 0.060(stat.)
$p_T^{J/\psi} > 1$ GeV/c	474 ± 27	623 ± 34	1.024 ± 0.057(stat.)

Table 8.3.1: *Measured J/ψ yields and $\alpha^{J/\psi}$ for two bins in $p_T^{J/\psi}$. A consequence of the p_T broadening is that the production at high p_T is relatively enhanced ($\alpha^{J/\psi} > 1$) in heavy nuclei.*

8.4 Summary

In this chapter we have studied the production of particles associated with the occurrence of a J/ψ. We have observed that the required presence of a J/ψ causes a bias, that leads to higher multiplicities than present in inclusive inelastic interactions. It can be understood within a simple probabilistic model, that also explains the higher mean multiplicity in triggered background events.

We have performed a first measurement of the pseudo-rapidity distributions of the charged stable particles produced in association with a J/ψ, and of the co-movers that may interact with the J/ψ during its short lifetime. We have argued that the theoretical calculations on suppression with hadronic co-movers have generally made two wrong assumptions on this co-mover density. Accidentally, they practically cancel.

The study of the p_T spectrum of J/ψ shows a broadening for heavier nuclei, consistent with previous measurements. We have implicitly confirmed that the number of primary tracks is a better measure of the path length than the total transverse energy, which is more often used. The statistical precision of the present data is poor. The measurements do however show that the HERA-B detector has a significant potential in providing understanding in nuclear effects in J/ψ production.

Bibliography

[1] J. H. Christenson, J. W. Cronin, V. L. Fitch, and R. Turlay, Phys. Rev. Lett. **13**, 138 (1964).

[2] A. D. Sakharov, JETP **5**, 24 (1967).

[3] M. Kobayashi and T. Maskawa, Prog. Theor. Phys. **49**, 652 (1973).

[4] S. W. Herb *et al.*, Phys. Rev. Lett. **39**, 252 (1977).

[5] CDF, F. Abe *et al.*, Phys. Rev. Lett. **74**, 2626 (1995), hep-ex/9503002.

[6] D. Groom *et al.*, The European Physical Journal **C15**, 1+ (2000).

[7] T. Perschke, *Inklusive Multiplizität geladener Teilchen beim Hera-B Fixed Target Experiment*, PhD thesis, MPI München, 2000.

[8] T. Lohse *et al.*, Hera-B Proposal, DESY-PRC 94/02, 1994.

[9] E. Hartouni *et al.*, Hera-B Design Report, DESY-PRC 95/01, 1995.

[10] Hera-B collaboration, Report on Status and Prospects, DESY-PRC 00/04, 2000.

[11] J. Flammer, *Development of the ECAL Pretrigger system simulation for the experiment Hera-B and analysis of efficiencies of the decays* $J/\psi \rightarrow e^+e^-$, PhD thesis, Universität Hamburg, 2001.

[12] R. Bouclier *et al.*, Nucl. Instrum. Meth. **A367**, 168 (1995).

[13] H. van der Graaf *et al.*, Nucl. Instrum. Meth. **A307**, 220 (1991).

[14] W. Hulsbergen, *Quarkonium Production at Hera-B*, PhD thesis, Universiteit van Amsterdam, 2001.

[15] BaBar, B. Aubert *et al.*, Phys. Rev. Lett. **87**, 091801 (2001), hep-ex/0107013.

[16] Belle, K. Abe *et al.*, Phys. Rev. Lett. **87**, 091802 (2001), hep-ex/0107061.

[17] Hera-B collaboration, Status and plans for 2001/2, HERA-B 01-064, 2001.

[18] Hera-B collaboration, Measurement of the $b\bar{b}$ production cross section at Hera-B with the 2000 data sample, HERA-B 02-005, 2002.

[19] J. S. Conway *et al.*, Phys. Rev. **D39**, 92 (1989).

[20] M. Bruinsma, Nuclear Effects in J/ψ Production, HERA-B 01-087, 2001.

[21] A. Schwartz, Triggering on Charm Decays with a Single-Lepton Trigger, HERA-B 00-186, 2000.

[22] M. Danilov *et al.*, Measuring of direct photon Production at Hera-B (Proposal), HERA-B 00-095, 2000.

[23] F. Saadi-Lüdemann, Trigger for Radiative B Decays at the Hera-B experiment, HERA-B 96-246, 1996.

[24] V. Balagura *et al.*, The possibility to observe b0s oscillations at Hera-B, HERA-B 00-013, 2000.

[25] I. Bigi and A. Sanda, *CP violation* (Cambridge University Press, 2000).

[26] H. D. Schulz, Nucl. Phys. Proc. Suppl. **44**, 441 (1995).

[27] J. Gläß *et al.*, Design of the Hera-B First Level Trigger, in *Proc. IEEE Nucl. Sci. Symp.*, pp. 612–616, San Francisco, CA, 1995.

[28] T. Fuljahn *et al.*, Concept of the First Level Trigger for Hera-B, in *Proc. IEEE Trans. on Nucl. Science, vol. 45, N4*, pp. 1782–1786, 1998.

[29] R. Frühwirth, Nucl. Instrum. Meth. **A262**, 444 (1987).

[30] T. Fuljahn *et al.*, Implementation of the Hera-B First Level Trigger, in *Proc. Computing in High Energy Physics*, pp. 246–248, Berlin, Germany, 1997.

[31] M. Villa *et al.*, The Reconstruction for the Electromagnetic Calorimeter of the Hera-B Experiment, in *Proceedings of the VII International Conference on Calorimetry in High Energy Physics*, pp. 537–546, 1997.

[32] L. Brugge, Nucl. Instrum. Meth. **A242**, 428 (1986).

[33] M. Boecker *et al.*, The Muon Pretrigger System of the Hera-B Experiment, in *IEEE Trans. Nucl. Sci.*, p. 118, Lyon, France, 2000.

[34] H. Riege, J. Schütt, R. v. Staa, and V. Popov, The Hera-B high-pT Level 0 Trigger Logic Electronics, in *Proc. LHC Electronics Workshop*, pp. 557–560, 1999.

[35] M. Bruinsma, J. Hogenbirk, and O. Steinkamp, Documentation on the First Level Trigger Linkboard, HERA-B 98-066, 1998.

[36] B. Schwingenheuer, private communication.

[37] T. Sjoestrand, Comm. Phys. Comm. **82** (1994) 74 (1994).

[38] H. Pi, Comm. Phys. Comm. **71** (1992) 173 (1992).

[39] R. Brun *et al.*, Geant: Simulation program for particle physics experiments. user guide and reference manual, CERN-DD-78-2-REV, 1978.

[40] R. Mankel and A. Spiridonov, HERA-B Note 98-206 (1998).

[41] C. Cruse, Hardware Proposal of the RICH VETO System, HERA-B 01-022, 2001.

[42] M. Adams, Study of Hit Multiplicities, HERA-B 01-059, 2001.

[43] M. Villa, Progress Report on the ECAL Reconstruction Software, HERA-B 97-005, 1997.

[44] R. Devijver and J. Kittler, *Pattern recognition, A Statistical Approach* (Pretince-Hall Int. London, 1982).

[45] J. Flammer, EcalSIM - The Ecal Pretrigger Simulation, HERA-B 01-054, 2001.

[46] J. Flammer, ECAL Pretrigger Lookuptables, Talk on Hera-B Coll. Meeting, 2000.

[47] V. Alberico *et al.*, The Reconstruction for the Electromagnetic Calorimeter of the Hera-B Experiment , in *Proceedings of the VII International Conference on Calorimetry in High Energy Physics*, pp. 537–546, 1997.

[48] H. Bethe and W. Heitler, Proc. Roy. Soc. Lond. **A146**, 83 (1934).

[49] H. Fleckenstein, Acceptance and Efficiency of the First Level Trigger, HERA-B 01-142, 2001.

[50] A. Arefev *et al.*, IEEE Trans. Nucl. Sci. **48**, 1059 (2001).

[51] B. Schwingenheuer, Electronics Commissioning Experience at Hera-B, in *Proc. VII International Conference on Electronics for LHC Experiments*, 2001.

[52] MOTOROLA, MC100SX1451FI100 AutoBahn Spanceiver datasheet, 1996.

[53] L. Soezueer, private communication.

[54] A. Michetti, D. Ressing, and I. Riu, HERA-B first level trigger test vector test, HERA-B 02-027, 2002.

[55] E. Gerndt, Hera-B Pretrigger and FLT latency, HERA-B 00-013, 2000.

[56] A. Michetti *et al.*, Track finding at 10 MHz hadronic event rate, in *Proc.2001 IEEE Real Time Conference*, 2001.

[57] I. Negri.

[58] R. Ellis, W. Stirling, and B. Webber, *QCD and Collider physics* (Cambridge University Press, 1996).

[59] L. M. Jones and H. W. Wyld, Phys. Rev. **D17**, 2332 (1978).

[60] CTEQ, H. L. Lai *et al.*, Eur. Phys. J. **C12**, 375 (2000), hep-ph/9903282.

[61] K. J. Eskola, H. Honkanen, V. J. Kolhinen, P. V. Ruuskanen, and C. A. Salgado, Eur. Phys. J. **C9**, 61 (1999), hep-ph/0110348.

[62] H. Plothow-Besch, Comput. Phys. Commun. **75**, 396 (1993).

[63] M. L. Mangano, P. Nason, and G. Ridolfi, Nucl. Phys. **B405**, 507 (1993).

[64] P. Nason, S. Dawson, and R. K. Ellis, Nucl. Phys. **B303**, 607 (1988).

[65] P. Nason, S. Dawson, and R. K. Ellis, Nucl. Phys. **B327**, 49 (1989).

[66] W. Beenakker, H. Kuijf, W. L. van Neerven, and J. Smith, Phys. Rev. **D40**, 54 (1989).

[67] W. Beenakker, W. L. van Neerven, R. Meng, G. A. Schuler, and J. Smith, Nucl. Phys. **B351**, 507 (1991).

[68] N. Kidonakis, E. Laenen, S. Moch, and R. Vogt, Phys. Rev. **D64**, 114001 (2001), hep-ph/0105041.

[69] G. A. Schuler, Quarkonium production and decays, 1994.

[70] H. Fritzsch, Phys. Lett. **B67**, 217 (1977).

[71] R. Baier and R. Ruckl, Phys. Lett. **B102**, 364 (1981).

[72] E. L. Berger and D. L. Jones, Phys. Rev. **D23**, 1521 (1981).

[73] R. Gavai *et al.*, Int. J. Mod. Phys. **A10**, 3043 (1995), hep-ph/9502270.

[74] E. Braaten, Introduction to the NRQCD factorization approach to heavy quarkonium, 1996.

[75] M. Beneke and I. Z. Rothstein, Phys. Rev. **D54**, 2005 (1996), hep-ph/9603400.

[76] M. Arneodo, Phys. Rept. **240**, 301 (1994).

[77] S. Gavin and J. Milana, Phys. Rev. Lett. **68**, 1834 (1992).

[78] S. J. Brodsky and P. Hoyer, Phys. Lett. **B298**, 165 (1993), hep-ph/9210262.

[79] R. Baier, Y. L. Dokshitzer, A. H. Mueller, S. Peigne, and D. Schiff, Nucl. Phys. **B484**, 265 (1997), hep-ph/9608322.

[80] R. Vogt, Phys. Rev. **C61**, 035203 (2000), hep-ph/9907317.

[81] NA50, M. C. Abreu *et al.*, Phys. Lett. **B499**, 85 (2001).

[82] Y. B. He, J. Hufner, and B. Z. Kopeliovich, Phys. Lett. **B477**, 93 (2000), hep-ph/9908243.

[83] R. Vogt, Phys. Rept. **310**, 197 (1999).

[84] NuSea, M. Leitch *et al.*, Nucl. Phys. **A661**, 554 (1999).

[85] R. Vogt, Nucl. Phys. **A700**, 539 (2002), hep-ph/0107045.

[86] T. Matsui and H. Satz, Phys. Lett. **B178**, 416 (1986).

[87] H. Satz, Nucl. Phys. Proc. Suppl. **94**, 204 (2001), hep-ph/0009099.

[88] H. Satz, (1997), hep-ph/9706342.

[89] NA50, M. C. Abreu *et al.*, Phys. Lett. **B477**, 28 (2000).

[90] A. Capella, E. G. Ferreiro, and A. B. Kaidalov, Phys. Rev. Lett. **85**, 2080 (2000), hep-ph/0002300.

[91] FNAL E772, M. B. Johnson *et al.*, Phys. Rev. Lett. **86**, 4483 (2001), hep-ex/0010051.

[92] S. Fredriksson, G. Eilam, G. Berlad, and L. Bergstrom, Phys. Rept. **144**, 187 (1987).

[93] B. Anderson, *The lund model* (Cambridge Univ. Press, 1998).

[94] I. Kisel and S. Masciocchi , CATS, A Cellular Automaton for Tracking in Silicon for the Hera-B Vertex Detector, HERA-B 99-242, 1999.

[95] R. Eckmann and D. Dujmic, Software for stand-alone RICH Reconstruction, HERA-B 00-004, 2000.

[96] M. Staric and P. Krizan, Nucl. Instrum. Meth. **A433**, 279 (1999).

[97] B. Fominikh, MUREC-A Reconstruction Program for HERA-B Muon Detector operating in Stand-alone mode, HERA-B 97-025, 1997.

[98] O. Igonkina, MARPLE -Version 1.03-, 1998.

[99] D. Emeliyanov *et al.*, Grover, 2001.

[100] R. Brun and F. Rademakers, Nucl. Instrum. Meth. **A389**, 81 (1997).

[101] E814, J. Barrette, Phys. Rev. **C52**, 2028 (1995).

[102] A. Somov, *Hard proton nucleus interactions and production of heavy flavours at Hera-B*, PhD thesis, Humboldt-Universität Berlin, 2000.

[103] Ivarson, J. , K. Kreuzer, and T. Lohse, PYTHIA and FRITIOF: Event Generators for HERA-B, 1999.

[104] T.-H. Chang, *Angular distribution of J/ψ decays in dimuon channel in 800 GeV proton-copper collisions*, PhD thesis, New Mexico State University, 1999, hep-ex/0012034.

[105] E789, M. H. Schub *et al.*, Phys. Rev. **D52**, 1307 (1995).

[106] W. Lee, *A Measurement of the Nuclear Dependence of J/ψ and ψ' Production*, PhD thesis, Georgia State University, 1999.

[107] S. Gavin and R. Vogt, Nucl. Phys. **B345**, 104 (1990).

[108] K. Goulianos, H. Sticker, and S. N. White, Phys. Rev. Lett. **48**, 1454 (1982).

[109] UA5, G. J. Alner *et al.*, Phys. Lett. **B167**, 476 (1986).

[110] A. Giovannini and L. Van Hove, Z. Phys. **C30**, 391 (1986).

[111] Z. Koba, H. Nielsen, and P. Olesen, Nucl. Phys. **B40**, 317 (1972).

[112] T. Osada, N. Nakajima, M. Biyajima, and N. Suzuki, Prog. Theor. Phys. **98**, 1289 (1997), hep-ph/9805256.

[113] A. Giovannini and L. Van Hove, Acta Phys. Polon. **B19**, 495 (1988).

[114] C. Gerschel and J. Hüfner, Ann. Rev. Nucl. Part. Sci. **49**, 255 (1999), hep-ph/9802245.

List of Figures

List of Tables

Summary

In this thesis we have reported on research performed at the HERA-B experiment at DESY, Hamburg. The main objective of HERA-B was a first measurement of CP violation in the B system. The detector and trigger were specifically designed to measure a CP asymmetry in the golden decay $\overline{\mathrm{B}}^0/\mathrm{B}^0 \to \mathrm{J}/\psi\,\mathrm{K}^0_\mathrm{S}$. This measurement provides a direct test of the Kobayashi-Maskawa hypothesis of CP violation in the Standard Model.

To this end, a unique target system was installed to parasitically exploit the 920 GeV proton beam of the HERA accelerator. Eight target wires can be moved to an arbitrary position inside the halo of the proton beam to obtain the desired luminosity, typically $\mathcal{O}(10^{33}\ \mathrm{cm^2 s^{-1}})$, which corresponds to an inelastic interactions rate of $\mathcal{O}(10$ MHz).

The main reason that the decay $\mathrm{B}^0 \to \mathrm{J}/\psi\,\mathrm{K}^0_\mathrm{S}$ is called 'golden' is that it is relatively easy to reconstruct experimentally. The J/ψ is easily identified through its decay into a lepton pair and the K^0_S is readily observed as a detached $\pi^+\pi^-$ pair. These signatures are not easily mimicked by background. However, at HERA-B only one in 100 billion inelastic interactions produce a B meson, and only a small fraction of those will decay to this final state. The high event rate and the extremely low signal to background ratio impose trigger requirements, that are only comparable to that of future LHC experiments such as CMS and ATLAS.

The trigger of HERA-B is specifically built to select J/ψ candidates. The main and most novel part of the trigger system is the First Level Trigger: a network of custom-made processor boards, that performs J/ψ mass reconstruction within 12 μs. Its computational power amounts to the processing of 1 Tb/s and the reconstruction of up to 500 million tracks per second in a hadronic environment.

In this thesis we have presented a description and a detailed analysis of the First Level Trigger, with emphasis on the performance for the reconstruction of $\mathrm{J}/\psi \to \mathrm{e}^+\mathrm{e}^-$ decays. The J/ψ trigger efficiency is a benchmark for the performance of HERA-B.

The reconstruction of electrons is initiated by the ECAL pretrigger, which performs a fast reconstruction of calorimeter clusters, that serve as starting point for the track search by the FLT. We have shown that the installed ECAL pretrigger hardware behaved largely as expected, but suffered from transmission errors between the readout electronics and the pretrigger boards. Simplifications of the pretrigger cluster reconstruction algorithm do not affect the performance as much as external effects do, such as Bremsstrahlung energy loss. Part of this energy loss, Bremsstrahlung before the magnet, can be recovered. Energy losses inside the magnetic field are, however, irretrievable.

The pretrigger efficiency for a J/ψ was less than 10% in 2000, mainly due to uninstalled or defective pretrigger electronics. We have shown that this efficiency can increase to over 25%, when the system is completed in 2002, and with some improved settings such as an enlarged search window size for the FLT. The removal of the tracking chambers in the magnet area will give an beneficial reduction of the irretrievable energy losses. This, and the inclusion of cut on the maximum of E/p (the ratio of the cluster and momentum of the track), give a significantly increase in the background rejection power.

We have presented a detailed analysis of the FLT performance for the reconstruction of the electron track. A major contribution to the track resolution was the misalignment of the Outer Tracker cells. Without energy loss effects, the momentum resolution of the FLT give a core mass resolution of the $J/\psi \to e^+e^-$ signal of 234 MeV/c^2. This resolution is sufficient for an efficient and restrictive mass cut at the FLT level.

The track finding efficiency was approximately 50%, mainly due to a low cell efficiency and a large amount of defective or wrongly mapped channels. There were also considerable problems with data transmission and cabling, which caused the FLT hardware to find only 50% of the tracks that it should have found according to the FLT emulation. The low cell efficiency, the large fraction of dead channels, and the abundantly present noise in the Outer Tracker, prohibited operation of the FLT in 2000. The main problems of the Outer Tracker have now been solved. Together with improvements to the channel mapping and the data transmission, the efficiency should reach 80% per track in future running.

With a modified trigger setup, HERA-B was still able to select $J/\psi \to e^+e^-$ and $J/\psi \to \mu^+\mu^-$ decays in 2000, although at a rate that was three orders of magnitude lower than designed. Part of the data had been taken with both a carbon and a titanium target inserted in the beam. We analysed these data to study nuclear effects in J/ψ production. A firm understanding of these effects is essential for the interpretation of data from heavy-ion experiments, which try to establish a Quark-Gluon-Plasma.

The primary goal of the analysis was a measurement of the A-dependence of the J/ψ production cross section. The key ingredient of this analysis is the measurement of the ratio of the luminosity for the two target wires. We have shown that this ratio can be measured with a systematic uncertainty of approximately 2.3%, which is lower than that of previous experiments such as E866.

The production of J/ψ was studied seperately for both leptonic decays. For both channels, we have found an accurate description of the invariant mass spectra. We have optimised the significance using various cuts, in order to minimise the statistical uncertainty. The measured A-dependence is in agreement with previous measurements, but as yet the statistical uncertainty is relatively large.

We have presented a study of the event, associated to the production of a J/ψ. Such an investigation was not possible at many of the previous J/ψ-experiments, since they used a hadron absorber near the target, which removes the majority of the associated particles. We have found that the associated multiplicity is 40-45% higher than the multiplicity in inclusive inelastic interactions. This increase had been overlooked in theoretical calculations. It is quantitatively understood to be caused by a bias,

introduced by requiring a J/ψ.

A first measurement of the pseudo-rapidity distribution of associated particles has been presented. This serves as input to models, that describe J/ψ suppression through interactions with co-moving hadrons. A Monte Carlo study shows that the density of hadrons, present during the formation of a J/ψ, is similar to the density of stable charged particles, observed in the detector.

HERA-B will resume data taking in may 2002. With the sample of J/ψ, ψ' and χ_c that is expected to be recorded, the experiment will make a significant contribution to the understanding of nuclear effects in charmonium formation. This thesis serves to show how the rich potential of the HERA-B spectrometer can be exploited for such measurements.

Samenvatting

Het doel van de natuurkunde is een zo eenvoudig mogelijke beschrijving te vinden voor de waarneembare verschijnselen. In de afgelopen eeuw heeft de natuurkunde een stormachtige ontwikkeling doorgemaakt, die uiteindelijk tot een succesvolle theorie heeft geleid voor de meest fundamentele processen, gebundeld in het 'Standaard Model'.

Alle verschijnselen zijn een manifestatie van een van vier fundamentele krachten: zwaartekracht (Isaac Newton, 1687), electro-magnetisme (Maxwell, 1873), de zwakke kracht (Fermi, 1933) en de sterke kracht (1973). De krachten komen tot stand door het voortdurend uitwisselen van verschillende kracht-deeltjes door materie-deeltjes. De kracht-deeltjes kunnen ook materie voortbrengen, maar dan altijd tegelijk een materie-deeltje en een anti-materie-deeltje. Als alle bouwstenen in het heelal onstaan zijn uit de krachtdeeltjes, dan valt te verwachten dat er evenveel materie als antimaterie moet zijn.

Opmerkelijk genoeg bevat het heelal zo goed als geen anti-materie en dit vormt een van de belangrijkste onopgeloste vraagstukken voor de moderne natuurkunde. Een mogelijke verklaring werd in 1964 aangedragen. Een vereiste voor deze verklaring was het bestaan van een verschil in het gedrag van materie en anti-materie, genaamd 'CP-schending'. Deze CP schending is in 1964 ontdekt en acht jaar later verklaard als eigenschap van de zwakke kracht. Deze verklaring kon echter, tot voor kort, nooit direct getest worden.

Met de komst van nieuwe detector technologiën konden in de loop van de jaren negentig experimenten ontworpen worden die dit wel konden testen. Aan HERA-B, een van deze experimenten, is het onderzoek voor dit proefschrift gedaan.

De installatie van de HERA-B detector was niet voldoende vergevorderd om een meting van CP schending te doen. Het onderzoek heeft zich daarom gericht op een bescheidener, maar daarom niet minder belangrijk, doel: de productie van J/ψ mesonen in proton-kern botsingen. Een J/ψ meson bestaat uit een een charm quark (een bepaald materie-deeltje) en een anti-charm quark (het bijbehorende anti-materie deeltje), gecreëerd en kortstondig bijeengehouden door de deeltjes van sterke kracht.

Als een charm-anti-charm paar geproduceerd wordt in botsingen van protonen met atoomkernen ondervindt het invloed van de materie in de atoomkern. Deze effecten kunnen er bijvoorbeeld voor zorgen dat het paar uiteenvalt, voordat het een gebonden toestand zoals de J/ψ vormt. Zo zijn er veel verschillende kern-effecten voorgesteld, maar of, en zo ja, in welke mate, deze effecten optreden is onduidelijk.

Het belang om deze effecten te meten en te begrijpen is in de laatste jaren toegenomen. Een aantal experimenten in de wereld bestudeert de eigenschappen van de sterke wisselwerking in materie van hoge druk en hoge temperaturen. Men

verwacht dat bij zeer hoge druk en temperatuur een fase-overgang plaats vindt: de fundamentele materie-deeltjes, die onder normale omstandigheden in groepen van twee of drie samengeklonterd zijn, kunnen dan vrij en ongebonden bewegen. In de eerste fractie van een seconde na het onstaan van het heelal bevond alle materie zich in deze toestand, genaamd 'quark-gluon-plasma'.

Men neemt aan dat de druk en temperatuur, die ontstaan in energetische en frontale botsingen van lood kernen, voldoende zijn om de fase-overgang te bewerkstelligen. In zulke botsingen kunnen ook J/ψ-mesonen geproduceerd worden, maar deze zouden in een quark-gluon-plasma onmiddelijk uiteenvallen en niet meer te meten zijn. Omgekeerd is een sterke afname van het aantal gemeten J/ψ-mesonen waarschijnlijk is de duidelijkste aanwijzing dat de fase-overgang plaatsgevonden heeft.

Zo lang echter andere mogelijke effecten, die ook een afname van het aantal J/ψ mesonen veroorzaken, onvoldoende begrepen zijn, kan met nooit met zekerheid zeggen of de fase-overgang daadwerkelijk gevonden is. Het is daarom belangrijk deze andere effecten goed in kaart te brengen.

Dit proefschrift behandeld twee, min of meer onafhankelijke, onderwerpen. Het eerste deel van het proefschrift is gewijd aan het functioneren van de 'trigger' van Hera-B. Deze trigger selecteert uit de miljoenen proton-kern botsingen die de detector elke seconde registreert, de 0.001% die interessant kunnen zijn voor verdere bestudering. Een goed functionerende trigger is essentieel voor het succes van het experiment. Het proefschrift beschrijft een aantal problemen van de trigger en doet suggesties om deze trigger te verbeteren.

Het tweede deel omvat een onderzoek naar kern-effecten in J/ψ productie. Het belangrijkste onderdeel is een meting van de afhankelijkheid van het aantal geproduceerde J/ψ mesonen met de grootte van de kern. Het proefschrift toont aan dat kern-effecten al te zien zijn in de HERA-B data van 2000. De metingen bevestigen al eerder gevonden effecten op J/ψ productie. Het toont ook aan dat HERA-B, met de gegevens die vanaf 2002 genomen worden, een belangrijke bijdrage zal kunnen leveren om het begrip over kern-effecten in J/ψ productie te vergroten.

Dankwoord

Dit proefschrift zou nooit tot stand gekomen zijn zonder de steun en adviezen van velen. Honderden mensen hebben meegewerkt aan het ontwerpen en opbouwen van het experiment, dat een uitdagende omgeving voor onderzoek heeft geboden. Velen hebben mij gedurende de afgelopen vijf jaar nuttige suggesties aan de hand gedaan die hun weerslag vinden in dit proefschrift.

Ik wil een aantal mensen in het bijzonder bedanken voor hun bijdrage.

In de eerste en voornaamste plaats mijn naaste collega's Wouter en Maaijke. Ik prijs me gelukkig met jullie als een team samengewerkt te hebben. Jullie tips en ondersteuning zijn onmisbaar geweest.

Olaf dank ik voor zijn begeleiding in de eerste fase van het onderzoek en voor het wegwijs maken in de Hera-B - bijenkorf.

Ik wil Jelle bedanken, die mij het nodige bijgebracht heeft over electronica en altijd behulpzaam is geweest bij het oplossen van de problemen die opdoken tijdens het testen en installeren van de linkboards.

Mijn co-promotor Thomas wil ik bedanken voor zijn hulp gedurende de laatste fase van het onderzoek. Door zijn steun heb ik ongehinderd aan mijn proefschrift kunnen werken. Zijn kritische lezen van het manuscript zijn zeker bevorderlijk geweest.

Ik dank Paul, mijn promotor, die ervoor gezorgd heeft dat het plotselinge vertrek van Adriaan geenszins een vertraging van het promotieonderzoek heeft veroorzaakt. Zijn correcties hebben dit proefschrift aanzienlijk leesbaarder gemaakt.

Gedurende mijn verblijf in Hamburg heb ik met veel plezier in de FLT groep van Hera-B gewerkt. De sfeer in deze groep was altijd zeer opbouwend. Mijn onderzoek naar het functioneren van FLT zou zonder hun hulp niet mogelijk zijn geweest. In het bijzonder wil ik daarvoor Dominik en Bernhard bedanken, die, elk op hun manier, een voorbeeld voor mij zijn geweest.

Ik heb de werkomgeving op het NIKHEF altijd als stimulerend en plezierig ervaren, waar ieders deur altijd open stond. Ik dank de collega's van de B-fysica groep voor hun steun en belangstelling en denk met plezier terug aan de levendige en informatieve groepsvergaderingen. Met mijn mede A.I.O.'s op het NIKHEF, in het bijzonder de leden van 'Probleem van de Dag', heb ik een mooie tijd beleefd.

Tenslotte wil ik mijn familie en vrienden bedanken voor hun belangstelling, geduld en begrip. Chiara, grazie per tutto il resto.